Novel single photon emitters based on color centers in diamond

Igor Aharonovich

Submitted in total fulfilment of the requirements of the degree of Doctor of Philosophy

November 2010

School of Physics
University of Melbourne

Abstract

Exploitation of emerging quantum technologies requires efficient fabrication of key building blocks. Single photon sources are one of these fundamental constituents that are presently pushing the bounds of existing materials and fabrication techniques. Color centers in diamond are very attractive in this respect since they are the only photostable solid-state single photon emitters operating at room temperature known to date.

The Nitrogen-Vacancy (NV) complex is one example of such an optical center and has been subject to intensive research due to the availability of optical readout of its individual electronic spin state. However, the NV center has fundamental limitations: strong phonon coupling of the excited state which results in a broad photoluminescence spectrum (~ 100 nm) of which the zero-phonon line makes up only 4%. Emission of single photons in the zero phonon line is then extremely weak, typically on the order of a few thousands of photons per second. Such count rates are insufficient for the realization of advanced quantum information processing protocols.

To move beyond the limitations of the NV there is an emerging need to identify and fabricate novel diamond based single photon emitters with improved photo-physical characteristics. Development of such emitters is the main goal of this thesis.

We first concentrate on the recent progress in materials science and fabrication techniques of high quality nanodiamond crystals. We demonstrate the ability to grow high quality, submicron sized diamond crystals with a control over their final size and density using a microwave assisted chemical vapor deposition.

We then study two methodologies to engineer diamond based single photon emitters in the grown nanodiamonds. In the first, nickel is implanted into the substrate onto which the nanocrystals are subsequently grown. During the diamond growth, the substrate is slightly etched and the nickel atoms diffuse and incorporate into the growing crystals. In the second we employ direct ion implantation of nickel into already deposited individual diamond nanocrystals. Optical and correlation spectroscopy measurements reveal that these methodologies are effective to fabricate nickel related single photon emitters, with zero phonon lines centered in the near infra-red and a short excited state lifetime (~3 ns).

Furthermore, the ability of diamond to host various luminescence centers prompted the discovery of a new class of ultra bright single photon emitters. These new emitters found in diamond crystals grown on sapphire substrate and assigned to chromium, which is present in the substrate and incorporated into the crystal during the growth. Nanodiamonds hosting these centers deliver outstanding performance such as narrow photoluminescence in the near infra-red and ultra bright single photon emission with count rate of ~ 3.2×10^6 counts/s – the brightest single photon source known to date. Importantly, some of the emitters exhibit a photon statistics without any photon bunching at saturation, indicating a two-level system without shelving states. This latter point is highly significant in the application of these centers to quantum metrology.

Employing ion implantation technique, we verify the presence of chromium in the new centers and show that bright chromium emitters can be successfully fabricated in bulk single crystal diamond. The emitters have an absorption dipole along one of the <100> directions and fully polarized emission with a zero phonon line centered at 749 nm. It also possesses an extremely short lifetime of 1 ns and exhibits a count rate of ~ 0.5×10^6 counts/s. The new class of chromium related centers surpasses all bulk single crystal diamond emitters, and are competitive with many nanodiamond systems and holds a great potential to be incorporated in quantum information processing and biosensing applications.

The dipole orientation of the chromium emitters is measured by recording the emission pattern of single emitters. The dipoles are found to be nearly orthogonal to the diamond air interface. Combining the imaging of the dipoles and measuring the decay rates of the emitters close to the diamond-air interface and in the unbounded medium, the quantum efficiency of the chromium centers is determined to be ~ 30%.

Finally, we study the photo-physical properties of the single defects embedded in nanodiamonds in cryogenic temperature (2 K). The spectral stability of the defects is investigated and optical resonance linewidth of 4 GHz is measured using resonant excitation on the zero phonon line. Although Fourier transform limited emission is not achieved, our results show that it should be possible to use consecutive photons emitted by single defects in diamond to perform two photon interference experiments, which is a highly significant milestone in the development of diamond based quantum emitters.

Declaration

This is to certify that:

(i) The thesis comprises only my original work towards the PhD except where indicated in the Preface,

(ii) Due acknowledgement has been made in the text to all other material used,

(iii) The thesis is less than 100,000 words in length, exclusive of tables, maps, bibliographies and appendices.

……

Igor Aharonovich

Preface

The following work was performed in collaboration with a number of researchers in various institutions, as follows:

- The initial characterization of the color centers using confocal microscopy was performed in collaboration with C. Zhou, J. F. Roch and F. Treussart, in Ecole Normale Supérieure de Cachan, France
- The measurements at cryogenic temperatures were performed in collaboration with P. Siyushev, V. Jacques, F. Jelezko and J. Wrachtrup in Physikalisches Institut, Universität Stuttgart, Germany and T Muller, M Atature, Cavendish laboratory, University of Cambridge
- Ion implantation was partially carried out in the Australian National University with the assistance of B Johnson and J. McCallum

In all the above circumstances I actively participated in the experimental work, designed and performed the measurements and analyzed the data.

In certain places in the thesis, figures from other sources have been used. An appropriate reference has been inserted in the figure caption to acknowledge the source of the figure.

Acknowledgments

I wish to acknowledge the Australian Research Network for Advanced Materials, the Australian Research Council for Nanotechnology Network, Sigma-Xi and SPIE for the travel funding which was provided during my PhD candidature.

I would like to thank the electrical and mechanical workshops in the School of Physics for providing the important technical assistance with our experiments. Nothing would have worked without you guys.

I would also like to acknowledge all the administrative staff, particularly Trish, Hayley, Cilla and Cheryl. Thanks for helping with the financial and the administrative paper work.

I wish to thank room 204 – especially Michelle, Jess, Nik, John, Jack and Virginia! The office always had a terrific vibe which helped a lot through my PhD. I also wish to acknowledge the rest of the students in the Diamond gang: Jinghua, Babs and Alastair. Thanks for the great team work and good luck with your own submission!

This thesis would have never been completed without an ongoing support of my friends here in Australia and overseas. Thank you for awesome leisure time spent together. Your support with my English abilities (or their lack) is also very much appreciated. I wish to especially thank Akina for her continuing encouragement. I am also thankful to all my friends, colleagues and superiors at International House, where I lived through most of my PhD and received a great support to pursue my studies.

Huge appreciation also to the research fellows who helped a lot with the experimental work and stimulated new discussions and ideas: Andrew Greentree, Julius Orwa, David Simpson, Brett Johnson, Brant Gibson, Kumar Ganesan, Alberto Cimmino, Paul Spizzirri, Sergey Rubanov and Andrew Alves.

I wish to thank our invaluable collaborators, particularly Fedor Jelezko, Mete Atature, Jean-François Roch and Charles Santori. Thank you for your kind hospitality in your labs and for providing me with important insights into quantum optics and the NV center. I

am also grateful to Lothar Bischoff for teaching me about focused ion beam techniques. Mark Newton and Daniel Twitchen are gratefully acknowledged for the help with diamond annealing. I am also thankful to Prof Malcolm Wallace for allowing me to use his cathodoluminescence microscope.

I wish to express an enormous gratefulness to Stefania Castelletto. I was privileged to work with her during the last two years of my PhD and obtained a vast knowledge in theoretical and experimental quantum optics. Your ongoing motivation and scientific curiosity generated more ideas than I can ever implement.

I wish to express sincere gratitude to my co-supervisors Prof Jeff McCallum and Prof David Jamieson. Your comments and suggestions were always helpful and valuable.

The most important, I wish to thank my supervisor Prof Steven Prawer. Steven, you are a faithful friend, an encouraging mentor and an outstanding supervisor. Thank you for your comprehensive guidance, for your allegiance, time and efforts. Thank you for the endless opportunities you granted me with and for your ongoing feedback which you provided regardless the geographical locations and the time zones. You made this PhD an amazing, enjoyable journey and showed me how fascinating science could be.

Finally, I wish to express a truthful and heartfelt appreciation to my family who despite being thousands of miles away always supported me and even came once for a visit. This thesis is dedicated to you.

Contents

List of Figures

Abbreviations

APD – avalanche photo diode

CL – cathodoluminescence

CVD – chemical vapor deposition

CW – continuous wavelength

EPR – electron paramagnetic resonance

FIB – focused ion beam

FWHM – full width at half maximum

HBT – Hanbury Brown and Twiss

HPHT – high pressure high temperature

IRF – instrument response function

LED – light emitting diode

MPCVD – microwave plasma chemical vapor deposition

NIR – near infra-red

PL – photoluminescence

QDs – quantum dots

QE – quantum efficiency

QIP – quantum information processing

QKD – quantum key distribution

SEM – scanning electron microscope

SPS – single photon source

SRIM – stopping and range of ions in matter

STED – stimulated emission depletion

ZPL – zero phonon line

Chapter 1

Introduction

The rapidly growing demand for faster computation, greater internet usage and reduced power consumption has been the driving force for the miniaturization of electronic components. New concepts of synthesis such as the "bottom up" approach and self assembly techniques have emerged as candidates for the fabrication of nano-electronic components[1, 2]. In parallel, in the past decade, quantum information processing (QIP)[3-5] came into sight harnessing the principles of quantum mechanics, to create a new paradigm for computing.

QIP includes many practical applications such as quantum key distribution (QKD)[6] (which allows perfectly secured communications protected by the laws of quantum mechanics), quantum metrology, quantum lithography and perhaps the most ambitious challenge of the 21st century – the quantum computer. These applications place stringent demands on the development of platforms that can host them and require new paradigms for their efficient fabrication and use. Furthermore, to engineer practical devices employing quantum effects, one needs to develop components, initialization methods, readout techniques and interconnects, bearing in mind the importance of scalability. Developing quantum devices will require a high degree of proficiency in fabrication and manipulation of individual quantum states on the sub nanometer scale.

The quantum state of light - a photon – exemplifies this need and has been proposed as a building block for QIP[7-10]. Transmission at the speed of light, low noise, decoherence free and a possibility for free space communication make photons extremely valuable for many applications in QIP. Individual photons can be easily employed as quantum bits (qubits) while the information can be encoded in their polarization. Indeed, practical QKD based on encoding the information into the polarization state of the photon has been demonstrated. Moreover, an algorithm for optical quantum computers based on linear

optical elements, single photon sources and single photon detectors has been proposed[11] and demonstrated[10, 12].

For the realization of quantum technologies based on the quantum state of light, systems which can generate pure single photons on demand (triggered single photon sources) are highly sought after. A perfect single photon source will have absolute photostability (no blinking or bleaching), emit only one photon per excitation pulse with a suppressed two photon emission probability and preferably generate indistinguishable photons. The last parameter is necessary for many QIP applications, apart from QKD.

Few single quantum emitters have been proposed to meet the criteria mentioned above: Single atoms[13], for instance, generate indistinguishable single photons on demand since the electronic transitions remain constant and isolated from the environment. However, manipulation and scalability of a single atom technology is challenging. Quantum dots, often called artificial atoms, are a much better choice. The fabrication techniques of quantum dots are well established. Since nanostructures can be engineered upon demand in terms of material composition and shape, their emission properties can be tailored[14-16]. Quantum optics with QDs has shown tremendous progress over recent years, particularly, due to its integration with photonic cavities which dramatically improves the quantum properties of the source in terms of efficiency and indistinguishability[16, 17]. Nevertheless, QDs suffer from blinking and require low temperature operation[14].

Color centers in diamond are also important candidates as ultimate single photon sources. Their superiority includes unprecedented photostability, room temperature operation and ease of fabrication. Diamond based single photon sources can boost the quantum photonics technologies and pave the way from a laboratory setting toward practical devices exploiting quantum mechanical effects.

One of the disadvantages of diamond is its high refractive index (2.4) which deters the light to be efficiently coupled to external optical structures. This hurdle may be overcome by using nanodiamonds – the benefits and challenges of which are explored throughout this thesis.

1.1 Diamond color centers for quantum information processing

Diamond is a very attractive material for QIP particularly due to the fact that the three common sources of decoherence – nuclear spins (which are limited by the ^{13}C concentration), low electron concentration (due to the wide bandgap) and low phonon scattering (due to the high Debye temperature) - are minimized[18]. Point defects in diamond (often a single impurity atom or a complex consisting of an atom and a vacancy), can be optically active and are called color centers. Some of these defects can generate single photons upon optical excitation[19, 20].

Color centers in diamond are found in either monolithic diamond or nanocrystalline diamonds, opening a wide range of opportunities for their integration and manipulation.

Several designs for large scale quantum architectures employing color centers in monolithic diamond have been proposed[21]. On the other hand, applications such as magnetic imaging at the nanoscale[22-24] or QKD employ single photon emitters in nanocrystalline diamonds.

The nitrogen-vacancy (NV) center is the most studied center for QIP applications owing to the availability of optical read-out of the individual spin state[25, 26]. However, the NV center has fundamental limitations - strong phonon coupling of the excited state which results in a broad photoluminescence spectrum (~ 100 nm) of which the zero phonon line (ZPL) makes up only 4%. Emission of single photons in the ZPL is then extremely weak, typically on the order of a few thousand photons per second. Such count rates are insufficient for the realization of advanced QIP protocols based on indistinguishable photons. These constraints introduce the need for much better diamond based single photon source with superior photo-physical properties.

To move beyond the limitations of the NV center, alternative diamond based single photon emitters such as the silicon vacancy (SiV)[20] or the nickel related complex (NE8)[27-29] have been investigated. However, the very low emission rates of the SiV center, and the difficulty of controllably fabricating these centers at the single center level, has motivated the search for alternative diamond based single photon sources. A major challenge in the material science community is to unambiguously identify new diamond based color centers. Such centers would ideally possess a narrow bandwidth

emission centered in the infra-red, high count rate, and be readily and reliably engineered in both bulk and nanocrystalline materials.

1.2 Summary of thesis

The research into diamond color centers on the single defect level and the use of diamond as a platform for QIP are still in their infancy. There are many open questions and unknowns, which makes the research extremely fascinating. The aim of this thesis is the controlled fabrication of novel ultra bright single photon sources from color centers in diamond.

Chapter 2 presents a brief introduction about diamond as a material – including growth methods, color centers and ion implantation techniques to modify the material. The definition of non classical light and quantum emitters is then discussed. Detection techniques, candidates for single photon generation and applications of single photon sources are also presented.

In chapter 3 the experimental methodologies and the equipment involved are explained. Fabrication techniques such as chemical vapor deposition (CVD) and ion implantation, and characterization methods including confocal microscopy and photoluminescence measurements are described.

Chapter 4 is the first experimental chapter of the thesis. It focuses on the growth of sub micron sized diamonds employing microwave assisted chemical vapor deposition technique. A unique approach to the growth of isolated, high quality nanodiamond crystals under high pressure plasma deposition conditions is presented and discussed.

Chapter 5 and 6 discuss novel methods for fabrication of color centers in bulk diamond and nanodiamond crystals. Chapter 5 is dedicated to ion implantation of nickel as a “post growth” approach for engineering of color centers, and chapter 6 introduces a new methodology to incorporate an impurity during CVD diamond growth. This method involves implantation of nickel atoms into the substrate onto which the diamonds are subsequently grown.

The discovery of novel chromium related color centers is the topic of chapter 7 and the prime result of the thesis. A new class of emitters originating from chromium related

defects in CVD diamond, exhibiting a count rate of millions of photons per second is presented. We show that these emitters can be fabricated by combining the ability to grow high quality sub micron diamond crystals (chapter 4) in conjunction with a technique to incorporate the impurity during CVD growth (chapter 6).

In the second part of this chapter, engineering the chromium related defects in single crystal diamond by ion implantation is presented. The excellent agreement between the photoluminescence spectra, in terms of the ZPL and full width at half maximum, in bulk diamond and nanodiamonds clearly indicates that this class of emitters can be attributed to chromium. Combining the imaging of the chromium emission dipoles and measuring the decay rates of the emitters close to the diamond-air interface and in the unbounded medium, the quantum efficiency of the chromium centers is determined to be ~ 30%.

The last experimental chapter, chapter 8, describes optical measurements of single photon emitters in the near infrared performed at cryogenic temperatures (liquid helium). A photoluminescence excitation spectrum from a single diamond color center reveals a narrow linewidth of 4 GHz. In addition, the indistinguishability of consecutively emitted photons is measured.

Finally, in chapter 9 the thesis is concluded and future work is outlined.

Chapter 2

Background

This thesis reports the controlled fabrication of single photon emitters from color centers in diamond. Therefore, the introduction is divided into two main sections: (1) Materials: which introduces diamond as a material, growth methodologies and ion implantation techniques relevant to diamond. (2) Optics: which includes the fundamental discussion about sub-Poissonian light, the second order autocorrelation function, detection schemes, photophysics of single photon emitters, and finally single photon source candidates and their applications.

2.1 Diamond

Diamond is a carbon allotrope with a complete sp^3 atomic configuration, where each carbon atom is bonded to four carbon atoms in a tetrahedral symmetry. The diamond unit cell belongs to the "diamond" crystalline lattice structure, which consists of two face centered cubic Bravais lattices, displaced by ¼ of the unit cell in each direction (Figure 2.1).

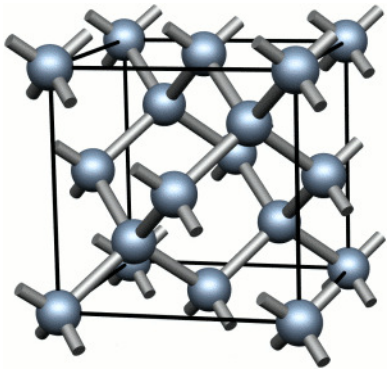

Figure 2.1 Crystallographic diamond structure.

Diamond is a unique material endowed with extreme physical properties: it is the hardest material with the highest Young's modulus (~1 TPa) and a high atomic density (3.5 g/cm^3), it possesses a wide band gap (5.5 eV at room temperature), it is chemically inert and biocompatible. The main physical and optical properties of the diamond are shown in Table 2.1. Nevertheless, despite all these amazing properties, diamond is not used as routinely as other materials, particularly, due to its cost, difficulty of fabrication and lack of well developed processing tools.

Density	3.5 g/cm^3
Crystal system	Cubic (two FCC shifted by (¼, ¼, ¼)
Lattice parameter	3.57 Å
Thermal conductivity	2×10^3 W/mK
Dielectric constant	5.7
Refractive index	~2.4
Young's modulus	~1 TPa
First Raman line	1332 cm^{-1}
Band gap	5.5 eV

Table 2.1 Main physical and optical properties of diamond

Diamond can be naturally extracted from the lithospheric mantle below the earth's surface, where high pressure and high temperature (HPHT) conditions are suitable for diamond formation. In the middle of the 20th century scientists and engineers from General Electric created similar conditions of HPHT and demonstrated the first synthetic diamond grown in a laboratory[30]. This process, however, is complicated and requires high cost maintenance equipment. Alternative methods of diamond synthesis like the chemical vapor deposition (CVD)[31-33] and detonation nanodiamond[34, 35] were introduced in following years.

The simplicity, flexibility and a control over incorporation of impurities are the main advantages of the CVD process over the HPHT fabrication. The main gas phase reactants of a typical diamond CVD process are methane and hydrogen. Methane is the source of carbon, while hydrogen is responsible for terminating the dangling carbon bonds on the

growth surface, thus preventing the formation of a graphite structure[33]. Since graphite is thermodynamically stable phase of carbon, CVD process is driven by kinetics and not thermodynamics. This is achieved by a high gas phase non equilibrium, where a very high fraction of hydrogen to methane (generally 96:4) is used.

There are a few variations to the CVD techniques[31-33, 36], including microwave, hot filament, cathode arc discharge and welding torch, which are all used to ionize the introduced gases. Since microwave plasma CVD (MPCVD) is used in our research, this topic is covered in more detail.

2.1.1 Microwave plasma chemical vapor deposition of diamond

Schematic illustration of diamond chemical vapor deposition is shown in Figure 2.2.

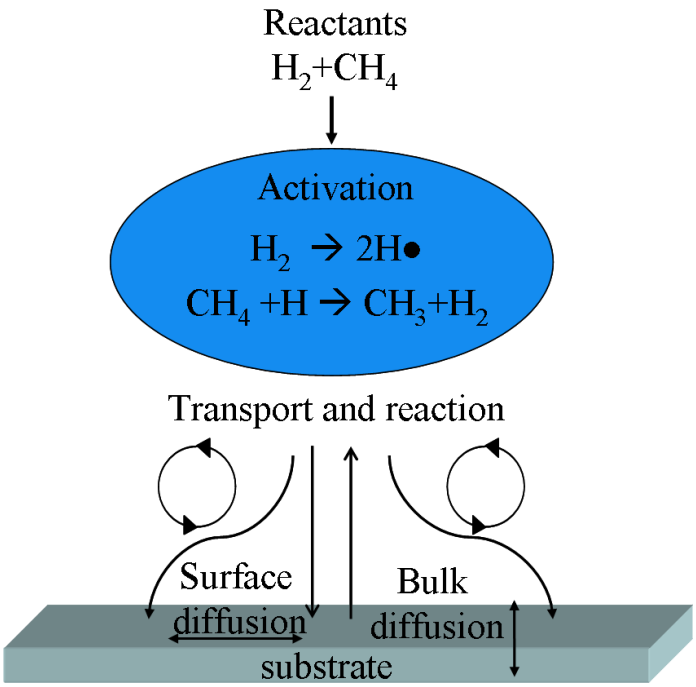

Figure 2.2. Schematic illustration of the chemical processes involved in a diamond CVD[37]. The reactant gases are ionized and radicals are formed. Through various transport mechanisms, the species are transported to the surface and build the diamond structure.

An understanding of diamond deposition is not yet complete[38]. Classically, it can be described as follows: methane and hydrogen enter a high temperature energetic region, in

which the gases are ionized by the plasma. The species are transported through diffusion or convection throughout the chamber and eventually reach the diamond surface. On the surface, various chemical processes such as adsorption, diffusion and chemical reactions can occur. Once the surface is stabilized and graphitic formation is terminated by the hydrogen, the atoms form a mixture of hydrocarbon species including reactive carbon-containing radicals. Surface radical sites are created by gaseous activation of H atoms and occasionally react with the gas phase carbon-containing radicals, resulting in an adsorbed carbon species. Finally, any remnants of sp^2 or sp carbon sites on the surface will react with the gaseous species to convert to sp^3 bonded carbon.

Typically, microwave radiation at a frequency of 2.45 GHz is used during the MPCVD process and the growth occurs in the temperature range 800-1100°C[39]. The substrate temperature can be controlled by a heater and its distance from the plasma ball can be varied as well.

Diamond CVD growth can be divided into two distinct types: homogeneous and heterogeneous. The first type refers to diamond grown on a diamond surface. Smooth stress free films can be grown on (100) surfaces while films deposited on (111) surfaces generally have a higher defect density and are subject to cracking to relief stress[33].

Growing diamond on non diamond substrates, also referred as heterogeneous growth, is challenging due to lack of native nucleation. The heterogeneous growth can be divided into two main streams: growth of individual diamond crystals[40-42] or growth of a continuous diamond film[43, 44]. For many years, diamond films attracted much more attention due to their technological applications. Therefore, very high nucleation densities were required to grow high quality diamond films. The nucleation was performed by abrasion[45] or seeding with nanodiamond powder[46]. To date, growth of diamond films have been demonstrated on many substrates including silicon, titanium, nickel, molybdenum and others[41].

To achieve growth of dispersed individual crystals, the substrate is seeded with nanodiamond seeds. The initial seed density determines the final crystal density on the substrate. The growth of diamonds from individual seed is three dimensional, and in case of a high nucleation density, these individual diamond crystals will eventually come into contact to form a polycrystalline film. When the growth of individual diamond crystals is

carried out, it is important to use smooth and clean substrates. Any morphological defects or contaminations on the surface may result in secondary nucleation of diamonds without the crystal being grown on the diamond seed. This will result in a large size distribution of the final crystals and inhomogeneous density on the substrate.

The general crystallite shape and the final morphology of the diamond crystal depends upon the growth conditions: Cubo-octahedra are produced at low carbon deposition rates[47], whereas more spherical and amorphous material results from higher carbon ratios. The transition of crystallite shape from cubic through cubo-octahedra to octahedra is determined by relative growth rates of (111) and (100) faces. For many applications, the morphological and crystalline nature of the deposited diamond crystals is important. Adhesion, wear behavior, and other interfacial characteristics may be affected by the surface structure. Control of surface morphology is therefore important to obtain optically smooth surfaces since final polishing rates are orientation-dependent.

The gas composition is a very important parameter of the CVD growth. Common variations include oxygen and a few percent of nitrogen or any other elements added explicitly for doping (B_2H_6 for boron doping for instance[48]). Addition of nitrogen, which is difficult to eliminate from the growth chamber, has been shown to modify the morphology and increase the growth rate[49, 50].

Intense modeling of MPCVD reactors and morphology development under different ambient conditions have progressively provided an important understanding of diamond growth[51, 52]. An enormous set of parameters (electromagnetic fields in the reaction chamber, gas heating, heat and mass transfer, charged and neutral species involved, real source gas mixtures (i.e. H/C or H/C/noble gas mixtures), species diffusion and gas–surface processes) has resulted in diamond growth being experimentally complicated. Nevertheless, as a result of the vast effort on both academic and industrial fronts, 1 inch CVD diamond wafers have become commercially available[53, 54].

In this thesis, the focus is on a controlled growth of dispersed, individual, sub micron diamond crystals with selected color centers. The nanometer size of the crystals is necessary in order to overcome the geometrical limitation of large crystals which hinders the collection of the emitted light due to high refraction index of the diamond and internal reflection.

2.1.2 Optical centers in diamond

Diamond hosts more than 500 optical centers with luminescence signals from deep ultra violet (UV) to the infrared, originated from various defects and impurities within its crystallographic lattice[55]. This characteristic of diamond is in fact the most relevant to this work. In this section the optical properties and formation mechanisms of some of these centers are discussed.

2.1.2.1 Vacancy and self interstitial

The simplest defect in diamond is an interstitial carbon or a vacancy. Systematic modeling suggests that split <100> interstitial is the most stable configuration of this defect, which is known as the R2 center[56, 57]. The ground state of the center has a D_{2d} symmetry[58]. It is produced by electron or neutron irradiation and has optical absorption lines around 735 nm. This defect is annealed out above 750 K. Further measurements of electron irradiated diamond enriched with ^{13}C revealed the two parallel nearest neighbor <100> split interstitials and finally three non planar parallel <100> split interstitials exist in diamond crystal[59-61].

Two charge states – negatively charged and neutral are known for the vacancy center in diamond[62]. The neutral vacancy, known also as the GR1 optical center, has a ZPL at 741 nm. The photoluminescence (PL) arises due to a transition from a doubly degenerate orbital (E) state to a triple degenerate (T) excited state in a tetrahedral center[63-67]. Upon annealing the vacancy migrates and couples with other impurities in diamond. This can be observed by monitoring the decrease and eventual disappearance of the GR1 peak[68].

Electron-paramagnetic-resonance (EPR) studies showed that only center labeled R4/W6 is prominent in the intermediate temperature range between 900 K and 1000 K. R4/W6 centers can be produced in type IIa diamonds, but only low concentrations were ever produced in rich nitrogen, type Ib diamonds, where nitrogen atoms trap the mobile vacancies. When the nitrogen concentration was greater than the vacancy concentration, the R4/W6 were not observed, even after annealing. Lea-Wilson then concluded that the R4/W6 was the nearest-neighbor divacancy center in the neutral charge state[69].

Subsequently, EPR studies of ^{13}C enriched diamond confirmed this identification[70]. The center has a C_{2h} symmetry at low temperatures (~30 K), while at higher temperature this symmetry is distorted, possibly due to rapid spin lattice relaxation[70].

In addition, vacancies play a central role in engineering other defects in diamond. Given the highly dense diamond matrix, some impurities which have larger dimensions than carbon tend to cause a local lattice expansion. This can be compensated and stabilized by an adjacent vacancy. Therefore, an annealing step is often used to allow the vacancies to become mobile and recombine with the other impurities in the lattice.

2.1.2.2 Nitrogen

Nitrogen is the most common impurity in diamond, particularly because it has a similar atomic size as carbon and it often present during the diamond growth. Nitrogen generally appears as a substitutional atom and creates a distortion along the (111) axis with the neighboring carbon atom[71-73]. The ZPL of the neutral single substitutional nitrogen has not been conclusively identified.

If a vacancy is neighboring the nitrogen along the (111) direction, a center known as a nitrogen vacancy (NV) is formed[74-76]. The atomic structure of this center is shown in Figure 2.3a. Other additional complexes of nitrogen and vacancies of the form of N_xV_y have also been modeled and observed[77]. The origin of the vacancies is generally proton or electron irradiation as will be discussed in the following section. A subsequent annealing to 800°C after irradiation of nitrogen containing diamond efficiently creates the NV centers[68].

The NV center has two charge states: the negatively charged, $(NV)^-$, center with a ZPL centered at 637 nm and a neutral, $(NV)^0$, center with a ZPL centered at 575 nm[78, 79]. The charge fluctuation from the negatively charged to the neutral NV was recently observed by monitoring individual NV centers in diamond[80]. At this stage it is unclear how to prevent the electron from hoping on and off the NV center and keep only one charge state stable.

2.1.2.3 Transition metals

Transition metals, specially nickel, are often present in synthetic HPHT diamond due to their role as catalysts[81, 82]. During the HPHT process, transition metals such as nickel and cobalt solely incorporated into the {111} growth sectors and their concentration can vary within the same growth sector[83]. It was also shown that faster growth rates increases the concentration of nickel and cobalt in the {111} sectors and of nitrogen in {001} sectors. Unexpectedly however, the increase in nickel or cobalt is accompanied by a reduction in the nitrogen concentration[83]. Although the exact reason for this is yet unclear, it was proposed that the presence of these large impurity atoms on the growing diamond surface, reduces the probability of nitrogen being incorporated[83].

The vast abundance of transition metals in natural diamond crystals has attracted major interest in the scientific community and significant research has been carried out to map out their optical and physical properties.

The most common nickel related defect shows a PL doublet around 883/885 nm[84, 85]. The center has a trigonal symmetry and the doublet structure is a result of the spin orbital interaction splitting the ground state of the center. A fine structure of the ZPL resolves that each peak consists of four components associated with stable nickel isotopes. This center is repeatedly observed in synthetic diamonds grown in the presence of a nickel catalyst.

In high nitrogen content diamonds, a family of nickel nitrogen complexes (NEx, $1 \leq x \leq 8$) is formed[81, 82, 86], as has been confirmed by electron paramagnetic resonance (EPR) measurements[81, 87]. In some cases an additional HPHT annealing process is applied to enhance the formation probability of these centers[88, 89]. It was also shown, that the NE4 defect, ascribed to a nickel atom in a di-vacancy[90, 91], acts as nucleus for aggregation of nitrogen atoms. Once the NE4 defect is formed, up to four nitrogen atoms can be captured consecutively in different configurations to form the rest of the NEx family[88]. Most of the NEx complexes were also observed optically, with the NE1 centered in the UV (ZPL at 472 nm) and NE8 centered in the near infra-red (NIR) (ZPL at 794 nm). The later, which consists of four nitrogen atoms neighboring a nickel atom, is particularly interesting for optical applications due to its narrow emission in the NIR. Its atomic structure is depicted in Figure 2.3b.

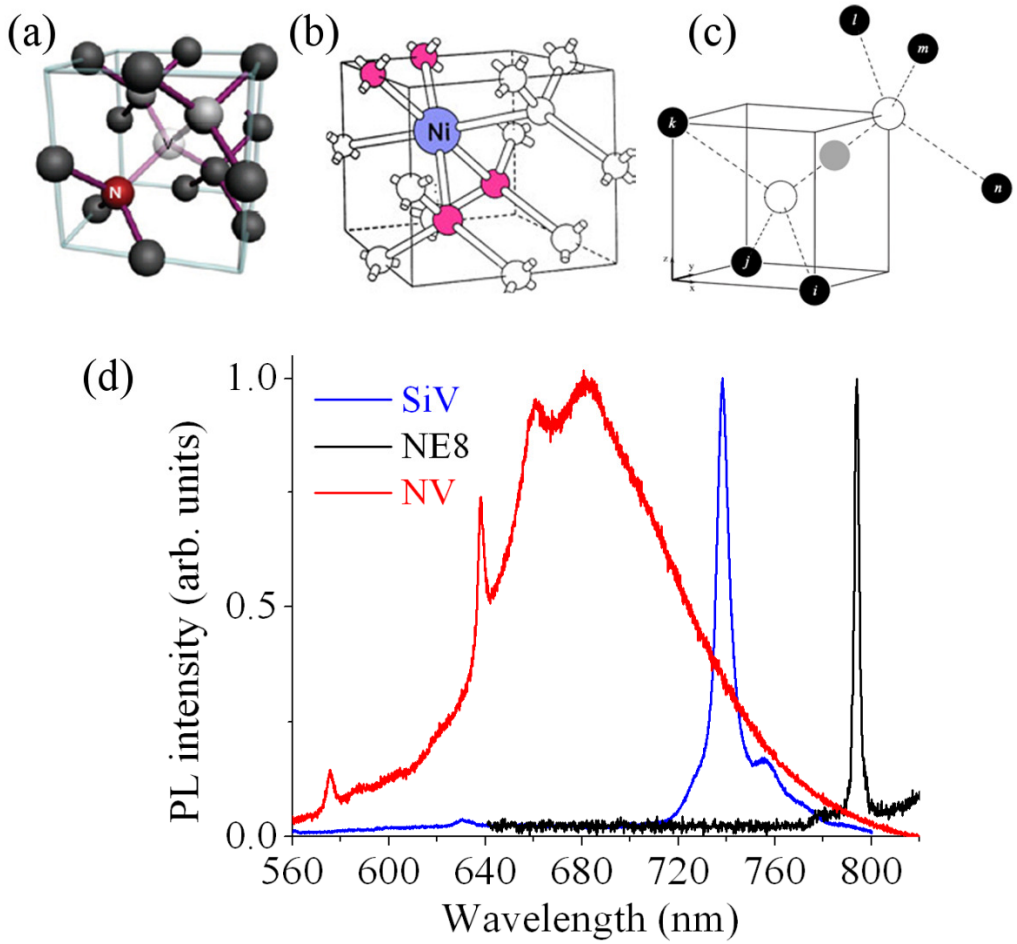

Figure 2.3. Crystallographic models of three defects in diamond which evolved particular interest in recent years due to their ability to emit single photons: (a) the NV center (image is taken from Ref [92]) (b) the nickel related NE8 center (image is taken from Ref [29]) and (c) the SiV center (image is taken from Ref [93]. (d) The PL spectra of each of these defects.

Besides nickel, other transition metals have shown PL and EPR features in diamond[59, 94]. Cobalt[95-97] and titanium[98] are particularly interesting since they exhibit narrow emission lines in the NIR. Similar to nickel, cobalt possibly forms centers with mobile nitrogen atoms. Indeed, no cobalt related defects were observed when nitrogen getters were used during diamond growth. The structure of the titanium related center is believed to be two titanium atoms occupying tetrahedral interstitial positions along the <110> axis[98].

2.1.2.4 Silicon defects

Silicon defects are very common in CVD grown diamond due to routine use of silicon substrates and quartz bell jars. The most abundant silicon related defect is the silicon vacancy (SiV) center, which has a ZPL centered at 737 nm as shown in Figure 2.3d. This line can be observed by an intentional addition of silicon to the diamond growth cell or by silicon implantation [99-101] into pristine diamond. The structure of the ZPL is complicated and consists of many lines, originating from the split ground and excited states as well as different silicon isotopes[99, 102]. The atomic structure of the 737 nm defect consists of a silicon atom splitting two vacancies, as was recently confirmed by EPR measurements[93]. There is a disagreement in the literature regarding the charge state of the complex, however, recent results suggest a negative charge state for this center[93]. Its atomic structure is depicted in Figure 2.3c.

2.1.3 Ion Implantation

Ion implantation is a widely used technique to modify physical, chemical and optical properties of a material by introducing external impurities into its matrix[103-105]. To perform an implantation, atoms are ionized, accelerated with an electric field and "bombarded" into the target material. The end of range of the implanted ions is determined by the acceleration energy (typically ranging from few keV to MeV). Due to an introduction of external atoms by bombardment, ion beam induced damage is always associated with the implantation. Therefore, a thermal annealing sequence is usually applied after the implantation to allow the material to recover. Combination of ion implantation and annealing (for dopant activation or defects removal) is technologically important and routinely employed in the semiconductor industry.

To predict the profile of the implanted ions in the implanted matrix, a Monte Carlo based modeling package known as Stopping and Range of Ions in Matter (SRIM)[106] was developed. The software is based on the estimation of different probabilities of collisions among the implanted ions while taking into account the lattice parameters such as density and lattice spacing. The output provides a useful prediction regarding the stopping range

of the implanted ions and its distribution, damage events, and concentration of the created vacancies.

Ion implantation is most commonly used in the semiconductor industry where dopants like arsenic, boron or phosphorus are implanted into a silicon matrix for electrical activation[107]. The aim of the implantation in this case, is to modify the intrinsic silicon structure to a p-doped or n-doped material to fabricate electronic devices. After the implantation, the silicon is thermally annealed and becomes conductive. On the other hand, ion implantation in diamond to modify its electrical properties turned out to be very challenging[103, 108, 109]. Diamond has a very dense lattice which limits the internal diffusion of impurities and inhibits an effective substitutional doping. Moreover, its tendency to irreversibly graphitize upon a high implantation fluence puts an upper bound of the possible implantation fluence. Out of all the elements, boron doped diamonds are the most promising for a p-doped material. Research is still continuing to discover the most efficient dopant for an n-type diamond, while phosphorus and lithium are the main candidates.

Creating color centers in diamond, which emit light upon optical excitation, is another application where ion implantation is employed[68, 110]. By introducing a foreign atom such as xenon, nickel, nitrogen or others, optical centers related to the implanted ions can be formed. Some optical centers consist of an external atom adjacent to a vacancy (such as NV or SiV). Implantation of any impurity into diamond crystal will introduce both the implanted atoms and the vacancies, which result in the formation of the centers (for instance, implantation of nitrogen will introduce nitrogen and vacancies simultaneously). If the impurity is natively present in the diamond, the vacancies can be also introduced by proton or electron irradiation.

Figure 2.4 shows an example of a SRIM profile simulation of nitrogen implantation into diamond using acceleration energies of 30 keV (red curve) and 300 keV (black curve). The end or range of the deep implantation is 299±36 nm, while for the shallow implantation it is 40±11 nm. Additional information to draw from this simulation is the number of vacancies and their distribution in the crystal. For 300 keV and 30 keV implantations, 376 vacancies/ion and 141 vacancies/ion are formed in the crystal, respectively. Higher implantation energies also cause longer tail of vacancies in the

crystal, as evident from Figure 2.4, due to longer range of the accelerated ions. Therefore, the formation probability of NV centers as a result of a deep nitrogen implantation is increasing due to excess availability of vacancies per nitrogen atom.

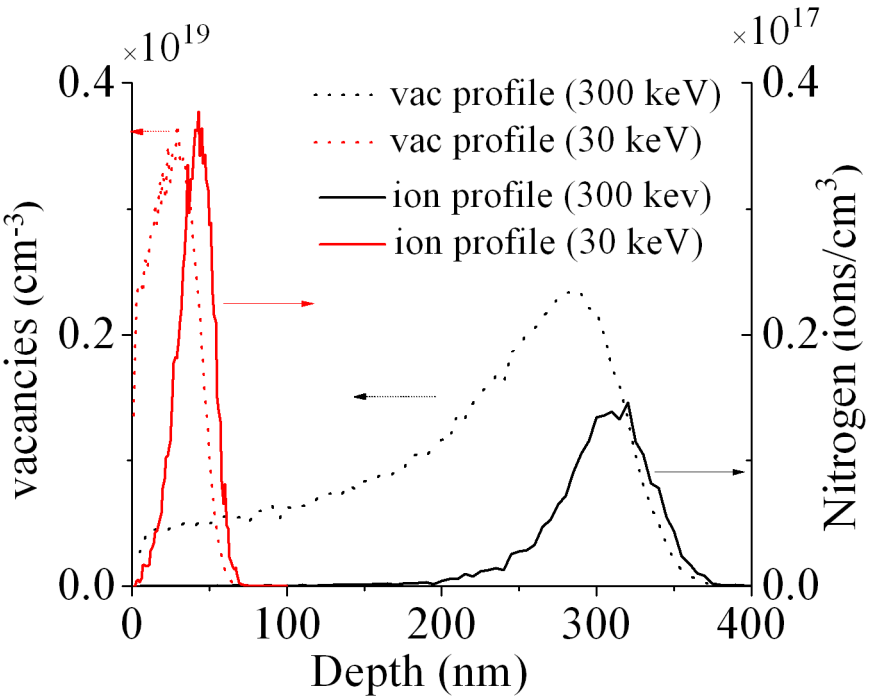

Figure 2.4 Example of a SRIM simulation of nitrogen implantation into diamond using acceleration energies of 30 kev (red curve) and 300 keV (black curve) with an implanted fluence of 1×10^{11} N/cm^2. The dashed lines are the vacancy concentration, formed due to the nitrogen implantations.

For quantum applications (as will be discussed in the following chapters), there is a need to access each color center individually. Thus, tight control of implantation parameters is required to achieve high precision. In the following paragraphs, the main results of ion implantation in diamond to produce individual emitters from various materials is presented.

2.1.3.1 Nitrogen implantation

Until the last decade, a significant part of nitrogen implantation work was motivated by the desire to modify the electrical properties of the diamond to achieve n-type doping and fabricate field emitting devices[105, 108, 111-113]. Nitrogen generally occupies a

substitutional site in diamond. Upon implantation of nitrogen and subsequent annealing, a few combinations of nitrogen defects are formed in the diamond lattice, such as substitutional nitrogen, nitrogen aggregates or nitrogen vacancy centers. Particularly, the promising quantum optical properties of the negatively charged NV center, spurred the research into fabrication methods of individual NV^- centers.

In 2005 Meijer et al[114] demonstrated an implantation of nitrogen (10^3-10^5 N atoms per shot) accelerated to an energy of 2 MeV. Using such a low dose of nitrogen, a single photon emission from the NV center was achieved. However, due to the created damage by the implanted nitrogen, they could not distinguish between the emission originating from the native nitrogen present in the samples or the implanted ones. To address this issue, Rabeau et al[115] implanted a different isotope of nitrogen, ^{15}N, and detected only the implanted emitters by resolving the different magnetic resonance signals. Furthermore, the lower implantation energy of 7 keV positioned the centers in a close proximity to the diamond surface, thus enabling better collection of the emitted light. To improve the lateral precision of the implantation, a new mask-less approach of single nitrogen implantation through a pierced AFM tip was attempted. The AFM tip acts as a collimator system in the nm range and provides a high implantation accuracy [116].

2.1.3.2 Other ions

Xenon ions were recently implanted into diamond to investigate their PL properties[117]. Xenon is particularly interesting since it exhibits narrow PL lines in the NIR and believed to have similar symmetry to the NV center[118]. Interestingly, xenon implantation enabled the use of diamond as a light emitting diode (LED) with xenon optical centers as active emitters[119]. This result is promising for a realization of electrical excitation of other single photon emitters. Polarization measurements and ion dose dependence measurements have been performed[118, 120] and the result concluded that xenon atom is occupying a semi di-vacancy site, V–Xe–V, oriented along the <111> direction. However, single photon emission from this center has not yet been demonstrated.

Nickel centers in diamond have been the subject of substantial research, as was discussed earlier. However, most of the work reported recently used native nickel color centers

present originally in HPHT crystals[81, 88, 121], rather than introducing nickel atoms by ion implantation. Earlier work, performed in the 80's showed that similar nickel related PL lines can be also found in CVD diamond implanted with nickel ions and subsequently annealed[122].

Boron is a *p-type* dopant in diamond and hence was implanted into diamond to achieve good electrical properties[123]. Low doses (below graphitization limit) of boron were implanted into a diamond held at low temperature followed by a rapid annealing[124]. Subsequent annealing to higher temperatures resulted in improved conductivity properties of the diamond[124]. Fontaine et al, demonstrated an *in-situ* annealing of boron implanted single crystal diamond[125], which showed good electrical properties. Furthermore, high carrier motilities of 600cm/V were measured from *p-doped* buried layers, which were fabricated by high energy (2 MeV) boron implantation and annealing to 1450°C[126].

Lastly, silicon related color centers have also been subject to a substantial research due to their vast abundance in CVD diamonds. There is an evidence of silicon implantation into diamond early in the 80's[101]. However most of the work from these color centers was performed on centers naturally found in HPHT diamond[127] or due to the incorporation of silicon during the CVD of diamond[93, 128, 129].

The first attempt to implant silicon into diamond for the purpose of creating individual optical centers was reported only recently in 2005 by Wang et al[20]. They fabricated the first SiV single photon emitter by implanting silicon atoms into pure diamond. Although the idea was promising, no following experiments of single SiV defects have been reported, mainly due to extremely low count rate and strong coupling to a non radiative shelving state of the SiV center.

2.2 Optical characterization of color centers

In this section the methods used to characterize the diamond color centers and the fundamentals of non classical emission are presented.

2.2.1 Confocal microscopy

Confocal microscopy employs far field illumination and far field detection, and widely applied in many scientific disciplines, ranging from biology to solid state physics. The basic idea of confocal microscopy, which was patented by Marvin Minsky in 1955, is based on the fact that only the light which originates from the focal area passes through the detection pinhole and hence reaches the detector. Laterally displaced beams will be blocked by the detector aperture and the beams originating from points displaced along the optical axis will not be focused in the detection plane. A schematic of the confocal principle is shown in Figure 2.5

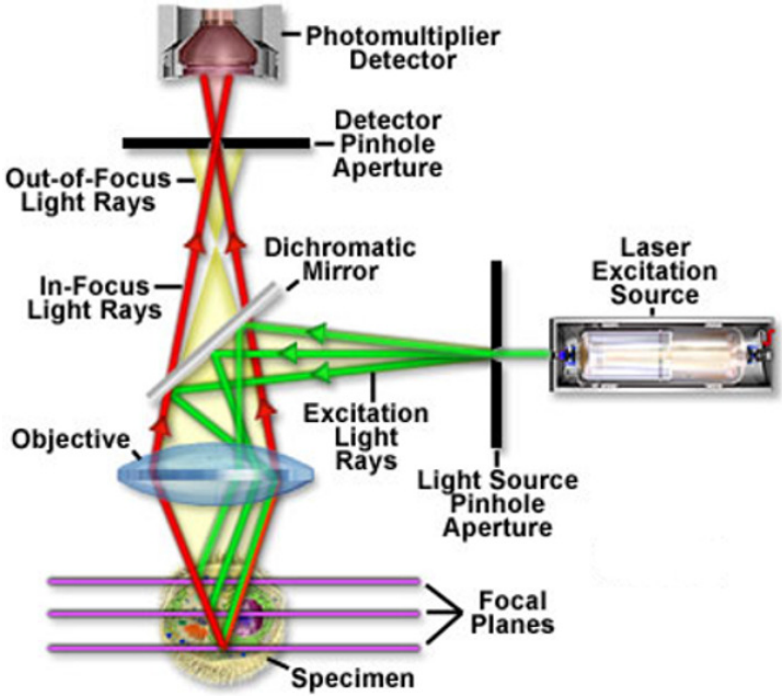

Figure 2.5. Schematic illustration of a confocal microscope, taken from ref [130]. The pinhole is the core of the confocal microscope. It blocks the luminescence originated from the 3D space below and above the focal plane, leading to only the light which is coming from the confocal plane to be detected.

Under laboratory conditions, the collimated laser light focused through an objective, excites the sample and produces scattered and reflected light (at the excitation and the emission wavelengths). The collected light is then separated from the incoming laser beam by a dichroic mirror (other techniques are also available) and focused onto a

pinhole in front of a detector. When fiber optics is used rather than a free space configuration, the core of the fiber is used as a pinhole.

The spot size, Δx, that is achieved on the sample depends on the numerical aperture (NA) of the objective and the excitation wavelength. It is also limited by the diffraction of the laser light. The spot size is given by:

$$\Delta x = 0.61\frac{\lambda}{NA} \tag{2.1}$$

For our experimental setup with a typical objective of NA=0.95 and excitation wavelength λ=690 nm, the resolution is limited to ~ 450 nm. The resolution limit of a traditional confocal microscope can be overcome by using methods of focal engineering such as stimulated emission depletion (STED)[131], which is capable of imaging with nanoscale resolution beyond the diffraction limit. The basic principle of this technique is to use stimulated emission to selectively reduce the excited state populations of a specific fluorescent dye in certain special regions in the focal area, while other regions remain unchanged.

2.2.2 Second order auto correlation function - $g^{(2)}(\tau)$

The second order autocorrelation function, $g^{(2)}(\tau)$, describes the intensity fluctuations of electrical field as a function of time. For the case of individual photons, $g^{(2)}(\tau)$ describes the probability of emitting a photon at a certain time $t+\tau$ if a previous photon was emitted at time t. Therefore, $g^{(2)}(\tau)$ provides information regarding the statistics of the emitted photons. By recording the $g^{(2)}(\tau)$ one can determine whether a single photon emitter is addressed.

The second order correlation function of the light is defined by:

$$g^{(2)}(\tau) = \frac{<\varepsilon^*(t)\varepsilon^*(t+\tau)\varepsilon(t+\tau)\varepsilon(t)>}{<\varepsilon^*(t)\varepsilon(t)><\varepsilon^*(t+\tau)\varepsilon(t+\tau)>} = \frac{<I(t)I(t+\tau)>}{<I(t)><I(t+\tau)>} \tag{2.2}$$

where $\varepsilon(t), I(t)$ are the electrical field and the intensity of the light beam, respectively, at time *t*. Assuming that the source emits at a constant average intensity, one can write: $< I(t) >=< I(t+\tau) >$ – which leads to the classical optical expression of $g^{(2)}(\tau)$:

$$g^{(2)}(\tau) = \frac{< I(t)I(t+\tau) >}{< I(t) >^2} \tag{2.3}$$

From a quantum mechanics point of view it can be shown that for pure single photon emission, the $g^{(2)}(\tau)$ equals to zero at zero delay time ($g^{(2)}(0) = 0$). Recalling from fundamentals of quantum mechanics, the photon number operator $\hat{n}$ is given by $\hat{n} = \hat{a}^{\dagger}\hat{a}$. The creation ($\hat{a}^{\dagger}$) and the annihilation ($\hat{a}$) operators are given by:

$$\hat{a}^{\dagger}|n> = (n+1)^{1/2}|n+1> \tag{2.4}$$

and

$$\hat{a}|n> = (n)^{1/2}|n-1> \tag{2.5}$$

The $g^{(2)}(\tau)$ can then be rewritten as:

$$g^{(2)}(\tau) = \frac{< \hat{a}_3^{\dagger}(t)\hat{a}_4^{\dagger}(t+\tau)\hat{a}_4(t+\tau)\hat{a}_3(t) >}{< \hat{a}_3^{\dagger}(t)\hat{a}_3(t) >< \hat{a}_4^{\dagger}(t+\tau)\hat{a}_4(t+\tau) >} \tag{2.6}$$

which leads to the following expression at zero delay time:

$$g^{(2)}(0) = \frac{< \hat{a}_3^{\dagger}\hat{a}_4^{\dagger}\hat{a}_4\hat{a}_3 >}{< \hat{a}_3^{\dagger}\hat{a}_3 >< \hat{a}_4^{\dagger}\hat{a}_4 >} \tag{2.7}$$

Since the light is arriving to the beam splitter from one side only, the input states can be described by: $\Psi = |\psi_1, 0_2>$ where ψ_1 is the arbitrary input state at port 1 and $|0_2>$ denotes the vacuum at port 2. Considering the relationship between the creation and annihilation operators of the output fields of the beam splitter to the input fields, while conserving the energy at the beam splitter, the $g^{(2)}(0)$ can be simply written as:

$$g^{(2)}(0) = \frac{<\psi_1|\hat{n}_1(\hat{n}_1 - 1)|\psi_1>/4}{(<\psi_1|\hat{n}_1|\psi_1>/2)^2} = \frac{<\hat{n}(\hat{n}-1)>}{<\hat{n}>^2} \tag{2.8}$$

where the values are determined from the input state of port 1. If the input is the photon number state $|n>$- then

$$g^{(2)}(0) = \frac{n(n-1)}{n^2} \tag{2.9}$$

For a true single photon emitter where only one photon is arriving at the beam splitter $n=1$ and subsequently $g^{(2)}(0)=0$

2.2.3 Habury Brown and Twiss setup

Hanbury Brown and Twiss (HBT) developed an interferometer to study coherence of light beams. At the time of the invention, they intended to study the angular diameter of radio stars, rather than individual photons[132]. The modern HBT setup, however, is typically used to characterize the photon statistics employing high efficiency avalanche photo diodes (APDs) instead of photomultiplier tubes. A schematic of a modern HBT setup is shown in Figure 2.6

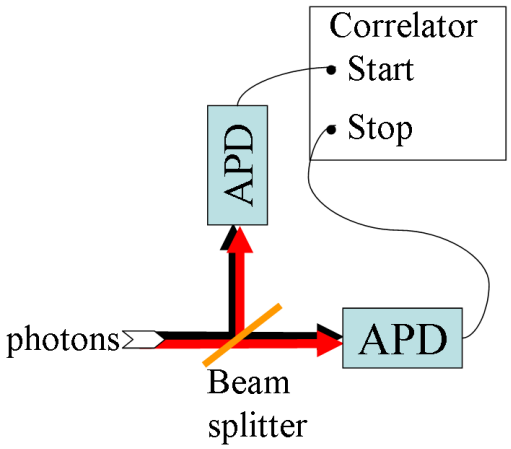

Figure 2.6. Schematic illustration of a modern HBT setup[17], used to characterize non classical light emission. The beam splitter directs the incoming photons to two APDs. The APDs are connected to a correlator card, which records the time between the start and the stop events.

The operation mode of the HBT setup can be described as follows: a stream of photons arrives at a 50:50 beam splitter and divided into two paths. The beam splitter outputs connected to two APDs for the photon detection. The outputs of the APDs are connected to the start and the stop inputs of a correlator card. Once a photon reaches the detector, a pulse is sent to the counter and activates the start/stop signal. The coincident card records the time events between the start/stop and the time elapsed between the events. The coincident events correspond to the histogram of time delays between two consecutive photon detections. Thus a histogram of events is built and shows the number of events registered at each time τ between the start and the stop.

Since the number of counts registered on the photon counter is proportional to the intensity, one can rewrite $g^{(2)}(\tau)$ from equation (2.2) as:

$$g^{(2)}(\tau) = \frac{< m_1(t) m_2(t+\tau) >}{< m_1(t) >< m_2(t+\tau) >} \tag{2.10}$$

where $m_i(t)$ is the number of counts registered on detector $i=1,2$ at time t. Therefore, $g^{(2)}(\tau)$ is proportional to the conditional probability of detecting a second photon at time $t=\tau$, given that a photon was detected at $t=0$. Hence, the result of the

HBT experiment gives a direct measure of the second order correlation function, $g^{(2)}(\tau)$, in the photon interpretation of light.

In case of a true single photon emitter, only one photon can arrive to the beam splitter at a time (*t=0*), and with a probability of 50% to activate the start of the clock. At the same time, however, there is 0% probability of the stop to be activated since only one photon was generated by the source. Consequently, the clock will be stopped in some other time, but not at the time of *t*=0. The result of the coincident statistics will be a dip at *t=0*. The obtained curve of the statistics events is generally known as "antibunching" curve.

To test whether a source emits single photons, an antibunching curve is recorded using a HBT setup. Figure 2.7 shows two examples of such curves recorded for continuous wavelength (cw) excitation and a pulsed excitation. The absence of the peak at zero delay time, $g^{(2)}(0)=0$, indicates that the source is a true single photon source (SPS).

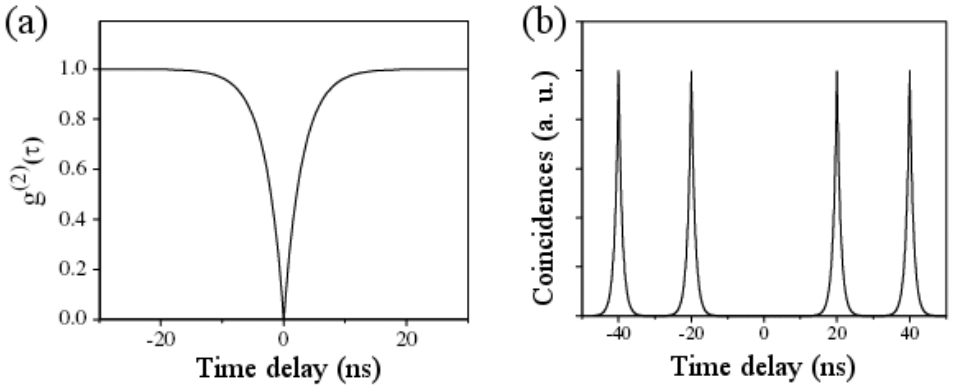

Figure 2.7. Example of antibunching curves recorded by (a) cw or (b) pulsed excitation laser[9]. At zero delay time, $g^{(2)}(\tau)$ goes to zero in a continuous mode and the peak at zero delay time is missing in pulsed mode, which indicates single photon emission.

In general, the classification of emitted light is based on the values of $g^{(2)}(\tau)$ and can be categorized as follows:

Bunched light: $g^{(2)}(\tau)>1$

Poissonian (coherent) light: $g^{(2)}(\tau)=1$

Antibunched light: $g^{(2)}(0)<1$

The Poissonian distribution is given by:

$$P(n) = \frac{\bar{n}^n}{n!} e^{-\bar{n}}, n = 1,2,3... \tag{2.11}$$

where $\bar{n}$ is the average number of photons within the beam. If the standard deviation, Δn is smaller than the square root of the mean (i.e. $\Delta n < \sqrt{\bar{n}}$), then the light has sub Poissonian statistics and is called non classical light.

Note, that an accurate normalization of the $g^{(2)}(\tau)$ is highly important to establish the non classical value for $g^{(2)}(0)$. From the experimental point of view, the normalization is done by assuming $g^{(2)}(\tau)=1$ for very long delay times since the statistics of the light at very long delay times is Poissonian.

2.3 Single Photon Sources

The definition of a single photon source is a confined system which emits only one photon per full cycle of excitation and relaxation. Before the next photon is emitted, the system has to undergo relaxation to its ground state[133]. On the detection side, only one photon must arrive to the detector at a time. Unlike coherent light, which has a Poissonian distribution and may include random time intervals between each photon in the stream, an ideal "train" of single photons has a constant time intervals between each photon.

The main requirements for a "perfect" single photon source are robust operation without blinking or bleaching, strong dipole moment and a short radiative lifetime, absence of non radiative decays and a bright polarized emission which can be easily observed over the background luminescence. To date, true single photon emission was demonstrated employing single atoms, single molecules, quantum dots, nanowires, carbon nanotubes and single defects in diamond. Each system has its own advantages and drawbacks, which are described in the following sections.

2.3.1 Candidates for single photon generation

2.3.1.1 Ions and atoms

Fundamental candidates for emitting single photons are individual atoms and trapped ions. The first observation of non classical light was reported by Kimble et al[13] in 1997 recording the light emitted from trapped sodium atoms. Recently, more sources based on optical trapping of calcium or rubidium atoms were demonstrated[134]. These sources are perfect single photon emitters since they are isolated quantum systems consisting of only one atom. Although recent results show a remarkable control over individual atoms by coupling them to micro resonators and chip scale realization has been proposed[135-137], scalability and manipulation of these sources is challenging and other single photon candidates are considered.

2.3.1.2 Quantum dots:

The first observation of non classical light from a quantum dot (QD) was demonstrated in 2000 by P. Michler et al[138]. They investigated CdSe/ZnS quantum dots which were dispersed on a silica substrate. Triggered single photon emission from quantum dots was reported one year later by C. Santori et al[14]. In their work, self assembly InGaAs QDs in a GaAs matrix were excited with a pulsed laser to generate single photon emission.

The QDs, although considered being a robust solid state system, are not homogeneous in their PL properties and the emission lines are shifted if the size of the QD varies slightly. Another major drawback is the blinking behavior of the emission due to nearby defects and trap charges. A very recent work, however, presented a technique which provides a plausible solution for the blinking problem[139] by synthesizing core-shell QDs. Last, most of the QDs require cryogenic temperatures which limit their future integration into a real quantum optical device operating at room temperature.

On the other hand, QDs can be easily integrated into photonic cavities[10] to enhance their emission. Their narrow bandwidth and short lifetime allowed the generation of indistinguishable photons[15, 140], which is highly important for a number of applications in quantum optics. In addition, the emission wavelength can be tuned by

modifying the size of the QD to achieve an appropriate single photon source in the telecom range [16].

2.3.1.3 Nanowires and Nanotubes

Recent work on SPSs revealed two new candidates for single photon generation. Carbon nanotubes[141] and nanowires[142]. In the case of carbon nanotubes, Auger processes and exciton localization are partially responsible for inhibiting two photon generation. For the nanowires, the authors in fact created an artificial QD within the nanowire by employing a two step molecular beam epitaxy process. The main drawback of these materials is the operation temperature, which is still significantly below room temperature. The carbon nanotube based SPS can only operate at liquid nitrogen (80 K) temperatures while the nanowire SPS generated single photon emission can be achieved at temperatures as high as 220 K.

2.3.1.4 Single Molecules

The first observation of non classical light from a single molecule (pentacene) was reported in 1992 by Basche et al[143]. Triggered SPS based on single molecules has also been demonstrated[144, 145]. Although single photon generation from molecules occur at room temperature and the achievable count rate is reasonably high (~900 kHz), severe blinking and photobleaching significantly limit these sources from being used in practical devices and applications. Many groups world wide are working on this problem, and recent results published by Toninelli et al[146] demonstrated that if single molecules (Dibenzoterrylene) are incorporated in a crystalline film of antracene, the photostability is increased and fewer molecules are subject to photobleaching.

2.3.1.5 Color centers in diamond

Out of more than 500 optical centers in diamond known to date, only four of them have shown single photon emission. These are the NV center[147, 148], the SiV center[20], one of the nickel nitrogen complexes – the NE8 [27, 29], and the interstitial related TR12

center [149-151]. This thesis will describe the discovery and the photophysics of a novel family of chromium related centers.

The NV is the most studied center, and it has been used already as a source of single photons in practical quantum cryptography (QKD) systems[7]. However, the NV center has a broad emission at room temperature, centered at 700 nm and strong coupling to phonons which results in only 4% of its total signal being emitted in the ZPL centered at 637 nm (Figure 2.3). For QKD applications these are negative characteristics, since for free space transmission under atmospheric conditions the emission at 637 nm results in high absorption and the large width of the emission results in high dispersion in fiber optical systems.

The NE8 and the SiV centers have narrower lines and emission centered in the NIR (Figure 2.3c). Nevertheless, a controlled fabrication of NE8 centers on a single level turned out to be extremely challenging and not feasible while the emission from the SiV center is extremely poor, reaching less than 2 kcounts/s at saturation. The emission of the TR12 is centered in the blue spectral region (ZPL at 470 nm) and has a broad phonon replica. At this stage, little is known about the photophysics of this center.

The main advantage of diamond color centers is their unprecedented photostability and room temperature operation. Diamond nanocrystals containing single emitters can also be manipulated[152, 153], which is advantageous for integrated quantum optical systems[154-156]. Furthermore, given that there are more than 500 available color centers, there is a substantial expectation to find alternative centers with improved photophysical parameters which surpass the current state of the art. One of the requirements for a diamond based single photon source is sufficient brightness which can be detected over the background luminescence. Further discussion regarding diamond based single photon emitters will be presented through the thesis in appropriate sections.

2.3.2 Photophysics of single photon sources

The photophysics of the PL emitted from a single color center can be described within the framework of a two level system comprising a ground and an excited state, or as a three-level system, whereby the single center is excited from its ground state to the excited

state, with a third, metastable, longer lived state providing an additional decay path from the excited state. These two systems are depicted in Figure 2.8

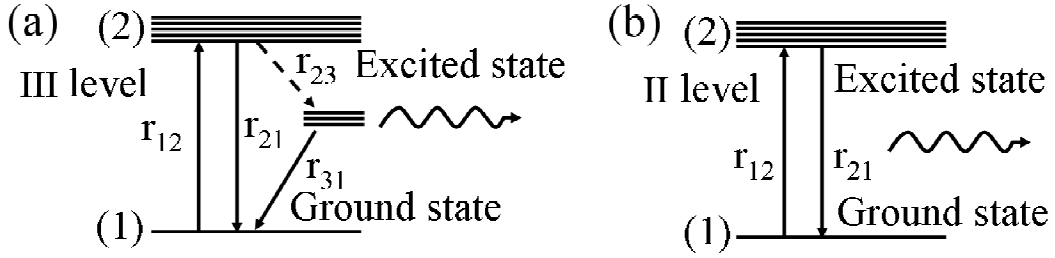

Figure 2.8 Schematic diagrams of a (a) three level system and (b) two level system. r_{ij} (*i, j = 1; 2; 3)* are the transition rates from level (*i*) to level (*j*).

The rate equations describing the populations of the two and three level systems can be written in matrix form as:

$$\begin{pmatrix} \dot{n}_1 \\ \dot{n}_2 \end{pmatrix} = \begin{pmatrix} -r_{12} & r_{12} \\ r_{12} & -r_{12} \end{pmatrix} \begin{pmatrix} n_1 \\ n_2 \end{pmatrix} \tag{2.12}$$

and

$$\begin{pmatrix} \dot{n}_1 \\ \dot{n}_2 \\ \dot{n}_3 \end{pmatrix} = \begin{pmatrix} -r_{12} & r_{21} & r_{31} \\ r_{12} & -r_{21}-r_{23} & 0 \\ 0 & r_{23} & -r_{31} \end{pmatrix} \begin{pmatrix} n_1 \\ n_2 \\ n_3 \end{pmatrix} \tag{2.13}$$

where the transition rates, $r_{i,j}$, are from level (*i*) to level (*j*) with *i, j=1,2,3* and $n_i(t)$ is the population in the *i* level. By solving these equations with the initial conditions n_1=1, n_2=0, n_3=0 (i.e the system is prepared in the ground state), the instantaneous emission probability of a photon being emitted from the excited state, $n_2(t)$, can be obtained. Under equilibrium conditions, the population of the excited state can be deduced and is:

$$n_2(\infty) = \frac{r_{12}}{r_{12} + r_{21}} \tag{2.14}$$

and

$$n_2(\infty) = \frac{r_{12}}{(1+\frac{r_{23}}{r_{31}})r_{12} + r_{21} + r_{23}} \tag{2.15}$$

for the two and three level models, respectively. Normalizing the probability of a photon being emitted from the excited state at time *t*, $n_2(t)$, to the probability of a photon being emitted at an infinite time $n_2(\infty)$, an analytical expression describing the second order correlation function, $g^{(2)}(\tau)$ can be obtained by:

$$g^{(2)}(\tau) = < n_2(\tau) > / < n_2(\infty) > \tag{2.16}$$

The respective analytical expressions for the two and three level cases are then given by:

$$g^{(2)}(\tau) = 1 - \exp(\lambda_1 \tau) \tag{2.17}$$

and

$$g^{(2)}(\tau) = 1 - (1+a)\exp(\lambda_1 \tau) + a\exp(\lambda_2 \tau) \tag{2.18}$$

respectively. The parameters λ_1, λ_2, a are given by: $\lambda_1 = r_{12} + r_{21}$, $\lambda_2 = r_{31} + r_{23}r_{12} / \lambda_1$, and $a = r_{12}r_{23} / (\lambda_1 r_{31})$.

The decay rate λ_1 depends on the excitation optical power, P_{opt} and it can be rewritten as:

$$\lambda_1 = r_{21}^0 (1 + \alpha P_{opt}) \tag{2.19}$$

where r_{21}^0 is the inverse of the excited state lifetime and α is a fitting parameter accounting for the optical excitation power dependence of the excited state decay rate. Similarly, for the three-level system, the decay rate λ_2, can be written in terms of r_{31}^0 in the limit of zero optical power as

$$\lambda_2 = r_{31}^0(1+\beta P_{opt}) + \frac{r_{23}r_{12}}{r_{21}^0(1+\alpha P_{opt})} \tag{2.20}$$

where β is a fitting parameter which takes into account the variation of the decay rate from the metastable state to the ground state with the optical excitation power. This parameter is relevant, since it justifies a power dependence effect of the deshelving metastable level. We assume that r_{23} is constant and independent on the excitation power. The absorption rate from the ground state is given by $r_{12} = \sigma I / h\nu$ with absorption cross section, σ, excitation intensity I, and excitation frequency ν. The photon emission rate is equal to $r_{21}n_2(t)$. Using the solutions for the population of the excited state and the absorption rate, one can obtain a general dependence of the single photon count rate on the excitation power:

$$R(P) = \frac{R_\infty P}{P_{sat} + P} \tag{2.21}$$

where $R(P)$ is the single photon count rate at excitation power P, R_∞ is the saturation count rate for $P \to \infty$ and P_{sat} is the optical saturation excitation power. The single photon count rate also depends on the collection efficiency of the setup, and this relation will be described later.

The fluorescence quantum efficiency (in some cases in the literature, this term referred as quantum yield), η_{QE}, of an emitter defined as the probability of an absorbed pump photon resulting in emitted photon, and can be written as

$$\eta_{QE} = \frac{k_{rad}}{k_{rad} + k_{nrad}} \tag{2.22}$$

where k_{rad} and k_{nrad} are the radiative and non radiative decay the bunching effect describes an enhanced rates, respectively.

For the three level system the fluorescence count rate can be also expressed in terms of the quantum efficiency by solving the rate equations in eq (2.13).

$$R = \eta_{QE} \times \eta_{CE} \frac{r_{21}}{1 + \frac{r_{21}}{r_{12}} + \frac{r_{23}}{r_{31}}} \tag{2.23}$$

where η_{QE} is the quantum efficiency of the emitter and η_{CE} is the collection efficiency of the setup. r_{ij} are the transition rates from different states of the emitter, as was described above.

Note that for diamond based single photon sources, the collection efficiency from nanocrystals is higher than the one in a bulk crystal due to elimination of total internal reflection of the light.

The measured auto-correlation function is given by the convolution of the $g^{(2)}(\tau)$ function for the two and the three level systems with the instrument time response function $J(\tau)$ (see appendix A):

$$g^{(2)}_{meas}(\tau) = \int_{-\infty}^{\infty} J(\tau - \tau') g^{(2)}_{corr}(\tau') d\tau' \tag{2.24}$$

This function was used to fit the $g^{(2)}(\tau)$ data in this thesis, unless otherwise stated. With an accurate determination of the second order correlation function one can determine the individual decay rates involved in the system and gain an understanding of the energy level structure. Upon inspection of the two and three level auto-correlation functions there is a clear distinction in the shape and nature of the exponential component. In the two level case the function exhibits a simple exponential behavior at a rate equivalent to the fluorescence decay rate from the excited state in the limit of zero optical excitation i.e. $r_{12} \to 0$. The three level expression, on the other hand, contains two exponential components each with a characteristic time constant. Depending on the transition rates from the excited state to the metastable state and from the metastable state back to the ground state, $g^{(2)}(\tau)$ can increase beyond 1 for delay times > τ_{rad}. The asymptotic value of the $g^{(2)}(\tau)$ at delay times >> τ_{rad} is 1.

The phenomenon of $g^{(2)}(\tau) > 1$ is commonly termed “photon bunching" and enables a clear distinction between two and three level systems. The second order correlation

function describes the probability of detecting a photon with a delay time τ after one photon has been detected at $\tau = 0$. Hence, the bunching effect describes an enhanced probability to detect a photon at short delay times rather than at longer times. Indeed after the system undergoes a transition to its metastable state, which has longer lifetime, there is a longer interval between the photons. Once the system has relaxed to the ground state and undergone a full emission cycle again, the normal photon rate is achieved again. The waiting interval while the system is trapped in the metastable state creates the bunching effect of the $g^{(2)}(\tau)$. Therefore, the observed bunching in the $g^{(2)}(\tau)$ function indicates of a presence of a third metastable state (thus three level system model) while an absence of bunching indicates a two level system.

The photophysics analysis of the quantum systems will be used intensively in chapters 5-8 to characterize the fabricated single photon emitters.

2.3.3 Applications of single photon sources

True single photon sources are highly sought after to test fundamental quantum mechanics and quantum optics experiments. They are also considered as fundamental building blocks in QIP applications.

For example, the Wheeler's delayed-choice experiment was demonstrated employing single NV centers[157]. Such sources have also been exploited to demonstrate the ability of imaging beyond the diffraction resolution limit of far field optics using stimulated emission depletion microscopy[131]. Due to the photostability of NV centers, and their practical atomic size, imaging with nanoscale resolution and angstrom precision as well as 3-D imaging is now available[158].

The rapidly developing field of QIP introduced a number of applications such as quantum metrology[159], quantum lithography[160] and quantum computation[161] which use single photons as their main building blocks. Moreover, practical QKD systems recently became commercially available. The QKD is believed to be the main applications for SPSs in the near future, and therefore, this section will describe in more detail the idea of QKD.

The aim of quantum cryptography is to provide a reliable method for transmitting a secret key and knowing that no one has intercepted it along the way[6, 8]. The process of sharing a secret key in a secure way, protected by the laws or quantum mechanics, is known as QKD. Note that quantum cryptography does not prevent eavesdropping but rather provides a failsafe way of knowing when the message has been intercepted. The main assumption of this technology is that you can not clone individual photons. The simplest protocol to demonstrate the operation of QKD was first proposed by the IBM researchers C. H. Bennett & G. Brassard in 1984[162], and so the process has also been dubbed BB84.

Following this protocol, the information is encoded as the polarization state of a single photon. '1' and '0' are represented by orthogonal polarization bases. Two bases of polarization are commonly used:

The ⊗ basis -'1' and '0' correspond to photons with polarization 45° and 135°, respectively.

The ⊕ basis - '1' and '0' correspond to photons with polarization 0° and 90°, respectively.

Figure 2.9 demonstrates the operation of QKD.

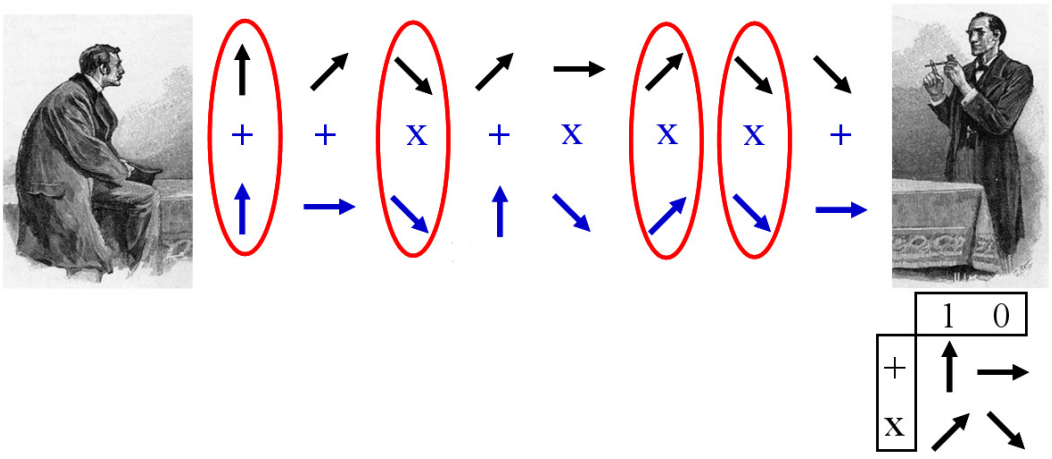

Figure 2.9. Schematic representation of the QKD algorithm. Alice sends a binary string to Bob using one of the polarization bases (first row, black arrows). Bob decodes the information by recording the corresponding bit '1' or '0' without knowing which basis Alice has chosen (third row, blue arrows). He then communicates with Alice over a public channel and tells her the sequence of the polarization bases he used without revealing the actual data (second row, blue signs). Alice confirms the subset of bits where they both used the same polarization basis and discard the rest (red ovals). Thus, a private key is formed.

If Alice wants to send a message to Bob, she randomly selects one of the polarization bases and sends a string of binary data which is encoded in one of the two polarization bases at her choice. Bob, on the other side of the channel, receives the string of information without knowing which basis Alice has chosen, which makes his own selection of bases random. For each basis selection he records the corresponding bit '1' or '0'. He then communicates with Alice over a public channel and tells her the sequence of the polarization bases he used without revealing the actual data. Alice confirms the subset of bits where they both used the same polarization basis and discards the rest. Thus, a private key is formed. If the error rate is lower than a specific number (25% at the maximum), no eavesdropping has occurred.

In principle, QKD can be realized with attenuated lasers rather than true single photon sources. This is done by reducing the photon flux until only one photon on average is emitted. However, due to the Poissonian nature of light, there is a finite probability of generating more than one photon per pulse. Therefore, this technique is susceptible to eavesdropping by performing a number splitting attack[6]. To minimize two photon generation, the signal has to be attenuated significantly and results in a low photon transmission rate. For long distances, the loss is so significant that secured communication is practically impossible. Therefore, for practical realization of QKD, a true single photon emitter is required.

To understand the eavesdropping process, let us assume that Eve uses the same polarization bases as Alice and Bob. Since Eve does not know Alice's choice of basis, her choice of detection is random. Eve will then transmit the photon to Bob using the same polarization. In the case where Bob chose the same polarization as Alice, but Eve guessed the polarization wrong, Bob will register random results on his detectors with a probability of 50%. The error therefore, is given by:

$$P_{error} = P_{Eve\ has\ wrong\ basis} \times P_{Bob\ gets\ wrong\ result} = 50\% \times 50\% = 25\%. \quad (2.25)$$

Therefore, errors higher than 25% are intolerable and indicate eavesdropping of the signal. The explanation above is somewhat simplified and many more technological problems exist: absorption or scattering of photons during their propagation, insufficient

light collection, filtering, detection efficiency and dark counts. To some extent these problems can be minimized by providing a "perfect" source of single photons: ultra bright polarized emission in a range of telecom wavelengths. The development of such a source is the essence of this thesis.

Chapter 3

Materials and experimental methods

In this chapter the diamond materials used during the course of the PhD are described. The experimental methodologies and the equipment involved are also explained and discussed.

3.1 Diamond samples

Two types of bulk diamond samples were used during the experiments: (1) an artificial type Ib diamond, produced by Sumitomo with ~100 ppm nitrogen concentration. This crystal was cut and polished from a large single crystal which was grown under HPHT conditions. Figure 3.1a shows a cathodoluminescence (CL) image recorded from the top [100] oriented polished face surface of HPHT diamond. Each color represents a different growth sector with different native nitrogen concentration and accordingly different optical properties. It is known that the incorporation of specific impurities varies from sector to sector[33]. For instance, nickel is predominantly incorporated along the (111) sector, which appears black in the image[163]. Likewise, there are low and rich nitrogen sectors, a factor which must be taken into account when performing implantation. In Figure 3.1a, region 'a' indicates a sector with high nitrogen, whilst region 'b' indicates low nitrogen sectors.

A typical PL spectrum recorded at cryogenic temperature (T<10 K) from sector 'a' of a pristine HPHT diamond is shown in Figure 3.1b. The ZPL of NV^- centered at 637 nm is clearly seen while the ZPL of NV^0 at 575 nm is absent, a feature that can be attributed to the large amount of nitrogen in this sample. The hump centered at 660 nm is the phonon sideband of the NV^- center.

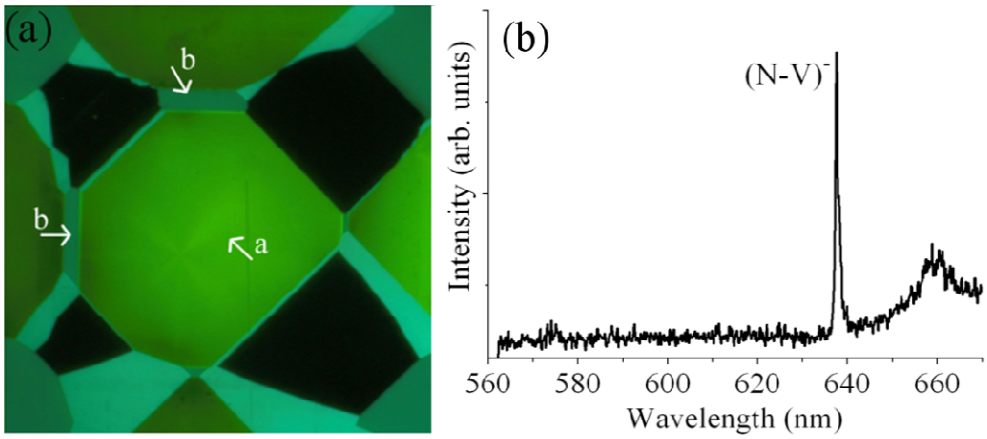

Figure 3.1 (a) Cathodoluminescence image of the top (100) Sumitomo HPHT diamond surface. Different colors identify different sectors in the diamond crystal, e.g. the black is the (111) growth sector. "a" indicates a high nitrogen sector while "b" indicates low nitrogen sectors. (b) A representative PL spectrum from a pristine HPHT diamond prior to the implantations recorded at 10 K from sector "a" recorded using a 532 nm excitation. The ZPL of $(NV)^-$ centered at 637 nm is clearly seen. The hump centered at 660 nm is the phonon sideband of the $(NV)^-$ center and the line at 572 nm is the first order Raman line.

(2) The second type of bulk diamond samples is a single-crystal CVD diamond (top, [100] oriented polished face), produced by Element 6 with nitrogen concentration <1 ppm. Figure 3.2 shows a typical PL spectrum from a pristine CVD sample recorded at cryogenic temperature (T<10 K).

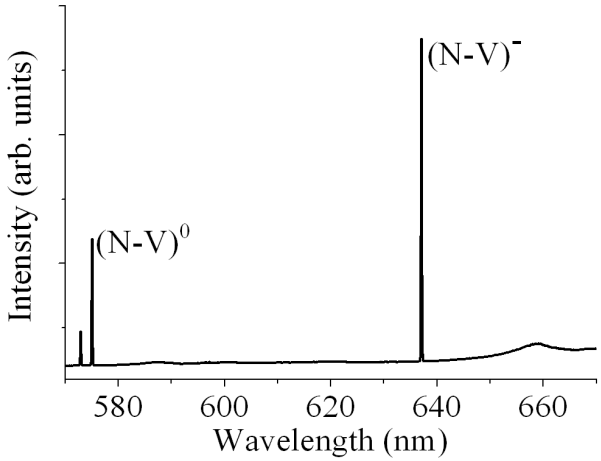

Figure 3.2 A representative PL from a pristine CVD sample recorded using a 532 nm excitation. The ZPL of (N-V)- centered at 637 nm is clearly seen. The hump centered at 660 nm is the phonon sideband of the (NV)- center and the line at 572 nm is the first order Raman line. Note that the width of the ZPL is much narrower for the CVD sample than for the HPHT sample due to lower nitrogen concentration.

The ZPL of NV^- and NV^0 centered at 637 nm and 575 nm, respectively, are clearly seen. The hump centered at 660 nm is the phonon sideband of the NV^- center and the line at 572 nm is the first order Raman line.

3.2 Ion implantation

Ion implantation of various elements into the diamond crystals was carried out using either a conventional low energy implanter, located in the Australian National University (ANU) or a focused ion beam (FIB) located in the University of Melbourne.

3.2.1 Focused ion beam

The dual scanning electron microscope (SEM)/FIB (Jeol JSM 5910) includes both electron and ion beams (Figure 3.3). In the frame of this experimental work, the FIB was used to implant nickel. The advantage of the FIB over a conventional implanter is the flexibility to perform implantation into an individual sub micron CVD crystal grown on the substrate, thus increasing significantly the control over the spatial resolution.

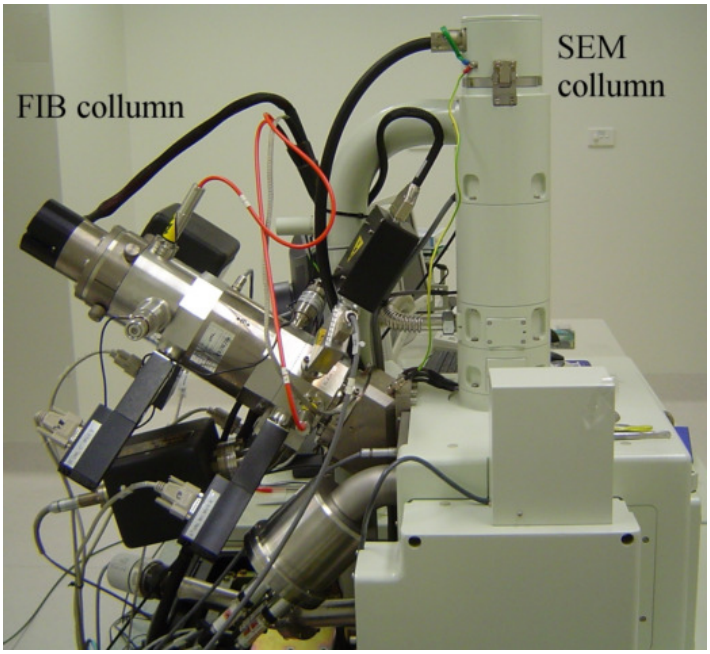

Figure 3.3 A photograph of the dual FIB/SEM microscope.

The origin of the nickel ions is a nickel–erbium or a nickel–neodymium liquid metal-ion source[164]. The nickel ions were isolated from the other species by using an electromagnetic filter (E×B). The mass spectrum of the nickel–erbium source as provided by the manufacturer is shown in Figure 3.4a.

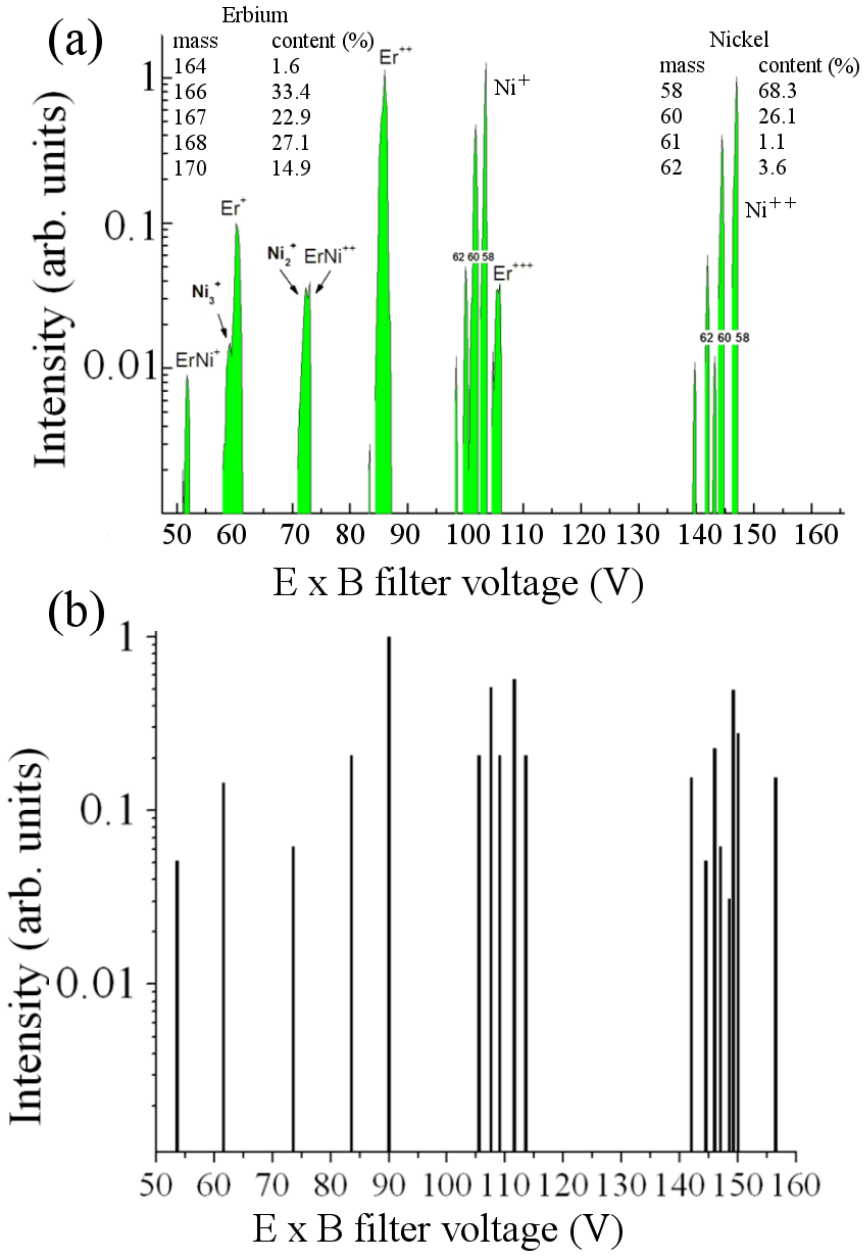

Figure 3.4 Mass spectroscopy of the dual FIB/SEM microscope. (a) Mass spectrum of the Ni/Er ion source as provided by the manufacturer (b) Measured spectrum of the Ni/Er ion source.

To verify this measurement, a scan over the beam intensity was performed as a function of E×B filter. The results are shown in Figure 3.4b.

The recorded mass spectrum is in a good agreement with the spectrum provided by the manufacturer. To achieve lower fluence of ions, the beam is passed through a set of apertures located in the FIB column. A typical 1–5 pA current was used to perform the implantation. The current was adjusted by moving the apertures in relation to the main ion beam, thus blocking part of the beam. The spot size of the beam can be reduced down to tens of nanometers, allowing implantation into an individual CVD grown diamond crystal. Typical implantation energies were around 30 keV so the end of range of the implanted ions would be in a close proximity to the diamond surface (SRIM simulations will be presented in relevant chapters). Fabrication of optical centers in a close proximity to the surface allows an efficient coupling of light to an external device (such as cavities and waveguides).

3.2.2 Low Energy Implanter

The conventional NEC implanter (located at Australian National University) is a versatile system which allows the implantation of many elements. Switching between different ion sources takes approximately an hour, and a rotatable stage allows the implantation of a number of samples during each run (Figure 3.5).

A suitable powder containing the desired material is first pressed densely into a small copper cylindrical cathode. A source of negative ions by cesium sputtering is used to generate the ion beam. The cathode is biased to typically 6 V which attracts the negative ions and the pressed powder is sputtered. The beam is accelerated by an extractor voltage and an Einzel lens which is used to focus the beam. Using a 90° magnet, only the ions with a specific mass to charge ratio and energy are selected. The beam is then electrostatically raster scanned to ensure a homogeneous distribution over the desired implantation region, which can be modified by an aperture.

The samples are affixed to a hollow nickel block with clamps. A cylindrical copper shield surrounding the target is cooled to 80 K to reduce contamination build up on the sample surface. The sample temperature is measured with a thermocouple inside the block, close to its surface. The sample holder is biased to -300 V with respect to the target for charge

suppression. Prior to each implantation cycle, the system was pumped down below 5×10^{-7} Torr.

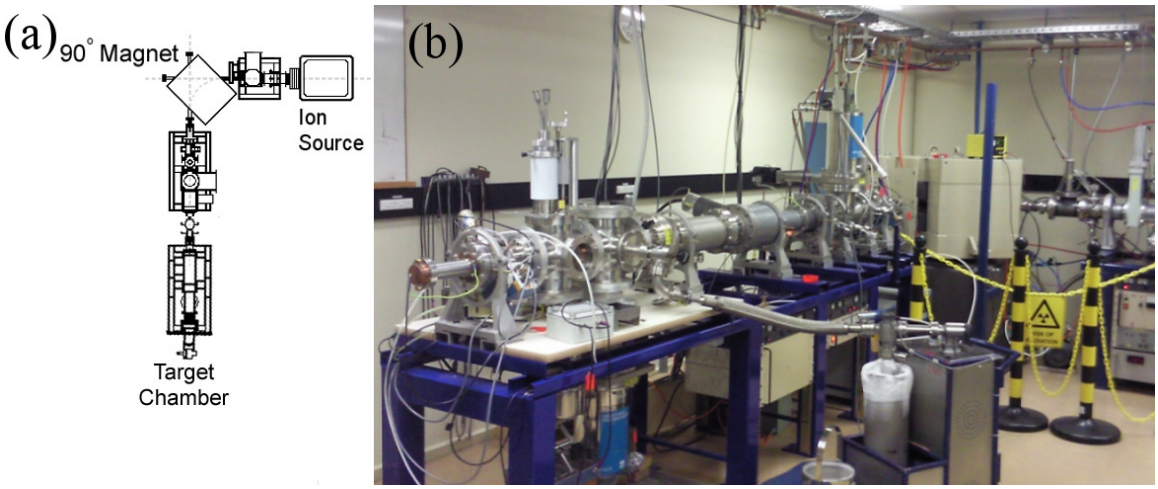

Figure 3.5 Schematic illustration and a photograph of the NEC implanter. The ion source is sputtered by Cs ions and the specific ion is selected by adjusting the 90° magnet.

3.3 Optical and spectroscopical measurements

3.3.1 Room temperatures measurements

The initial measurements of single photon detection were performed in the laboratory of Prof J.-F. Roch in Cachan, France using a free space confocal microscope with HBT setup. Later on, a fiber coupled confocal microscope with HBT interferometer was built in the University of Melbourne and most of the experiments described in the following chapters were performed using the Melbourne system.

The Melbourne setup (Figure 3.6) consists of a fiber coupled cw diode laser emitting at 682 nm or a 690 nm pulsed diode 200 ps pulse width (repetition rate from 10 MHz up to 80 MHz) which were interchanged for excitation. The laser polarization was controlled by a Glan Taylor polarizer and a half-wave plate. The diamond sample was mounted on a piezo XYZ stage with 0.2 nm resolution, allowing 100 μm^2 scans. The residual laser line was filtered by a dichroic beam splitter, a F1 band-pass filter centered at 794 (160 nm full width at half maximum (FWHM)) and a F2 broad (10 nm FWHM) band-pass filter centered at 740 nm, 750 nm, 760 nm or 770 nm, depending on the PL from a specific

crystal. The spatial resolution of the microscope is approximately ~ 400 nm and a depth of field is ~ 800 nm.

The PL from the emitting centers was then coupled into a 62.5 mm core multimode fiber, which acts as an aperture. A 50:50 fiber-coupled beam splitter guided the photons to two single photon counting detectors (APDs) and their outputs were sent to the start and stop inputs of the time correlator card. The PL was recorded without the band pass F2 filter using a fiber-coupled spectrometer with a cooled CCD array. All the measurements were performed at room temperature.

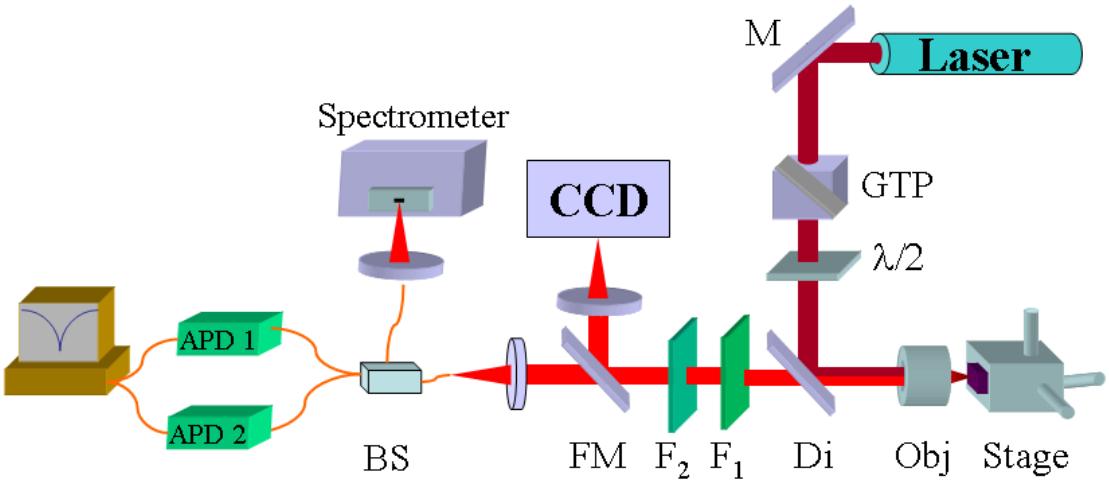

Figure 3.6 Experimental setup. A diode laser at 682 nm operating in CW and a pulsed 690 nm laser were alternatively coupled to a single mode fiber, and then collimated and polarized by a Glan Taylor polarizer (GTP). The laser polarization was varied by an half wave plate (λ=1/2). A variable neutral density filter was used to change the excitation power. The samples were mounted on a Physics Instruments XYZ piezo stage in closed loop operation and excited by focusing the laser light using a high numerical aperture (0.9) objective (Obj) with 100x magnification. A dichroic mirror (Di) transmitting from 720 nm, was used to separate the laser line form the sample fluorescence emission, when collected back from the same objective. F1, F2 are band-pass filters, 794±80 nm and alternatively 770±12 nm, 760±12 nm, 750±12 nm or 740±12 nm, to isolate the single photon emission lines. A 100 mm focal length lens was used to send the single photon emission to a multimode-fiber, providing an aperture for the confocal imaging. A 50:50 fiber beam splitter (BS) was used to verify the single photon emission by performing the auto-correlation between two low-dark counts (150 counts/s) single photon counting modules (APD). To perform spectroscopy, the light was coupled into a different fiber and sent to a spectrometer. Flipping mirror (FM) was used to image directly the emission pattern on a cooled CCD camera.

3.3.2 Measurements at cryogenic temperatures

Some of the optical characterization described in the thesis has been performed in cryogenic temperatures (T~2K). This setup is located in the laboratory of Prof J. Wrachtrup in Stuttgart, Germany. In this particular configuration, the objective and the sample are located inside a bath cryostat and cooled down by liquid helium to a temperature of ~2 K. The optical excitation was carried out using a titanium:sapphire (Ti:Sap) laser (Coherent Mira) operating at the wavelength λ= 700 nm, either in a continuous mode or in a femtosecond pulsed regime at a repetition rate of 76 MHz. The laser beam was focused on the sample with a microscope objective (NA=0:85) immersed in the helium bath cryostat. PL was collected by the same objective and spectrally filtered from the remaining pump light using a 750 nm long-pass filter combined with a 785 nm short-pass filter. Following standard confocal detection scheme, the collected light was then focused onto a 100 μm diameter pinhole and directed either to a spectrometer or to a HBT interferometer used for photon correlation measurements. Lateral (x-y) raster scanning of the sample was realized using a scanning galvanometer mirror system combined with telecentric lenses, while z-scan was provided by a high resolution piezoelectric stepper (Attocube) on which the substrate with the CVD-grown nanodiamonds was glued.

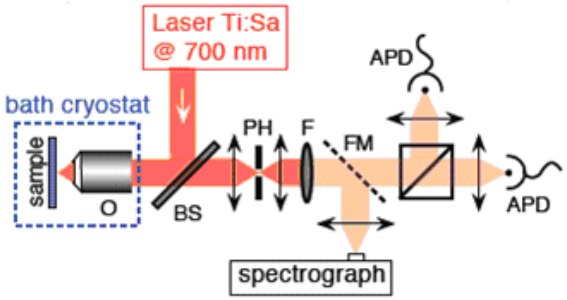

Figure 3.7 Experimental setup of a customized confocal microscope operating at cryogenic temperatures. The setup is located at the laboratory of Prof Wrachtrup in the University of Stuttgart, Germany. BS: quartz plate with 5% reflectance; O: microscope objective with a numerical aperture of 0.85 immersed in the helium bath; PH: 100 μm diameter pinhole; F: combination of a 750 nm long-pass filter and a 785 nm short-pass filter; FM: flip mirror directing the PL either to an imaging spectrometer (Acton research) equipped with a back-illuminated cooled CCD matrix, or to a HBT interferometer placed on the output ports of a 50:50 beam splitter.

Chapter 4

Growth of sub-micron sized diamonds using MPCVD technique

Diamond nanocrystals are rapidly becoming the medium of choice for a broad spectrum of applications: from bio-marking[165, 166] and drug delivery[167] through to use as building blocks for future quantum devices[22, 24]. For quantum optical application in particular, there is a demand for controlled synthesis of submicron size, individual diamond crystals containing single color centers. The first experimental chapter of the thesis describes the controllable method to grow sub-micron sized diamond crystals using MPCVD technique.

4.1 Introduction

Recent experiments such as nano-magnetometry[22-24] and QKD[7] which make use of single photon emission from diamond color centers, have highlighted the need for precise control over the attributes of the host diamond to successfully conduct quantum optical experiments. For the case of nanodiamonds in particular, a number of factors may influence the quantum properties of the color centers used for QIP. These include the influence of surface states, the incorporation of impurities and the presence of defects and non-diamond bonding. Indeed, residual sp^2 carbon on the diamond surface is very luminescent and considerably decreases the signal to noise ratio.

In addition, isolated high quality diamond crystals of subwavelength size are highly desirable. There are number of reasons for this stringent demand: First, the emitted photons can be collected with higher efficiency than is possible from large single crystals or continuous films due to suppression of total internal reflection inside the diamond. Preferably, the crystal size would be less than λ/n, where λ is the emitted wavelength and

n is the diamond refractive index (2.4). Therefore, crystals hosting centers with an emission wavelength in the NIR (~750 nm), should be smaller than 300 nm to improve the collection efficiency of the emitted light. Second, in an ideal case, one nanodiamond crystal would contain only one color center, without any background fluorescence from other emitters. This is a major problem, since most of the CVD grown diamonds do contain various optically active centers.

The growth of high quality homoepitaxial single crystal has been demonstrated[168-171] and recipes for the growth of continuous nanodiamond and ultrananodiamond films on non-diamond substrates are well established[44, 172-174]. For instance, enhanced diamond nucleation was achieved by biased enhanced nucleation[175], which is a well developed technique. Other methods to generate high nucleation density include polishing of the substrate with diamond powder or ultrasonic treatment of the substrate in a slurry of micron or smaller sized diamond powder[36, 41, 172, 176]. However, methods for controlled growth of sub-micron diamond crystals on different substrates are far less developed[177-179].

Recently, diamond nanocrystals were grown on silica[180] and optical fibers[181] for optical applications. For seeding purposes, the substrate was exposed to metal/diamond slurry in an ultrasonic bath. The use of nanopowder of a few hundreds of nanometers in size as seeds hindered the control over the final size of the crystals. Furthermore, the use of ultrasonic treatment damages the surface of the substrate along with any topographical features which have been manufactured onto the surface. The literature is therefore still lacking of an adequate recipe for the formation of dispersed, individual high quality micro or nanodiamond crystals on a non-diamond substrate. Of particular interest is the ability to deposit particles with low defect density, with well defined morphology and size, which are well dispersed over the substrate, allowing individual addressing and manipulation.

This is essentially a new scientific challenge since most of applications to date required very high nucleation density[36, 42, 44]. In particular, synthesis of nanodiamond of optimum size and with optical and quantum properties approaching that of the best quality single crystal diamond has not yet been accomplished.

The first step to tackle this problem is to propose alternative seeding technique. Growth from nanodiamond seeds with a size below 10 nm allows improved control over the final size of the crystals. Avoidance of ultrasonic treatments may provide a better control of the density of crystals on the substrate without damaging it.

The second major problem is the termination of any residual sp^2 carbon and elimination of secondary nucleation. Spontaneous nucleation in locations where no nanodiamond seed was seeded will result in very high distribution of the final size of the crystals. To address the problem of controlling the growth of individual sub micron diamond crystals, high quality homoepitaxial techniques used on large samples were applied to grow the nanodiamonds. The use of a high microwave power density entails an increased dissociation of the gas species, particularly hydrogen and methane. The dissociation of hydrogen leads to larger atomic hydrogen concentration which etches the non diamond material and suppresses graphite formation. Under these conditions methyl radicals are also efficiently produced from the dissociation of methane. These radicals possess sp^3 configuration and are energetically favored to be incorporated into the growing diamond crystal[182]. Therefore, employing high plasma density conditions should result in the formation of high quality diamonds with smooth facets, better morphology and very low incidence of spontaneous secondary nucleation when compared to low pressure CVD grown nano-diamonds.

4.2 Experimental details

For the purpose of growing individual crystals, the following seeding procedure was developed: diamond nanopowder (4–6 nm size, Nanoamor) was dissolved in methanol and ultrasonicated for 20 min to break the agglomeration of the nano-diamond particles. Various concentrations of the nanopowder in the solvent in the range 0.125 – 0.5 μg/ml were prepared.

After the ultrasonication, the suspension was sprayed onto the substrate (silicon, silica or sapphire). The sample was then immediately rinsed with methanol and deionized-water and dried under a stream of nitrogen. The spraying was performed far enough from the substrate so that the liquid droplets dry on the substrate without joining to form larger

droplets, thus prohibiting the transport of seeds across the surface. Note that no ultrasonication of the sample was employed after the substrate was sprayed with the seeds. This spraying technique allows control of the density of the nuclei on the substrates by controlling the solution concentration and spray duration. After seeding the substrate, the samples were transferred to the MPCVD reactor chamber. The schematic illustration and the photograph of the CVD reactor is depicted in Figure 4.1

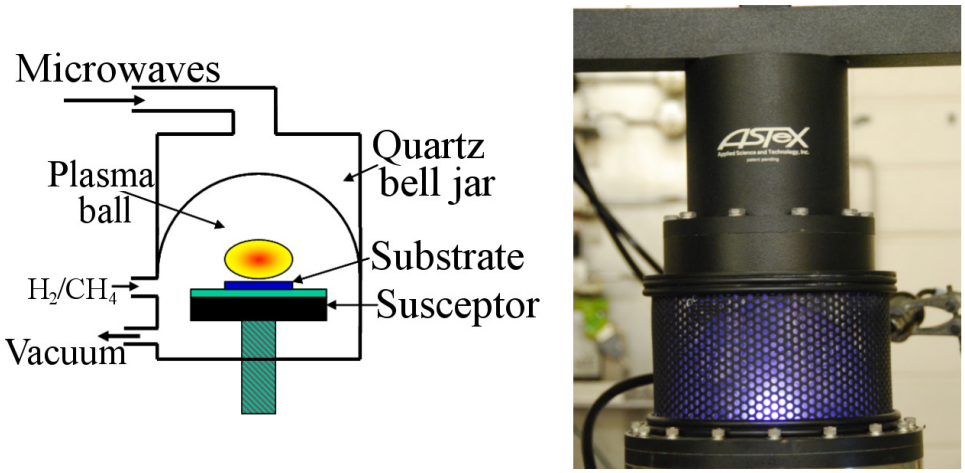

Figure 4.1 Schematic illustration and the photo of the microwave plasma chemical vapor deposition reactor used to grow the submicron diamond crystals. The height of the substrate can be adjusted. Additional gasses such as nitrogen can be also introduced.

Microwaves enter into the reaction chamber from a proprietary antenna which converts a rectangular WR284 microwave signal into a circular mode. The microwave proceeds through a silica window into the plasma enhanced CVD process chamber. The size of the luminous plasma ball will increase with increasing microwave power. The substrate sits on a molybdenum block below the plasma ball.

The parameters for the diamond crystal growth are: microwave power ~ 900 W, pressure ~ 150 Torr, substrate temperature ~ 800°C, gas mixture composition ~ 2% CH_4 in H_2 unless otherwise stated. No nitrogen was intentionally introduced and the system was pumped down below 8×10^{-4} Torr. The leak rate into the system was negligible and hence the N/C ratio was dominated by the impurities in the source gases. The upper limit of N/C ratio in the gas mix is hence estimated to be less than 0.1%. Such concentration may result in up to 1 ppm [183, 184] of nitrogen in the grown crystals, however, the employed

high plasma density and power should reduce the nitrogen incorporation into the crystals. This N/C ratio may be further reduced by using Palladium purifiers.

Before the methane was introduced to the CVD chamber, the substrate was etched using oxygen plasma (2% O_2 and 10% Ar in H_2). It is not expected that the addition of Ar is crucial, however it has been previously reported to be effective in increasing the etching rate under certain conditions[185]. The aim of this step was to remove any non-diamond carbon residue that may remain on the surface of the sample, which could act as unwanted nucleation sites. In our CVD reactor, the height of the stage on which the samples are placed can be adjusted and the samples can be moved closer to or further from the plasma ball. For optimum growth conditions, the distance between the sample and the plasma was kept to approximately 1 cm.

Morphological characterization of the grown diamond samples was performed using an FEI Nova high resolution SEM operating at 20 kV. Optical properties and Raman spectra were recorded using Renishaw RM 1000 Raman Stellar Pro 514 Modulaser (514 nm excitation source) with 13 mW power at the sample.

4.3 Experimental results

Figure 4.2(a-d) show SEM images of typical CVD diamond crystals grown under these conditions from 4-6 nm nanodiamond seeds.

As can be observed, the crystals are well faceted and no cauliflower morphology is observed. The average size of the crystals can be controlled by changing the growth duration, as it is illustrated in Figure 4.2. A one hour deposition leads to a final average diamond size of approximately 1.5 μm while a short time of 8 minutes leads to crystals with a final size below 200 nm. Figure 4.2(e) shows an Atomic Force Microscope (AFM) scan of 2 diamond nanocrystals with an approximate size of 30 nm, deposited for 6 minutes. Inset is the line scan over one of the crystals. The sharp peak in the line scan indicates that the nanodiamond crystal is faceted and has a well defined morphology. Therefore, the size of the diamond nanocrystals can be controlled by tuning the growth time, with the lower limit being the size of the nanodiamond seeds (4-6 nm in our experimental conditions).

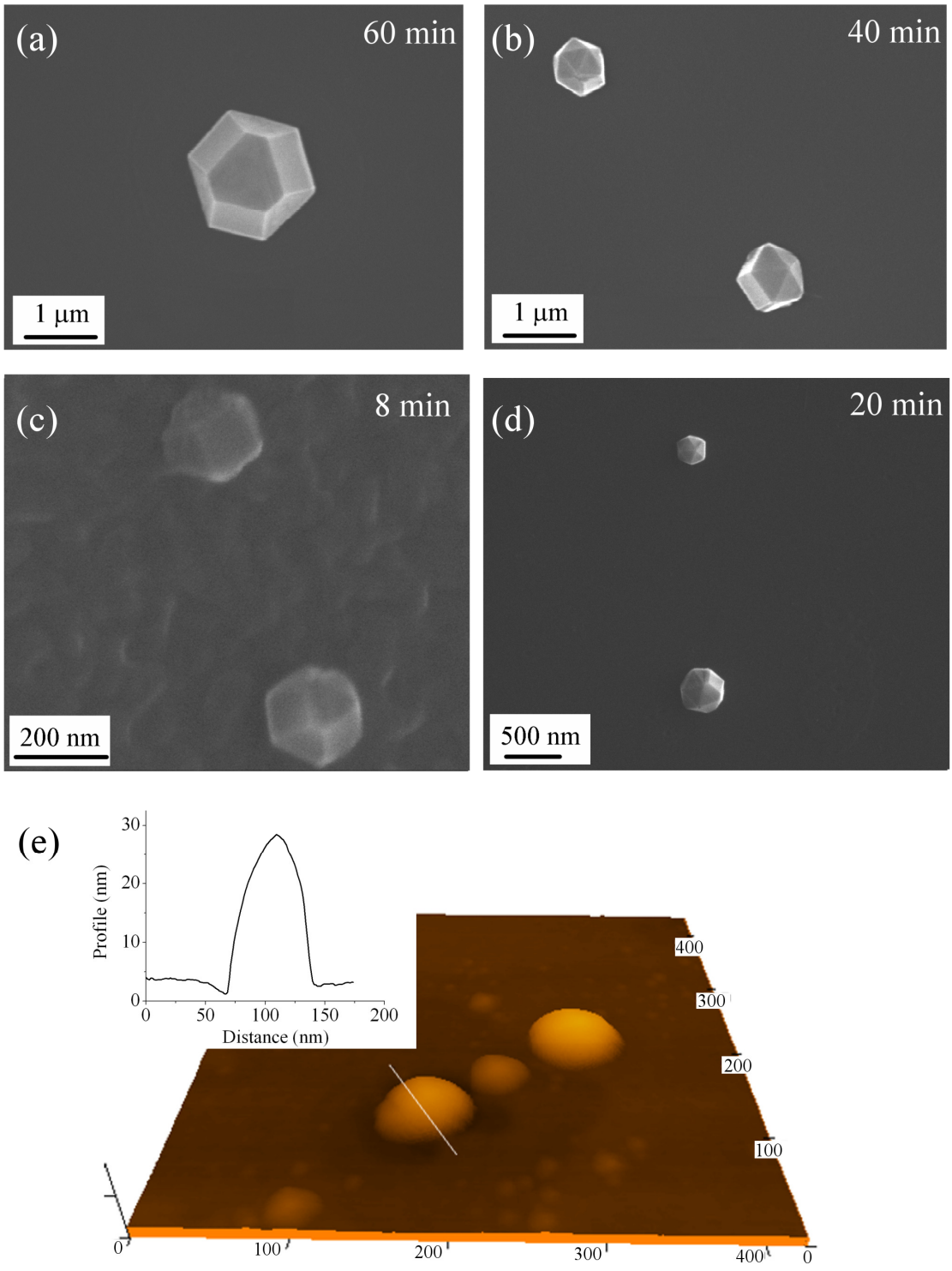

Figure 4.2 SEM Images of sub-micron diamond crystals deposited for different periods of times. (a) 60 minutes deposition, (b) 40 minutes deposition, (c) 20 minutes deposition (d) 8 minutes deposition. (e) AFM scan over 30 nm diamond crystals deposited for 6 minutes, demonstrating the possibility to grow sub 100 nm isolated diamond crystals. Inset is the line scan over one of the crystals.

Figure 4.3 shows the average diamond size determined in this fashion as a function of the deposition time. Note that due to the different orientations of the faceted diamonds with respect to the substrate, it is hard to define a single parameter to describe the size of the crystal. We found that averaging the longest and the shortest measurement of the crystals provided a useful method to evaluate the average size.

According to our experimental data, an approximately linear growth rate of about 22 nm/min or 1.3 μm/hr was deduced for the diamond growth. This rate is comparable with the reported in the literature[171, 186] for similar parameters (4% methane and 800°C deposition temperature). Higher growth rates using MPCVD can be generally achieved by increasing the methane concentration (up to 7.2%)[171]. Since we are not interested in production of continuous thick diamond films, such an experiment has not been attempted.

The linear line fit does not pass through the origin. Because of the slow build-up of methane in the chamber, at relatively high pressure (150 torr) it takes about 4 minutes to reach the desired methane concentration in the chamber. Therefore for the initial few minutes a linear growth rate is not expected. Nevertheless, as shown in Figure 4.2e, we found that after 6 minutes, diamond crystals of approximately 30 nm can be synthesized.

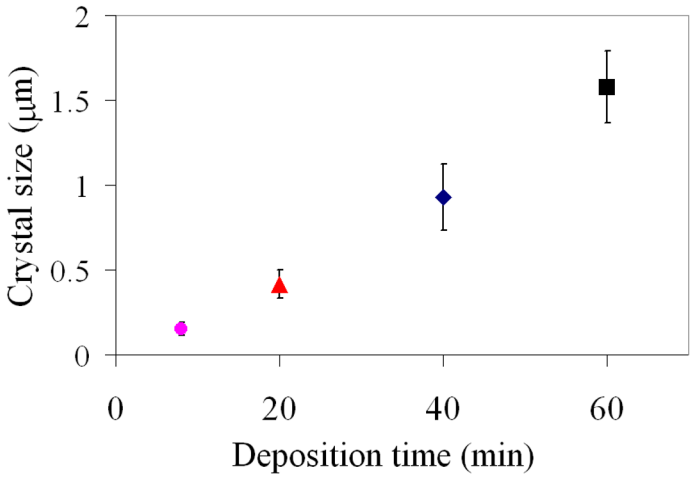

Figure 4.3 A graph showing the average size of the diamond crystals as a function of deposition time. The growth rate is 22 nm/min.

Figure 4.4 demonstrates the ability to synthesize various crystal densities by using different concentrations of the nanodiamond seeds in the suspension. For concentrations exceeding 0.5 μg/ml, a continuous film of nanodiamond is obtained after only 30 minutes of growth. This demonstrates that diamond films can be grown without any substrate pre-treatment mediated nucleation (such as coating with carbon compounds, ultrasonic treatment or scratching) which damages the substrate.

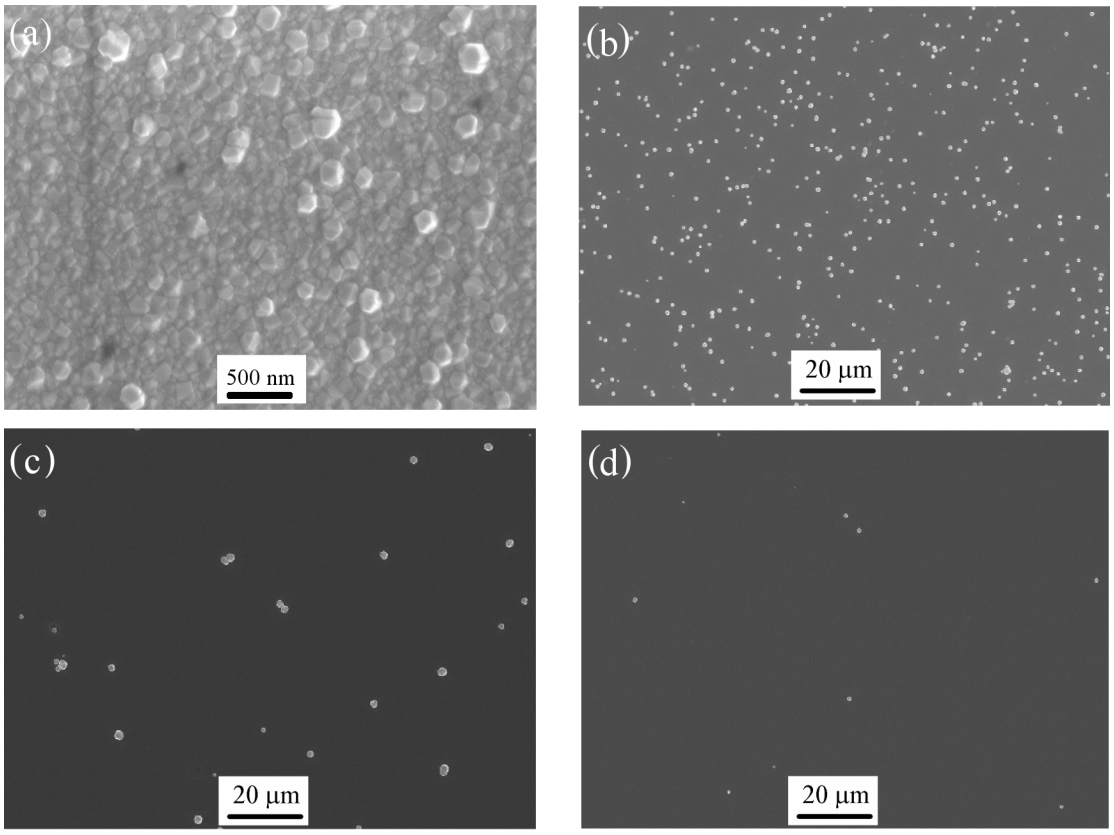

Figure 4.4 Various controllable nucleation densities of the diamond crystals on silicon substrates. (a) a diamond film obtained spraying a high seed concentration suspension. (b-d) Individual diamond crystals obtained by spraying lower seed concentration suspension. A relatively dense growth can be seen in (b) while very sparse growth of nanodiamonds is seen in (d).

For seed concentrations of less than 0.5 μg/ml, individual diamond crystals were grown (Figure 4.4b-d). The crystal density varies from hundreds of crystals in an area of 100×100 μm^2 to only a few crystals in the same area. This flexibility is very advantageous for optical characterization using a confocal microscope which has a typical scan area of 100×100 μm^2 thus allowing individual crystals to be addressed.

Spraying nanometer diamond particles which act as seeds provides a controlled low density of diamond nuclei which all begin to grow simultaneously. By employing a relatively high microwave power density (estimated to be ~200 W/cm^3) and low carbon concentration, a large flux of atomic hydrogen[182] is produced. The hydrogen effectively etches any secondary nucleation on the polished substrate surface, inhibiting spontaneous nucleation on the substrate and unwanted secondary nucleation on the surface of the growing crystal. Avoidance of secondary nucleation on the growing surface allows the formation of well faceted, individual diamond crystals, rather than clusters of small crystals with remnants of sp^2 carbon or cauliflower morphology.

The inhibition of spontaneous nucleation on the substrate is verified by the Gaussian distribution in the final size of the crystals, as can be seen in Figure 4.5. If secondary nucleation is present, the distribution of the sizes will not be Gaussian since every new crystal will serve as a nucleation spot and enhance the growth of more crystals, until a continuous film is obtained.

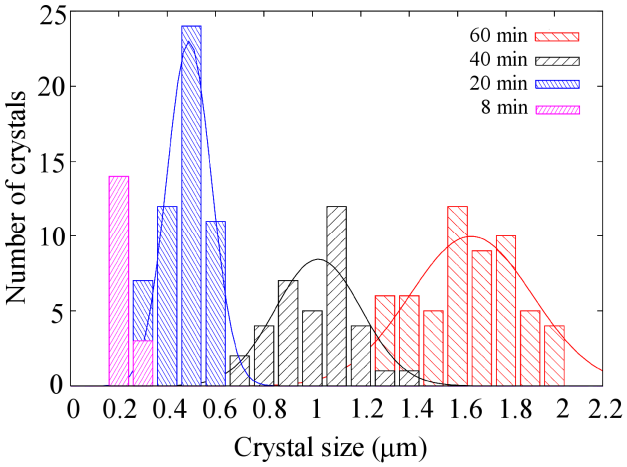

Figure 4.5 Histogram of the size of diamond crystals grown on silicon substrate as a function of growth time for 8, 20, 40 and 60 minutes. The comparatively narrow distribution of sizes is indicative of the suppression of spontaneous nucleation under our growth conditions.

The distribution variance varies with growth time monotonically, which indicates that shorter growth times should lead to smaller variances as is indeed the case. No Gaussian fitting was done for the lowest 8 minutes growth regime because most of the crystals have a uniform size within the bin width of the histogram binning. To completely exclude

the possibility of spontaneous nucleation, a virgin silicon substrate without any nanodiamond seeds deposited on surface was tested. No spontaneous nucleation was observed and no diamond crystals were grown under same experimental conditions.

To estimate the quality and the purity of the CVD grown diamonds, Raman and PL measurements were performed. Figure 4.6 shows Raman spectra recorded at room temperature from a 1μm single diamond crystal and a cluster of a few separate 40 nm diamond crystals (offset for clarity).

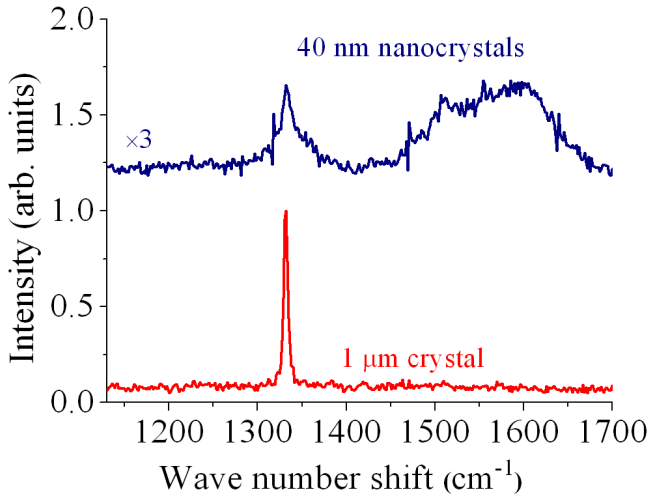

Figure 4.6 Raman characterization of the CVD diamonds. Raman spectrum recorded from a few 40 nm crystals (blue curve) and Raman spectra recorded from a 1 μm diamond crystal (red curve). The Raman data from 40 nm crystals is scaled up by a factor of 3 and offset for convenience.

For the 1μm crystal a sharp line at 1332cm^{-1} (FWHM is less than 6 cm^{-1}) represents the diamond Raman line. No amorphous carbon signature could be observed proving unambiguously the high quality of the grown crystals. For the 40 nm crystals, a clear Raman line can be seen but additional graphitic sp^2 feature is observed at ~ 1560 nm (G band). The graphitic peak originates due to residual sp^2 carbon in between the diamond crystals if they bonded into a cluster. A clear 1332 cm^{-1} peak observed from these crystals shows explicitly that a significant diamond phase is present. Moreover, most of the literature reports concerning Raman measurements from nanodiamonds[187, 188], show rather a wide peaks ~1326 cm^{-1} or an additional feature ~ 1140 cm^{-1} attributed to

nanodiamonds, while the first Raman line is often missing due to an increased graphite on the grain boundaries[187, 189]. Unfortunately, the detection of our equipment is not sensitive to record a measurement from individual 40 nm crystal, hence Raman from a few crystals is presented.

Figure 4.7a shows a PL spectrum recorded at room temperature from an individual 1μm diamond crystal grown on silicon (black curve). The intense line at around 738nm is attributed to the SiV complex in diamond and originates due to the incorporation of silicon during the diamond deposition. The main source of the silicon is the silicon substrate on which the CVD diamonds are grown. Due to etching of the substrate, silicon atoms are exposed to the plasma and incorporated in the growing crystal. Additional source of silicon is the quartz bell jar which is exposed partially to the plasma and to the high temperature of the chamber.

To minimize the silicon incorporation into the growing crystals alternative substrates which do not contain silicon were considered. Figure 4.7a (red curve) shows a PL spectrum recorded at room temperature from an individual diamond crystal grown on sapphire. The absence of SiV exemplifies that a formation of optical centers in diamond can be controlled by a right choice of the growth substrate. Inset, is the magnified region of the first Raman line.

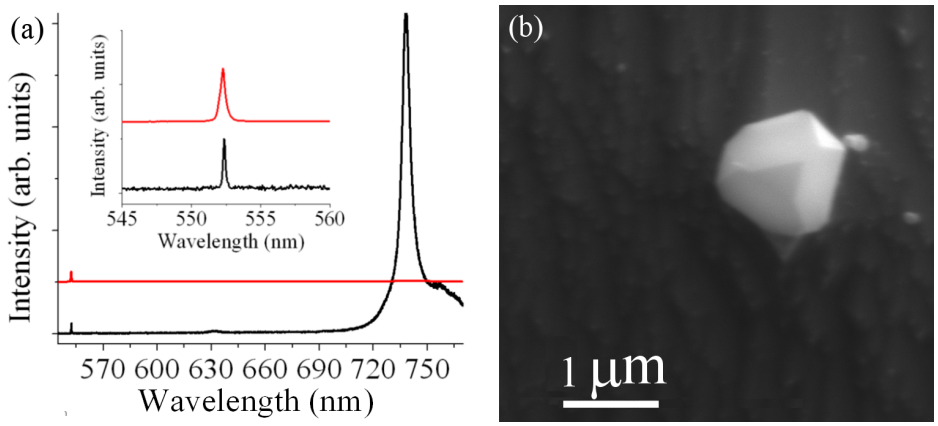

Figure 4.7 (a) PL spectrum of individual CVD diamond crystals deposited on silicon (black curve) and on sapphire substrates (red curve). All the spectra were recorded using 514 nm excitation at room temperature and are normalized to the Raman line. Inset, is the magnified region of the first Raman line. (b) SEM image of a high quality diamond crystal grown on a sapphire substrate.

Figure 4.7b shows a SEM image of a diamond crystal grown on sapphire, convincingly demonstrating that employing the high plasma density growth condition, high quality crystals can be grown on a substrate of choice (sapphire in this case).

Employing conventional PL systems, PL due to NV centers was not observed from the diamond crystals at room temperature. However, low temperature measurements might reveal some luminescence due to NV centers. Nitrogen is a common impurity in the CVD gas environment originated from air leaks or residual impurities in the reactant gases and it is preferentially absorbed inside the diamond lattice. Subsequently, NV centers are often reported for CVD grown diamond[27, 180] even if the nitrogen is not intentionally introduced. The reduction of residual NV production under our experimental conditions is mainly attributed to the high plasma density and the leak free CVD chamber. Reduced background luminescence due to NV centers is an indication of the high purity of these crystals, which is highly important for QIP applications. This opens the possibility to introduce the NV centers in a controllable manner into grown diamond nanocrystals.

Another hypothesis to the absence of luminescence from NV centers is the lack of available vacancies. In this case, nitrogen could present in the crystal, however, the NV center will not be optically active. Vacancies are however, known to be present in CVD grown diamonds[36, 129], as evident from the PL originated from the SiV. More likely in this case, is that all the vacancies are trapped by the silicon or other impurities in the lattice. To investigate this issue further, vacancies were introduced to the CVD grown diamond crystals by ion irradiation. After the growth, the CVD crystals were implanted with 30 keV Ni/Er ions and subsequently annealed to 900°C in a forming gas (95% Ar-5% H_2) ambient. However, once again no optically active NVs were detected using the same optical excitation (514 nm laser excitation). Under similar conditions, when the same irradiation and annealing process was applied to a bulk type IIa CVD diamond crystal with known substitutional nitrogen content (1 < ppm) a significant enhancement of the NV signal was observed.

4.4 Discussion

4.4.1 Morphology

The results presented above demonstrate a technique to seed and grow high quality, individual diamond crystals from nanodiamond seeds. The seeds vary in their purity, perfection and orientation and hence it is not surprising that diamond crystals with various morphologies were observed. The diamond morphology can be correlated with a parameter α, which is defined as $\alpha = \sqrt{3}v_{100}/v_{111}$, where v_{100} and v_{111} are the growth velocities of the (100) and the (111) surfaces, respectively. For $\alpha \leq 1.5$ the (111) surface is the fastest growing and therefore (111) texture is obtained, while for $1.5 \leq \alpha \leq 3$, the (100) surface is the fastest growing surface and (100) texture is obtained. The parameter α is determined by the growth conditions. The α parameter increases with an increasing methane concentration and decreases with increasing substrate temperature[47]. For CVD single crystals, the α parameter can also be derived by the truncation lengths of the crystals facets, using the following equations[47] and the parameters a,b,c,d as depicted in Figure 4.8a :

$$\alpha = \frac{a + \sqrt{2b}}{a + \frac{2}{3}\sqrt{2b}} \text{ for } 1 \leq \alpha \leq 1.5 \tag{4.1}$$

$$\alpha = 3\frac{c + d}{c + 2d} \text{ for } 1.5 \leq \alpha \leq 3 \tag{4.2}$$

It is anticipated that any twinned seed will grow into a twinned crystal, and that the elimination of twinned seeds will result in only cubo-octahedron crystals under the experimental conditions given. Butler et al[190], proposed that the twinning originates from the formation of a hydrogen-terminated four carbon atom cluster on a local {111} surface morphology, which also serves as a nucleus to the next layer of growth.

Figure 4.8(b-e) show different morphologies of the diamond crystals grown under our experimental conditions. Nearly perfect icosahedral, decahedral and cubo-octahedral

shapes with calculated α=1.5 were all observed under our experimental conditions. The icosahedral are ball like shapes consist of twenty (111) facets. The decahedra formed out of five (100) facets aligned with additional ten (111) facets completing a pentagonal tube. The cubo octahedra consists of (100) and (110) facets.

Although twinned morphology was observed during our growth (Figure 4.8), we believe that many of the seeds already contain the twins, and so it is unlikely our growth induced any more twinning. Unfortunately, the twinned crystals are unavoidable in the currently available commercial nanopowder which was used as seeds. One may envisage that in the future, growing diamond crystals from Adamantane molecules employing the growth conditions presented here may result in untwined crystals. The effect of twins in diamond crystals on the formation of color centers and optical properties is as yet unknown.

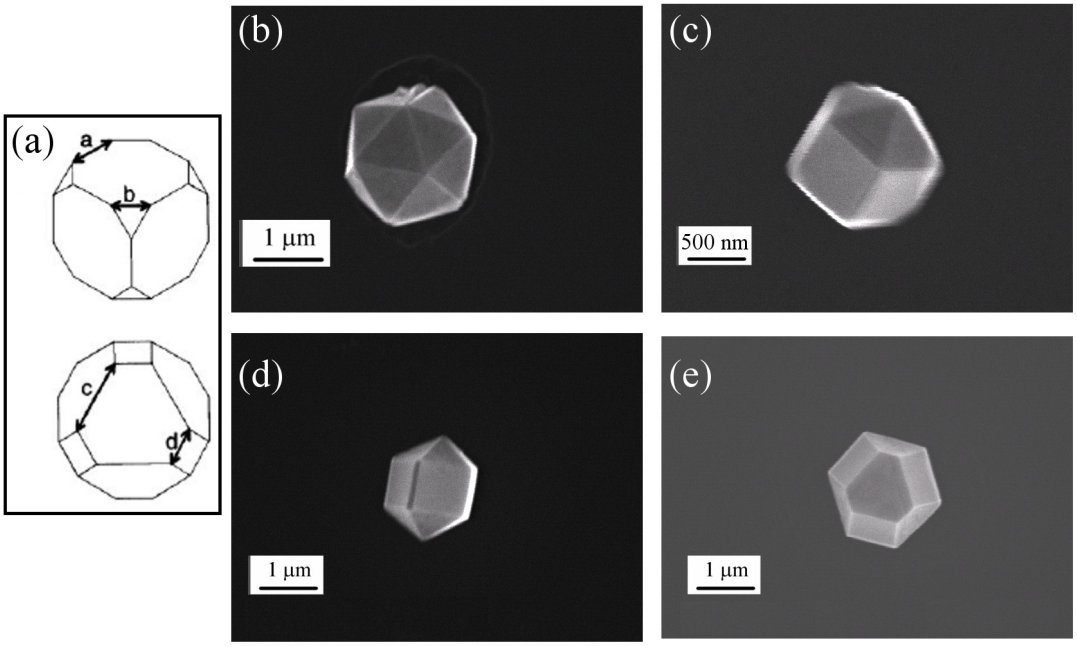

Figure 4.8 Morphological properties of the diamond crystals grown by MPCVD. (a) Various crystal shapes with the parameters a,b,c,d adopted from ref [47]. (b) twinned, icosahedral shape diamond crystal with calculated α=1.5 and (c) twinned, decahedral shape diamond crystal with calculated α=1.5. (d) untwined cubo-octahedral diamond crystal with calculated α=1.5 and (e) untwined cubo-octahedral diamond crystal with calculated α=2.4.

The five fold symmetry crystals have twins along the (111) crystal planes[191] and the five fold axis is a common <110> axis of each twin. The cubooctahedron shape, by

contrast, does not include any twins and it is a perfect crystal. A cubo-octahedron structure can be obtained during the continuous transformation between a perfect cube and a perfect octahedron during the growth[47]. The combination of these observations leads to a conclusion that the growth of CVD diamonds under the conditions of high microwave power density in combination with the elimination of the spontaneous nucleation provides a better control over the final size of the crystal as well as faceted morphology.

4.4.2 Seeding

A common problem with the use of nano-diamond powder as a seeding reagent is the clustering of the individual particles into agglomerates[192]. The commercially available powder, with particle sizes < 10 nm, tend to form tightly bound aggregates. Even after a powerful ultrasonic treatment, diamond agglomerates are still found in the solution[167]. The de-agglomeration of nanodiamonds into their primary size is therefore an important, though complicated task. Few methods based on mechanical de-agglomeration of nanodiamond suspension by stirred media milling[192], bead-assisted sonic disintegration[166, 167, 192, 193] or using chemical modification and detergents were investigated[167, 194]. All these treatments however, are not suitable for a fast routine use of nanodiamonds as seeds.

In the growth sequence employed in this work, an etching step using microwave plasma is carried out prior the actual diamond growth. This etching step is believed to break the agglomerates and leave individual diamond seeds[167]. This hypothesis was confirmed by the following experiment: a silicon substrate was seeded with nanodiamond seeds and broken into two parts. The first part was immediately imaged with an AFM while the second part was etched in the plasma (without the actual growth) and then imaged in an AFM for comparison. Figure 4.9a shows an AFM scan of the seeded substrate before the plasma. Diamond agglomerates are clearly seen in the image. The linescan over one of the agglomerates (Figure 4.9b) reveals its size of few hundreds of nanometers. An AFM scan of the second part of the substrate which was subject to a plasma etching did not

reveal any agglomerates, as evident from Figure 4.9c. The linescan (Figure 4.9d) over this substrate reveals a surface roughness was less than 10 nm.

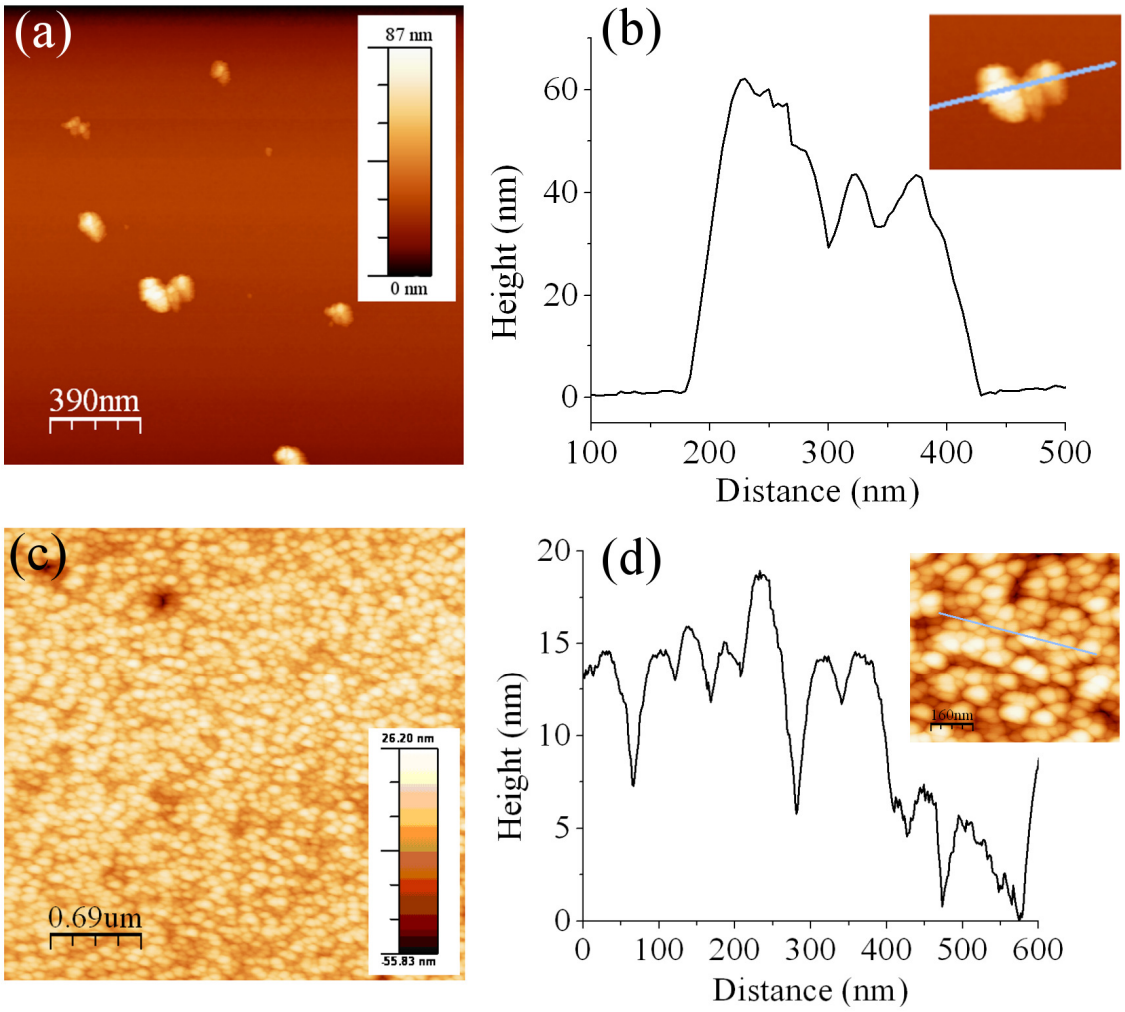

Figure 4.9 (a) AFM scan over a substrate which was seeded with nanodiamonds before etching. (b) Line scan over the agglomerated nanodiamonds. (c) AFM scan over a substrate which was seeded and undergo an etching step in the plasma (without the growth). No agglomerates can be observed. (d) Line scan over the substrate demonstrating a roughness of few nanometers without any agglomeration.

To verify that the seeds were not etched away and remained on the surface, this same substrate was inserted into the reactor for diamond growth. The fact that diamond crystals could then be grown on this same substrate is evidence that the de-agglomeration process was successful (see as example SEM images in Figure 4.2). Therefore, the pre-growth etching step employed prior to each growth breaks the agglomerates, leaving behind

nucleation centers less than 10 nm in size which lead to well faceted individual diamond crystals. The faceted crystals are an additional independent indication that the original seed was not an agglomerate of few seeds.

4.4.3 Growth parameters

To understand which parameters in our setup are the most crucial to the formation of high quality diamond crystals, the growth pressure and the distance of the substrate from the plasma ball were varied. The pressure impacts the microwave power density, gas temperature, and H atom concentration which subsequently affect the temperature of the substrate and the etching rate of the diamonds during the growth. The distance from the plasma ball mainly controls the etching rate of the growing species and the substrate temperature. Reducing the pressure to 30 Torr (while keeping the rest of the parameters constant), produces an estimated microwave power density in the plasma of approximately 10 W/cm^3 and causes low quality diamond formation with a cauliflower morphology (Figure 4.10a). Cauliflower morphology is an indication of a spontaneous nucleation which is a result of the low microwave power density growth regime. Achard et al.[182] have shown clearly that by increasing the microwave power density, during single crystal film growth, the flux of atomic hydrogen impacting the growth surface can be increased, thus increasing the etching of unwanted carbon phases. By ensuring that the flow of methyl radicals onto the growth surface is significantly smaller than the flow of atomic hydrogen, and by using a high microwave power density, the growth of only high quality nanodiamonds is promoted. The flow of methyl radicals can be controlled by adjusting the methane/hydrogen mixture into the system. This parameter was kept constant in our experimental procedure.

The distance of the substrate from the plasma ball was varied until high quality diamond crystals with well defined facets were observed (Figure 4.2). An optimum distance to of 1 cm was found to satisfy this criterion. When the substrate was moved closer to the plasma ball, no growth of diamonds on the substrate was observed. This is due to a high etching rate that hindered the growth. On the other hand, when the distance from the plasma increased, the diamond crystals were not faceted and had cauliflower morphology and

showed sp^2 signatures in their Raman spectrum. In this case, the etching rate was assumed to be too low, leading to sp^2 carbon accumulated on the diamond surface, preventing the desired morphology. Note also, that the distance from the plasma ball strongly affects the substrate temperature which is a crucial parameter of the diamond crystal growth. The distance from the sample to the plasma is likely to be an important additional parameter; however, it is unclear from the existing literature whether this is solely due to the induced sample temperature change or whether the different chemistry in the plasma at different positions plays a more important role.

The effect of nitrogen addition was also investigated. Nitrogen was introduced in the gas phase (5% N_2 in H_2) during the CVD process. Amounts ranging from 0.1%-10% of N_2 were added during the growth. Nitrogen is known to enhance the growth rate of the diamond crystals[49, 168, 195]. Indeed, as can be seen from Figure 4.10b,c diamond crystals were grown to a ~ 2 μm size after only 30 minutes of deposition (comparable to ~1.5 μm after 1 hour without a nitrogen addition, Figure 4.2). However, in addition to the growth rate enhancement, defects are observed on the surface of the diamond crystals. Addition of nitrogen enhances the growth of <100> or the <110> directions[50] and therefore, more morphological features present on the facets of the crystal.

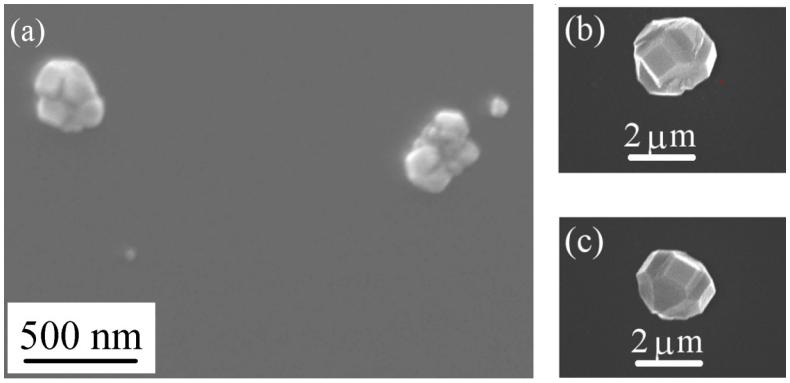

Figure 4.10 (a) A SEM image demonstrating cauliflower morphology of the diamonds grown in low plasma density CVD. (b, c) SEM images demonstrating the morphology of the diamond grown with an addition of 10% of nitrogen during the growth.

4.5 Conclusions

High quality, individual single crystalline sub micron sized diamonds were grown from nanodiamonds seeds (4-6) nm using MPCVD under conditions usually employed for homoepitaxial single crystal growth. The introduced seeding technique enables growth of individual submicron crystal on a substrate of choice. The growth from nano seeds rather than other nucleation techniques allows improved control over the final size of the crystals and the density of crystals on the substrate. Various parameters of the growth were studied and the microwave power density was found to have the major influence on the crystal morphology. Higher microwave power densities lead to high quality, faceted diamonds while lower power densities result in diamond crystals with cauliflower morphology. The elimination of PL originated from SiV defects can be realized by using non silicon (e.g. sapphire) substrates.

This achievement of a high control over the diamond CVD (size, density of crystals, purity) constitutes an enabler for future integration of diamond nanocrystals in quantum information processing applications.

Chapter 5

Fabrication of optical centers by ion implantation

Once a recipe for growing high quality diamond crystals was established, we now turn to fabricate single photon emitters within the crystals. The first methodology to be investigated is ion implantation. Fabrication of optical color centers in diamond by ion implantation was attempted in the past for a few elements, including silicon, nitrogen, xenon and the transition metals[55, 94]. However, only silicon[20], nitrogen[114] and the carbon related[151] single photon emitters were successfully produced in diamond by ion implantation. The scope of this chapter is the fabrication of single photon emitters in diamond by ion implantation. We first concentrate on fabricating the centers in bulk diamond crystals and then reiterate the implantation process into nanodiamonds.

5.1 Direct implantation into nitrogen containing bulk diamond crystal

Prior to a fabrication of optical centers in diamond, especially on a single level, one should precisely characterize the target materials. For the case of NV centers, as an example, implantation of nitrogen into nitrogen containing diamond would be futile since the amount of the background nitrogen exceeds the implanted ones (unless a different isotope of nitrogen which can be distinguished using magnetic resonance techniques is used [115]). However, irradiating nitrogen containing diamond to enhance vacancy formation[68, 110] is a proven methodology to engineer NV centers. Alternatively, nitrogen can be implanted directly into a pure diamond sample[115, 116]. By using lithographic masks or patterning, an array of color centers can be created[110, 114, 151].
For diamonds grown by HPHT method, a metal catalyst like iron, nickel or cobalt is generally used. Optically active centers based on these elements are therefore often found

in these types of diamonds. Furthermore, since nitrogen is an abundant gas in the atmosphere, it is easily incorporated during the growth. Therefore, many metal-nitrogen complexes are found in natural and synthetically grown diamonds and the research to identify their structure is currently pursued by many groups world wide. A quick and efficient way to characterize diamond surfaces, particularly synthesized by HPHT method, is recording a CL map, similar to the one presented in the Materials and Methods section (Figure 3.1a). These maps show distinct sectors with definite impurities concentrations.

On the other hand, ultra pure CVD bulk diamond crystals with impurity concentration at the ppb level, offer a pristine diamond target for ion implantation. These samples are very expensive, however, cheaper alternatives with higher impurity concentration (at the ppm level) are routinely used for various purposes. The CVD bulk diamonds have an advantage of not containing an initial metal contamination, thus providing a clean substance for metal ion implantation.

To fabricate metal related color centers in a controlled manner in a pristine diamond, the species should be implanted directly into the crystal. Implantation of zinc, thallium, titanium, chromium, nickel and other metals, were attempted in various types of diamond[94]. Controlled implantation of impurity into pure diamond can provide important information about the centers such as its ZPL emission, vibronic features and atomic composition. Interestingly, to date, implantation of various metals into diamond did not result in a fabrication of SPSs based on these materials.

Having this in mind, we were motivated to fabricate the nickel nitrogen (NE8) center by ion implantation of nickel into nitrogen containing diamond. Upon annealing, the nickel should bond to the nitrogen atoms to form the NE8 center. As was mentioned in the introduction, the NE8 center is attracting some attention as a SPS due to its narrow emission in the NIR (ZPL centered at 793 nm). Previously, nickel-nitrogen related complexes were identified in diamonds grown by HPHT method[29, 196] on a single level. These centers were natively present in the crystal, most likely due the use of nickel as a catalyst. Although the ZPL of the centers varied, they were commonly attributed to the NE8 center. Nevertheless, there were no reports in the literature regarding a controlled fabrication of the NE8 center by ion implantation. This is rather surprising

since this defect can be routinely observed in bulk quantities (although not on a single level) after HPHT annealing of nickel containing diamonds[81, 82, 86, 88]. This may indicate that a single NE8 center is a dim center and can not be resolved optically over the background PL.

Therefore, in this section a nickel implantation into nitrogen containing HPHT synthetic diamond was attempted with a motivation to fabricate nickel related SPSs, particularly the NE8 center.

5.1.1 Experimental results

A dose of 1×10^{13} Ni/cm^2 was implanted though a metal mask with 1 µm holes and 10 µm spacing. The implantation was performed into the top [100] surface ({001} growth sector, which does not contain nickel) of a nitrogen containing HPHT sample. A schematic cartoon of the diamond and the mask are shown in Figure 5.1a. Figure 5.1b shows a SRIM simulation of nickel ions implanted into diamond with acceleration energy of 30 keV. The end of range of this implantation is ~ 20 nm below the diamond surface. Inset is the SEM image of the mask.

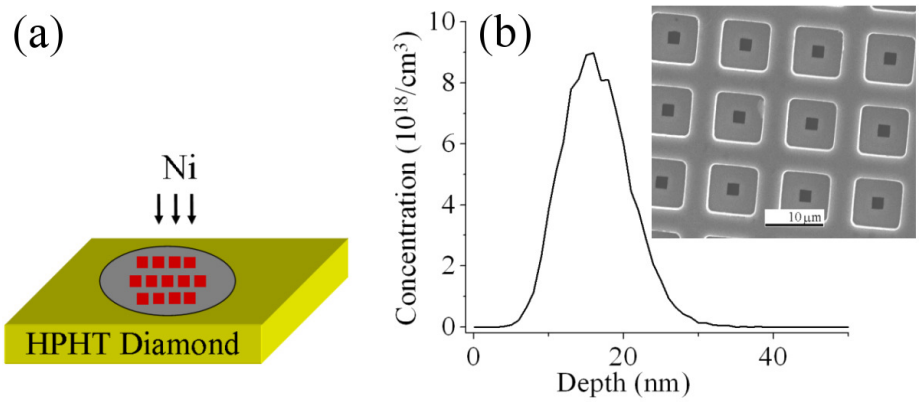

Figure 5.1. (a) A schematic cartoon of the diamond and the mask used for the implantation. (b) SRIM simulation of nickel ions implanted into diamond with acceleration energy of 30 keV. Inset, is the SEM image of the mask.

The HPHT diamonds contain significant amount of nitrogen (~100 ppm), thus increasing the probability for the formation of NE8 which requires four nitrogen atoms for each

nickel. After the implantation, the diamond sample was subsequently annealed for 1 hour in a forming gas ambient (95% Ar-5% H_2) to a temperature of 1000°C.

5.1.2 The 883/885 nm center (1.4 eV center)

A scan over the post-implanted (1×10^{13} Ni/cm^2) and annealed region using a confocal microscope revealed bright fluorescence squares originated from the optical centers created within the diamond by the nickel implantation (Figure 5.2a). Using a periodic mask template is an efficient way for creating a periodic array of optical centers in diamond and to identify the implantation region.

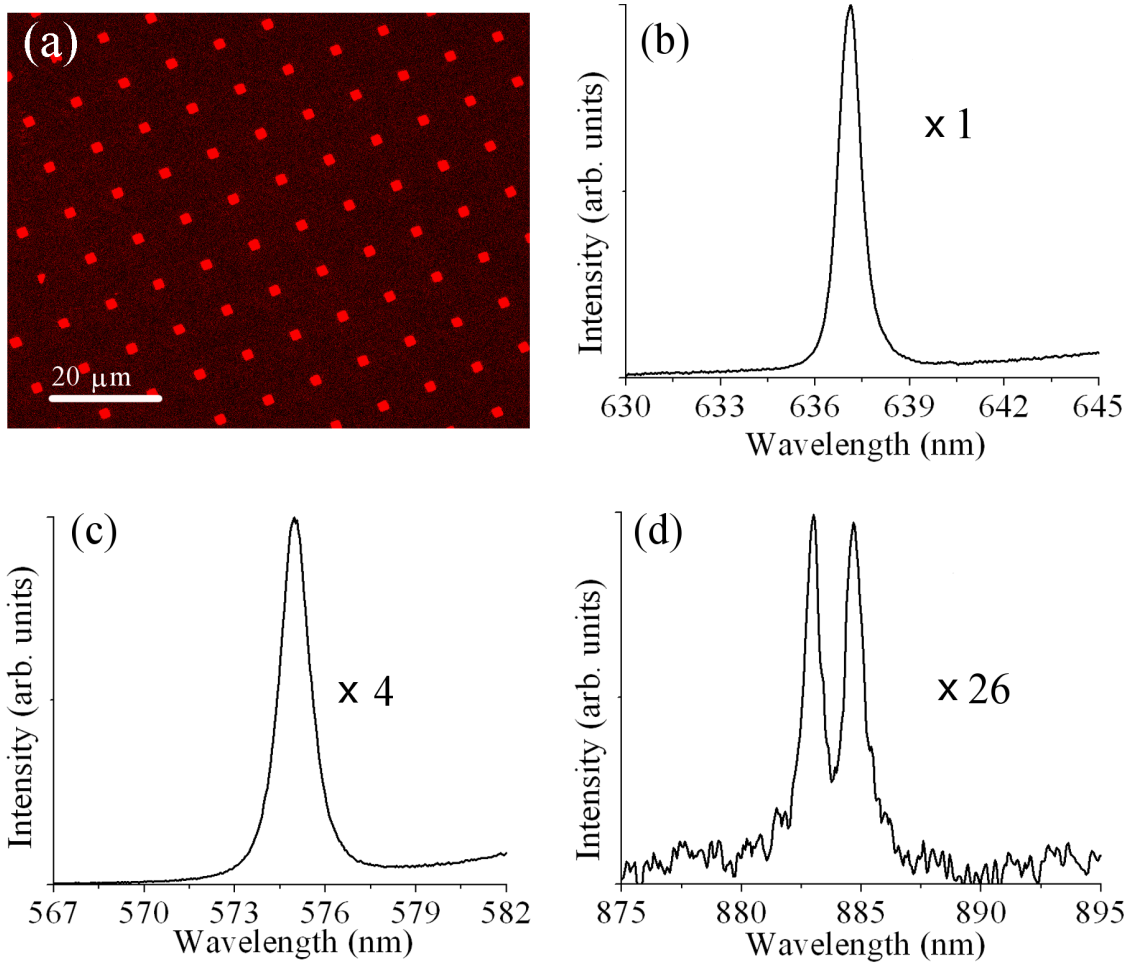

Figure 5.2 (a) A confocal map of nickel implanted HPHT bulk diamond recorded using a 325 nm excitation. The red squares represent the implanted spots. PL spectrum recorded using a 514 nm excitation laser at 80 K from one of the squares showing the (b) $(NV)^-$ ZPL (c) $(NV)^0$ ZPL (d) nickel related doublet centered at 883/885 nm. The spectra of $(NV)^0$ and the nickel center were scaled up to the intensity of the $(NV)^-$ center.

As expected, the damage associated with the implantation created a significant concentration of NV centers, which dominate the detected emission from each square in the confocal map. Figure 5.2(b,c) show the PL recorded from one of the spots using a 514 nm excitation laser at liquid nitrogen temperatures (80 K) revealing the PL due to the negatively and the neutrally charged NV centers. In addition to the NV centers, a nickel related complex centered at 883/885 nm was formed due to the implantation. Figure 5.2d shows the nickel related PL doublet recorded from the same spot. The PL data of the NV^0 and the nickel related center were scaled up to the intensity of the NV^- center.

The nickel related PL doublet originates from a transition between an excited state and two ground states[85] which can be resolved only at cryogenic temperatures, below 170 K, as can be seen in Figure 5.3. Both lines split into multiplets in which the line intensity corresponds to the natural abundance of nickel isotopes (can be seen at ~10 K). Using electron spin resonance techniques, the center was assigned to a Ni^+ ion in the center of a di-vacancy in a diamond lattice[84] where the nickel atom is probably not bonded to the neighboring carbon atoms. Uniaxial stress techniques revealed trigonal symmetry of the defect. A remarkable property of the 883/885 nm center is that it is exclusively incorporated into the <111> growth sectors of HPHT diamond.

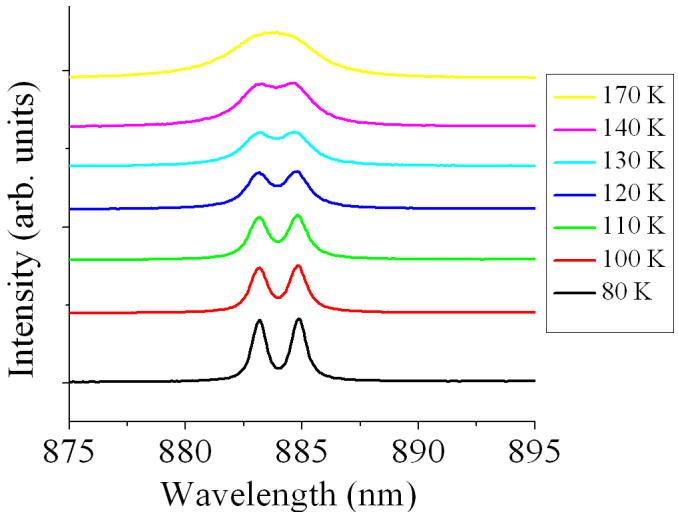

Figure 5.3. PL measurement as a function of temperature for the 883/885 nickel related doublet. The spectra were displaced for clarity.

The photon statistics of PL light from the 883/885 nm doublet was then studied by measuring the normalized second-order autocorrelation function, $g^{(2)}(\tau)$, using the HBT interferometer. Figure 5.4a shows a raster confocal scan from one of the dots recorded using 680 nm excitation laser at room temperature. Figure 5.4b shows a pulsed $g^{(2)}(\tau)$ function recorded from the same dot. No dip at zero delay time was observed and the statistics of light from the nickel defect has a Poissonian distribution.

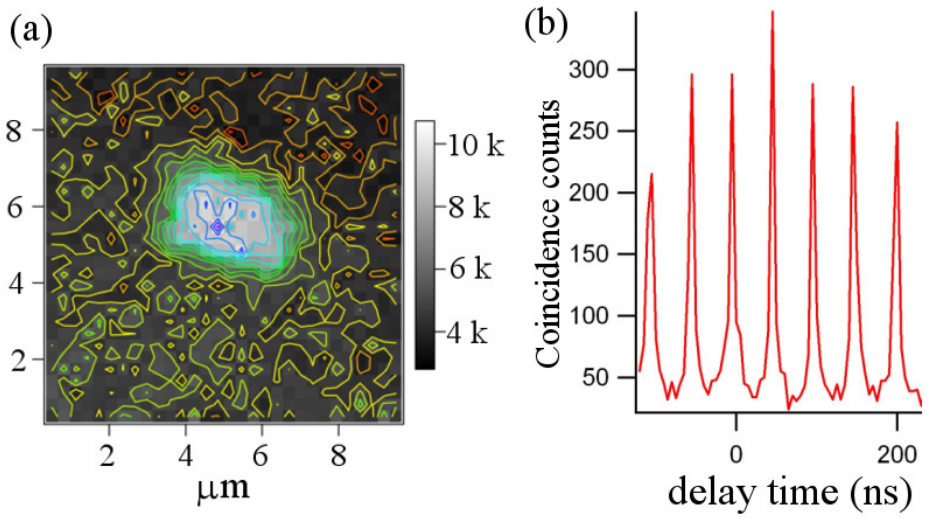

Figure 5.4 (a) Raster confocal scan over one of the implanted dots excited by 680 nm excitation at room temperature. (b) Pulsed second order autocorrelation function, $g^{(2)}(\tau)$, showing no dip at zero delay time, exhibiting a Poissonian statistics of light.

To generate individual nickel centers which could be resolved over the background PL, the implantation dose was reduced down to (~1×10^{11} Ni/cm^2). However, single photon emission from this center has not been observed. Lower doses of nickel could not been resolved over the background fluorescence using a conventional confocal microscopy, which indicates that this center is dim and may not be promising for various quantum optical or biological applications.

Despite the fact that the 883/885 center is the most studied nickel related center, the excited state lifetime of this center has not been reported. Figure 5.5 shows a direct excited state lifetime measurement of the 883/885 nm emitter excited by a 500 ps pulsed laser operating at ~ 667 nm. A lifetime of 11.6 ns is deduced from a mono exponential fit, which is comparable to the NV^- center in bulk diamond. Given the lifetime similarities of

the two centers, the fact that the 883/885 nm doublet could not been resolved on a single level, indicates that this center is less efficient than the NV center. This suggests that the 883/885 nm center possesses additional non radiative decay paths or metastable states with longer lifetime which quench the luminescence.

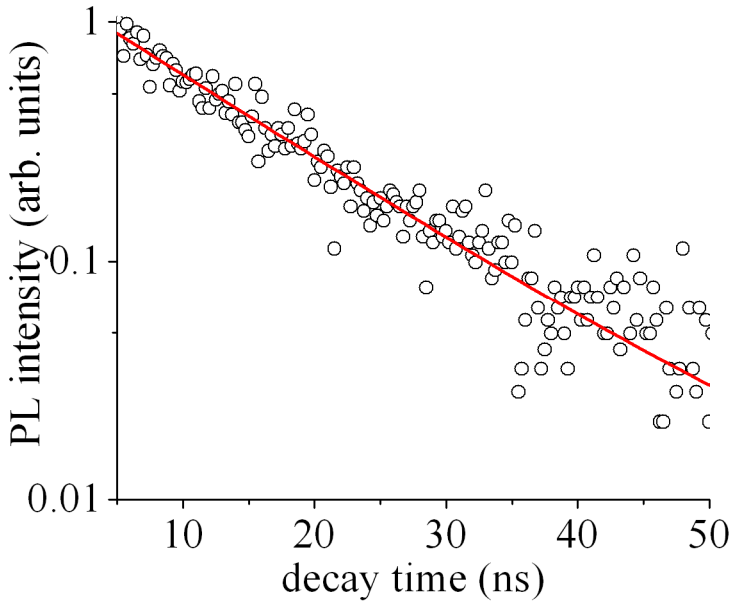

Figure 5.5 A direct excited state lifetime measurement of the 883/885 nm center. The single exponential fit results in an excited state lifetime of 11.6 ns.

5.1.3 The NE8 center

No NE8 centers were found after the implantation and annealing procedure, most likely because the nitrogen atoms are not yet mobile at 1000°C. To enhance the mobility of the nitrogen atoms, higher annealing temperatures of up to 1600°C were applied, however, the PL due to the NE8 complex was not observed. To understand the lack of formation of the NE8 complex, a careful reexamination of the NE8 formation mechanism is required. The following reaction sequence describes the structuring of the NE8 center[81]:

$$Ni_s^- \rightarrow NE4 + C_i$$
$$NE4 + 2N \rightarrow NE1$$
$$NE1 + N \rightarrow NE2$$
$$NE2 + N \rightarrow NE8$$

Ni_s^- denotes a nickel atom occupying a substitutional location and C_i is a carbon atom in an interstitial location. From the proposed mechanism, it can be seen that the nitrogen atoms are added one by one to the nickel atom. One hypothesis for the lack of the NE8 formation is that the diffusion of four nitrogen atoms to bond the nickel is a very low probability process which requires longer annealing times and higher annealing temperatures. In addition, the NE8 formation first requires the nickel atom to be in an interstitial position, in a nearest neighbor di-vacancy, VNiV, to form the NE4 complex. The VNiV fragment serves as nucleation center for the migrating nitrogen atoms into its ligand shell, and this is the precursor of the nickel – nitrogen centers. The transformation of nickel into an interstitial requires diffusion of carbon atoms and interstitials in diamond which once again requires more extreme annealing conditions.

To enhance the formation probability of the NE8 complex, an HPHT anneal is required. For practical equipment limitation, this process requires the sample to have small dimensions of less than $1mm^3$. Therefore, nickel ions with same energy and doses of ~1×10^{11} Ni/cm^2 and ~1×10^{13} Ni/cm^2 were implanted into the smallest HPHT diamond and annealed under HPHT conditions (the annealing was done by Mark Newton, at the University of Warwick, UK). At these extreme conditions nickel and nitrogen atoms have enough energy to be mobile and form the nickel – nitrogen complexes

Figure 5.6 shows the PL recorded from the implanted and HPHT annealed samples. A clear signature of the NE8 with the ZPL at 793 nm can be observed. As expected the PL signal is scalable with the implantation dose, demonstrating that the formation probability of this center is increasing with an increasing nickel dose. A confocal raster scan over these samples at room temperature using 680 nm excitation laser, did not however resolve any single NE8 centers.

A dose of 1×10^{11} Ni/cm^2 equals to 1000 Ni/μm^2. Since individual centers were not resolved in the scans, each spot consisted of at least ~10 NE8 centers (a practical limit where no dip in the autocorrelation function can be detected over the background counts). This indicates that a conversion probability from an implanted nickel ion to an optically active NE8 center is in the order of ~ 1 %. This is a tentative lower bound for the

formation probability of NE8 centers following nickel ion implantation and HPHT annealing sequence.

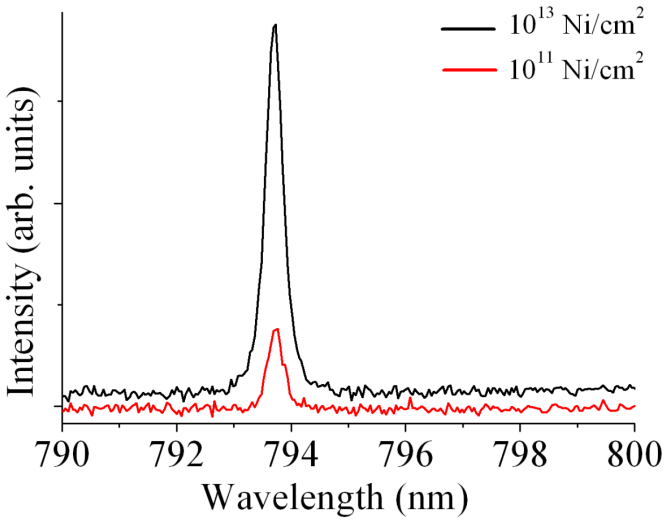

Figure 5.6 PL spectra recorded from nickel implanted and HPHT annealed diamond sample showing the NE8 centers for doses of ~1×10^{11} Ni/cm^2 and ~1×10^{13} Ni/cm^2. The graph representing the ~1×10^{13} Ni/cm^2 implantation dose was displaced for clarity.

5.2 Implantation into CVD grown sub-micron diamond crystals

Ion implantation into small CVD grown nanodiamonds or commercial nanodiamond powder, have potentially a great advantage over the bulk material. In an ideal case, a center of choice can be fabricated by ion implantation within the nanodiamond, providing a versatile method to modify their optical properties. Moreover, an identification of a luminescent center using confocal microscopy followed by a post selection and manipulation [152, 153] of a single nanocrystal hosting this optical center enabled fabrication of novel photonic structures. Using this method, for example, coupling of NV centers to micro resonators[156] or enhancing the emission through plasmonic coupling[155, 197] have been demonstrated. Furthermore, irradiation of nitrogen containing nanodiamonds was found to be an effective method for a mass production of florescent nanodiamonds for biological applications[198, 199].

Using a dual beam SEM/FIB to create SPSs in a desired crystal and in a preferred position constitutes significant progress towards a scalable control and fabrication of

multi-qubit quantum optic devices by affording the ability to locate implantation zones within optical nano-structures. It may even give rise to a 'step and repeat' technology[200], which would be of great benefit to large-scale integrated quantum devices.

To date, the literature concerning ion implantation into nanodiamonds have concentrated only on the formation of NV center. In fact, in most cases the implantation was an irradiation process introducing vacancies using protons[199, 201] or electrons[202], rather than a direct nitrogen implantation.

To move beyond the limitation of NV and to fabricate SPSs in the NIR, materials like nickel should be considered as candidates for implantation into CVD grown sub micron diamonds. Using ion implantation of nickel, we address some of the challenges towards spatially controlled fabrication of nickel related SPSs in diamond.

Given the potential of nickel – related color centers, there have been some attempts at their controlled manufacture in CVD diamond. Previously demonstrated techniques to incorporate nickel into CVD diamond films included seeding the substrate with slurry containing nanodiamonds and nickel powder [27] or a more recent report of incorporation of nickel through a gas phase during a CVD growth using an evaporated nickelocene[203]. These techniques however did not allow a controlled formation of the nickel centers in a specific diamond crystal or in a preferred location. Furthermore, the interaction between various impurities within the diamond (such as nitrogen and nickel or silicon and nickel) is still unclear which makes the controlled fabrication of nickel related optical centers a challenging task.

In this section, the formation of nickel related SPSs will be demonstrated by FIB implantation of nickel into individual CVD diamond nano-crystals. The use of a dual SEM/FIB allows the imaging of a specific crystal prior to implantation with a precise accuracy suitable for past processing and scalability. This method allows fabrication of optical centers in a specific crystal of choice as well as in a given space, in contrast to previous approaches where the incorporation of the nickel into diamond crystal was not dependent on the crystal selection.

5.2.1 Experimental details

The diamond crystals were grown using a microwave CVD technique following a procedure reported in chapter 4. Briefly, the substrate (sapphire or silica coverslip) was seeded with nanodiamond powder (4-6 nm, Nanoamor Inc., Houston, TX, USA) without ultrasonic treatment followed by a diamond growth using microwave plasma (900W, 150torr) CVD. After growth, the substrate was transferred to a dual SEM/FIB (see materials and method chapter, Figure 3.3) to perform the nickel implantation. The surface was first imaged by the SEM to determine the diamond density and location. After choosing a specific crystal, a nickel FIB beam with a typical 1-5 pA current was used to perform the implantation into the same crystal. The spot size of the beam was reduced down to few tens of nanometers, allowing implantation into an individual CVD grown diamond crystal. Nickel ions were implanted with an acceleration energy of 30 keV which results in a stopping range of around 20 nm beneath the diamond surface (Figure 5.1b). After implantation, the crystals were annealed at 1000°C in 95% Ar-5% H_2 ambient for 1 hour. Time correlation of photoluminescence intensity was performed with an HBT setup. For this measurement a cw laser diode excitation source at a wavelength of 687 nm was used.

5.2.2 Experimental results

Using the seeding method as described in chapter 4, we were able to control the surface density of crystals on the substrate, thus allowing easy imaging by both the SEM/FIB and the detection using a confocal microscope. The diamond crystals were grown on sapphire or silica substrates to the size of about 200-600 nm which is small enough to eliminate the total internal reflection of the light, thereby enhancing the collection efficiency.

A scan over the post implanted and annealed region using a confocal microscope revealed bright fluorescence originated from the optical centers created within the diamond as shown in Figure 5.7a. Bright emission has been observed only in the nickel implanted regions. Figure 5.7b shows a confocal map of non implanted crystals, with no fluorescent bright spots.

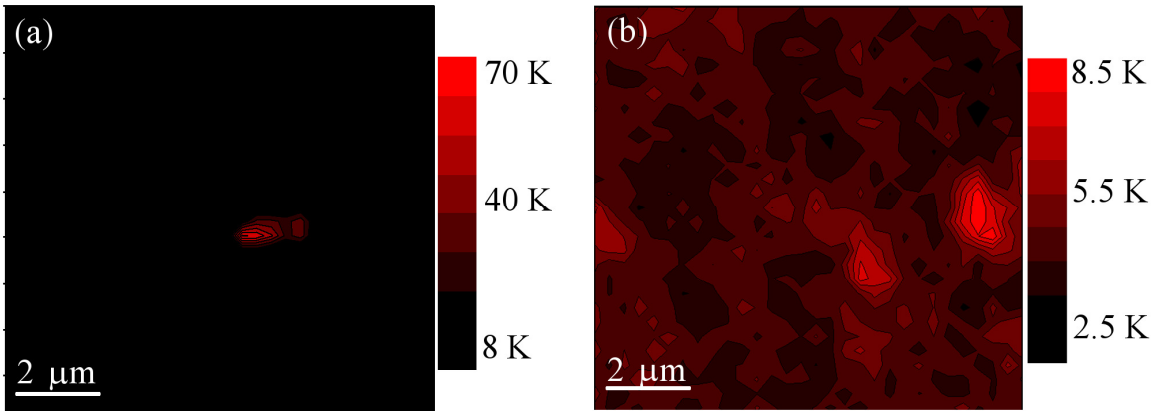

Figure 5.7 (a) Confocal raster scan over the sapphire with the grown diamonds showing a bright fluorescence due to the implantation. (b) Confocal raster scan over the CVD diamonds on sapphire in the unimplanted region, showing no bright fluorescence.

Figure 5.8a shows a PL spectrum recorded at room temperature from an individual fluorescent diamond crystal, related to the formed nickel color center. A strong narrow band luminescence (FWHM ~ 7 nm) with no significant phonon side band is observed at 768 nm. Approximately 90% of the emission intensity is concentrated in the ZPL. This center does not emit at the same wavelength as the previously reported NE8 or one of its variants[27-29]. Most of the implanted crystals revealed a similar emission peak around 770 nm while no PL was detected in the unimplanted regions, convincingly indicating that the origin of the signal is due to the FIB nickel implantation.

Figure 5.8b shows the normalized second order autocorrelation function recorded with a cw laser at room temperature from a color center in an individual diamond crystal located in the implanted area, with the emission spectrum shown in Figure 5.8a. The normalization of the $g^{(2)}(\tau)$ function is described in appendix 1. The dip of $g^{(2)}(\tau)$ at zero delay time indicates non classical emission. In particular, if $g^{(2)}(0) < 0.5$ the emitter is considered a single photon emitter. Single photon characteristics were found in crystals implanted with doses lower than 5×10^{10} Ni/cm^2. Considering that the average crystal size is few hundreds of nanometers, this dose equals to ~100 Ni ions per crystal, depending on the exact orientation and the size of the crystal. Therefore, the formation probability of this center is approximately ~ 1%. This value is comparable with the probability of forming optically active NV centers while nitrogen implantation into single crystal is employed[114, 115]. Implantation doses of ~10^{11} Ni/cm^2 produced double emitters with a

$g^{(2)}(0)$ ~ 0.5, and higher doses resulted in emitters exhibiting Poissonian emission, i.e. $g^{(2)}(0)$ ~ 1. During all the measurements, the center was stable and no photo bleaching or blinking behavior were observed.

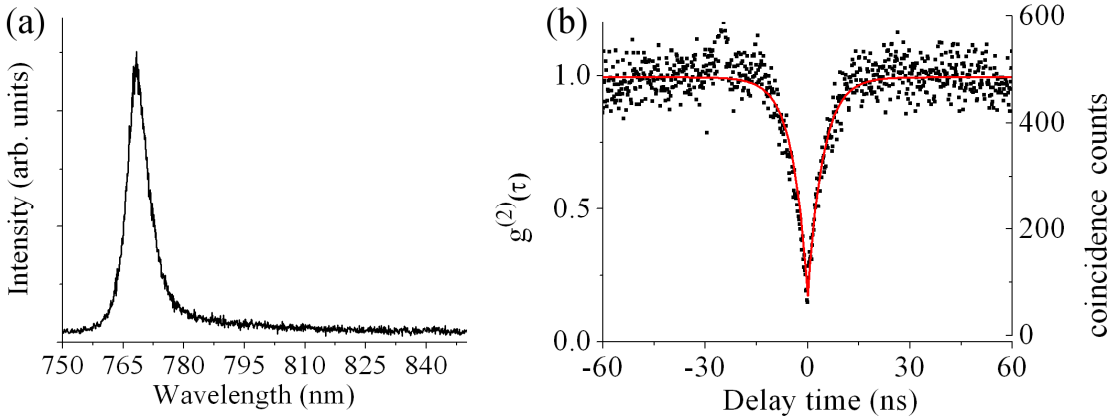

Figure 5.8. (a) PL spectrum from individual nickel implanted diamond crystal under 687 nm excitation recorded at room temperature. (b) Corresponding $g^{(2)}(\tau)$ of the PL signal recorded at room temperature. The excitation power is 100 μW and the integration time is 300 s with a coincidence time bin of 154 ps. The dip at zero delay time with $g^{(2)}(0)$=0.16, indicates single-photon emission. The dots indicate the experimental data while the solid line is a fit of $g^{(2)}(\tau)$ taking into account background, instrumental response function due to finite time resolution of the APDs and the correlation electronics. The slight bump at τ=-30 ns is due to remaining cross talk.

The $g^{(2)}(\tau)$ function was also recorded with increased cw laser excitation power to measure the decay time of the emitter. By extrapolating a linear fit to zero excitation power, the lifetime of the center is deduced to be as short as 2 ns. This value is 6 times shorter than the typical lifetime of an NV center in a CVD crystal and thus makes this nickel related center attractive for quantum photonic applications with a theoretical emission rate as high as 0.5 GHz operating at room temperature. Furthermore, this value is close to currently developed high speed QKD systems with clock rates of 2 GHz[204].

The fluorescence intensity was measured as a function of laser power to evaluate the emission rate at saturation (Figure 5.9). The data were fit using equation (2.21). From the fit curve, the total count rate at saturation excitation power is estimated to be 280×10^3 counts/s. This value is already higher than the saturation count rate of NV color centers reported in the literature. Optimization of the diamond growth substrate, for example

using a highly reflective mirror[147] or coupling to waveguide structures[181, 205], should then lead to the realization of a very efficient SPS.

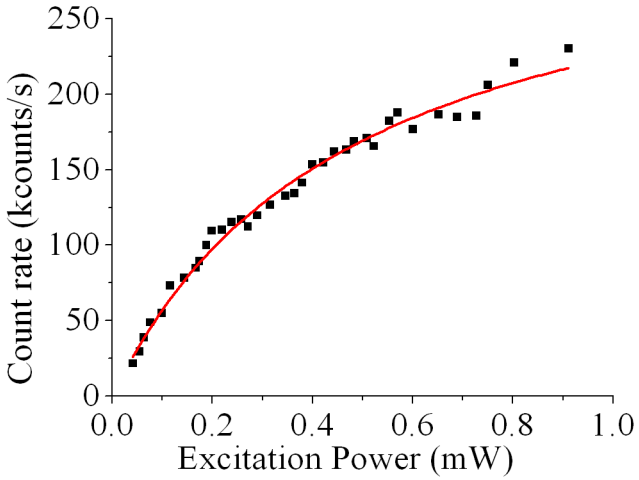

Figure 5.9. Background corrected single photon emission count rate recorded from the same single Ni-related color center shown in Figure 5.8a, as a function of excitation power. The background counting rate is 1.8 kcounts/s for an excitation power of 0.9 mW. The data were fit using equation (2.21).

Finally, the atomistic structure of this center is discussed. It is clear from our experimental data that the observed center is not the nickel nitrogen (NE8) center. The luminescence was observed only from implanted crystals, and therefore it is likely that the centers are nickel related. Previous work reported various emission lines characteristic of nickel impurities in diamond[88], however, an emission around 770 nm was not observed or assigned to any particular nickel related center so far. Besides nitrogen, the most common and favorably incorporated impurity is silicon, which forms a common SiV center within the diamond lattice. Therefore, we assumed that the center is related to a complex containing both nickel and silicon atoms.

To check our assumptions, we performed a control experiment by implanting both silicon and nickel into pure type IIa, 3×3×0.5 mm, CVD diamond produced by Element 6. Nickel ions were implanted with an energy of 37.5 keV while silicon ions were implanted using 25 keV (doses of 1×10^{13} ions/cm^2). According to SRIM simulations[106](Figure 5.10a), the stopping range of both nickel and silicon ions at these energies are around 20 nm beneath the diamond surface and their implantation profile is practically overlapping.

The implantation was followed by the same annealing procedure as used on the CVD grown diamond nanocrystals.

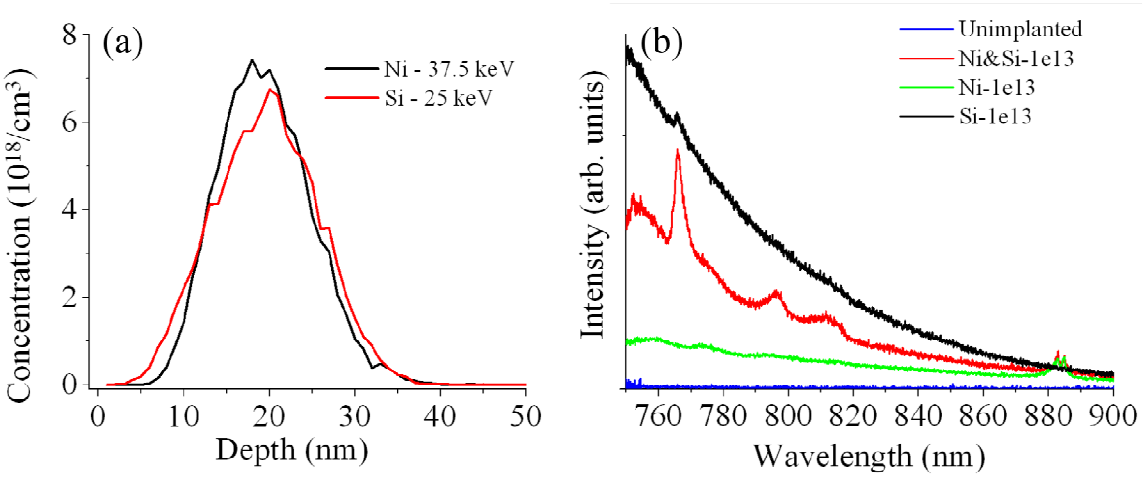

Figure 5.10 (a) SRIM simulation of 37.5 keV nickel and 25 keV silicon implantation into diamond. (b) PL spectra from an unimplanted region (blue curve), nickel only implanted region (green curve), co-implanted Ni/Si region (red curve), and a silicon only implanted region (black curve) of a type IIa e6 CVD diamond. The pronounced peak around 770 nm is clearly observed only in the Ni/Si co-implanted sample. The measurement was taken at 80 K under 514 nm excitation.

PL spectrum recorded from a type IIA diamond co-implanted with nickel and silicon revealed similar emission line centered at 766 nm (Figure 5.10b). A nickel or a silicon only implantation into the same crystal did not result in the formation of this specific emission line (Figure 5.10b). Note that the doublet around 883/885 nm is associated with a known nickel defect in diamond[84, 85] and as expected appears in both nickel implantations.

A similar vibronic feature around 768 nm was previously assigned to a local defect mode[128] or to a local phonon mode of the SiV center[129, 206]. It is important to note that in both cases the origin of the diamond seed used for the CVD growth may have contained nickel impurities. In ref[128] it was a type Ib Sumitomo diamond while in[129, 206] it was a commercial diamond powder. Our experimental data clearly demonstrates that the center is not a SiV center due to a different ZPL, a longer lifetime and a higher count rate[20]. In addition, the demonstrated implantation technique shows that nickel

appears to play a crucial role in enabling the emission. Therefore, we concluded that the PL line at around 770 nm is due to a center containing both nickel and silicon atoms.

Note that nickel and silicon each create a large distortion in the diamond crystal lattice. Hence, it is possible that upon annealing a vacancy is combined with those two atoms and the actual structure consists of silicon and nickel impurities neighboring a vacancy. Given that the CVD diamonds do not show NV emission, it is unlikely that the complex also contains N. The source of the silicon inside the grown CVD diamond crystals may possibly originate from the growing substrate (silica or sapphire) and from the quartz made CVD chamber. An incorporation of a few ppm of silicon into the diamond crystals during the growth is hence likely. The concentration might be too low to be observed as SiV because that center is not an efficient emitter but when it complexes with an implanted nickel ion, it may lead to the formation of the observed centers, even for very low silicon concentrations.

In this context it should be pointed out that the possibility that the nickel plays a crucial role by changing a local environment of the crystal, and giving rise to the PL signal without being bonded to a silicon or any other atom, can not be excluded. At this point of time, an unambiguous conclusion regarding the actual atomic structure of the center can not be made.

Recent follow-up work by Steinmetz et al. [207] confirmed that the PL signal around 770 nm is indeed due to a complex which contains nickel and silicon. Steinmetz and his colleagues co-implanted nickel and silicon atoms deep into a single crystal diamond using high MeV energies and observed PL features at the range of 760-790 nm. Furthermore, they observed single photon emission from the center and estimated the excited state lifetime to be 1.1 ns, comparable with our measurements.

5.3 Conclusions

In this chapter fabrication of color centers by ion implantation have been investigated and discussed. In the first part, it was shown that ion implantation is an effective route to manufacture nickel related centers in bulk diamond. The experimental data suggests that the nickel related 883/885 nm defect is dim and not appropriate to use in various optical

applications. In addition, a controllable manner of fabricating the NE8 defect was demonstrated by annealing a nickel implanted bulk diamond in HPHT condition. Nevertheless, individual NE8 centers have not been resolved over the ensembles. These experiments stress the difficulty to fabricate nickel related single photon emitters in bulk diamond.

In the second part, an efficient SPS based on nickel-silicon complex in individual CVD diamond crystal has been engineered. The center possesses a short lifetime of only 2 ns which resulted in a total high count rate of more than 250×10^3 counts/s at room temperature. These centers were formed via FIB nickel implantation into selected diamond crystals which gives rise to potentially high spatial accuracy. The combination of room temperature operation, high brightness and step and repeat fabrication compatibility, makes the Ni/Si emitter an attractive solid state single photon source. Co-implantation studies using nickel and silicon, strongly suggest that the emitter is a hybrid nickel-silicon complex, as was independently confirmed by another research group[207].

The co-implantation of ions for the purpose of fabrication of new optical centers opens new avenues and new defect centers to be explored as building blocks for quantum optical engineering networks. The co-implantation of nickel and other elements (such as silicon or nitrogen) is likely to spur substantial research into the physical structure and properties of such composites.

Chapter 6

Fabrication of optical centers by incorporation of impurities from the growth substrate

In the previous chapter fabrication of optical centers by ion implantation was highlighted and discussed. Although ion implantation provides the means of precise fabrication ability with the versatility of choosing the implanted species, it is always associated with damaging the diamond matrix. Furthermore, ion implantation leaves the implanted ion in an unknown lattice location; it is during the annealing phase that vacancies and interstitials become sufficiently mobile so the dopants can occupy lattice sites. To cause the implanted atom to migrate within the stiff diamond lattice requires quite often extreme annealing conditions. As was shown previously for the NE8 center, for instance, a mobility of four nitrogen atoms is required to bond one nickel atom. Conventional annealing conditions (high temperature, atmospheric pressure) are not sufficient for the diffusion process to occur.

Alternative routes of incorporating an external atom, while maintaining the desired optical properties are thus preferred. The nanotechnology revolution emphasized the tremendously expending "bottom up" approach – where the nanostructures are built "atom by atom" rather than the not efficient "top down" methodology – where etching of a bulk material is applied to obtain the desired confinement. Using the bottom up approach many nanostructures including nanowires[1] and carbon nanotubes[1] have been synthesized. Inspired by the "bottom up" approach, we would like to incorporate the desired impurity *in-situ*, during the growth of the nanodiamonds.

6.1 Introduction

It is known that during the growth, diamond incorporates various impurities. Diamonds grown using the HPHT method from a metal catalyst (nickel, cobalt or iron) often have optical centers originated from the incorporated metals[55]. For instance, HPHT diamonds grown from nickel catalyst always show the nickel related 883/885 PL doublet. While CVD method is employed, the diamonds generally incorporate the substrate material. The initial work on SiV centers was performed on diamonds grown on silicon substrates[129] and the SiV center formed due to incorporation of silicon atoms from the substrate into the grown diamonds. Additional techniques to incorporate an impurity during the diamond CVD growth include mixing the original diamond seeds with the metal of choice. Rabeau et al., prepared a slurry made of nickel nanoparticles and nanodiamonds[27]. Then, a growth substrate (silica) was exposed to the slurry in an ultrasonic bath. This method provided the effect of nucleation for the purpose of diamond growth and introduction of small amount of nickel to be incorporated during the growth. Although this technique resulted in the formation of an optical center in the NIR, it is unclear if the center was formed as a result of nickel addition to the slurry or from an impurity already present within the nanodiamond seeds. Note that some of the seeds originated from crushing type Ib bulk diamonds and thus may include metal impurities such as nickel or iron.

Recently, a very interesting experiment of introducing nickel through a gas phase during the CVD process was reported[203]. This was done by flowing nickelocene in addition to the methane gas. PL lines in the NIR were observed in the diamond samples exposed to nickelocene during their growth, although no single photon emission was shown. In addition, same PL lines were found in diamonds which were grown without intentional introduction of the nickelocene. This, as proposed by the authors, was due to residual nickel from former depositions. Although few drawbacks still to be resolved, the idea of introducing an impurity through the gas phase looks promising. Indeed, an effective doping of diamond with phosphorus for electric purposes was available only via its incorporation during the growth in a gas phase[208]. However, while implanted into pure diamond, very poor n-type characteristic was recorded from these samples[108].

In this work a novel technique of incorporation a metal during the CVD growth is presented. Combining the flexibility of ion beam techniques and the idea of introducing the impurity during the growth, a novel method of diamond doping is introduced. The element of choice is implanted into the substrate onto which the diamonds are subsequently grown. The plasma etches the substrate during the growth and thus exposes the implanted species (along with the substrate material) to the plasma ball and through gas phase diffusion the impurities are incorporated into the growing diamond crystal. This chapter will elucidate this technique and provide as an example fabrication of nickel related optical centers in diamond.

6.2 Implantation of nickel into the substrate

Figure 6.1 illustrates the experimental procedure of the technique.

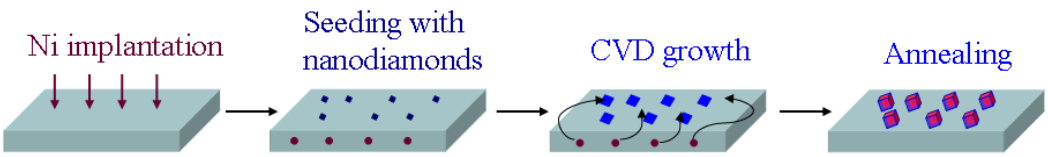

Figure 6.1 Schematic illustration of the fabrication process to create optical centers within CVD diamond nanocrystals. First, nickel (or other ion of choice) is implanted into the substrate followed by seeding with nanodiamond for nucleation purposes. Then, the substrate is inserted into a CVD chamber for the crystal growth. Finally, the sample is annealed to relief any residual stress and to enhance the activation of the optical centers.

The technique to incorporate an impurity from the substrate includes a number of experimental steps. First, Ni ions were implanted into 150 µm thick silica cover slips (Esco-products Inc.) using energies of 20 and 30 keV and doses varying between 1×10^{10} Ni/cm^2 and 1×10^{12} Ni/cm^2 (Table 6.1). The implantation was carried out employing the low energy implanter (see materials and methods, Figure 3.5). To differentiate between implanted and un-implanted regions, half of the substrate was covered with a thick metal mask (~1 mm).

After the implantations, the substrates were seeded with 4-6 nm diamond seeds as described in chapter 4 and transferred into the MPCVD reactor. Once the diamond

growth was finished, the samples were annealed at 1000°C in a forming gas ambient (95% Ar-5% H_2) for 1 hour. To achieve optimal density of diamond crystals for confocal microscopy characterization, an average density of 5–10 nanocrystals in a 100 μm^2 area were grown as confirmed by inspecting the samples with a SEM (Figure 6.2).

Energy [keV]	Dose [Ni/cm^2]	End of range [nm]	Sample N^0
20	1×10^{12}	22±6	1
20	1×10^{11}	22±6	2
20	1×10^{10}	22±6	4
30	1×10^{12}	30±11	5
30	1×10^{11}	30±11	6
30	1×10^{10}	30±11	7

Table 6.1. Summary of the doses and the energies applied for nickel implantations into silica, onto which nanodiamonds were subsequently grown.

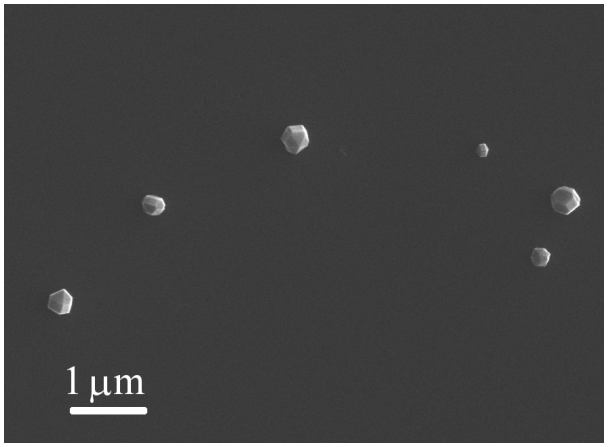

Figure 6.2 SEM image of the nanodiamonds grown on Ni implanted silica substrate.

6.2.1 Experimental results

The crystals were first investigated using a conventional Raman/PL technique. Figure 6.3 shows PL measurements of the grown diamonds recorded at 80 K using a 514 nm excitation laser. A dense forest of PL lines can be observed in the spectrum recorded from crystals grown on the nickel implanted area (red curve). At this stage it is hard to

correlate each line to a known nickel center, however, the experimental data suggests most of them are nickel related[55]. The black curve is the PL recorded from diamond nanocrystals grown on an unimplanted area, which primarily show the peak centered at 738 nm. This line appears in both spectra and attributed to the SiV defect in diamond. It originates due to incorporation of silicon from the silica substrate into the diamond crystal.

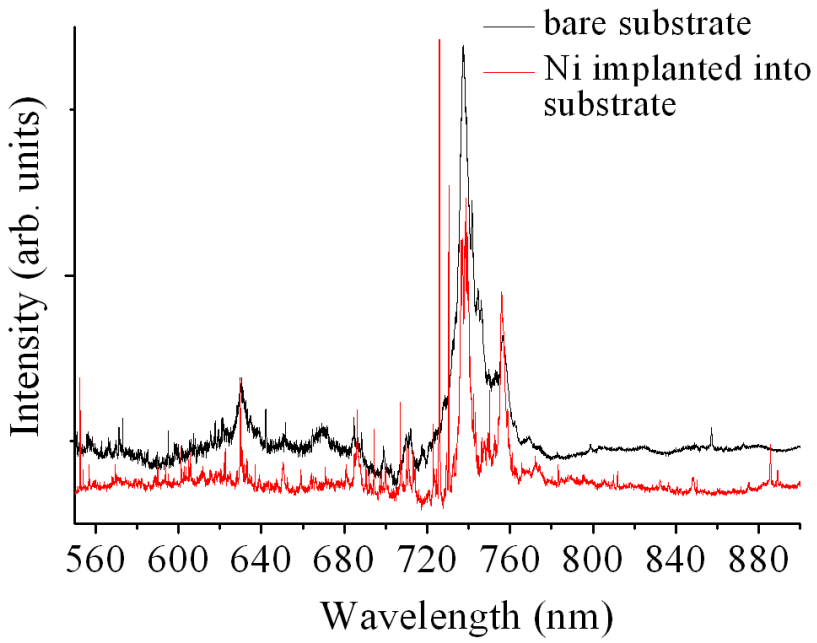

Figure 6.3 PL measurements recorded at 80 K using a 514 nm excitation laser from diamond nanocrystals grown on nickel implanted silica (red curve) and on a bare silica substrate (black curve).

Figure 6.4 shows PL spectra recorded at room temperature using 514 nm excitation from the diamond nanocrystals grown on the silica substrate. The black spectrum is recorded from a diamond nanocrystal grown on a non-implanted region while the remaining three spectra were recorded from individual diamond crystals grown on nickel implanted regions. The signal at 552 nm is the one-phonon diamond Raman line while the PL peaks in the NIR region of the spectrum are attributed to different nickel–related centers in the CVD grown diamonds[55].

The scans were recorded from individual diamond crystals which indicates that different crystals host different nickel-related centers. During all the scans we have not observed

any crystal with more than one characteristic nickel–related PL line which supports the assumption that each crystal hosts only one type of nickel related defect. Note that we have not observed any emission which can be attributed to the NV^- or the NV^0 or the nickel–nitrogen, NE8, center.

Previous work on nickel centers in diamond suggested different atomic structures and models possible for interstitial/substitutional nickel atoms in diamond[55, 81, 88] as well as nickel–vacancy defects[90]. Our PL results are in agreement with previously reported nickel related PL features in the NIR region although we still can not point out the precise atomic structure of these centers. More complicated centers involving bonding to silicon, nitrogen or oxygen atoms as well as to vacancies are possible. Indeed, due to the use of silica as a substrate, SiV centers were formed due to an incorporation of silicon from the growing substrate. Its characteristic PL line at 738 nm was observed in the inspected diamond crystals (spectral region is not shown in Figure 6.4).

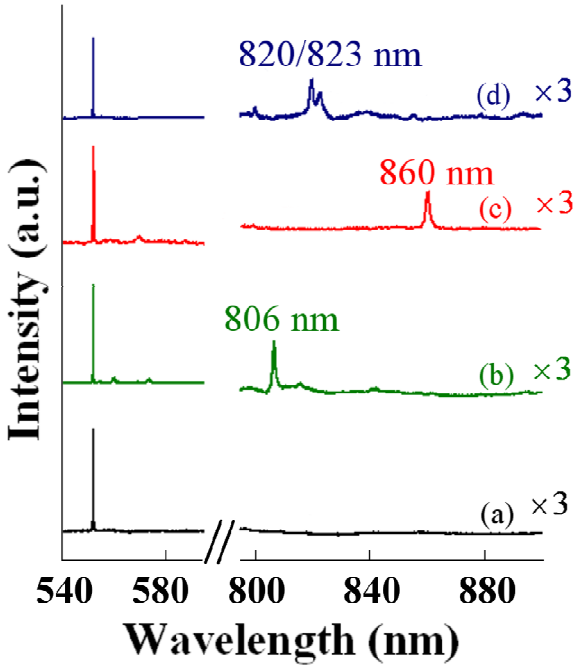

Figure 6.4 PL spectra recorded from individual diamond crystals with/without incorporated nickel, excited by a 514 nm cw laser at room temperature. The bottom black line (a) is representing a PL from a crystal located in an unimplanted area of the silica substrate while the green (b), red (c) and blue (d) lines are representing the PL from crystals located in the nickel implanted area of the substrate. The spectra are normalized to the Raman line and displaced vertically for clarity. The data for wavelengths above 800 nm are enhanced by a factor of 3 for convenience.

To test whether single emitters were formed in this process, HBT setup was employed. Figure 6.5 shows the $g^{(2)}(\tau)$ function recorded from a diamond crystal grown on the Ni-implanted area. The dip of $g^{(2)}(\tau)$ at zero delay time (τ=0) indicates that the observed Ni-related center is indeed a single photon emitter. The very small value of the $g^{(2)}(0)$, $g^{(2)}(0)$=0.08, proves that there is no residual background and the use of nanodiamonds is beneficial for achieving an ideal single photon source.

By recording the $g^{(2)}(\tau)$ as a function of excitation power, the lifetime of this single nickel–related color center is deduced to be ~ 3 ns. This lifetime is shorter that the typical lifetime of NV centers in nanodiamonds[147, 148], which indicates a strong dipole transition of the nickel related center. This lifetime is in agreement with previous reports on other nickel related centers in diamond[28, 196], although it is important to stress that these are not the same centers as reported previously by other groups[27, 28]. The short lifetime and an emission centered in the NIR are very attractive characteristics for facilitating these nickel related centers in practical applications such as QKD.

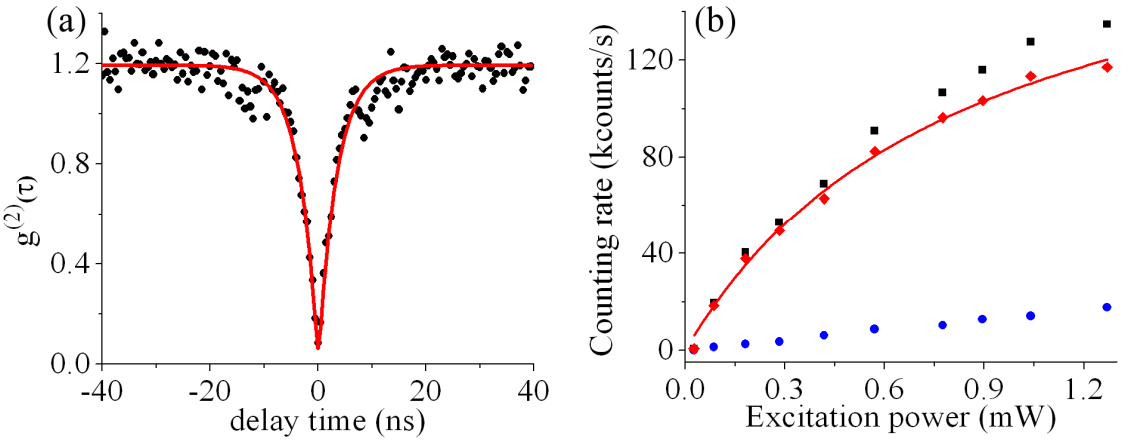

Figure 6.5 (a) Normalized $g^{(2)}(\tau)$ function associated to the PL signal from a Ni-related color center in a nanodiamond grown on a nickel implanted silica. The histogram bin is 0.5 ns. The dip at zero delay time with $g^{(2)}(0)$=0.08, indicates a single photon emission. The dots correspond to the experimental data while the solid line is an exponential fit taking into account the instrumental response function due to finite time-resolution of photodetectors and correlation electronics. Data were recorded using cw laser diode emitting at 687 nm, with an excitation power of 0.3 mW. (b) Saturation curve of the nickel related single photon emitter. The blue circles represent the background noise; the black squares represent the raw data and the red rhombs represent the background corrected count rate. The data were fit using equation (2.21).

A full saturation single photon emission rate from the same Ni-related emitter was then measured as a function of excitation power. Figure 6.5 shows the experimental data. The curve is the fit using equation (2.21). From the fit, the saturation count rate is estimated to be ~ 150×10^3 counts/s. This rate is higher than the values previously reported for the NE8 center observed both in nanodiamonds[28] and in bulk diamond crystals[29].

To evaluate the formation probability of the nickel related centers, confocal maps and corresponding SEM images were analyzed. In a typical 100 μm^2 confocal PL raster scan, one to two centers are detected, as shown in Figure 6.6. Using the spray seeding technique presented earlier, a low surface density of diamond nanocrystals was achieved.

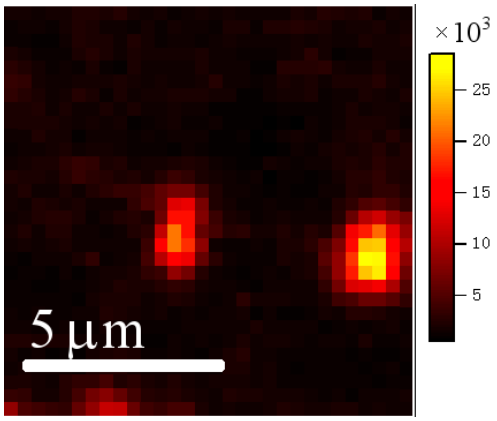

Figure 6.6 A typical confocal map of the nanodiamonds hosting nickel centers. The PL intensity confocal raster scan showing two nickel related color centers.

A typical SEM image of the grown diamonds was shown in Figure 6.2. Combining such SEM images and PL scans, one can infer that on average one in ten nanodiamonds contains at least one nickel related color center. Compared to previously reported results regarding the NE8 centers, where a maximum of one NE8 center in a 100 μm^2 of a continuous diamond film was found[27], a significantly improved fabrication methodology of optically active centers in CVD nanodiamonds is demonstrated. By employing the fabrication technique described here, there is a high probability of finding a single nickel related optically active quantum emitter in an individual nanodiamond crystal in a 100 μm^2 scan, which is suitable for further processing for SPS applications.

We now discuss the mechanism for nickel incorporation into the nanodiamonds. The general route for the synthesis of the nickel related centers consists of four main steps, as

illustrated in Figure 6.1. (1) an implantation of nickel (in general can be applied for any other material) into a silica substrate, (2) seeding the substrate with nanodiamond seeds, (3) growth of diamond crystals using MPCVD technique, and (4) annealing the sample to relief any post growth stress and stabilize the crystal structure and the optical centers. According to SRIM simulations (Figure 6.7a), the implantation of nickel into silica, using energies of 20 keV or 30 keV results in a high nickel atoms concentration at depths of ~ 20 nm and ~ 30 nm, respectively.

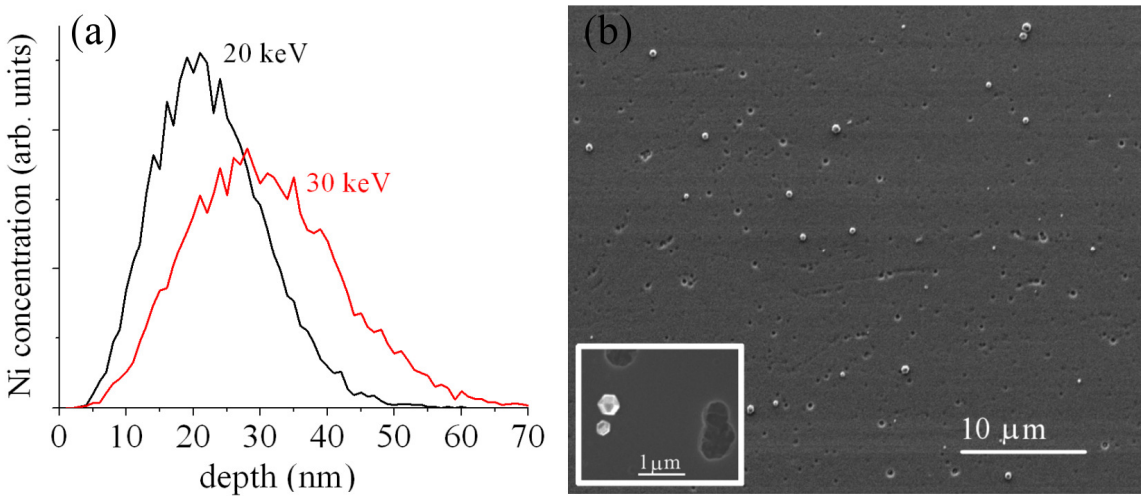

Figure 6.7 (a) SRIM simulations of nickel implantation into silica using 20 keV and 30 keV. (b) SEM image of an etched silica surface. Inset is a high magnification image, clearly demonstrates etching deeper than 50 nm.

The diffusion coefficient, D, of nickel in silica at 1373 K is estimated to be in the order of 1.7×10^{-14} – 9.68×10^{-16} cm^2/s, depending on the ratio of Si:O[209]. This leads, using a typical diffusion length, $x \sim \sqrt{Dt}$, to an estimated diffusion path of only several nanometers during the $t=1$ hour of growth and annealing at the temperature range applied in our experiments. However, the long annealing time which is required to boost the nickel diffusion in silica towards the diamond crystals over the range of tens of nanometers, is overcome by the etching of the silica coverslip during the CVD growth. Since the silica is located less than a few centimeters below the plasma ball, it is partially etched as can be evident from the SEM picture (Figure 6.7b). Inset is a high magnification image, clearly demonstrates etching deeper than 50 nm. During the silica etching, nickel atoms are exposed to the plasma and through gas phase diffusion are

incorporated into the growing nanodiamonds. The CVD process continues for at least 8 min to achieve a reasonable diamond crystal size of tens of nanometers and this time is sufficient to etch the silica substrate for the desired depth[210].

Note that growing nanodiamonds on an evaporated thin nickel film (rather than implanting the impurities into the substrate) is problematic since nickel is known to catalyze carbon nanotubes and sp^2 carbon. Therefore, the presented here technique offers unique opportunity to grow high quality nanodiamonds while at the same time incorporate nickel atoms into the growing crystals.

The purpose of the final annealing process is to enhance the vacancy diffusion and to relieve any post growth residual stress, thus enhancing the formation of the nickel related optically active color centers. Although different doses of nickel were implanted into the substrate, there was no significant influence of the ion dose on the PL signals and the obtained nickel related centers. Even at high doses of 1×10^{12} Ni/cm^2 the nickel atoms are distributed with a sufficient homogeneity to prevent cluster formation, while lower doses were sufficient to incorporate nickel into the growing nanodiamonds.

6.3 Summary

In this chapter a novel methodology for fabrication of optical emitters in CVD nanodiamonds by incorporating an impurity during the growth was introduced and discussed. The technique endows with the unique opportunity to engineer single quantum emitters on demand in high quality nanodiamonds without damaging the grown crystal by ion implantation. Fabrication of nickel related SPSs in individual CVD diamond nanocrystals was achieved by implanting nickel into the substrate prior the diamond growth. This technique has greatly improved the formation probability of the nickel related single photon centers in nanodiamonds. The low background noise and the enhanced counting rate compared to bulk diamond make this technique highly valuable for fabrication of quantum emitters.

This methodology has a number of clear advantages. First, the impurity is introduced during the diamond growth and therefore the atoms will occupy a lattice site with

minimum energy rather than being accelerated into a random lattice location by a post ion implantation process. Second, this technique is versatile, and although demonstrated only with nickel in this case, it can be potentially applied for the incorporation of any other impurity in diamond nanocrystals. Particularly, one may choose substrates which already host a significant number of impurities and use it as a growth platform for the diamond crystals. One such substrate is sapphire, which hosts high concentration of Cr atoms. This will be thoroughly discussed in the next chapter.

Chapter 7

Ultra bright single photon sources

In the previous chapters, nickel related SPSs were introduced and a number of avenues to manufacture these sources in nanodiamonds were presented and discussed. The motivation for the development of these sources was to find a narrow band width, bright emitter in the NIR. Prior to this work, the highest reported emission count rate from a known diamond related SPS was ~75×10^3 counts/s[29] which is not be sufficient for a realization of a quantum optical device competitive with attenuated lasers. Although a count rate of few hundreds kcounts/s was obtained from nickel related SPSs embedded in diamond nanocrystals, much brighter sources are required for many practical applications. This chapter will thoroughly describe the fabrication of ultra bright single photon emitters and present their photophysical properties.

7.1 Introduction

One way to achieve an ultra bright single photon emission is to modify the collection efficiency of the emitter by means of cavities or to modify the decay paths through coupling to plasmons. Research groups world wide have recently demonstrated both effects, employing the NV center in diamond[155, 211-213]. These procedures, however, are highly non trivial. For the cavity technology to work, for instance, single crystal diamond etching is required. Then, the probability of a single emitter being in the right position to achieve an effective coupling with the cavity mode is very low. To couple a quantum emitter to a plasmonic structure (nanowires or a metal sphere), a cumbersome manipulation of individual diamond nanocrystals is required. Moreover, for both processes, even if successful, emission from only few emitters would be enhanced. Therefore, true ultra bright SPSs available on demand, are highly sought after.

The breakthrough came in 2009 when Simpson et al[214] reported on an unknown center with a ZPL at 734 nm emitting millions of photons per second and exhibiting a two level electronic system. The origin of the center or its possible atomic structure is unfortunately unknown. It is likely that this unique center was present in the diamond seed, which was used to grow the diamond crystals using a CVD technique.

In addition of having emission rate in the MHz regime, Simpson's discovery unveiled that diamond color centers can exhibit two level behavior, which was confirmed by an absence of bunching in the $g^{(2)}(\tau)$ function. (The two level scheme implies that there is no intermediate or shelving states between the excited and the ground state of the emitter, Figure 2.8b). The absence of a metastable state was partially responsible for the high brightness of the center. This was the first diamond based optical center which was known to have a two level system without any metastable state. The other single emitters, such as the NV, NE8 or SiV all behave like a three level systems. They exhibit a photon bunching in their second order autocorrelation function and possess a metastable or a shelving state.

Although reproducing such an unknown center is practically impossible, this discovery spurred the research for bright diamond based single photon emitters. This chapter is focused on a controlled fabrication of ultra bright SPSs originated from point defects in diamond.

7.2 Ultra bright single photon sources in CVD diamond crystals

The technique of incorporating impurities from the substrate during the CVD growth was presented in the previous chapter. To take full advantage of this technique, a different growth substrate which natively hosts a significant number of impurities should be used. The substrate of choice is sapphire, and there are a number of reasons for this selection. First, sapphire hosts a high concentration of chromium atoms, which form a very bright luminescent defect, named R1[215]. The emission of this defect is centered around 700 nm and was used as the first solid state optical laser exactly 50 years ago[216]. The chromium may therefore diffuse into the growing diamond crystal from the sapphire substrate. Second, sapphire does not contain a significant amount of silicon, thus, the

probability of incorporation of silicon into the growing diamond and the formation of SiV centers is reduced. Third, sapphire is not a metal, and thus would not catalyze sp^2 carbon. It was shown in chapter 4 that high quality diamond crystals can be grown on sapphire.

7.2.1 Experimental results

The CVD diamond crystals were grown to an average size of few hundreds nanometers from diamond seeds (4-6 nm, Nanoamor Inc.) on sapphire substrates (Crystal systems) using a microwave CVD technique (900 W, 150 Torr) as described in chapter 4. A laboratory built confocal microscope at the University of Melbourne (Figure 3.6) with a spatial resolution ~ 400 nm (100 × objective, 0.95 N.A.) and HBT interferometer were used to identify the emitting centers and measure the time correlation of PL intensity.

Figure 7.1a shows a 20×20 μm^2 PL confocal map of the diamond nanocrystals grown on sapphire recorded at room temperature using an excitation power of 60 μW at 682 nm. Roughly, one out of ten crystals shows a very bright emission of more than 100×10^3 counts/s. Figure 7.1b shows a representative SEM image of nanodiamonds grown on a sapphire substrate. Inset, is the image of a typical diamond nanocrystal shown at high magnification (the scale bar is 500 nm).

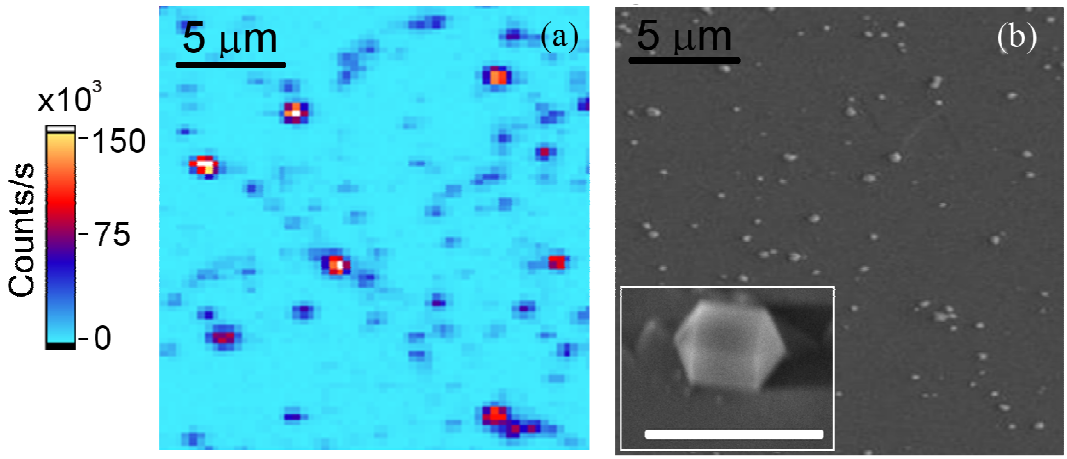

Figure 7.1 (a) A typical photoluminescence intensity confocal map (20 × 20 μm^2) showing fluorescent nanodiamonds grown on a sapphire substrate recorded using a cw laser diode emitting at 682 nm with an excitation power of 60 μW. (b) Typical SEM image (20 × 20 μm^2) of the nanodiamonds grown on a sapphire substrate. Inset, a high magnification SEM image of a typical diamond nanocrystal. The scale bar is 500 nm.

Figure 7.2a-d shows PL spectra recorded from the bright nanodiamonds.

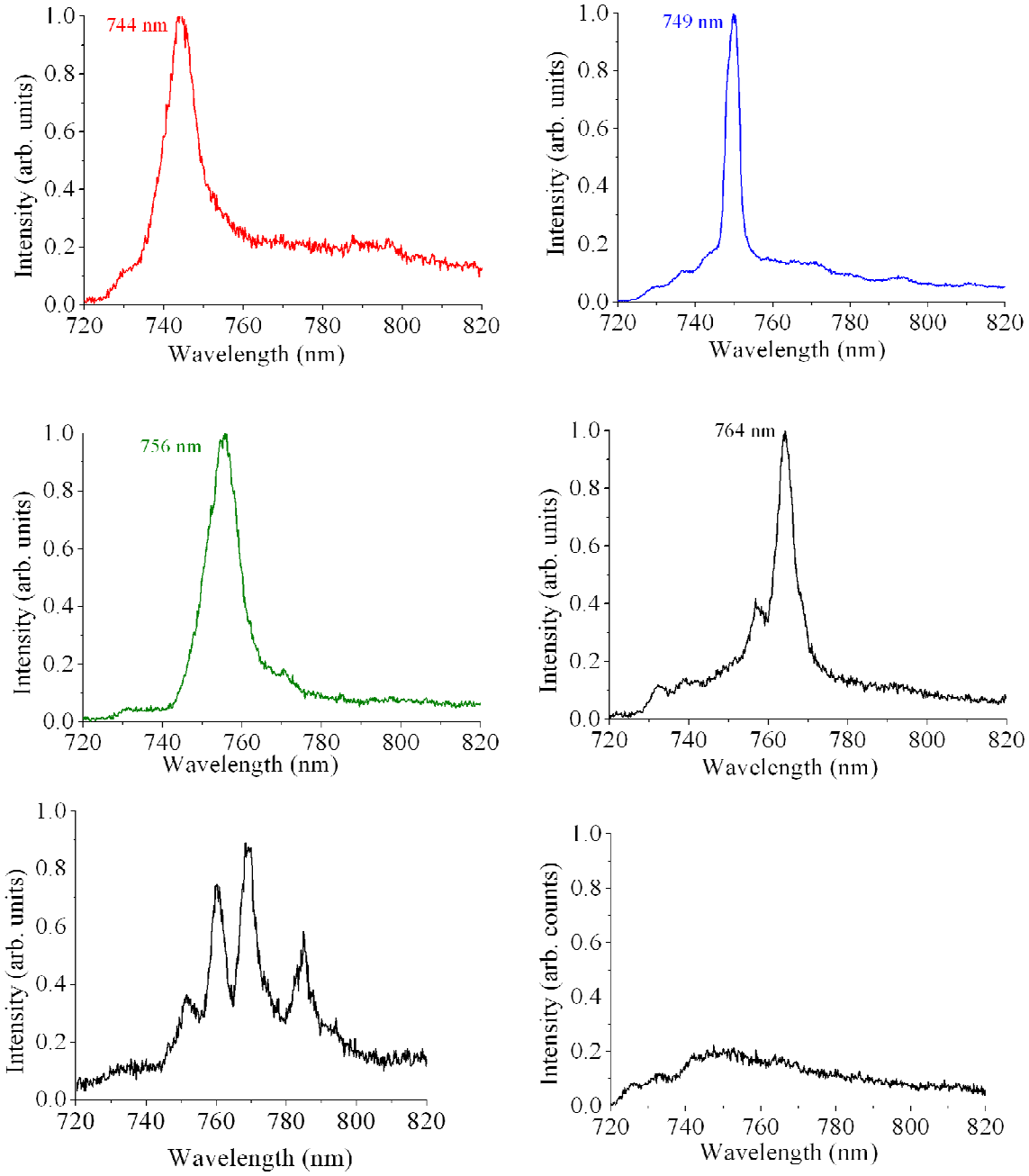

Figure 7.2 Typical PL spectra recorded at room temperature from bright individual CVD diamond crystals as shown in the confocal raster scan of the sample in Figure 7.1a. The peak emission lines centered at (a) 744 nm (red), (b) 749 nm (blue), 756 nm (green) and 764 mn (black). (e) Demonstration of similar emission lines which were found all together in one crystal. (f) A typical PL spectrum recorded from an arbitrary crystal grown on the sapphire substrate, which does not show any extreme brightness or a narrow PL line.

At least four typical emission lines centered at 744 nm, 749 nm, 756 nm and 764 nm were observed from the inspected crystals. These lines exhibit a FWHM of a few nanometers and do not have significant phonon sidebands. These lines are most likely associated with a Cr impurity within the diamond crystal, incorporated from the sapphire substrate during growth. This will be discussed in detail below. In some cases two or more PL lines were found in one crystal, as shown in Figure 7.2e, with the relative intensity of the lines varying from crystal to crystal. Figure 7.2f shows a typical PL spectrum recorded from an arbitrary crystal on the sapphire substrate, which does not show any extreme brightness or a narrow PL line.

Figure 7.3a-d shows the corresponding normalized second-order autocorrelation function, $g^{(2)}(\tau)$, for the respective PL lines (centered at 744 nm, 749 nm, 756 nm and 764 nm), for excitation powers below and above the optical saturation power, *P*. The excitation power used to record each curve is written to the right of the curve. Single photon emission from these centers was verified first by recording the $g^{(2)}(\tau)$ function at low excitation powers. With higher excitation powers, the $g^{(2)}(0)$ increases due to the finite time response jitter of the photo detectors and correlation electronics. The dip at zero delay time indicates a single photon emission. The deviation from zero is attributed to the jitter of the electronics and residual polarization dependent background. Among the observed bright emitters, roughly 30% of the crystals showed the bunching behavior and the rest did not show any bunching in the $g^{(2)}(\tau)$ function.

From the experimental data, the centers with a ZPL at 744 nm, 756 nm and 764 nm exhibit two level behavior without any bunching of the $g^{(2)}(\tau)$ function. The emitter with a ZPL at 749 nm exhibits a three level behavior with a clear bunching observed in the $g^{(2)}(\tau)$ function. Therefore, the two level emitters were fit by equations (2.17) and (2.24), while the center with a ZPL at 749 nm was fit by equations (2.18) and (2.24). The $g^{(2)}(0)$ of the 744 nm, 749 nm, 756 nm and 764 nm centers are 0.44, 0.16, 0.2, and 0.09, respectively.

By extrapolating the decay rate λ_1 to zero optical excitation power, the excited state lifetime of the two level emitters is obtained. Figure 7.4 shows the values of λ_1 as a function of excitation power for various emitters. From the fit to equation (2.19) , the

lifetime of the 744 nm, 756 nm and 764 nm emitters are deduced to be 3.8 ns, 3.7 ns and 13 ns, respectively.

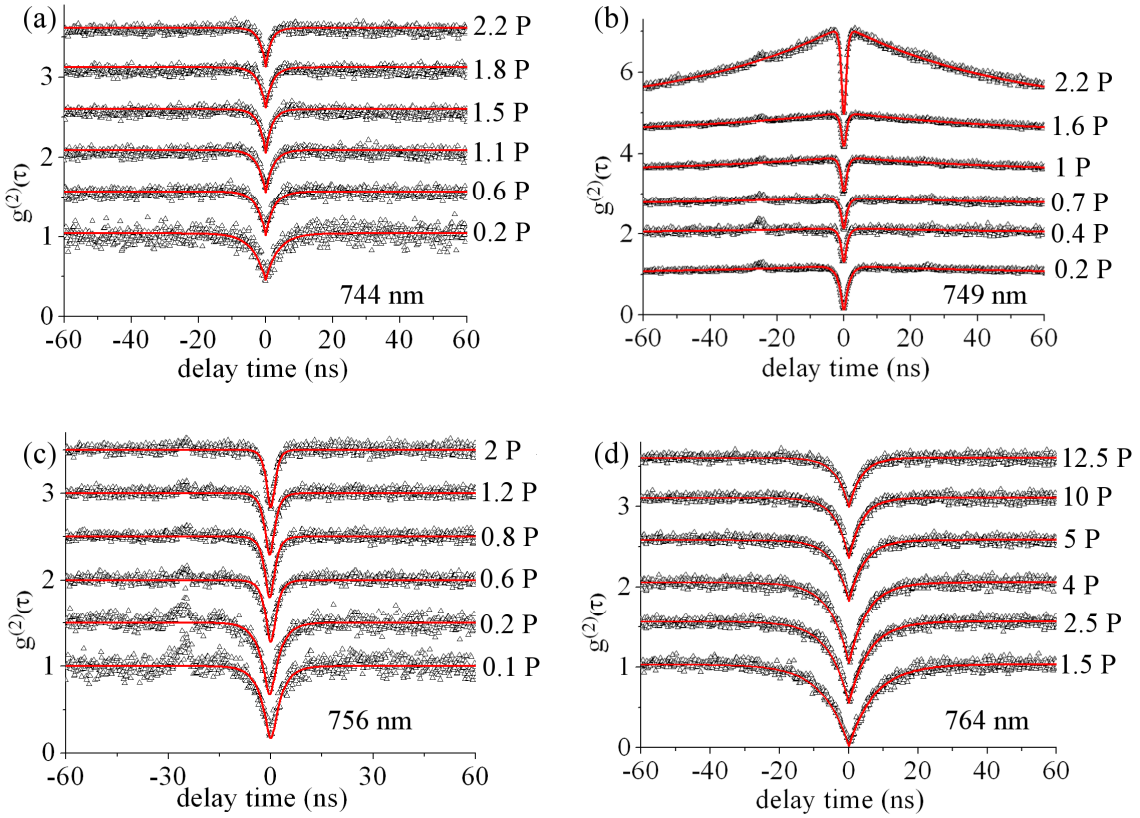

Figure 7.3 Background corrected $g^{(2)}(\tau)$ measured with 154 ps coincidence time bin for 300 s at different optical powers for the (a) 744 nm line, (b) 749 nm line (c) 756 nm line and (d) 764 nm line. The two level emitters were fit using equations (2.17) and (2.24) and the three level emitter was fit using equations (2.18) and (2.24). The number to the right of the curves corresponds to the fraction of the saturation excitation power (P) which was used to record the $g^{(2)}(\tau)$. The peaks at -20 ns and at 30 ns in (b) and (c) are due to crosstalk between the APDs, which has been removed by replacing the flat fiber patch cord with an angled one, eliminating the effect in the other figures. The plots in each graph were shifted for clarity.

The fit applied to the second order correlation function for the 749 nm emitter contains two exponential decay rates λ_1 and λ_2. The extrapolation of these rates to zero optical excitation power allows the excited state lifetime and shelving decay rates to be determined by fitting the data to equations (2.19) and (2.20). The excited state lifetime of the 749 nm emitter is deduced to be 1.1 ns (880 MHz). The decay rate, λ_2, as a function

of optical power is shown in the inset of Figure 7.4b. The resulting values of r_{31}^{0} and r_{23} are 6.2 MHz (16.1 μs) and 0.89 MHz (1.1 μs), respectively and are much longer than the excited state decay rate (Figure 7.4).

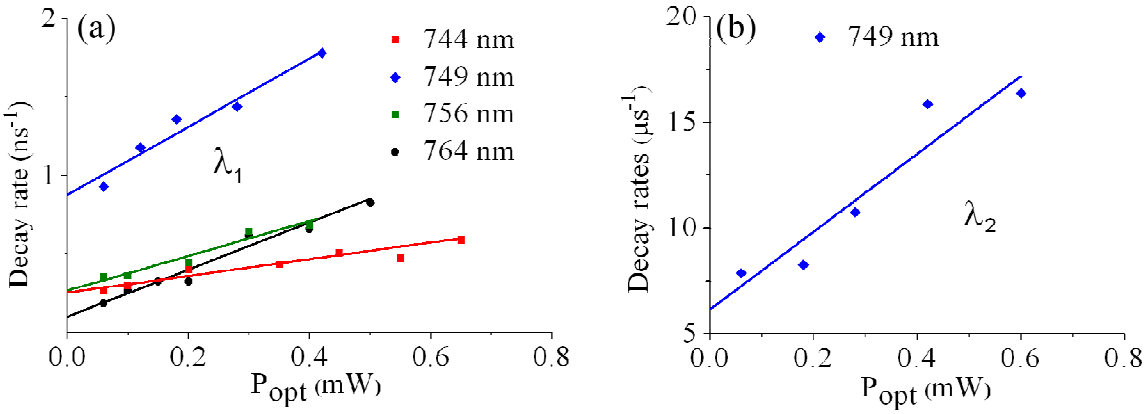

Figure 7.4 (a) λ_1 parameter measured versus the optical excitation power for the centers at 744 nm (red squares), 749 nm (blue diamonds), 756 nm (green triangles) and 764 nm (black circles). At the limit of zero optical power the lifetimes of the centers are τ_{21}=3.8±0.3 ns, τ_{21}=1.1±0.1 ns, τ_{21}=3.7±0.5 ns, and τ_{21}=13±1 ns, respectively. The data were fit with equation (2.19). (b) The behavior of λ_2 versus the optical power of the emitters at 749 nm. The estimated values r_{31} =6.2 MHz (161 ns), and r_{23}=0.89 MHz (1.1 μs), α= 2.5 mW^{-1}, β= 3.1 mW^{-1} are deduced for this emitter. The data were fit with equation (2.20);

The single photon emission count rate as a function of optical excitation power P_{opt} is shown for each emitter in Figure 7.5. The measured count rates (corrected for the background) are given by the sum of the counts on the two APDs in the HBT setup. For the 744, 756 and 764 nm emitters, the saturation curves were fit using equation (2.21), yielding saturation count rates, R_{∞} , of 2.1×10^6, 3.2×10^6 and 1.3×10^6 counts/s, respectively. The saturation curve of the three level 749 nm emitter was fit using equation (2.23), with the values of r_{21}, r_{12}, r_{31}, r_{23} obtained from the fit to $g^{(2)}(\tau)$ as a function of pump power. The single fitting parameter, which represents the quantum efficiency and the collection efficiency, $\eta_{CE}\times\eta_{QE}$, was then obtained from a least squares fit to the saturation curve.

Extremely high count rate of 3.2×10^6 counts/s was deduced from the fit for the emitter with a ZPL at 756 nm. To the best of our knowledge, this is the brightest single photon

source observed at room temperature to date. The measured count rate is comparable with the ultra fast cavity based SPS based on QD[217]. However, unlike the QD, which requires cryogenic temperatures, the fabricated diamond based SPS is operating at room temperature. Moreover, the measured count rate was achieved without the enhancement of the collection efficiency by integration of the SPS in cavities[212, 213] or with plasmonic structures[155]. Such a high count rate can be explained by the proposed two-level energy scheme, which allows the center to be efficiently pumped and eliminates the possibility of population leaking into any longer lived dark states.

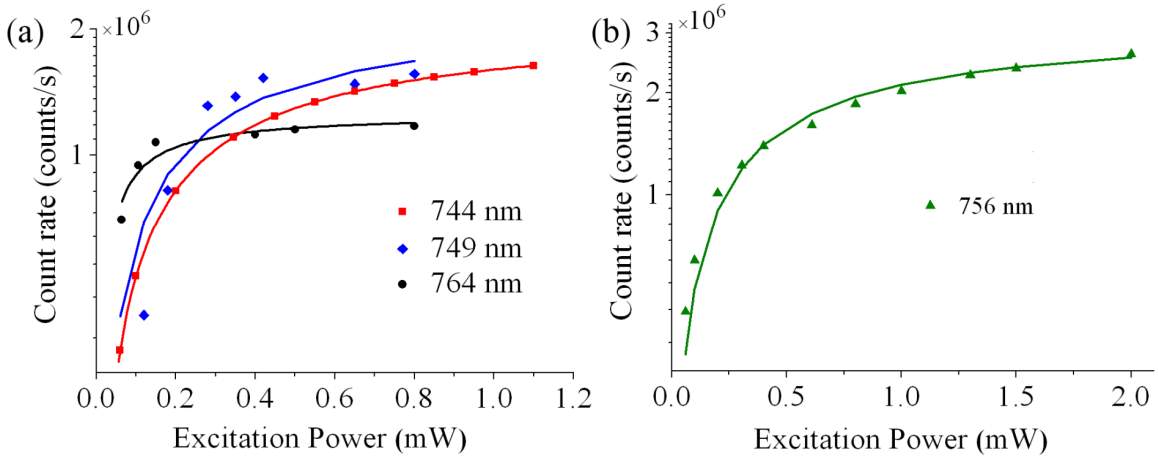

Figure 7.5 (a) Single photon emission count rate for the emitters centered at 744 nm (red squares), 764 nm (black circles) and 749 nm (blue diamonds). The data of the two level emitters (centered at 744 nm and 764 nm) were fit using equation (2.21) while the data of the three level emitter (centered at 749 nm) were fit using equation (2.23). (b) The brightest single photon emitter with a ZPL at 756 nm (green triangles) with the count rate at saturation reaching $R_\infty = 3.2\times10^6$ counts/s.

Figure 7.6a shows a direct measurement of the lifetime recorded from the emitters using the pulsed excitation at 20 MHz repetition rate. The single exponential fit to the fluorescence decay rate of each emitter, resulted in a measured excited state lifetime of 4.1 ns, 1.4 ns, 3.9 ns and 14.2 ns for the 744 nm, 749 nm, 756 nm and 764 nm centers, respectively. Upon inspection of the fluorescence decay of the 744 and 749 nm centers there is a fast component of the fluorescence decay which occurs on a time scale less than 0.5 ns. This component is attributed to the background within the emitting crystal. The lifetime of the emitters in this case is determined by fitting the fluorescence decay for

times greater than 0.5 ns. The measured lifetimes are in a good agreement with the lifetimes estimated from the CW measurements for the 744 nm and 749 nm emitters. The discrepancy with the 764 nm center can be due to the lack of the CW $g^{(2)}(\tau)$ measurements at excitation powers well below saturation, which affects the fit to a zero excitation power. The variation of the lifetime (4 ns to 14 ns) of the two level system emitters can be attributed to nanocrystals geometry experiencing local modification of electric field and/or differences in the atomic structure.

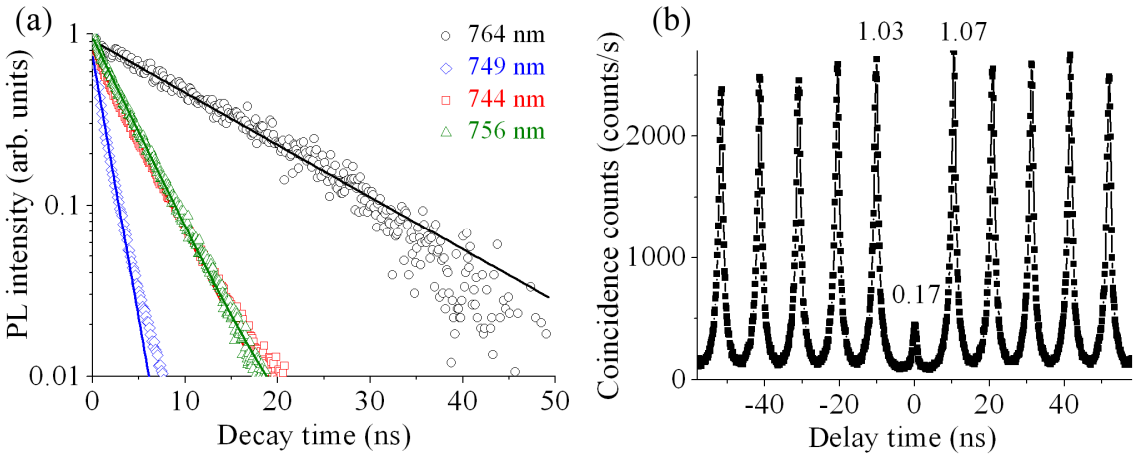

Figure 7.6 (a) Direct measurement of the lifetime for the centers at 744 nm (red squares), 749 nm (blue diamonds), 756 nm (green triangles) and 764 nm (black circles), using a pulsed laser at 20 MHz repetition rate with 200 ps pulse width. The data were fit with a single exponential. The deduced lifetimes of the centers are 4.12 ± 0.06 ns, 1.41 ± 0.02 ns, 3.90± 0.06 ns, and 14.2 ± 0.2 ns, respectively. (b) Anti-bunching measurement recorded from a single emitter at 749 nm under pulsed laser excitation at 40 MHz and average power of 70 μW.

Figure 7.6b is an example of the second order correlation function measurement under pulsed excitation recorded from the 749 nm emitter. The peak at $\tau=0$ is the probability of having multi-photon emission in the same pulse, indicating the presence of only one photon ($g^{(2)}(0)=0.17$). The observed deviation from zero is due the background luminescence from the nanodiamond crystal, which is not negligible in this case. To reduce the unwanted background for practical applications, temporal filtering of the single photon source can be implemented[218].

Figure 7.7 shows the stability measurement of single photon emission from the 756 nm center. The center was photostable and no bleaching or blinking was observed over the

whole measurement (more than 6 hours). All the single photon emitters, including the one who exhibit bunching in the $g^{(2)}(\tau)$ function were stable over period of hours.

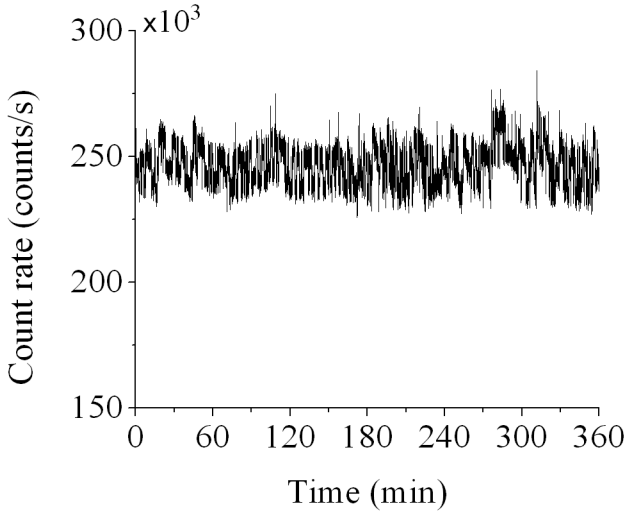

Figure 7.7. Single photon count rate from the 756 nm center recorded for six hours demonstrating an absolute photostability of the center.

The ratio between the average "off" and "on" periods of sources exhibiting a three level system is given by the ratio r_{23}/r_{31} which equals to 0.14 for the 749 nm emitter. This value indicates that the probability of a transition to the metastable state is moderate, as shown by the slight bunching of the $g^{(2)}(\tau)$ function (Figure 7.3b). Previous determinations associated to NE8 complex in bulk type IIa diamond [29, 196], and CVD nanodiamonds [28] showed a ratio r_{23}/r_{31} of 2.8, 1.6 and 0.8 respectively, justifying much lower saturation rates of the NE8 center with respect to the 749 nm emitter. In addition, the 749 nm center possesses a shorter lifetime than NE8, which also contributes to the higher emission rates.

The measured photo physical parameters of the chromium emitters are summarized in Table 7.1. In general, two level emitters possessed a ZPL with a FWHM of ~ 10 nm, whilst the three level emitters exhibited a FWHM of ~ 4 nm. To date, all the known diamond-based single photon emitters (SiV, NV, and the NE8) reveal a third long-lived metastable state in the electronic structure that is responsible for the bunching behavior[20, 30, 140, 141, 176]. The centers reported here endow with s positive outlook

on diamond based single photon emitters which possess a two level system and therefore exhibit high count rate.

System	ZPL (nm)	R_∞ (counts/s)	τ_{21} (ns) (pulsed)	τ_{21} (ns) (CW)	r_{31} (MHz)	r_{23} (MHz)
Two-level	744	2.1×10^6	4.12 ± 0.06	3.8 ± 0.2		
Two-level	756	3.2×10^6	3.90± 0.06	3.7 ± 0.2		
Two-level	764	1.3×10^6	14.2 ± 0.2	13.0 ± 0.7		
Three-level	749	2.7×10^6	1.41 ± 0.02	1.1 ± 0.1	6.2 ± 0.6	0.89±0.09

Table 7.1 Summary of the photophysical parameters of Cr related single photon emitters embedded in nanodiamonds.

The simple two-level nature of stable single photon emitters at room temperature can be very significant for future metrological applications. One can envisage that SPSs possessing two level behavior could be implemented as a "single photon standard", able to link classical radiometric measurements to fundamental quantum optical entities. In particular, in the long term such a single photon standard could contribute to a re-definition of the standard units for optical radiation in terms of the "quantum candela"[219]. A solid understanding of the fabrication methods for an effective two level emitter is expected to progress the technology to the point where they can become practical quantum information and metrology devices.

7.2.2 Origin of the emitters

The origin of the centers is discussed in detail in this section. In order to ascertain whether the ultra bright emitters are associated with a particular ion, e.g. Cr or Ni, and to check for the effects of ion induced damage that might accompany the implantation, three different batches of samples were prepared. (i) CVD grown diamond nanocrystals on a sapphire substrate, which aims to check whether the emitters are formed due to an incorporation of an impurity from the sapphire substrate. (ii) CVD diamond nanocrystals implanted with nickel ions with acceleration energy of 30 keV and a dose of 5×10^{11} Ni/cm^2 grown on a sapphire substrate. This batch aims to check whether the centers are

nickel related. (iii) CVD diamond nanocrystals implanted with argon ions with acceleration energy of 14 keV and a dose of 1×10^{11} Ar/cm^2 grown on a sapphire substrate. This batch will give information of the formation probability of the centers when additional vacancies are introduced by inert ions. All the samples were then annealed at 1000°C in 95% Ar-5% H_2 ambient for 2 h. According to SRIM simulations, the stopping range of the implanted ions is 10-20 nm beneath the diamond surface. The damage created by the implanted argon and nickel is 1.17×10^{13} and 1.38×10^{13} vacancies/cm^3, respectively.

The confocal scans of the implanted and annealed samples revealed that bright emitters were formed in all three batches. However, significantly more bright optical centers were formed on samples which were implanted with Ni or Ar than at the unimplanted ones. Remarkably, no difference in terms of brightness of the centers or their photophysical properties was observed between the Ni or Ar implantations. The bright, narrow PL signals from all sets (implanted with Ni or Ar or a bare sapphire) were similar to the ones shown in Figure 7.2. This implies that ion implantation plays a significant role to enhance the formation probabilities of the centers by introducing vacancies within the crystals. However, the composition of the observed emitters is not related to either Ar or Ni ions.

In the previous chapter it was shown that during CVD growth impurities present in the substrate can be incorporated into the diamond nanocrystals by diffusion through the gas phase during the CVD process. These impurities, while in the diamond lattice can lead to stable single photon emitters. In the present case, the diamond nanocrystals were grown on sapphire substrates, which contain a significant amount of Cr atoms (~ppm). This was confirmed by exciting the sapphire with 514 nm excitation laser and the observation of strong luminescence at 693/695 nm (Figure 7.8). This PL doublet is attributed to a substitutional Cr^{3+} atom in a sapphire lattice and its electronic levels are well known[215, 220].

Our growth conditions of high pressure and high density plasma (see chapter 4) lead to considerable etching of the substrate, exposing its constituents to the plasma ball and enhancing the probability to be incorporated into the growing crystals. It is therefore proposed that chromium atoms diffuse from the sapphire into the growing nanodiamond and form the optical centers. To test this hypothesis, the same growth – implantation –

annealing sequence was repeated, but this time into diamond nanocrystals grown on a silica substrate, which does not contain any chromium atoms. The PL studies of the diamond nanocrystals grown on silica did not reveal any of the narrow PL lines shown in Figure 7.2 or any bright single emitters at all. Therefore, one may conclude that the incorporation of an impurity from the sapphire substrate, most likely chromium, into the growing diamond nanocrystals gives rise to the observed PL lines.

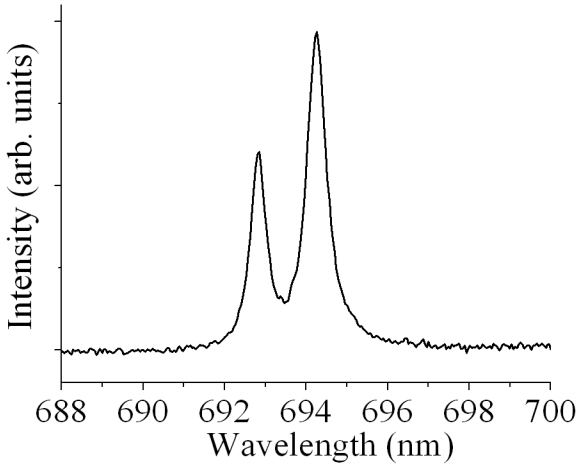

Figure 7.8 PL recorded from a bare sapphire substrate at room temperature using a 514 nm excitation. The doublet centered at ~700 nm is known as R1 center, originated from a substitutional Cr^{3+} ion in sapphire and used as the first solid state optical laser exactly 50 years ago[216].

One must bear in mind that the incorporation of oxygen or aluminium from the sapphire substrate is also possible, since these are the main elements of the sapphire crystal. The incorporation of silicon from the quartz bell jar chamber can not be neglected as well. Given that we do not observe any of these centers in samples grown on silica substrates, it would appear that silicon is not strongly implicated in the center. Nevertheless, an interaction between various co-dopants to form a specific center within the diamond crystal should be considered.

During the growth, the impurities from the substrate are randomly dispersed within the crystal. Assuming that Cr atoms do indeed play a crucial role, but need to be paired with another impurity (such as aluminium, oxygen, silicon), there is only a finite chance for such an event to occur. Note that the relatively low annealing temperature of 1000°C is not sufficient to cause a migration of heavy atoms like Cr, Si, or even O; however, the

diffusion of vacancies toward the specific atom to stabilize the optical properties of the center is expected. This may explain why only some of the crystals exhibit the desired narrow luminescence signals, while others do not.

To date, very little is known about chromium centers in diamond[55, 94]. Initial work by Zaitsev et al [55, 94] revealed a number of lines at 741 and 754 nm in the CL spectrum recorded from 300 keV Cr implanted diamond at 80 K (Figure 7.9). However, ion implantation of any elements into diamond creates the radiation GR1 line, centered also at 741 nm. Since the main line of chromium is overlapping with the radiation GR1 line, there was no solid evidence that the observed PL signals are indeed Cr related. Nevertheless, these CL signals are similar to the observed PL lines from some of the diamond crystals grown on sapphire, which support the assumption that chromium is involved in the new centers.

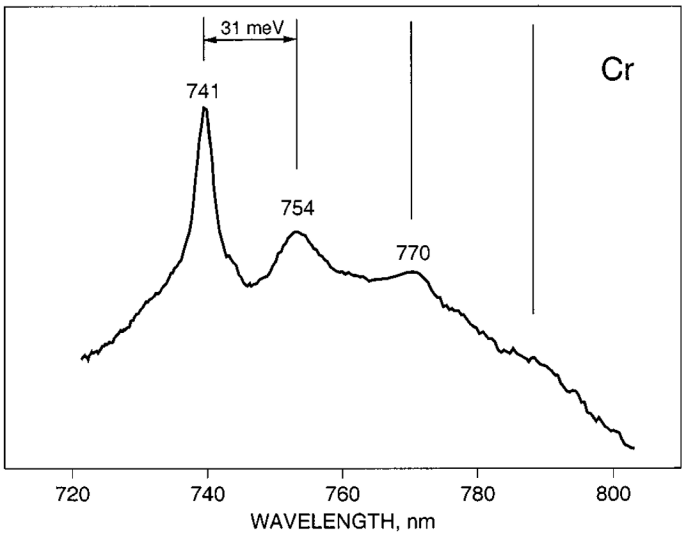

Figure 7.9 CL spectrum taken at 80 K of a very-low-nitrogen natural diamond implanted with 300 keV Cr^+ ions at a dose of 10^{14} cm^{-2} and subsequently annealed at a temperature of 1400 °C. Vertical lines show structure due to interaction with quasilocal vibrations of two Cr atoms. The graph is taken from[94].

The explanation of what leads to two or three level emitters is at this point of time unclear. One assumption is that the number of chromium atoms forming the center or its charge determines the photophysics of the center. Unfortunately, the charge state of the chromium complexes and the number of atoms involved in each center are unknown at

this stage. One may assume that the strain within the crystal may also have a significant effect. Indeed, it was shown for NV centers that strain can modify the transition from being spin conserving to a Λ system geometry[221]. Similarly, the strain can modify the electronic transition within the nanodiamonds and enhance/suppress the relaxation to a third metastable state.

To unambiguously determine the involvement of Cr in these centers, a post growth implantation of Cr into a pure single crystal diamond is required. However, this process involves substantially different formation kinetics and thermodynamics. Hence it is not obvious that the same set of centers will be found, nor is it obvious that they will share the same properties. The experimental results of the implantation of chromium into a bulk diamond are presented and discussed in the following section.

7.3 Ultra bright single photon sources in bulk diamond

Circumstantial evidence of Cr-related centers in nanodiamonds grown on sapphire substrate has been presented in the previous section. However an unambiguous determination of their composition is yet to be ascertained. To explore the origin of novel color centers and their fundamental physical properties, the fabrication of these centers in monolithic single crystal diamond, rather than nanocrystals is necessary. Ion implantation offers the unique advantage of being able to fabricate optical centers based solely on the constituents used in the implantation process along with the known and well characterized elements present in the bulk diamond. The implantation technique is particularly advantageous when trying to identify the origin of an unknown color center.

Cr-related luminescence has been identified in sapphire[215] and silicon[222]. The origin of the luminescence in silicon is still under investigation[223]. One hypothesis is that the Cr appears as interstitial or paired up with substitutional boron, creating Cr_iB_s pairs[223]. The atomic structure of the Cr related center in sapphire is attributed to a substitutional Cr^{3+} ion[215] (R1 center) and the radiative transition occurs as a result of a relaxation from the excited (^2E) state to the ($^4A_2$) ground state. The radiative lifetime of the R1 center is in the ms range (~3 ms) and the internal quantum efficiency of 50%[215].

With this in mind, the co-implantation of Cr and O atoms into single crystal diamond was performed. The co-implantation aims to modify the oxidation state of the chromium in the diamond lattice. At this point, it is important to stress that no prior knowledge in the literature is available on Cr centers implanted into single crystal diamond. Therefore, our only anchor was the Cr related luminescence centers in other solids.

The results of this section describe the fabrication strategies and the photophysics of Cr related centers in bulk single crystal diamond by ion implantation. The results are compared with the ones obtained from the nanodiamond samples and a discussion regarding the chemical composition of the center is presented.

7.3.1 Experimental results

Figure 7.10a shows a fluorescence confocal map recorded from the (100) oriented single crystal diamond (CVD, type IIA, [N] < 1 ppm, [B] < 0.05 ppm, Element Six) after the co-implantation of 1×10^{11} Cr/cm^2 and 1.5×10^{11} O/cm^2, accelerated to 50 keV and 19.5 keV, respectively, and subsequent annealing at 1000°C in a forming gas ambient. The implantation was performed in the low energy NEC implanter (see Figure 3.5). The bright spots in the confocal image correspond to the optical centers from the ion implantation process.

The implantation energies were chosen to maximize the proximity of the oxygen and the chromium atoms. Figure 7.10b shows a Monte Carlo simulation using the SRIM modeling package of implanted chromium and oxygen atoms accelerated to 50 keV and 19.5 keV, respectively. The end of range of these implantations was approximately 25 nm below the diamond surface. Note that the annealing step applied after the implantation (1000°C) is not sufficient to cause any diffusion of chromium or oxygen atoms in the stiff, dense, diamond lattice; hence the formed centers are indeed located in the depth of the implantation.

Figure 7.10c shows a narrow PL spectrum, recorded at room temperature from one of the bright spots on the confocal map shown in Figure 7.10a (red curve), with a ZPL centered at 749 nm and a FWHM of 4 nm. Similar PL lines were consistently observed from different bright spots across the sample. Pristine unimplanted diamond samples or

samples which were implanted with elements other than chromium (such as Ti, Ni, Si) did not show these or similar PL lines.

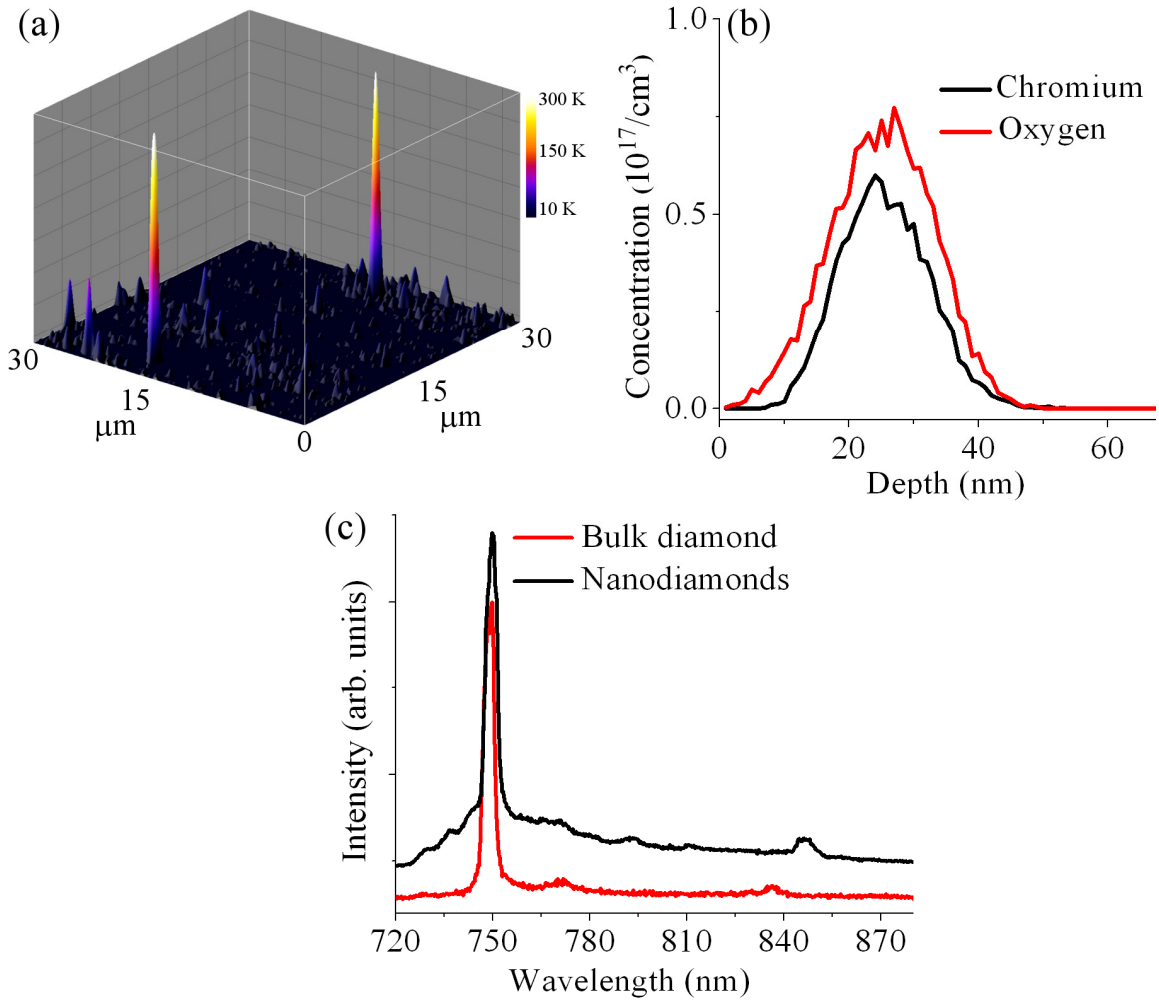

Figure 7.10 Chromium implanted diamond. (a) A confocal map recorded from the diamond sample co-implanted with 1×10^{11} Cr/cm^2 and 1.5×10^{11} O/cm^2. The bright spots correspond to Cr centers in diamond (b) Monte Carlo simulation of chromium and oxygen concentration inside a diamond following 50 keV chromium and 19.5 keV oxygen implantation. (c) PL spectrum recorded at room temperature from a bright spot on the confocal map shown in figure 1 (red curve). The black curve is the PL spectrum recorded from nanodiamonds grown on sapphire. The data from the nanodiamonds was displaced vertically for clarity.

The black curve in Figure 7.10c shows as a comparison a PL spectrum recorded from a center in nanodiamond grown on a sapphire substrate. The excellent agreement between the PL spectra, in terms of the ZPL and FWHM, in bulk diamond and nanodiamonds clearly indicates that these classes of emitters can be attributed to Cr.

Figure 7.11a shows the corresponding normalized second order autocorrelation functions recorded at room temperature from the 749 nm center. The dip at zero delay time $g^{(2)}(0)=0.2$ is characteristic of non classical light and verifies single photon emission. The deviation from zero at $\tau=0$ is attributed to the background within the single crystal diamond. The photon bunching ($g^{(2)}(\tau)>1$) observed at longer delay times is indicative of a three level system with a long lived metastable state[29, 148, 224]. Similar PL statistics, with a bunching at the $g^{(2)}(\tau)$ function, were also observed for the 749 nm emitters embedded in nanodiamonds, as was shown earlier (see Figure 7.3b).

To verify single photon emission on demand, a key feature for many quantum optical applications, the center was excited with a pulsed laser with a repetition rate of 80 MHz, as shown in Figure 7.11b. The vanishing peak at $\tau=0$ indicates that only one photon is emitted per excitation pulse. The measurement of the excited state lifetime of the same emitter is shown in Figure 7.11c and was obtained under pulsed excitation at 40 MHz. From the single-exponential fit to the fluorescence decay, an excited state lifetime of 1.0±0.1 ns is deduced. The measured lifetime is in agreement with the one measured for the center in nanodiamonds (1.1±0.1 ns). This is a short fluorescence lifetime when compared to other known single photon emitters in diamond[29, 148], indicative of a very strong dipole moment in the radiative transition.

The relation between the radiative lifetime and the dipole moment in atoms can be described by[225]:

$$\Gamma_{vac} = \frac{w^3 |D|^2}{3\pi\varepsilon_0 \hbar c_{vac}^3} \tag{7.1}$$

Where Γ_{vac} is radiative broadening of an atom emitting into vacuum (in our case this is the inverse of the radiative lifetime (1.1 ns^{-1}), w is the frequency of the optical transition, D is the dipole moment, ε_0 is the permittivity constant, and c_{vac} is the speed of light in vacuum. For the case of the 749 nm emitter in bulk diamond, which located only ~20 nm below the diamond surface, the derived dipole moment is estimated to be 37 Debye. We

ignore the diamond medium and the diamond refractive index since the center is located in a close proximity to the surface in respect to its emission line (20 nm << 749 nm).

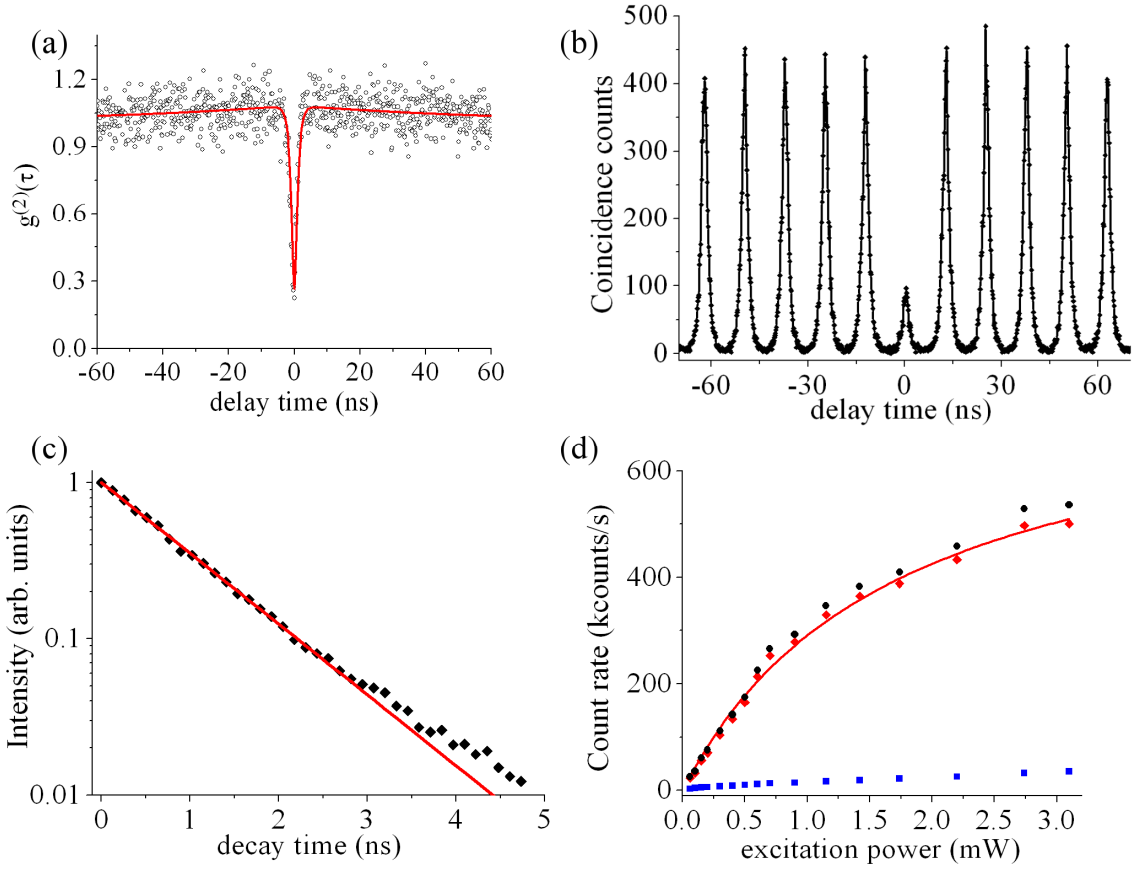

Figure 7.11 Optical characterization of the Cr center. (a) A normalized second-order correlation function, $g^{(2)}(\tau)$, corresponding to the PL line shown in Figure 7.10c, demonstrating single photon emission ($g^{(2)}(0)=0.2$). The bunching ($g^{(2)}(\tau)>1$) indicates of a presence of a third metastable state. The red line is the theoretical fit based on a three level model, taking into account the time response of the detectors. (b) Triggered single photon emission is verified by exciting with a pulsed laser at 80 MHz. The deviation from zero of the $g^{(2)}(0)$ under cw excitation is attributed to the background and the time response jitter of the photo detectors and correlation electronics, while in the pulsed regime the deviation from zero can be attributed to background due to non perfect polarization condition of the pulsed excitation laser. (c) A direct lifetime measurement (dots) with a fit of a single exponential (red curve). A lifetime of 1.0 ± 0.1 ns is deduced from the fit. (d) Single photon emission count rate recorded from the same emitter as a function of excitation power. The blue squares represent the background noise; the black circles represent the raw data and the red rhombs represent the background corrected count rate. The fit (red curve) was obtained from the solution of a three level system.

The single photon efficiency was studied by measuring the emission count rate as a function of the excitation power. Figure 7.11d shows the measured single photon count rate as a function of excitation power. A measured count rate of ~0.5×10^6 counts/s makes the Cr center the brightest reported single photon source in a monolithic single crystal diamond to date. Remarkably, the chromium center is brighter than NV centers embedded in pillars or solid immersion lenses which enhance the collection efficiency. Table 7.2 summarizes the photon count rate recorded from various single emitters in monolithic single crystal diamond.

Single photon emitter (in single crystal diamond)	*Count rate (counts/s)*	*Reference*
Silicon Vacancy	1.5×10^3 (counts/s)	Wang et al [20]
Nickel-nitrogen (NE8)	75×10^3 (counts/s)	Gaebel et al [29]
Ni-Si complex	78×10^3 (counts/s)	Steinmetz et al [207]
Nitrogen vacancy	50×10^3 (counts/s)	QCV [226]
Nitrogen vacancy embedded in a pillar*	1.7×10^5 (counts/s)	Babinec et al [212]
Nitrogen vacancy embedded in solid immersion lens*	3.5×10^5 (counts/s)	Hadden et al [213]
Cr center	5×10^5 (counts/s)	Aharonovich, Thesis

Table 7.2. Summary of single photon emission from various centers in monolithic single crystal diamond. (*) denotes that the collection efficiency was enhanced by other means.

To gain more information regarding the dipole orientation of the Cr center within the single crystal, excitation polarization measurements on emitters with a ZPL centered at 749 nm were performed[227, 228]. Prior to each measurement, an antibunching curve was recorded to verify that only single emitters are addressed. All single 749 nm centers studied here were found to exhibit a dependence on the incident excitation polarization. Two distinct polarization dependencies were identified by characterizing numerous single 749 nm emitters and are shown in Figure 7.12a for four separate single emitters. By varying the incident polarization angle by 90 degrees in the respective configuration the

PL intensity evolves from maximum to minimum intensity, with extinction ratios of 96%, as seen in Figure 7.12a. This is in agreement with the characteristic dipole transition behavior.

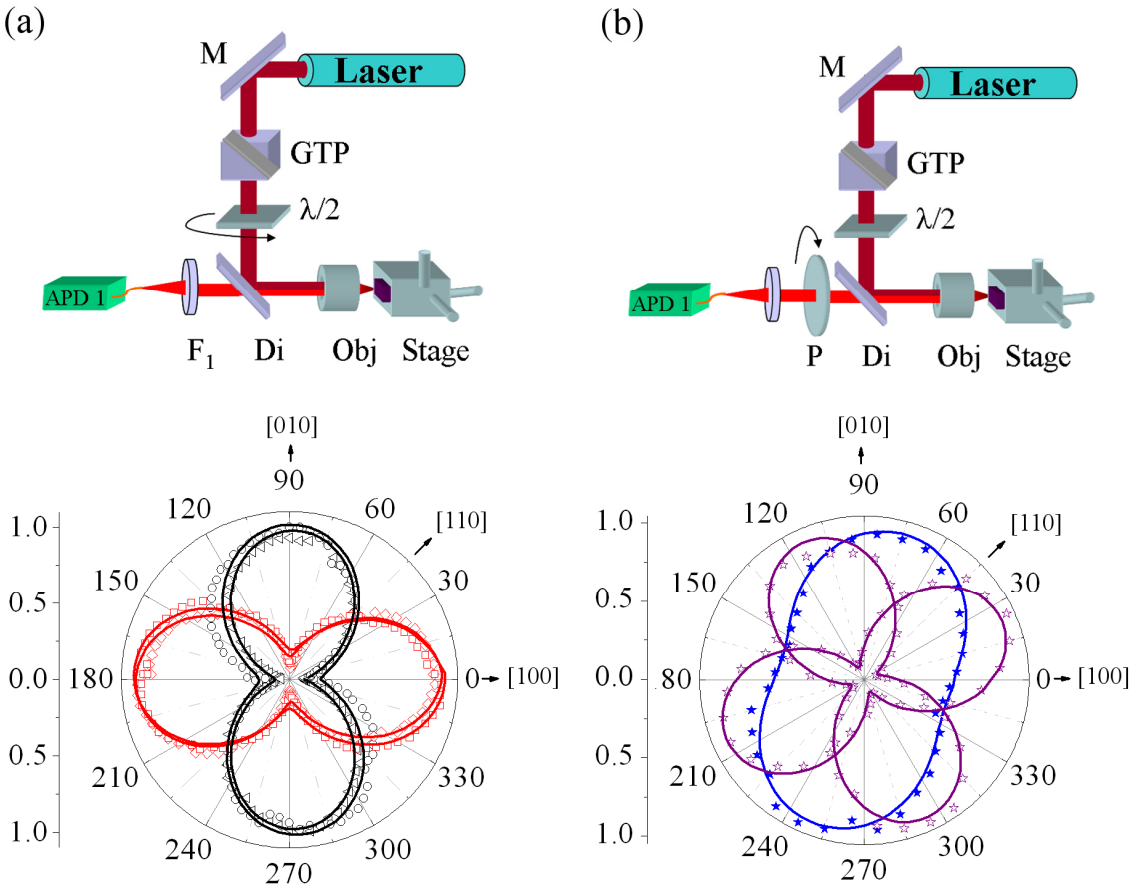

Figure 7.12 Polarization properties of the Cr center. (a) Polarization measurements of the 749 nm emitter represented in polar coordinates recorded by rotating the excitation laser polarization. θ is the polarization angle referred to the main crystallographic axes. PL intensity versus polarization of the excitation laser for four different single photon emitters (black triangles, black circles, red squares and red diamonds) with a ZPL centered at 749 nm. An extinction of the signal down to the typical background level is demonstrated. A period of nearly 90 degrees between the maximum and the minimum of different emitters (black and red colors) is observed. (b) Modulation of the emission intensity measured by rotating a linear polarization analyzer at the detection channel, with a fixed polarization of the excitation field (blue stars). By introducing a quarter wave plate before the analyzer, full polarization contrast was achieved. Purple stars show two possible polarization emissions for two different wave plate positions.

Given that the diamond sample is (100) oriented, the direction of the center excitation transition dipole moment may be determined. The electric field of the incoming laser is parallel to the (100) plane of the crystal. Since the modulation of the excitation polarization angle results in an absolute extinction of the PL, the dipole of the center must be aligned in the [0yz] direction, otherwise full extinction of the PL would not be observed. Furthermore, the period of the minima (or the maxima) of the emitters is 90 degrees, which indicates that only two different projections of the dipole on the (100) plane are possible. Due to the diamond structure, the only crystallographic directions that meet these conditions are the [010] or [001]. Note that the dipole of the center can also be aligned along the [100] direction, however, in this case the excitation dipole transition of the center is perpendicular to the electric field of the incoming laser beam and will not be excited. Thus, the excitation transition dipole moment of the Cr related center is aligned in one of the <100 > crystallographic directions.

The emission polarization of the Cr centers was studied by fixing the polarization excitation to maximum and rotating the polarizer at the detection channel. The non perfect degree of polarization of the emitted light (Figure 7.12b, blue stars) may be attributed to the fact that the excitation and the absorption dipoles are not parallel. The difference between the absorption and excitation dipole orientation is due to a redistribution of the electrons upon photon absorption.

Upon introduction of a quarter wave plate in the detection channel before the analyzer, a full extinction of the emitted light (Figure 7.12b, purple open stars) was observed, confirming that the emitted light is fully polarized. Different orientations of the modulated emission were obtained by varying the quarter wave plate position, as shown in Fig. 3b for two different positions (recorded from the same emitter). The angle between the maxima of the emitted light and the cube main axis does not give information of the relative orientation of the emission and absorption dipoles, which requires more accurate evaluation of the anisotropy using polarization microscopy techniques[229]. The fully polarized light indicates that transitions such as thermal relaxation within the excited state manifold do not exist under our experimental conditions and the decay to the ground state occurs from an individual excited state level[230, 231]. This is an important characteristic for the generation of indistinguishable

single photons and quantum entanglement[161]. Therefore the polarization measurements indicate that the chromium centers behave like a dipole relative to the absorption of the incoming excitation laser and have a fully polarized emission.

Fabrication of emitters in a bulk material has a number of other benefits besides establishing the constituents of the emitters and identifying their transition dipole orientation. Color centers in monolithic single crystal diamond are more suitable for QIP compared with those in nanocrystals due to reduced strain effects. Indeed, a stable Fourier transformed PL line was measured from an NV center in a bulk diamond[232, 233], as well as coherent population trapping effect[221, 234]. Bulk crystals can also provide a platform of an ultra pure isotopically engineered material in terms of paramagnetic impurities (by using ^{12}C atoms instead of ^{13}C), which enabled a demonstration of an electron spin longest dephasing time at room temperature of ~1.8 ms[92]. Furthermore, when these centers are integrated with the recent diamond based antennas[212] or solid immersion lenses[213], even higher count rates can be expected. Note that the center is located only a few tens of nm below the diamond surface which is crucial for efficient coupling of the emitted light to external cavities or waveguides[205, 235, 236]. Therefore, producing the center in a controlled manner in bulk diamond is a remarkable achievement which opens new experimental avenues for further studies of these centers.

7.3.2 Atomic structure of the chromium center

We now discuss the atomic structure of the Cr center in diamond. A substitutional atom in a diamond lattice generally exhibits tetrahedral symmetry and would possess different excitation polarization dependence than the observed here. Furthermore, a substitutional atom generally has similar size to the atom of the host matrix such as nitrogen in diamond. In particular, most of the substitutional atoms in diamond form complexes aligned along the <111> axis (e.g. substitutional nitrogen adjacent to a vacancy). The excitation polarization measurements in this work reveal a complete extinction of the PL which indicates that the excitation dipole of the center is located on the {001} planes.

Since the size of the Cr atom is significantly larger than the size of the carbon atom, an interstitial related location is more stable than a substitutional one. A distortion of the crystal around the Cr atom is possible to stabilize the structure. It is therefore likely that the Cr atom occupies an interstitial related site, with a possible distortion of a surrounding diamond lattice. At this stage we can not exclude the possibility of the Cr occupying a non defined site (such as Cr in the center of a di-vacancy) where Cr is not bonded to the surrounding carbons. This defect geometry was shown recently by an electron spin resonance study for the 883/885 nm Ni related defect[91]. Neither we can categorically rule out a substitutional chromium defect, since other large atoms such as nickel were found in substitutional locations in the diamond lattice[237].

We then investigated the effects of local vibrations due to the number of atoms forming the defect. A defect consisting of an impurity atom of mass M_I located in a matrix with host atom mass M_C, generates quasilocal vibrations which can be described by the following equation[94]:

$$\omega_{QL} = \omega_D \sqrt{M_C / 3(kM_I - M_C)} \tag{7.2}$$

where $\omega_D = 150\,\text{meV}$ is the Debye frequency of the diamond lattice and k is the number of impurity atoms involved in the quasilocal vibration[94]. Assuming that only one Cr atom is involved, the vibration should occur 47 meV from the ZPL. Therefore, in the case of ZPL= 749 nm, the vibration should occur at 771 nm. Following the measured PL from the bulk diamond presented in Figure 7.10, a vibronic feature is observed at 771 nm, which corresponds to 47 meV shift from the ZPL. We therefore tentatively conclude that only one chromium atom is involved in the structure of the center. Although it is hard to envisage that more than one chromium atom is involved, other analytical techniques should be performed to confirm this assumption.

7.3.3 Fabrication strategies of the chromium centers

The co-implantation technique of Cr and O with the doses and energies specified above yielded 5-10 Cr related centers per 100×100 μm^2. This indicates rather low conversion

probability of implanted Cr into an optically active defect. To investigate the fabrication process of the chromium centers more implantations were carried out. Particularly, we modified: the type of diamond which is subject to implantation, the implantation doses and interaction of Cr with other dopants. The annealing conditions of all samples were same as the original samples (i.e. 1000°C in a forming gas ambient). The acceleration energies of the various dopants are summarized in Table 7.3 and the full detailes of the implantations are summarized in Table 7.4.

Element	Implantation energy [keV]	End of range [nm]
Chromium	50	25±7
Oxygen	19.5	25±8
Silicon	34	25±7
Boron	13	25±8
Sulfur	38	25±7
Nitrogen	18	25±8

Table 7.3. Implanted elements and the corresponding implantation acceleration energies.

The results of the implantations are very intriguing. The chromium centers was routinely observed in Type IIA diamonds (samples 7-20). However, when same implantation was applied to an ultra pure or a type Ib diamond, the chromium enters were never observed (samples 1-6 and 21-25, respectively). The main difference between these diamonds is the amount of nitrogen. While in an ultra pure sample, the level of nitrogen is extremely low, less than ppb, in type Ib the concentration of nitrogen is extremely high (~100 ppm). It is therefore obvious that nitrogen may play a role in the formation of the centers.

The influence of nitrogen is likely to dominate the charge state of the center. If its concentration is too high or too low, the required charge state of the chromium center is not formed. Surprisingly, however, even when low doses of nitrogen were co-implanted into the ultra pure material along with chromium and oxygen (samples 5-6), no single centers or narrow PL lines were observed.

Diamond type	Implantation details	Comments	Sample N
Ultra pure [N] < 5 ppb, [B] < 1 ppb	1×10^{11} Cr+1.5×10^{11} O	No single centers or narrow PL lines were found at all	1
	2×10^{11} Cr+3×10^{11} O		2
	2×10^{10} Cr		3
	2×10^{10} Cr+2×10^{10} B		4
	1×10^{11} Cr+1.5×10^{11} O + 1×10^{9} N		5
	1×10^{11} Cr+1.5×10^{11} O + 1×10^{11} N		6
Type IIA [N] < 1 ppm [B] < 0.05 ppm	1×10^{11} Cr+1×10^{11} Si	1-2 centers in 100×100 μm^2	7
	1×10^{13} Cr+1×10^{13} Si	1-2 centers in 100×100 μm^2	8
	1×10^{11} Cr	1-2 centers in 100×100 μm^2	9
	1×10^{13} Cr	1-2 centers in 100×100 μm^2	10
	1×10^{10} Cr+1.5×10^{10} O	5-10 centers in 100×100 μm^2	11
	2×10^{10} Cr+3×10^{10} O	5-10 centers in 100×100 μm^2	12
	1×10^{11} Cr+1.5×10^{11} O	5-10 centers in 100×100 μm^2	13
	1×10^{11} Cr+5×10^{11} O	5-10 centers in 100×100 μm^2	14
	1×10^{11} Cr+2×10^{12} O	5-10 centers in 100×100 μm^2	15
	1×10^{12} Cr+1.5×10^{12} O	5-10 centers in 100×100 μm^2	16
	1×10^{13} Cr+1.5×10^{13} O	1-2 centers in 100×100 μm^2	17
	1×10^{11} Cr+3×10^{11} S	5-10 centers in 100×100 μm^2	18
	1×10^{11} Cr+1×10^{11} B	1-2 centers in 100×100 μm^2	19
	1×10^{11} Cr+1×10^{12} B	1-2 centers in 100×100 μm^2	20
Type Ib [N] <100 ppm [B] < 0.1 ppm	1×10^{11} Cr+1×10^{11} Si	No single centers or narrow PL lines were found at all.	21
	1×10^{13} Cr+1×10^{13} Si		22
	1×10^{11} Cr		23
	1×10^{13} Cr		24
	1×10^{11} Cr+1.5×10^{11} O		23
	1×10^{13} Cr+1.5×10^{13} O		25

Table 7.4. Various implantation routes employed to investigate the formation of Cr related centers. The ultra pure and the type IIA diamonds were purchased from Element Six while the Type Ib diamond was purchased from Sumitomo).

It is also evident from the results that a donor (oxygen or sulfur) is required to efficiently engineer the centers (samples 11-16, 18). Since sulfur and oxygen are located in the same

column in the periodic table, they are expected to behave similarly when introduced in the diamond lattice. The ratio of chromium centers observed in the co-implantation of chromium and oxygen/sulfur compared to other implantations was as high as 10:1. Since similar results were obtained with co implantation of chromium – oxygen and chromium – sulfur, it is more likely that oxygen and sulfur play a donor role and set up the charge of the center and are not chemically bonded to the chromium. It may be analogous to other transition metals in solid which show PL signals only if they are in the right charge state. For instance, erbium in silicon becomes optically active only if a specific charge state of Er^{3+} is achieved. Furthermore, it has been shown that co implantation of erbium and oxygen into silicon greatly enhanced the emission from this defect[238, 239]. We can not at this stage unambiguously identify the role of the oxygen or sulfur in the co-implantation except to note that the co implantation significantly enhances the formation probability of the chromium emitters.

A co implantation of silicon and chromium was performed to test the damage effects associated with the implantation. Silicon should not modify the charge state since it has similar electronic configuration as carbon, however, a co-implantation of silicon with chromium will induce damage and introduce more vacancies. This implantation procedure followed by the same annealing treatment resulted in only limited number of chromium emitters (samples 7-8). Similar results were obtained when chromium only was implanted (samples 9-10). These outcomes strongly supports that the role of the oxygen/sulfur is related to a charge transfer rather than assisting in generation of vacancies.

To test for a co implantation of chromium and an acceptor, chromium and boron were co implanted (samples 19, 20). As expected at this point, only a limited number of bright emitters were obtained. In the cases where no donor was co-implanted with chromium, the charge, necessary to form the bright narrow bandwidth chromium emitters, could be picked up from the surrounding impurities within the diamond (e.g. from nitrogen). However, as was shown experimentally, the probability of this process to occur is significantly reduced.

No significant dose dependence was observed in the samples implanted with Cr and oxygen or sulfur (samples 11-16, 18). When the Cr dose rise above 1×10^{12} Cr/cm^2, the

number of the observed centers decreased (sample 17). The quenching of the luminescence may be caused by excessively high implantation dose, which resulted in aggregation of the implanted species (e.g. chromium) rather than a formation of single centers. Samples implanted with 1×10^{10} Cr/cm^2, 1×10^{11} Cr/cm^2 or 1×10^{12} Cr/cm^2 (samples 11, 12, 16) all showed similar statistics in the number of the observed single Cr related centers. This indicates that the bottle neck for the conversion efficiency of the implanted chromium to an optical center does not directly depend on chromium but rather on another impurity or the specific charge state of the center. Therefore, based on our experimental results, the best recipe for producing the chromium related emitters is implanting chromium and a donor with doses ranging from $1\times10^{10} - 1\times10^{12}$ atoms/cm^2 .
One of the open questions remains after the implantation sequences is why two state emitters were never observed in a single crystal diamond (i.e. fabricated by ion implantation), although were routinely found in CVD nanodiamonds grown on sapphire (see Figure 7.2). A careful analysis of the ultra bright center, with a ZPL centered at 756 nm, reveals that a vibronic replica is observed at 770 nm, which corresponds to 31 meV shift from the ZPL. Fitting this value into equation (7.2) yields two Cr atoms per center. If this is indeed the case, it explains well why the two level emitters have not been observed by ion implantation. The low formation probability of the chromium emitter, which involves only one Cr atom, would have been dramatically reduced, since two Cr atoms would have been required to form a single center. In addition, we do not possess any knowledge about the additional elements which might be required to form the ultra bright two level emitter. Further experiments will be required to try and replicate the two state emitters by ion implantation.

7.3.4 Statistics of the Cr related emitters

Until now, we have concentrated on the emitter with a ZPL centered at 749 nm since it has a full correlation with the emission from Cr centers in nanocrystals. However, a further characterization of the implanted areas of the bulk diamond samples revealed a statistical distribution of the ZPLs. Figure 7.13a shows a histogram of ZPLs recorded from the implanted samples. Most of the emitters are centered around 750 nm, while

some emitters have a red shifted ZPL. The distribution of the ZPLs may arise due to local chemical environment, strain or charge fluctuations. Remarkably, although the ZPL is varied, the FWHM of all the emitters was preserved and equals to 4 nm. It is also important to stress that none of the presented PL lines were found in unimplanted areas and the narrow PL lines were observed only in samples which were implanted with chromium according to Table 7.4.

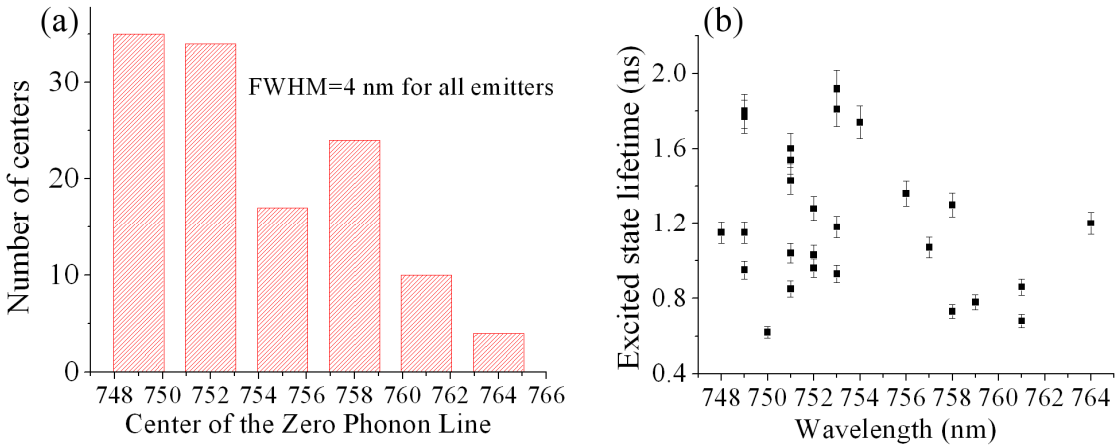

Figure 7.13 (a) Histogram of the ZPLs of various Cr related emitters as a function of wavelength. (b) distribution of the excited state lifetime of different Cr related emitters as a function of wavelength.

Figure 7.13b shows the distribution of the excited state decay rates measured from individual single emitters as a function of the ZPL. In this case, although a fluctuation of the lifetime is observed, there is no clear dependence of the excited state lifetime on the wavelength. The average lifetime for all the emitters is estimated to be 1.2 ns. The fluctuation of the excited state lifetime may arise due to strain which presents in these samples[221, 234]. Another hypothesis for the lifetime modification is the distance from the surface of various emitters. The radiative lifetime depends on the optical environment of the dipole and hence depends on the distance from the dielectric interface[240]. Since the emitters are formed by ion implantation which results in a Gaussian distribution of the end of range of the ions (see Figure 7.10b), a number of emitter are likely to be located in a different distance from the surface.

We then investigated the photon statistics of the emitters with respect to their ZPL. Figure 7.14a shows four typical $g^{(2)}(\tau)$ functions (red, pink, green, black) recorded at excitation

power above saturation from four Cr related emitters with ZPLs centered at 749 nm (red), 753 nm (pink), 757 nm (green) and 762 nm (black) (Figure 7.14b). It is clearly seen that the photon bunching of the center increases and becomes predominant with a red shifted PL. This indicates that the probability of transition from the excited state to the metastable state increases when the ZPL is shifted to the red. Subsequently, the emitters become less efficient because the transition to the metastable state increases.

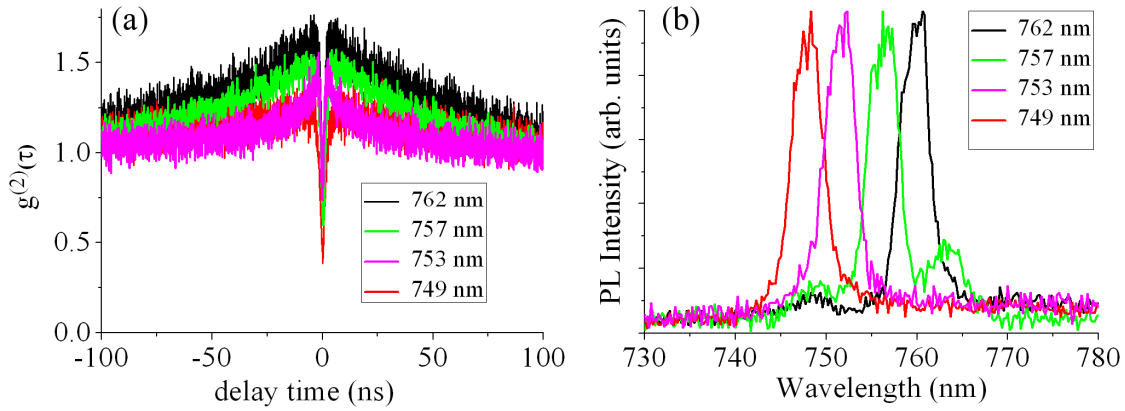

Figure 7.14 (a) Four typical $g^{(2)}(\tau)$ functions (red, pink, green, black) recorded at excitation power above saturation from four Cr related emitters with ZPLs centered at (b) 749 nm (red), 753 nm (pink), 757 nm (green) and 762 nm (black). Photon bunching of the centers increases with a red shifted PL.

To confirm this, we recorded the photon statistics of two different emitters (749 nm and 758 nm) in a pulsed regime, as shown in Figure 7.15a. In this case, each peak is proportional to the total number of coincidence counts. The normalized area of each peak m is then given by[14]:

$$C_N(m \neq 0) = 1 + \frac{T_{off}}{T_{on}} \exp[-(\frac{1}{T_{off}} + \frac{1}{T_{on}})|m|\theta] \tag{7.3}$$

where T_{on} is the time when the emitter is emitting and T_{off} represents the time when the emitter is trapped in the metastable state and no photons being emitted. θ is the repetition period. The normalized area of each peak, C_N, is plotted in (Figure 7.15b) for the emitters with a ZPL centered at 749 nm and at 758 nm. By fitting the experimental data with the

equation above, the characteristics T_{on}, T_{off} times are deduced for the 749 nm and the 758 nm emitters, respectively.

The ratio of $T_{on}/(T_{on}+T_{off})$ is representing the internal efficiency of the emitters. For the emitters discussed here, the values are 0.68 and 0.63 for the 749 nm and the 758 nm emitters, respectively. It is clear therefore, that the 749 nm emitter is more efficient which supports the high brightness recorded from this emitter and low bunching of the $g^{(2)}(t)$ function. In addition, the chromium emitters present a better efficiency than the NV and the NE8 centers, which show $T_{on}/(T_{on}+T_{off})$ ratio of 0.54 and 0.56, respectively[28, 148].

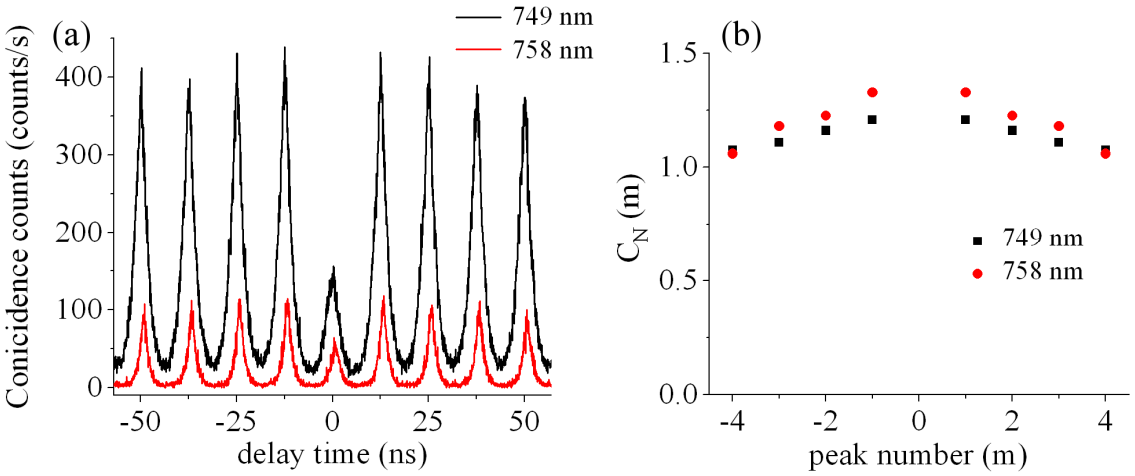

Figure 7.15 (a) Second order autocorrelation function recorded for two different emitters (749 nm and 758 nm) in a pulsed regime. (b) Normalized peak area of the pulsed $g^{(2)}(\tau)$ function showed in (a) as a function of a peak number, m.

We believe that all the above emitters, although possess different ZPLs, belong to the same family, or in fact the same emitter. This hypothesis is strongly supported by the same FWHM of the ZPL, similar excited state lifetimes, similar photon statistics and comparable brightness. The shift of the ZPL may arise due to a different local chemical environment or charge fluctuations.

7.4 Quantum efficiency and collection efficiency

The knowledge of quantum efficiency (QE) (equation (2.22)) of single emitters is vital for applications requiring a single photon source on demand and for tackling challenges such as strong light-atom interaction or long distance entanglement protocols by means of integrated waveguides and microcavities in solid state systems[10, 12, 156, 241]. Furthermore, the knowledge of QE is particularly essential to design an optimal optical structure (e.g. nanocavities or plasmonic) which enhances the collection efficiency or modifies the radiative or/and non-radiative decay paths of the emitter [155, 242-245]. In these cases a precise measurement of the QE is necessary to accurately quantify any improvement obtained in the detected photons from the coupling to optical structures.

Direct measurements of QE are challenging and require a priori knowledge of the emission dipole orientation, and a separate measurement of the radiative and non radiative decay rates. To determine the dipole orientation of single molecules and colloidal quantum dots, methods such as defocused[246, 247] or direct imaging[248] have been successfully demonstrated. This is achieved by imaging the emission pattern of the collected photons with a high numerical aperture objective in the back focal plane (or the back-aperture plane for an infinity corrected system).

To extract information about radiative and non-radiative decay rates for an emitter close to a material-air interface, one can modify the local dielectric environment of the emitters. This is enabled by adding a medium with a matching[240] or a different refractive index[249] to the emitter environment. Using such approaches, radiative and non radiative decay rates of single molecules and quantum dots were separately obtained. In an alternative method, a scanning metal mirror was brought close to a single molecular dipole. From the modification of the molecule radiative decay rate, the QE of single emitting dipole was then measured[250].

Despite the progress achieved in recent years investigating single emitters from color centers in diamond, a direct measurement of QE of any diamond color center is still lacking. For the SiV center, time resolved PL was measured and compared with a standard dye to deduce that the quantum efficiency of this center is only a few percent. To date, it was anticipated in the literature that the QE of the NV and the NE8 centers is close to unity[29, 148, 251], This argument is however questionable since both centers

show a clear bunching in the autocorrelation function, which indicates a presence of shelving or a third long lived state, which suppresses the emission. Moreover, it is unclear if non radiative decay paths exist in these centers. For the NV, the only measurement supportive of the absence of any non radiative decay paths was the independence of the fluorescence decay time on the temperature[252]. However, there is no evidence in the literature regarding a direct measurement of QE of any diamond color centers to date.

In this section, the QE of chromium color centers is discussed. We first present a methodology to estimate the QE of emitters embedded in nanodiamonds. In the second part we present a technique to measure directly the QE of chromium related emitters engineered in a bulk diamond.

7.4.1 Quantum efficiency of chromium emitters in nanodiamonds

One way to evaluate the QE is through determining the collection efficiency of the setup. The collection efficiency can be estimated by calculating the contribution of each component to the total collection efficiency[196]. This method however, is not accurate since quantitative information regarding each component contribution, including the collection from the sample itself, is missing and an accumulative error can be significant. A better method to evaluate the collection efficiency is to measure the proportion of the detected count rate (R_{det}) at excitation saturation power versus the theoretical emission rate, based on the inverse of the radiative lifetime (τ) for a single emitter ($\eta_{QE} \times \eta_{CE} = R_{det}/\tau$). This measurement can be undertaken also in a pulsed regime, where the collection efficiency is calculated from the laser repetition rate (R_{rep}) and the detected count rate. In the condition where the laser excitation energy is above saturation, the temporal separation between laser pulses is longer than the typical detector dead time (50 ns) and the source lifetime, the efficiencies are given by $\eta_{QE} \times \eta_{CE} = R_{sat}/R_{rep}$ where (R_{sat}) is the count rate at saturation.

We measured the value $\eta_{QE} \times \eta_{CE}$ directly, by exciting chromium related two-level emitters embedded in nanodiamonds (see section 7.2) in a pulsed regime as each excitation pulse generates one emitted photon. As an example, exciting the 764 nm

emitter with a laser repetition rate of 10 MHz, the product $\eta_{QE} \times \eta_{CE}$ =0.015±0.001 is obtained. By measuring $\eta_{QE} \times \eta_{CE}$ for each chromium related two level emitter in a cw excitation mode, an average value from all the measurements, $\eta_{QE} \times \eta_{CE}$ =0.013±0.004 is obtained, in accord with the estimation from the pulsed measurements. The discrepancy in this value for various two level emitters may be attributed mostly to a variation associated to the unknown dipole orientation of the emitter within the crystal and/or residual polarization dependent background, which can influence the total saturation count rate R_{sat}. The value $\eta_{QE} \times \eta_{CE}$ =1.3% is in fact the lower bound for the collection efficiency of our setup. If the quantum efficiency of the emitters is lower than 1, the collection efficiency of the setup would be even higher.

Once the value of $\eta_{QE} \times \eta_{CE}$ was established, we now can determine the relative QE of the 749 nm emitter with respect to the two-level emitters. Assuming similar collection efficiencies for all the emitters (based on the fact that they embedded in nanodiamonds with similar size, which is smaller than the wavelength), a relative quantum efficiency of $\eta_{QE}^{3-level} / \eta_{QE}^{2-level} = 0.24$ is determined from the saturation count rate of the three level emitters. Therefore, the QE of the three level emitters is approximately four times lower than the emitters exhibiting two level system.

Our analysis demonstrates a clear advantage of a two-level system, which has a higher QE, over a three-level system. In particular the absence of an intersystem crossing rate could facilitate the accurate determination of the variation of radiative and non-radiative decay rates in the presence of electric field modification induced by the environment[240, 250]. It is important to underline at this point that in order to establish an actual standard for fluorescence emission measurements, an absolute measurement of the fluorescence QE of diamond color centers, as reported for CdSe nanocrystals and single molecular dipoles[240, 250], would be required.

Finally, one can speculate that the QE of the two level emitters presented earlier is close to unity. Two level emitters do not possess any intersystem crossing rate to a metastable state therefore the quantum efficiency is limited only by a presence of non radiative decays. The fact that the emitters are very stable over hours of laser illumination and no

bleaching or blinking was observed indicates that non radiative paths are likely to be absent or have a negligible contribution. Quantum emitters which have non radiative decay paths, generally suffer from severe blinking behavior. However, a direct measurements of non radiative decays is required to unambiguously prove this point.

7.4.2 Quantum efficiency of chromium emitters in bulk diamond

To measure directly the QE of single emitters the orientation of the emitter has to be known and the decay rate of the emitter has to be measured in two different dielectric environments. Fabrication of chromium emitters in monolithic diamond gives access to such a measurement since the emitters can be engineered in different depths from the diamond interface and therefore have different dielectric environment. Employing this approach, we first imaged the emission patterns of single chromium emitters to identify their emission dipole orientation. Then, employing ion implantation we fabricated the emitters in different proximities from the diamond surface and measured their total decay rates.

To fabricate the emitters close to the diamond-air interface, chromium and oxygen ions were implanted using acceleration energy of 50 keV and 19.5 keV, respectively. To modify the dielectric environment of the emitters, a second implantation of chromium and oxygen in the same type of diamond was performed using acceleration energy of 6 MeV and 3.6 MeV, respectively. The projected range of the shallow implantation (50 keV) is approximately 25 nm below the diamond surface, while the projected range of the deep implantation (6 Mev) is 1.5 μm below the diamond surface. Figure 7.16a shows the SRIM simulations of the implantations.

Note that the annealing step applied after the implantation is not sufficient to cause any diffusion of the chromium or the oxygen atoms and the end of range of the two implanted chromium ions does not overlap. Figure 7.16b shows a schematics of an emitting dipole with respect to the diamond sample and the optical axis (z) of the objective, identified by the polar angle θ and the azimuth angle Φ.

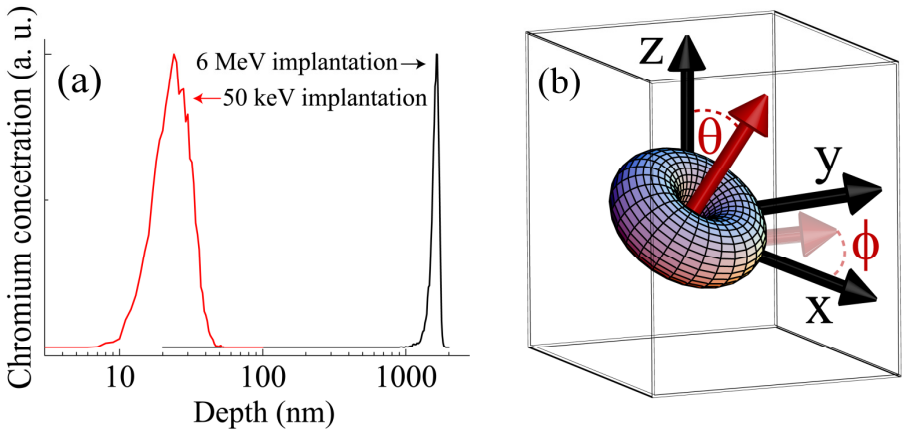

Figure 7.16 (a) SRIM profiles of implanted chromium ions into diamond using an acceleration energy of 50 keV (red curve) and 6 MeV (black curve). (b) An illustration of the emitting dipole orientation with respect to the diamond sample and the optical axis (z) of the objective, identified by the polar angle θ and the azimuth angle Φ.

In the first part of the experiment, the emission dipole orientation was imaged by recording the angular intensity distribution of single emitters in the back focal plane of a high numerical aperture objective using a CCD camera. Such images of single emitters are crucial as they provide a clear indication regarding the dipole orientation. Figure 7.17a shows a typical objective back-focal-plane dipole image recorded from a single chromium center in bulk diamond (ZPL at 750 nm). Concentric doughnut-shaped rings, associated with being imaged through the aperture of a dry objective, are observed in the CCD image [253]. The uniform intensity distribution of the bright rings with dark centers indicates that the emitter is oriented nearly orthogonal to the diamond-air interface. The orthogonal orientation of the emission dipole with respect to the diamond surface is a result of the symmetry of the center and the position of the excited state orbital. This suggests that the dipole is not aligned along the <111> direction and that the symmetry of the center is not trigonal. Consequently, the structure of the center is not likely to be chromium – vacancy, as then a trigonal symmetry is expected. Several single emitters in bulk diamond were imaged, all confirming a very similar dipole orientation with polar angles between 0 and 2 degrees, which are within our method sensitivity.

In the previous section it was determined that the absorption dipole for the chromium centers in bulk diamond is aligned along one of the main crystallographic axis on the plane of the surface and the emitted light is not completely polarized. The nearly

orthogonal emission dipole observed using the dipole imaging technique elucidates that the emission dipole of the chromium centers in bulk diamond is nearly perpendicular to its absorption dipole.

For the sake of comparison, Figure 7.17e shows a typical objective back-focal plane dipole image of the Cr centers created in sub-micron CVD nanodiamonds (Figure 7.2b), with the same ZPL as the emitter shown in Figure 7.17a. In this case, as expected, the emission dipole orientation changes from crystal to crystal and it is clearly not parallel to the optics axis.

Figure 7.17(b,f) show a magnified area of the central rings of the images shown in Figure 7.17e (a,e), respectively. Figure 7.17(c,g) show the cross section data and the fit of the emission pattern shown in Figure 7.17(b,f), respectively, according to the theory presented in [9]. From the fit, the dipole polar coordinate, θ, was estimated to be less than (1±1)° and the azimuth angle ϕ=(0±5)°. On the other hand, for this particular nanocrystal, θ=(49±2)° ϕ=(69±2)° are obtained. Figure 7.17(d,h) show a two dimensional calculated pattern of the dipole emission shown in Figure 7.17(b,f) using the parameters from the fit. Excellent agreement between the theory and experiment is obtained for the dipole orientation measurement. Dipole imaging technique can therefore be successfully applied to color centers in bulk and nanodiamonds to fully determine their 3D orientation.

In the second part of this experiment, the total excited state lifetime and the QE of individual emitters in bulk diamond was measured. It is well known that the radiative lifetime of an emitter in a homogeneous medium of refractive index n is inversely proportional to n. In the more complex situation of a linear dipole located at a distance $d < \lambda$ from a dielectric interface, Lukosz and Kunz [254] showed that the radiative decay rate (k_{rad}) depends on the distance d, the refractive index of each dielectric medium and the excitation dipole orientation polar angle θ, with respect to the normal to the interface.

We denote $k_{\infty} = k_{nr} + k_{rad}^{\infty}$ as the total decay rate of an emitter in an unbounded homogeneous medium and a parameter α as $\alpha(d,\theta,n_1) = k_{rad}(d,\theta,n_1)/k_{rad}^{\infty}$ the modification of the decay rate in the presence of the dielectric interface. $n_1 = n_2/n$, being n_2 the index of refraction of the medium after the interface.

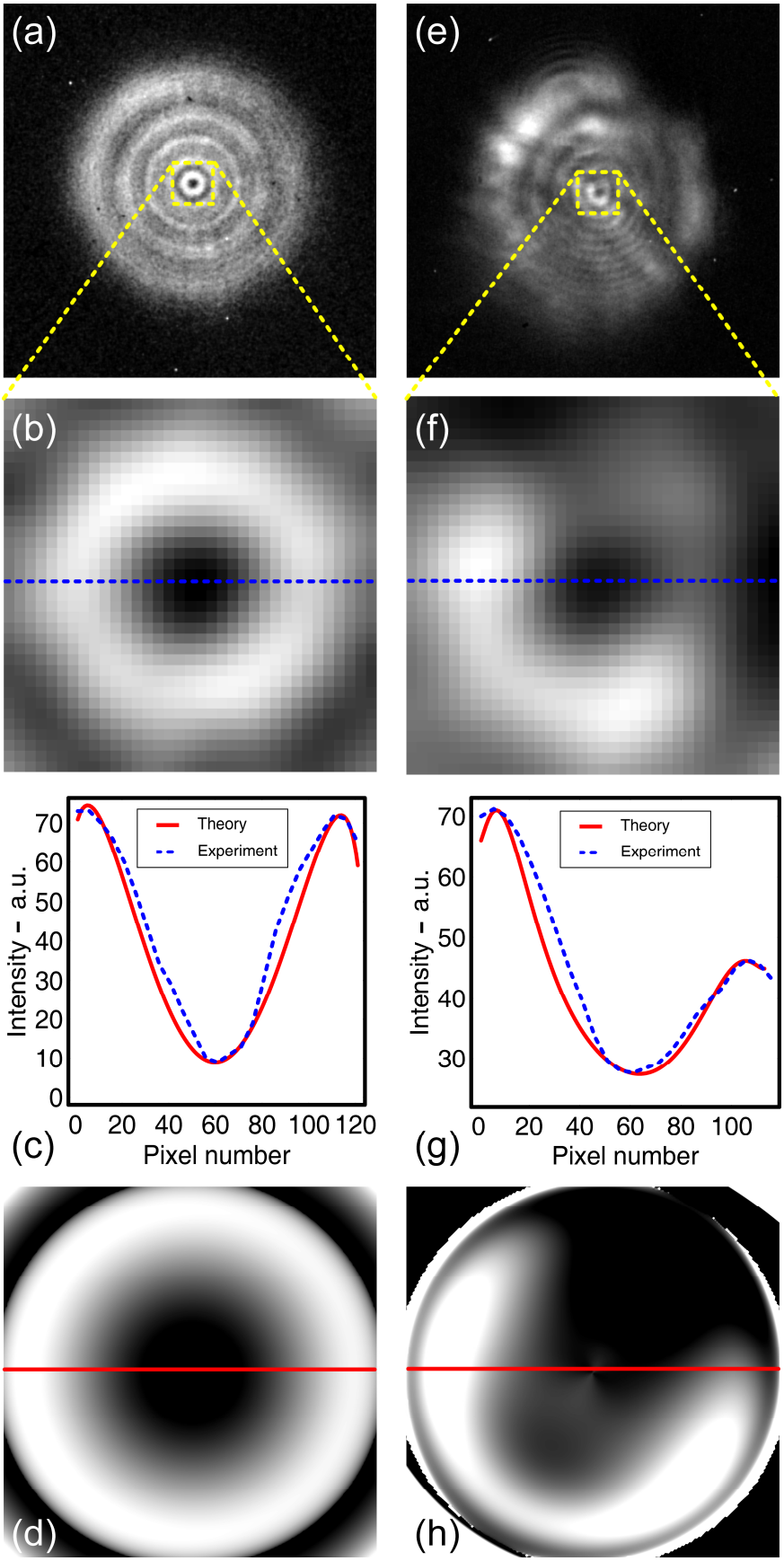
(a)
(e)
(b)
(f)
Theory
Experiment
Intensity - a.u.
70
60
50
40
30
20
10
0
0 20 40 60 80 100 120
Pixel number
(c)
Theory
Experiment
Intensity - a.u.
70
60
50
40
30
0 20 40 60 80 100
Pixel number
(g)
(d)
(h)

Figure 7.17 (a, e) Two images of the intensity distribution of the emission dipole, from chromium single photon emitters (ZPL at 750 nm) created in bulk diamond and in sub-micron diamond crystal, respectively. Integration times were 200 s and 60 s, respectively. (b,f) Magnified area of the central ring of the images depicted in (a, e). (c, g) The cross section experimental data and the theoretical fit of the emission pattern are shown in (b, f). The polar angles of the emitters are $\theta=(1\pm1)°$ and $\theta=(49\pm2)°$ for the bulk and sub-micron diamond, respectively, while the azimuth angles are $\phi=(0\pm5)°$ and $\phi=(69\pm2)°$. (d, h) are calculated patterns of the dipole emission shown in (b, f) using the parameters from the fit. An excellent agreement between the theory and the experimental data is obtained for each dipole orientation.

The physical interpretation can be qualitatively described by classical electrodynamics. When the dipole radiates, its field is partly reflected by the interface. The dipole can then interact with its own field. This self interaction modifies the oscillation amplitude (and frequency) of the dipole and, as a consequence, affects its radiative decay time.

The total decay rate for a linear dipole can thus be generally written as

$$k(d,\theta) = k_{nr} + k_{rad}^{\infty}[\alpha(d,n_1)_{\parallel}\sin^2(\theta) + \alpha(d,n_1)_{\perp}\cos^2(\theta)] \tag{7.4}$$

where $\alpha_{\parallel}$ and $\alpha_{\perp}$ refers to a parallel and an orthogonal dipole orientation in respect to the interface, respectively, with the algebraic expression given in Ref [254]. If an emitter is moved far from the interface or the refractive index difference of the interface is reduced to zero $\alpha_{\parallel},\alpha_{\perp}=1$ and the excited state lifetime is independent of the dipole orientation. From the decay rates of dipoles close to an interface and in an unbounded medium, we deduce the value $\beta = k(d,\theta)/k_{\infty}$ and the QE can be rewritten as $QE = (1-\beta)/[1-\alpha(d,\theta,n_1)]$ [240, 255].

To engineer emitters in an unbounded medium, chromium and oxygen ions were implanted with energy of 6 MeV and 3.6 MeV, respectively. The end of range of such an implant is $d \approx 1.5$ μm (Figure 7.16a) which is considered to be in an unbounded medium since $d > \lambda$ and the emitters are located far from the diamond-air boundary. On the other hand, centers created using a 50 keV implantation are located near a dielectric interface since the end of range of this shallow implant is only $d \approx 25$ nm (Figure 7.16a). Therefore, measuring the excited state lifetime of chromium centers created by a deep

implantation will provide direct information of k_∞, while measuring the decay rates of chromium centers engineered near the surface will allow to deduce $k(d,\theta)$. To exclude any wavelength dependent effect, only emitters with the same peak emission were compared. Note that since the centers are embedded in the diamond matrix, the immediate surroundings in both the shallow and the deep implantations are the same and therefore k_{nr} can be assumed to remain constant [255].

Figure 7.18a shows PL spectra from single emitters with same ZPL fabricated by a deep (black curve) and a shallow implantation (red curve). Figure 7.18b shows the fluorescence decay rates from single chromium emitters with the same ZPL (centered at ~ 750 nm) engineered by shallow and deep implantations. The angle of the emission dipole of this emitter was found to be θ = (1±1)° (Figure 7.17a). The data were fit by using mono-exponential curve with a relative uncertainty of 0.5%. The reduction of the total decay rate for emitter located near the diamond air interface is clearly seen from these measurements. From the measured decay rates for the shallow and the deep implantations, the value $\beta = k(d,\theta)/k_\infty$ was deduced. For the single emitters at 750 nm the calculated parameter α, and the measured value of β yielded a QE=0.42±0.06. To the best of our knowledge, this is the first direct measurement of QE of a single color center in diamond.

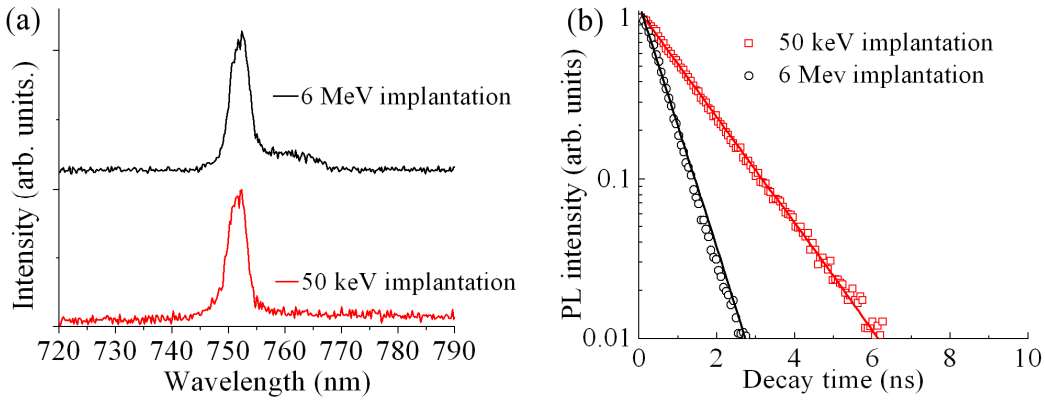

Figure 7.18 (a) Example of PL spectra of chromium related centers with the same zero phonon line created by ion implantation using energies of 50 keV (red curve) and a 6 Mev (black curve). (b) Direct lifetime measurement of a single emitter with a ZPL centered at 750 nm close to the diamond air interface (squares) and of an emitter with the same ZPL located 1.5 μm below the diamond surface (circles). The data were fit using a single exponential fit (solid line).

In the last part of the experiment, we measured the average QE of an ensemble of single chromium emitters in bulk diamond, regardless of their peak emission wavelength. The average excited state lifetime for the centers located near the diamond-air interface was measured to be 1.24±0.13 ns, while the lifetime of the centers located deep in the diamond crystal was measured to be 0.92±0.09 ns. A clear reduction of the excited state lifetime for the emitters located in an unbounded medium is noticeable also in an ensemble measurement. This result confirms that the centers are associated with a linear, 1D dipole since a 2D dipole orthogonal to the surface would not provide such a variation in the measured excited state life time in the shallow and deep implantation [17].

The QE was computed for various polar angles and values of β and is plotted in Figure 7.19a (black lines). A magnified region of interest for only small polar angles is shown in Figure 7.19b. The nearly orthogonal emission dipole observed for the centers yields an ensemble value of α=0.098 [16] and results in an averaged QE=0.28±0.04 for chromium emitters in bulk diamond, regardless their peak emission wavelength. The experimental values of the QE of several single centers with the same ZPL and of the ensemble measurement are shown in Figure 7.19.

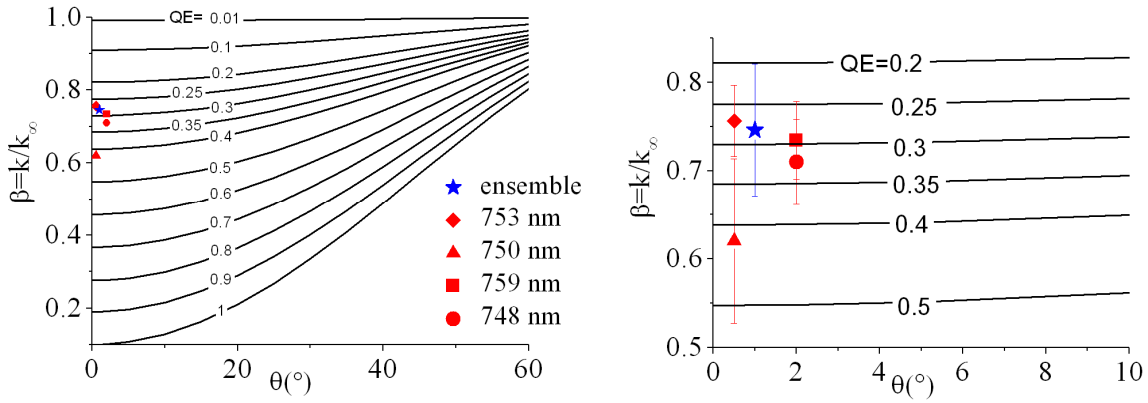

Figure 7.19 Orientation dependence of the ratio β on the polar angle θ. The solid black lines correspond to calculated values for different values of QE and with d = 25 ± 5nm. The measured values of β from an ensemble measurement (blue star) and several single centers with different ZPL (red circle, square, triangle and diamond) are superimposed. Inset: Enlarged area with standard deviation of the measured data.

A QE in the range of 30% can be associated to the presence of a metastable state or to additional non radiative process such as decay paths through phonons, ionization or heat, which strongly depend on the environment. The inter-system crossing rate for the chromium emitters is k_{ISC}=5.1 MHz as was deduced from analyzing the second order autocorrelation function. From the total decay rate and the QE values, one may infer that the radiative decay is k_{rad} ~ 226 MHz and the non-radiative decay is k_{nr} ~ 581 MHz. Therefore, the leakage to the metastable state is negligible compared to k_{rad} and k_{nr} and does not significantly reduce the value of the QE.

A number of important implications can be drawn from these results. The peculiarity of an emission dipole nearly always orthogonal to the bulk diamond surface is particularly advantageous for the integration of these emitters with cavities or diamond nano-antennas. In fact the major drawback of the recently fabricated diamond antennas incorporating NV centers [212] was the nondeterministic emission dipole orientation of the NV centers, due to its trigonal symmetry and polarization absorption anisotropy. This drawback can be overcome by using the chromium emitters in similar geometries and by using bulk diamond crystals with different crystallographic orientations. Finally, a similar approach could be used to determine the actual QE of the NV center, which is commonly inferred on the basis of circumstantial evidence[224, 252].

7.5 Summary

To summarize, we have controllably engineered and characterized novel single photon emitters based on chromium defects in diamond operating at room temperature. For the first time, two level ultra bright, chromium related single photon emitters were fabricated in a controllable manner in individual CVD grown nanodiamonds. The most promising emitter has a ZPL centered at 756 nm with a FWHM of 11 nm and exhibits photon statistics which are described well by a two-level model, confirmed by the absence of "bunching" in the $g^{(2)}(\tau)$ function above saturation. This is the brightest (3.2×10^6 counts/s) single photon source reported to date.

We then successfully demonstrated, for the first time, the controlled engineering of a chromium bright single photon source in bulk diamond, by ion implantation of

chromium. The center is located in a close proximity to the diamond surface (~25 nm), has fully polarized emission with a ZPL centered at 749 nm, FWHM of 4 nm, an extremely short lifetime of ~ 1 ns, and exhibits a count rate of approximately 0.5×10^6 counts/s, making it the brightest single photon source in bulk diamond to date. The excellent agreement between the PL spectra, in terms of the ZPL and FWHM, in bulk diamond and nanodiamonds clearly indicates that this class of emitters can be attributed to chromium.

The center exhibits an absorption dipole along one of the <100> directions and most likely consisting of one interstitial chromium atom. The enhanced properties of the chromium centers compared with the known diamond centers and the scalable fabrication technique, suggest that the chromium related centers will be important for a range of applications including quantum metrology, quantum cryptography, biomarking and hold a great potential to realize future fundamental quantum optics experiments.

Comprehensive experiments of various co-implantations of chromium with other elements showed that the most efficient way to fabricate these centers is by co-implanting chromium with a donor (sulfur or oxygen in our case). The successful fabrication of these centers only in type IIA diamond crystals, suggests that nitrogen plays a central role in the formation probability of these centers.

Finally, we presented for the first time, emission dipole pattern images of single color centers in bulk and nanodiamonds and a direct measurement of their quantum efficiency in bulk diamond. The dipoles are nearly orthogonal to the bulk diamond-air interface and to its absorption dipole, suggesting a non trigonal symmetry for these centers. By employing ion implantation techniques, we were able to fabricate the emitters at various distances from the diamond surface, thus modifying their radiative lifetime. Combining the imaging of the dipoles and measuring the decay rates of the emitters close to the diamond-air interface and in the unbounded medium, the quantum efficiency of individual centers and of an ensemble of centers in monolithic diamond was determined to be ~ 30%.

Chapter 8

Low temperature spectroscopy

The discovery of ultra bright, two level, single photon emitters, opened new perspective for advanced experiments in quantum optics which were not feasible with the traditional NV source due to its low count rate. The first experiment, which was attempted employing the new ultra bright emitters, is “two photon interference” (emission of two consecutive indistinguishable photons by the same source). The first attempt of this experiment was performed employing the chromium centers embedded in nanodiamond crystals.

Controllable generation of indistinguishable photons is one of the major tasks for realization of optical quantum algorithm schemes and in the heart of linear optical quantum computation[9, 11, 12, 161]. Although down conversion is a promising method for generating “twin photons”, its emission is governed by Poissonian statistics which results in very low single photon flux. With a development of true SPSs from quantum dots or single molecules, brighter SPSs became available. However, the controlled generation of indistinguishable single photons in solid-state systems remains challenging because strong interactions with the host matrix partially destroy the coherence between consecutively emitted single photons. Nevertheless, indistinguishable photons have been demonstrated by trapped ions[136], semiconductor quantum dots[15, 140, 256] and single molecules[257-259]. So far, this effect has not been demonstrated with color centers in diamond.

To demonstrate photon indistinguishability, Fourier-transform (FT) limited emission is generally required. FT limited emission from the ZPL of a single NV defect in diamond has recently been reported using resonant excitation at cryogenic temperatures[232, 233]. However, NV defects exhibit a broad spectral emission associated with a Debye–Waller factor of the order of 0.05, even at low temperature. Emission of single photons in the ZPL is then extremely weak, typically of the order of a few thousands of photons per

second. Such counting rates are insufficient for the realization of two photon interference and advanced QIP protocols. Important to notice, that with recent progress of enhancing the collection efficiency and the count rate from a single NV center[212, 213], such an experiment is definitely in the horizon.

The chromium centers exhibit high count rate, mostly concentrated in the ZPL and thus have a clear advantage over the NV center. In this chapter optical properties of single photon emitters at liquid helium temperature (~ 2 K) are discussed. The spectral stability of the chromium related SPSs embedded in nanodiamonds is investigated, prior to an attempt of generation of indistinguishable photons. In the second part, the optical properties of chromium emitters engineered in a bulk diamond are presented. All the measurements described in this chapter were conducted at the laboratory of Prof Jelezko in the University of Stuttgart, Germany.

8.1 Indistinguishable photons

When two photons enter simultaneously a 50:50 beam splitter, they can be reflected or transmitted. If the photons are indistinguishable, quantum mechanics predicts that they will follow the same path – either reflected or transmitted (Figure 8.1) – thus interfere. The wave packets of indistinguishable photons must be identical and perfectly overlap[9]. If the spectrum of a SPS is FT limited, i.e. each photon is described by the same coherent wave packet, then two photons can be indistinguishable if they have same spatial mode as well. However, in some cases, the spectrum of a source is broadened. The broadening can arise from fluctuations of the optical resonance frequency, which can be described as dephasing or spectral diffusion[9]. Dephasing is generally associated with fast fluctuations and occurs due to interaction with the lattice phonons (or collisions in a gas phase) which leads to loss of coherence of the emitter. Spectral diffusion is generally a slower process which associated with spectral jumps. If the photons are emitted faster than the jump occurs, this process can be practically neglected and two photon interference is still feasible.

The first observation of two photon interference was reported in 1987 by Mandel and co workers[260] who used parametric down conversion to generate identical photons.

Recently, two photon interference was observed from photons emitted from two independent sources[256], an important achievement towards scalable optical quantum computation. Furthermore, two photon interference was demonstrated between two independent source with different coherence times[261].

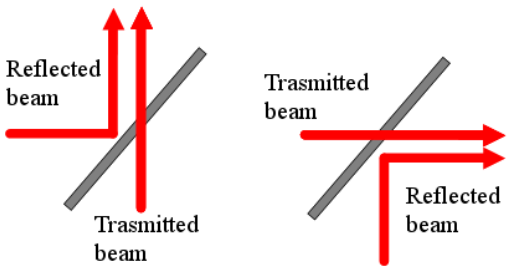

Figure 8.1 Schematic illustration of photon coalescence on a beam splitter.

8.2 Optical properties of emitters embedded in nanodiamonds

Diamond nanocrystals grown on sapphire (see chapter 7), hosting ultra bright single photon emitters were investigated at 2 K. For the imaging and basic spectroscopical studies, a laboratory built confocal microscope (Figure 3.7) was used. For the attempt of two photon interference, additional optical parts were added to this setup as shown in Figure 8.2

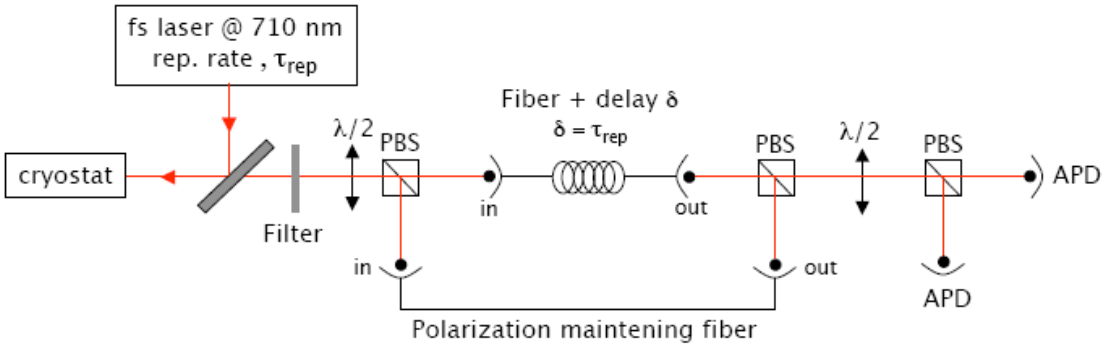

Figure 8.2 Schematic illustration of the experimental setup built to perform the two photon interference experiment.

The PL spectra of a single defect recorded at 2 and 300K are shown in Figure 8.3a. The emission is highly concentrated into a sharp ZPL at a wavelength around 770 nm. At room temperature, a small phonon side band is observed around 780 nm, which is no longer visible at low temperature. Consequently, the Debye–Waller factor, i.e. the ratio between the intensity of the ZPL and the total intensity of the emission spectrum, is extremely high (>0.9) at liquid helium temperature. For comparison, the PL associated with NV defects in diamond at low temperature exhibits a Debye–Waller factor on the order of 0.05 [9]. The emitter is most likely associated with Cr and belongs to the same class of emitter reported in the previous chapter.

The statistic of the emitted photons was then investigated for the same emitter by recording the second order autocorrelation function. Figure 8.3b shows the $g^{(2)}(\tau)$ function recorded while exciting the studied defect in a continuous mode at the wavelength λ=700 nm. A pronounced dip at zero delay time, $g^{(2)}(0)$=0.16, is the signature that a single emitter is addressed. The deviation from a perfect single-photon regime ($g^{(2)}(0)$=0) is due to a residual background PL of the diamond sample, which produces uncorrelated photons associated with Poissonian statistics, and to the detection setup time response function, which is limited by the single-photon detector jitter.

Figure 8.3c shows the $g^{(2)}(\tau)$ function recorded using a femtosecond pulsed excitation at a repetition rate of 76 MHz. After normalization to a pulsed Poissonian light source, the area of the peak at zero delay is found around $g^{(2)}(0)$=0.11. In such a pulsed measurement, this value gives the intrinsic quality of the single-photon source, which is only limited by the signal-to-background ratio. Fitting each peak of the autocorrelation function with exponential decay, a radiative lifetime τ_{21}=2.0±0.1 ns was deduced. This value is in a good agreement with the lifetimes measured at room temperature for other Cr related emitters in the previous chapter and is almost one order of magnitude shorter than that associated with NV defect in diamond nanocrystals[147].

To evaluate the emission rate at saturation, the single photon count rate was measured as a function of the laser power (Figure 8.3b). Experimental data were then fitted using equation (2.21), yielding a saturation count rate of 170×10^3 counts/s. Saturation emission rates of up to 400×10^3 counts/s have been measured for other single defects emitting in the NIR (at a temperature of ~2 K).

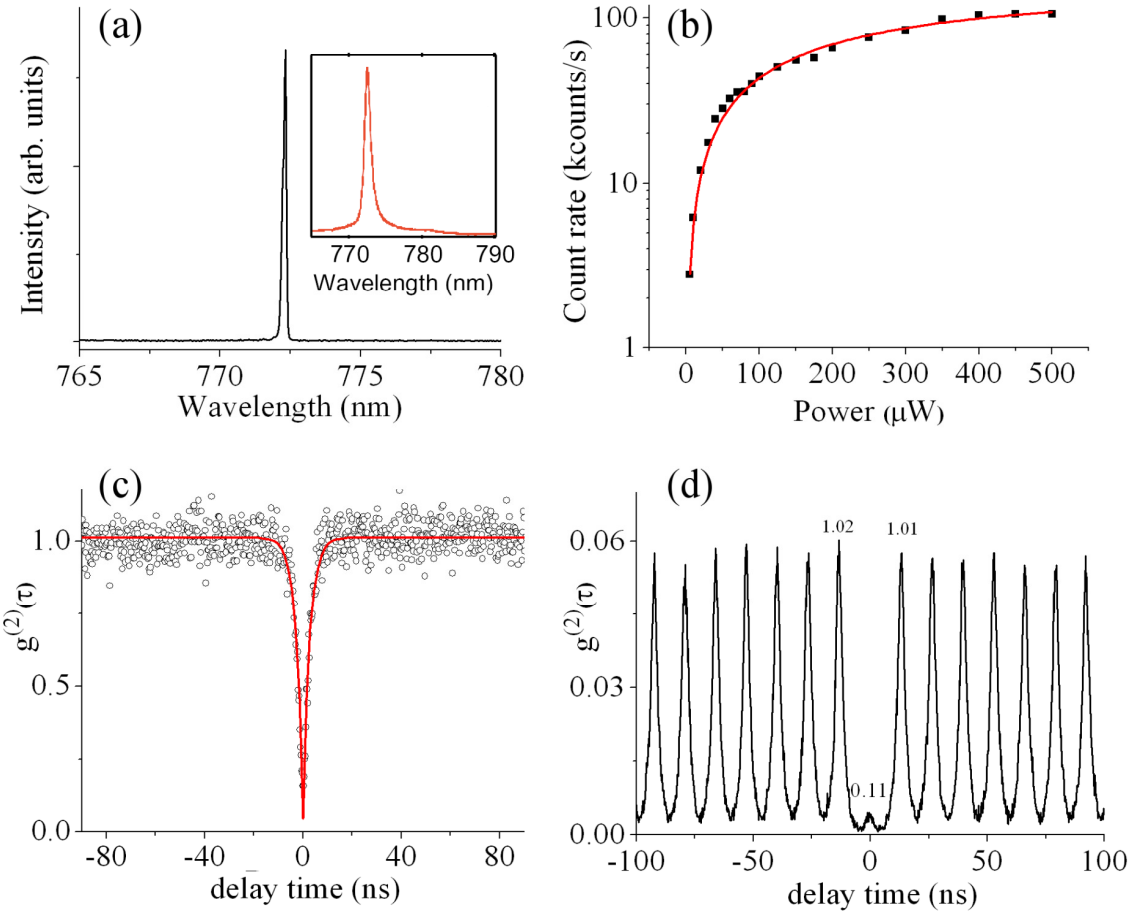

Figure 8.3 (a) PL spectrum of a single defect showing a sharp PL in the NIR centered at λ=772 nm, without any visible phonon sidebands at liquid helium temperature. The width of the ZPL is limited by the resolution of the imaging spectrometer, of the order of Δν≈100 GHz. The inset shows the PL spectrum recorded at room temperature, where the first phonon side band can be observed around 780 nm. (b) Background-corrected PL intensity as a function of the excitation power. The solid line is data fitting using equation (2.21). Data were taken by exciting the defect in a continuous excitation mode. The signal-to-background ratio is of the order of 10 for an excitation power of 300μW. (c, d) $g^{(2)}(\tau)$ function measured for the same single defect excited 700 nm excitation laser (b) in a continuous mode and (c) in a femtosecond pulsed regime at a repetition rate of 76 MHz. (d) Values written above peaks correspond to their respective area after normalization to a pulsed Poissonian light source.

These rates are lower than the ones measured at room temperature in Melbourne due to a different configuration of the setup (better objective, fiber optics confocal). Variation of the saturation count rates among different single emitters can be explained by different dipole orientations of the defects inside the nanocrystals, corresponding to different efficiencies of light collection. For NV defects, the saturation emission rate is on the

order of 50×10^3 counts/s using the same low-temperature experimental setup. More importantly however, since only 4% of the NV emission is concentrated in the ZPL, the counting rate in the ZPL is then around 2×10^3 counts/s. This is two orders of magnitude smaller than the emission associated with the Cr related defects emitting in the NIR. Polarization properties of the same defect are shown in Figure 8.4.

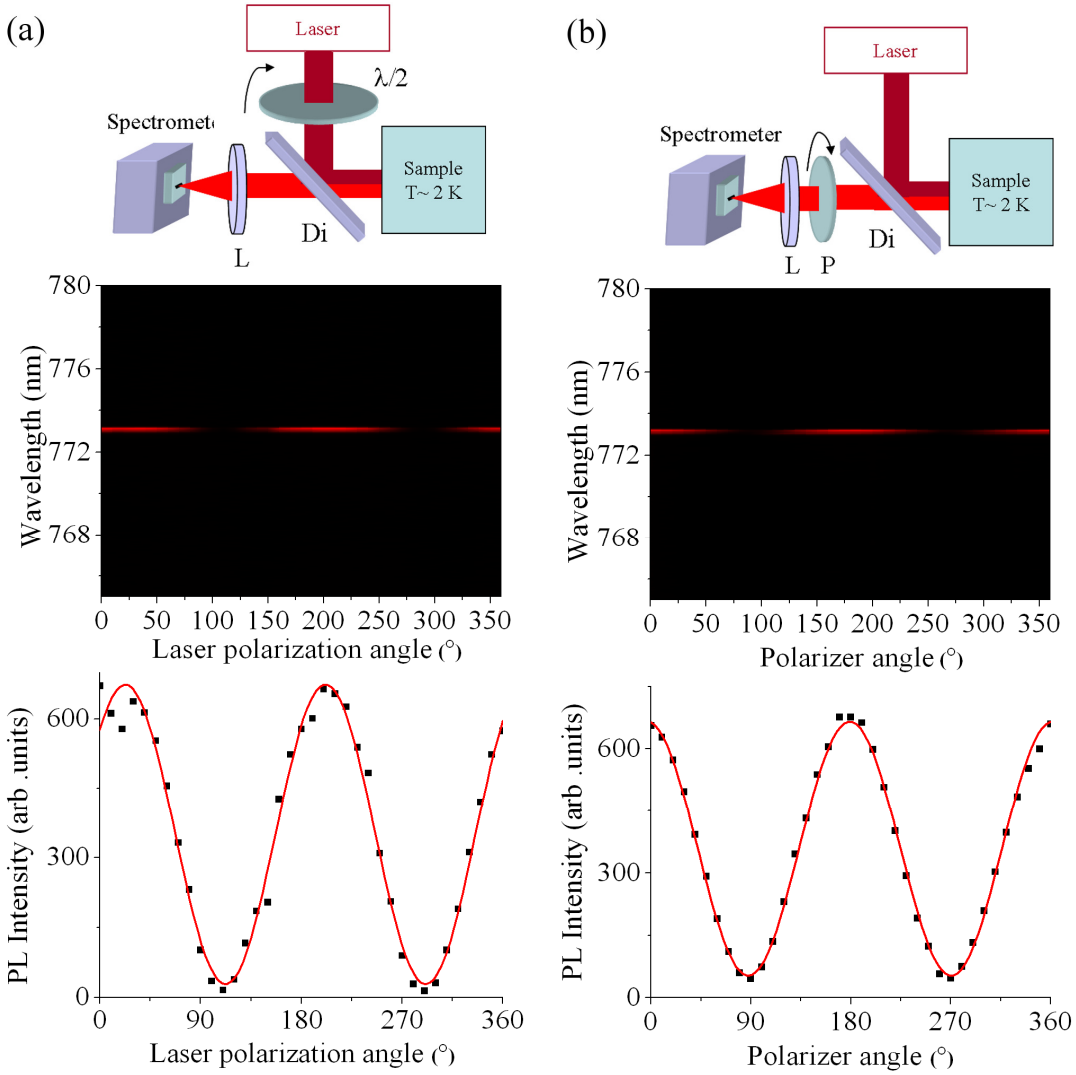

Figure 8.4 Polarization properties of the 772 nm emitter (a) PL intensity as a function of the excitation laser polarization angle, recorded by accumulating emission spectra while rotating the excitation laser polarization with a half-wave plate. The acquisition time for each spectrum is 1 s. The solid line is data fitting using a Malus-type law, yielding to a contrast of 97%. (b) PL intensity as a function of the angle of a polarizer (P) installed in the detection channel in front of the spectrometer. The solid line is data fitting using a Malus-type law, leading to a contrast of 92%. The decrease of the modulation contrast in emission is due to a slight elliptical polarization accumulated along the optical path from the sample to the single photon detector.

Figure 8.4a depicts an accumulation of PL spectra recorded while rotating the excitation laser polarization. By integrating such spectra, the PL intensity is displayed as a function of the laser polarization angle. As shown in Figure 8.4a, a modulation with a contrast of 97% was observed, which is the signature that the defect behaves as a perfect single dipole relative to absorption of light.

The polarization properties of the emitted photons were investigated by fixing the excitation laser polarization angle parallel to the dipole orientation, and by introducing a polarizer in front of the spectrometer. Following the method described above, PL spectra were then accumulated while rotating the polarizer in the detection channel (see Figure 8.4b). Once again, a modulation with a contrast close to unity was observed, indicating that the defect also behaves as a single emitting dipole. This is in opposition to NV defects where two orthogonal dipoles are always involved[227, 231]. The polarization properties are very important for the use of single-photon emitters in practical quantum key distribution applications, where the information is encoded in the polarization of the single photons[6].Some of the investigated diamond nanocrystals hosting single defects with a ZPL within a range of 770±15 nm showed spectra jumps. Figure 8.5 shows an example of single emitter with observed spectra jumps of up to 6 nm.

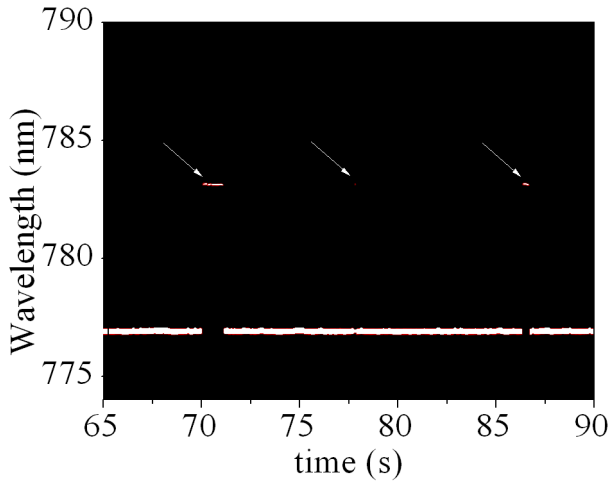

Figure 8.5 Real-time acquisition of PL spectra recorded for a single defect at liquid helium temperature. Spectral jumps of up to 6 nm are observed (white arrows).

Since the precise atomistic structure of the defects is still unknown, it is hard to identify the physical processes leading to spectral jumps. They might be associated with a

modification of the defect configuration such as a charge hoping on/off the defect, therefore changing its emission line. A fluctuating strain at the location of the defect, which is known to change drastically the energy level structure of color centers in diamond[233, 234], can also be a reasonable explanation. Furthermore, previous studies on NV defects in diamond have shown that strain effects are much stronger in diamond nanocrystals than in bulk samples[233, 262] and usually exhibit poor spectral stability in diamond nanocrystals while FT limited emission can be achieved in bulk samples[232, 233].

We now concentrate only on the photostable defects, to investigate whether FT limited emission can be achieved. As mentioned in the introduction, prior to two photon interference measurement, generation of FT limited emission should be demonstrated. For that purpose, a frequency-stabilized single-mode tunable laser (Ti:Sapphire) with a linewidth smaller than 1MHz and a mode-hop free frequency tuning around 20 GHz was used to excite resonantly the defects on their ZPL. The red shifted PL was detected using a 785 nm long pass filter and monitored while sweeping the single mode laser frequency. As the Debye–Waller factor is high, the rate of red shifted PL is low, typically of the order of a few kcounts/s.

Once a stable emitter with spectrometer limited linewidth was found, and single photon emission was verified, a photoluminescence excitation spectrum was recorded. Figure 8.6a shows a resonant excitation spectrum of a single defect with a ZPL around 760 nm (inset). The data are well fitted by a Gaussian profile with a FWHM around 4 GHz.

Owing to the previously measured radiative lifetime τ_{21} =2 ns, the lifetime limited linewidth $\Delta\nu_{FT}$ is given by[9]:

$$\Delta\nu_{FT} = \frac{1}{2\pi\tau_{21}} \approx 80 \ MHz \tag{8.1}$$

Therefore, the excitation linewidth is not Fourier transform limited. The broadening of the optical resonance does not arise from power broadening as the emission linewidth does not change with increasing excitation power, as shown in the inset of Figure 8.6a.

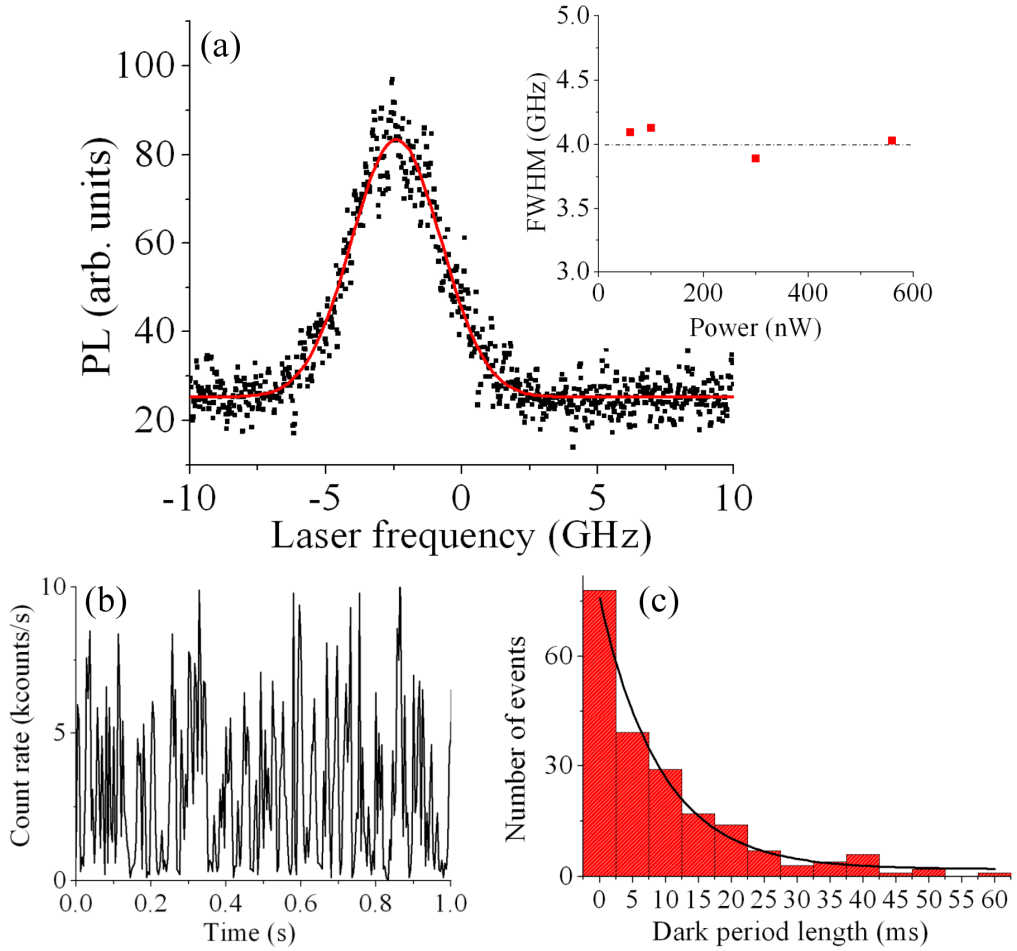

Figure 8.6 (a) Resonant excitation spectrum of a single defect emitting in the NIR in a CVD-grown diamond nanocrystal. For this emitter, the ZPL is centered at 760 nm. The total integration time is 16 min, corresponding to 120 sweeps of the laser frequency. The solid red line is data fitting using a Gaussian profile. The inset shows the evolution of the optical resonance linewidth as a function of the excitation power. (b) PL time-trace recorded while exciting the defect at resonance with a power of 400nW. The integration time per point is 5 ms. The observed blinking behavior is the signature of slow spectral jumps. (c) Histogram of the length of the dark periods in the PL-time trace over an observation time of 5 s. The solid line is data fitting using a single exponential decay, giving a spectral diffusion time of 10±2 ms.

Spectral broadening results from fluctuations of the optical resonance frequency, either by dephasing or by spectral diffusion[9]. Pure dephasing processes are fast, and arise from interactions with phonons in the crystalline matrix. Such processes lead to an homogeneous broadening, which follows a Lorentzian profile. Owing to the measured Gaussian profile of the optical resonance, we tentatively conclude that dephasing is not

the predominant broadening process. Spectral diffusion leads to comparatively stronger fluctuations, associated with slow frequency drifts and jumps, which can be observed by recording the red-shifted PL time-trace while exciting the defect at resonance, as shown in Figure 8.6b. The histogram of the length of the dark periods is shown in Figure 8.6c. Data fitting with a single exponential decay gives an estimate of the spectral diffusion time T_{sd} = 10±2 ms, much longer than the radiative lifetime τ_{21}.

If two consecutive photons are emitted within a time interval shorter than the characteristic spectral diffusion time, these two photons might be indistinguishable, as the slow spectral diffusion process could be neglected[15]. Consequently, owing to a spectral diffusion time in the millisecond range, it should be possible to use this and other Cr related defects emitting in the NIR in diamond to perform a two-photon interference experiment. Furthermore, we stress that approximately 20% of the studied defects were exhibiting an optical resonance linewidth in the GHz range. For other studied defects, high amplitude spectral jumps (>100 GHz) could be observed in real-time acquisition of PL spectra, as depicted in Figure 8.5.

8.2.1 Two photon interference

Although the PL signal was broadened and not FT limited, two photon interference experiment was attempted. We used the setup shown in Figure 8.2. There are four options for two consequent photons to reach the APDs: when the first photon goes through the short arm (SA) and the second photon through the long arm (LA), both go through the LA, both travel through the SA or the first photon goes through the delay line and the second one goes through the short arm. Only in the last case, the two photon interference can occur since two successive photons reach the second beam splitter simultaneously. Due to this photon statistics if the photons are distinguishable the central peak area at zero delay time should have a relative area of 0.5 while the peaks at $\pm 1\tau$ should have an area of 0.75 and the rest of the peaks at unity. If the photons are indistinguishable, the peak at zero delay time should be further reduced.

Without the last half wave plate the single photons would have parallel polarization and thus can be indistinguishable. In this case the peak at zero delay time should be

suppressed since the photons recombine on the last beam splitter and activate only one of the APDs (thus, no coincidence at $\tau=0$ is expected). As a test experiment, a second half plate was inserted. In this case, the photons would have orthogonal polarization and loose their indistinguishability, which would result in a relative area of the central peak of approximately half of the area of the peaks at times > 24 ns.

Figure 8.7a shows the result of the experiment. The black curve shows the interference of two photons with a parallel polarization and the peak at $\tau=0$ is suppressed. As a controlled experiment, photons with orthogonal polarization were measured (red curve). The data was offset for clarity. As expected in both measurements the peaks at $\pm 1\tau$ have smaller area. However, after normalization no obvious distinction in the central peak area between the two measurements is observed. The peaks at $\tau=0$ have similar areas and therefore, no indication of indistinguishable photons can be made at this stage (Figure 8.7b).

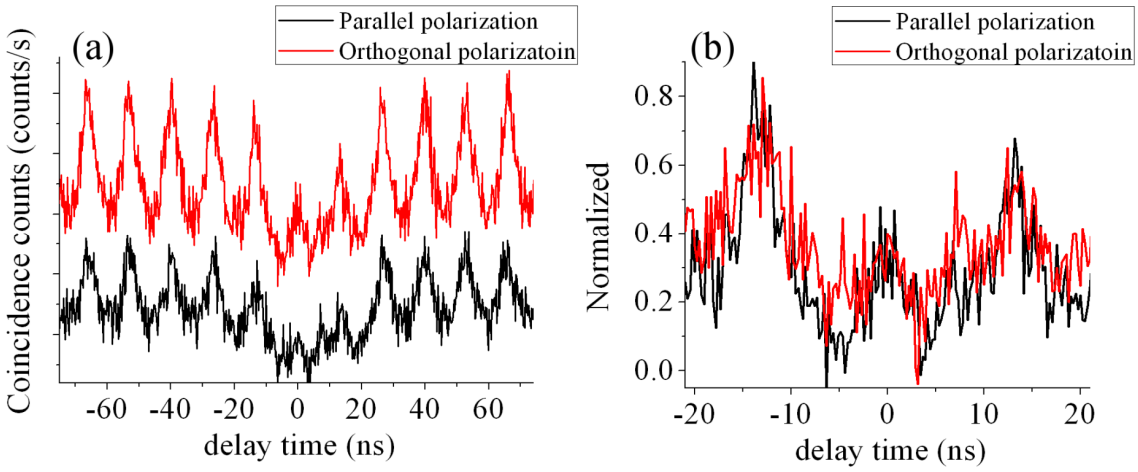

Figure 8.7 Results of the two photon interference experiment. (a) The correlation data recorded with parallel single photons arriving at the beam splitter (black curves) and orthogonal single photons (red curves). The red curve was offset for clarity. (b) Enhancement of the peaks around zero delay time which shows no clear sign of indistinguishability.

8.3 Optical properties of chromium related defects in single crystal diamond

In the last part of this chapter we present optical properties measured at cryogenic temperatures of chromium emitters fabricated in bulk diamond. In principle, emitters embedded in single crystal diamond should possess better spectral stability than the ones in nanodiamonds[233, 262] due to reduced strain and surface effects. High resolution spectroscopy of emitters in bulk diamond can also assist in revealing the structure of the emitters.

Figure 8.8a shows a number of PL spectra recorded at liquid He temperature (~2 K) from individual chromium centers engineered in bulk diamond by ion implantation of chromium and oxygen (see Table 7.4). Narrow lines limited by the spectrometer resolution were repeatedly observed. The emitters exhibited an average emission count rate of 30-50×10^3 counts/s, although in some cases emission rate as high as 80×10^3 counts/s was observed

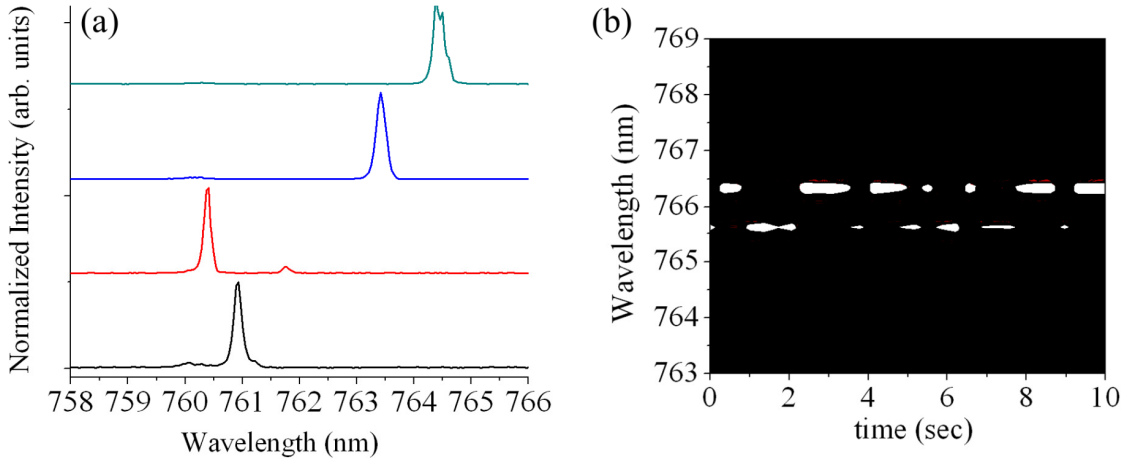

Figure 8.8 (a) PL spectra of a single chromium centers showing sharp PL in the NIR, recorded at liquid helium temperature. The width of the ZPL is limited by the resolution of the imaging spectrometer, of the order of $\Delta\nu \approx 100$ GHz. The excitation wavelength is λ=700 nm. (b) Real-time acquisition of PL spectra recorded from a chromium related defect. Spectral jumps of the order of 1 nm are observed. Each spectrum was accumulated for 1 sec.

Some of the lines showed spectral jumping, as evident from the PL time trace (Figure 8.8b). The blinking is most likely associated with an electric field fluctuation in a close vicinity to the centers. Note that the centers are located only 25 nm beneath the diamond surface, thus any surface modification would affect the charge configuration of the centers.

Only stable emitters which exhibited narrow lines limited by the spectrometer resolution were excited on resonance using a frequency-stabilized single-mode tunable laser (Ti:Sap) with a linewidth smaller than 1MHz and a mode-hop free frequency tuning around 20 GHz. Similarly to the nanocrystals, the red-shifted PL was detected using a 785 nm long-pass filter and monitored while sweeping the single-mode laser frequency. Unfortunately, PLE spectrum from these centers was not observed during our experimental work.

To test that enough photons are collected through the side band, we performed on resonant excitation with a broad band laser (linewidth of ~12 GHz). Although this measurement does not provide accurate information regarding the natural linewidth, it would confirm that resonant excitation is possible and enough photons are collected. Figure 8.9a shows a resonant excitation measurement from a chromium related emitter with a ZPL at 763 nm employing a broad band laser. The line is clearly seen, which indicates that enough photons are collected using a long pass 785 nm filter. Figure 8.9b shows a corresponding real time PL trace from the same center while exciting it resonantly. Strong blinking is observed which indicates spectral diffusion. This severe blinking hampers an accumulation of a proper PLE measurement since the lines spectrally diffuse over a wide frequency range.

Two remarks should be pointed out from this result: first, the fact that PLE signal was not observed does not indicate that a future two photon interference experiment will not be possible. Similar to the nanodiamond case, if the spectral diffusion is slow enough, two consecutive photons may be indistinguishable. Second, the chromium centers investigated here were fabricated only 25 nm below the surface and thus strongly affected by the charge fluctuation on the surface. Repeating the PLE measurement on centers created by a deep implantation may result in FT limited signal from these centers. Indeed, even the NV centers which are formed by a shallow implantation do not show PLE signal

and the line is significantly broadened, while natural NVs or NVs created by a deep implantation (~few microns below the surface) show a FT limited linewidth[233]. A successful high resolution spectroscopy study of these centers in bulk diamond is essential for further identification of the structure of the center. The measurements of deep chromium implantations are currently undergoing in collaboration with Prof Jelezko.

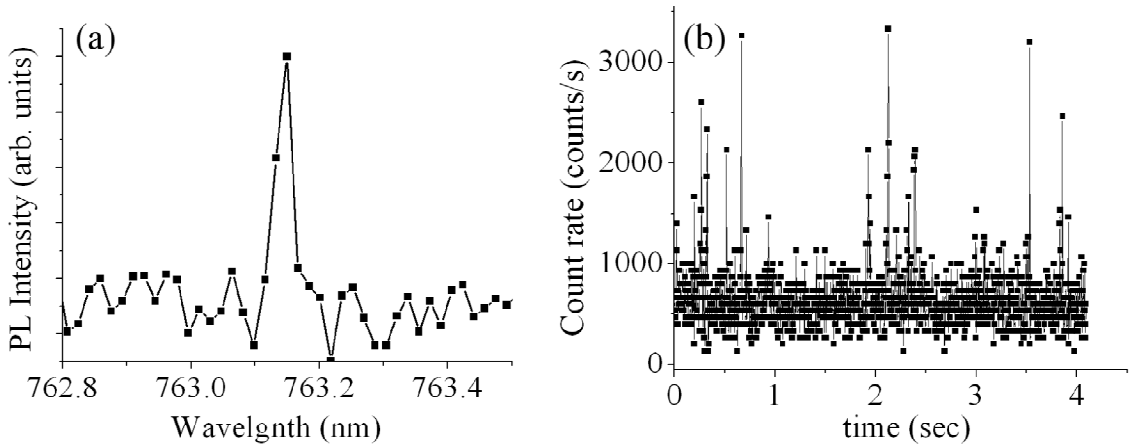

Figure 8.9 (a) Resonant excitation spectrum of single chromium emitter in a bulk diamond recorded with a broad band laser. The measurement is an average of 10 sweeps of the laser over the line. (b) PL time-trace recorded while exciting the same center resonantly. The integration time per point is 4 ms.

8.4 Summary

In this chapter optical properties of Cr related single defects emitting in the NIR were studied at liquid helium temperatures. Such defects, when embedded in nanodiamonds exhibit several striking features: (i) a sharp PL in the NIR associated with a high Debye–Waller factor (>0.9), (ii) high counting rates, (iii) a short radiative lifetime (2 ns) and (iv) linearly polarized excitation and emission (contrast higher than 90%). An optical resonance linewidth of 4 GHz is measured for the first time from a diamond single photon source emitting in the NIR using resonant excitation on the ZPL. The broadening of the optical resonance results from spectral jumps occurring at the millisecond timescale.

An attempted PLE on Cr centers fabricated by a shallow implantation into a bulk diamond was not yet successful and severe blinking was observed. However, the successful fabrication of these sources deep inside the crystal should improve their spectral stability. Such results are promising for the future realization of an efficient source of indistinguishable single photons using single defects in diamond.

In particular, the spin structure of the defect could be investigated by recording resonant excitation spectra while applying a magnetic field. Owing to the coherence properties of spin states in diamond, such experiments could open many perspectives in the context of coupling between spin states and optical transitions. Such experiments were set up in collaboration with Dr Mete Atature from Cambridge University.

Chapter 9

Conclusions and outlook

The fundamental research question which was addressed in this thesis is the development of ultra bright, narrow bandwidth, single photon emitters in the near infra-red operating at room temperature.

Figure 9.1 shows the evolvement of single photon emission rate of diamond based single photon emitters over the last decade. It clearly emphasizes the achievement of this work in developing novel ultra bright emitters, which are orders of magnitude brighter than other known emitters in diamond and show a better performance than NV centers embedded in cavities or solid immersion lenses. Remarkably, over the last decade alone the count rate improved by more than two orders of magnitude from 10^4 counts/s to more than 10^6 counts/s. We further envisage that higher count rates would be available once the chromium related sources are integrated with solid immersion lenses or other structures which increase the collection efficiency.

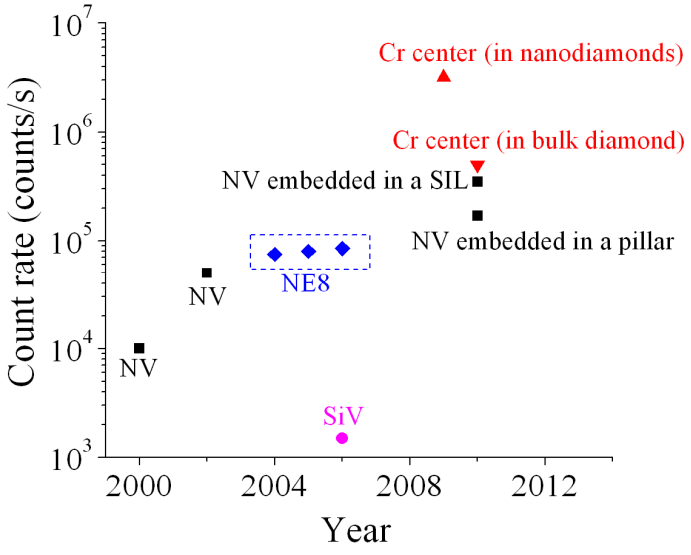

Figure 9.1 Improvement of the emission rate of diamond based single photon emitters over the last decade.

The main conclusions which are drawn from this thesis are summarized below:

1. High quality diamond nanocrystals were synthesized on a substrate of choice employing high microwave power density chemical vapor deposition technique. The growth from nanodiamond seeds under high pressure (150 torr) eliminated secondary nucleation and enabled the control over the lateral density and the final size of the grown diamond crystals.
2. A very efficient method for incorporating an impurity into diamond crystal during chemical vapor deposition process was developed. Implantation of nickel into a substrate onto which diamond crystals are subsequently grown, results in an efficient formation of nickel related single photon sources. The substrate is etched during the diamond growth and the exposed implanted ions are incorporated into the growing crystal through plasma assisted diffusion. Moreover, this technique can be potentially applied for an incorporation of any impurity into diamond nanocrystals.
3. Implantation of nickel into bulk diamond did not result in the formation of single NE8 centers, regardless the nitrogen concentration. Furthermore, it was shown that the NE8 center is formed only after high pressure high temperature annealing. However, isolated, single NE8 centers were not identified.
4. A new class of chromium related emitters was discovered by combining the ability to grow high quality sub micron diamond crystals in conjunction with a technique to incorporate the impurity during chemical vapor deposition growth. The emitters are formed through a diffusion of chromium from the sapphire substrate into the growing diamond crystal and exhibit a count rate of millions of photons per second.

   The most promising emitter has a zero phonon line centered at 756 nm with a full width at half maximum of 11 nm and exhibits photon statistics which are described well by a two-level model, confirmed by the absence of “bunching” in the $g^{(2)}(\tau)$ function above saturation. This is the brightest (3.2×10^6 counts/s) single photon emitter reported to date and it operates at room temperature.
5. Controlled engineering of chromium related single photon emitters in bulk diamond by ion implantation of chromium was then successfully demonstrated.

Implantation of chromium into a bulk type IIA diamond crystal confirmed the initial assignation of the new centers to chromium. The brightest chromium related center exhibits a count rate of 0.5×10^6 counts/s, making it the brightest single photon emitter in bulk diamond to date. Polarization measurements revealed that the absorption dipole of the chromium emitters is oriented along one of the <100> directions and the emission is fully polarized.

A co implantation of chromium with a donor (oxygen or sulfur) significantly increased the production yield of these centers. The family of chromium centers was successfully fabricated in type IIA diamond crystals, however, was not observed in ultra pure and in type Ib materials. This indicates that nitrogen plays an important role in the kinetics formation of these centers. At this stage the precise model of the center and its charge state are unknown.

6. A direct measurement of quantum efficiency of a single photon emitter in diamond was demonstrated for the first time. Employing ion implantation techniques the chromium centers were engineered in different proximities from the diamond surface. The dipole orientation was measured by recording the emission pattern of single emitters. The dipoles were found to be nearly orthogonal to the diamond air interface. Combining the imaging of the dipoles and measuring the decay rates of the emitters close to the diamond-air interface and in the unbounded medium, the quantum efficiency of the chromium centers was determined to be ~30%.
7. Photoluminescence excitation measurements recorded at cryogenic temperatures (~2 K) from the chromium related emitters embedded in the nanocrystals revealed an optical resonance linewidth of 4 GHz. This is the first photoluminescence excitation spectrum of a diamond based single photon emitter in the near infra-red. The spectral stability of the defects embedded in the nanocrystals showed spectral jumps in the millisecond range. Resonant excitation of chromium centers created by a shallow implantation was not successful due to extreme spectral diffusion. Such experiment with chromium related centers engineered deep inside a bulk diamond are currently undergoing and may lead towards a realization of indistinguishable single photons from color centers in diamond.

Outlook

Quantum information processing is dominating the research fields of solid state physics and quantum optics. Without any doubt, integrating a diamond based single photon emitter into a practical application to take advantage of its unique properties will be a milestone in the 21st century. Despite a great progress in the last decade in developing diamond as a suitable platform for quantum applications, there are yet a few obstacles to prevail.

In the near future, diamond emitters have to be integrated with emerging micro and nanophotonics structures for enhancing the photon collection. A successful integration should enhance the photon count rates above 1×10^7 counts/s. When such a technological gap is bridged, novel optical standards based on fundamental quantum phenomena would be possible. Furthermore, for quantum information processing, an integration of diamond emitter with diamond based photonic crystal cavity with high quality factor (Q) is necessary. Such a demonstration will endow with an "all diamond" platform, suitable for quantum technologies and metrology.

Mapping out the spin properties of the discovered chromium centers is the next trivial experiment to pursue. If optical spin readout is available in this system, it would be a revolutionary result. Exploring other optical centers in diamond may reveal new emitters, surpassing even the ultra bright chromium related centers. Furthermore, the scientific community has 'launched' a search for alternative systems to the most popular NV in diamond, which should have an optical spin read out associated to much better optical properties[263]. Finally, the discovery of a solid source emitting in the telecom wavelength of 1550 nm is an important and an accessible challenge.

For the integration of many components on a single chip, one may envisage diamond based emitters excited by an electrical pulse, a technique well established in a quantum dots community. This can be achieved through plasmonic coupling, which can mediate between the photonic and electronic components.

For biological applications, emission in the near infrared is highly desired to avoid interference with the auto-fluorescence of the cell. A major breakthrough can therefore arise from employing nanodiamonds hosting the ultra bright emitters as bio-markers. In

this respect, systematic studies of nanodiamond surfaces are crucial for better understanding of the physics of optical centers in single digit nanodiamonds. Modification of the surface to conjugate various biological species will be a central research in future years.

Diamond is no longer only a glamorous gemstone. It is now a leading player in exploiting quantum information effects and bringing the quantum technology from laboratory settings to commercial products. Generation of single photons and realization of qubits at room temperature is the commencement of a new diamond era. Sophisticated sculpturing of cavities and waveguides made of diamond, and increasing efforts to synthesize high quality material endow the scientists with a suitable platform to realize novel quantum devices. The perspectives of diamond in the quantum world are unlimited, and it is only a matter of time until the first diamond based quantum device emerges.

Bibliography

1. W. Lu and C.M. Lieber, *Nanoelectronics from the bottom up.* Nature Materials, **6,** 841-850 (2007)

2. E. Braun, Y. Eichen, U. Sivan, and G. Ben-Yoseph, *DNA-templated assembly and electrode attachment of a conducting silver wire.* Nature, **391,** 775-778 (1998)

3. C.H. Bennett and D.P. DiVincenzo, *Quantum information and computation.* Nature, **404,** 247-255 (2000)

4. A. Imamoglu, D.D. Awschalom, G. Burkard, D.P. DiVincenzo, D. Loss, M. Sherwin, and A. Small, *Quantum information processing using quantum dot spins and cavity QED.* Physical Review Letters, **83,** 4204-4207 (1999)

5. T.D. Ladd, F. Jelezko, R. Laflamme, Y. Nakamura, C. Monroe, and J.L. O'Brien, *Quantum computers.* Nature, **464,** 45-53 (2010)

6. N. Gisin, G.G. Ribordy, W. Tittel, and H. Zbinden, *Quantum cryptography.* Reviews of Modern Physics, **74,** 145-195 (2002)

7. A. Beveratos, R. Brouri, T. Gacoin, A. Villing, J.P. Poizat, and P. Grangier, *Single photon quantum cryptography.* Physical Review Letters, **89,** (2002)

8. R. Alleaume, F. Treussart, G. Messin, Y. Dumeige, J.F. Roch, A. Beveratos, R. Brouri-Tualle, J.P. Poizat, and P. Grangier, *Experimental open-air quantum key distribution with a single-photon source.* New Journal of Physics, **6,** (2004)

9. B. Lounis and M. Orrit, *Single-photon sources.* Reports on Progress in Physics, **68,** 1129-1179 (2005)

10. J.L. O'Brien, A. Furusawa, and J. Vuckovic, *Photonic quantum technologies.* Nature Photonics, **3,** 687-695 (2009)

11. E. Knill, R. Laflamme, and G.J. Milburn, *A scheme for efficient quantum computation with linear optics.* Nature, **409,** 46-52 (2001)

12. J.L. O'Brien, *Optical quantum computing.* Science, **318,** 1567-1570 (2007)

13. H.J. Kimble, M. Dagenais, and L. Mandel, *Photon anti-bunching in resonance fluorescence.* Physical Review Letters, **39,** 691-695 (1977)

14. C. Santori, M. Pelton, G. Solomon, Y. Dale, and E. Yamamoto, *Triggered single photons from a quantum dot.* Physical Review Letters, **86,** 1502-1505 (2001)

15. C. Santori, D. Fattal, J. Vuckovic, G.S. Solomon, and Y. Yamamoto, *Indistinguishable photons from a single-photon device.* Nature, **419,** 594-597 (2002)

16. M.B. Ward, T. Farrow, P. See, Z.L. Yuan, O.Z. Karimov, A.J. Bennett, A.J. Shields, P. Atkinson, K. Cooper, and D.A. Ritchie, *Electrically driven telecommunication wavelength single-photon source.* Applied Physics Letters, **90,** (2007)

17. V. Zwiller, T. Aichele, and O. Benson, *Quantum optics with single quantum dot devices.* New Journal of Physics, **6,** (2004)

18. A.D. Greentree, B.A. Fairchild, F.M. Hossain, and S. Prawer, *Diamond integrated quantum photonics.* Materials Today, **11,** 22-31 (2008)

19. C. Kurtsiefer, S. Mayer, P. Zarda, and H. Weinfurter, *Stable solid-state source of single photons.* Physical Review Letters, **85,** 290-293 (2000)

20. C.L. Wang, C. Kurtsiefer, H. Weinfurter, and B. Burchard, *Single photon emission from SiV centres in diamond produced by ion implantation.* Journal of Physics B-Atomic Molecular and Optical Physics, **39,** 37-41 (2006)

21. S.J. Devitt, A.G. Fowler, A.M. Stephens, A.D. Greentree, L.C.L. Hollenberg, W.J. Munro, and K. Nemoto, *Architectural design for a topological cluster state quantum computer.* New Journal of Physics, **11,** (2009)

22. J.R. Maze, P.L. Stanwix, J.S. Hodges, S. Hong, J.M. Taylor, P. Cappellaro, L. Jiang, M.V.G. Dutt, E. Togan, A.S. Zibrov, A. Yacoby, R.L. Walsworth, and M.D. Lukin, *Nanoscale magnetic sensing with an individual electronic spin in diamond.* Nature, **455,** 644-U41 (2008)

23. J.M. Taylor, P. Cappellaro, L. Childress, L. Jiang, D. Budker, P.R. Hemmer, A. Yacoby, R. Walsworth, and M.D. Lukin, *High-sensitivity diamond magnetometer with nanoscale resolution.* Nature Physics, **4,** 810-816 (2008)

24. G. Balasubramanian, I.Y. Chan, R. Kolesov, M. Al-Hmoud, J. Tisler, C. Shin, C. Kim, A. Wojcik, P.R. Hemmer, A. Krueger, T. Hanke, A. Leitenstorfer, R. Bratschitsch, F. Jelezko, and J. Wrachtrup, *Nanoscale imaging magnetometry with diamond spins under ambient conditions.* Nature, **455,** 648-U46 (2008)

25. F. Jelezko and J. Wrachtrup, *Read-out of single spins by optical spectroscopy.* Journal of Physics-Condensed Matter, **16,** R1089-R1104 (2004)

26. R. Hanson, F.M. Mendoza, R.J. Epstein, and D.D. Awschalom, *Polarization and readout of coupled single spins in diamond.* Physical Review Letters, **97,** (2006)

27. J.R. Rabeau, Y.L. Chin, S. Prawer, F. Jelezko, T. Gaebel, and J. Wrachtrup, *Fabrication of single nickel-nitrogen defects in diamond by chemical vapor deposition.* Applied Physics Letters, **86,** (2005)

28. E. Wu, J.R. Rabeau, G. Roger, F. Treussart, H. Zeng, P. Grangier, S. Prawer, and J.F. Roch, *Room temperature triggered single-photon source in the near infrared.* New Journal of Physics, **9,** (2007)

29. T. Gaebel, I. Popa, A. Gruber, M. Domhan, F. Jelezko, and J. Wrachtrup, *Stable single-photon source in the near infrared.* New Journal of Physics, **6,** 98-104 (2004)

30. H.P. Bovenkerk, F.P. Bundy, H.T. Hall, H.M. Strong, and R.H. Wentorf, *Preparation of diamond.* Nature, **184,** 1094-1098 (1959)

31. D.J. Poferl, N.C. Gardner, and J.C. Angus, *Growth of boron-doped diamond seed crystals by vapor deposition.* Journal of Applied Physics, **44,** 1428-1434 (1973)

32. M. Kamo, Y. Sato, S. Matsumoto, and N. Setaka, *Diamond synthesis from gas-phase in microwave plasma.* Journal of Crystal Growth, **62,** 642-644 (1983)

33. F.G. Celii and J.E. Butler, *Diamond chemical vapor deposition.* Annual Review of Physical Chemistry, **42,** 643-684 (1991)

34. O.A. Shenderova, V.V. Zhirnov, and D.W. Brenner, *Carbon nanostructures.* Critical Reviews in Solid State and Materials Sciences, **27,** 227-356 (2002)

35. V.Y. Dolmatov, *Detonation synthesis ultradispersed diamonds: Properties and applications.* Uspekhi Khimii, **70,** 687-708 (2001)

36. S.T. Lee, Z.D. Lin, and X. Jiang, *CVD diamond films: nucleation and growth.* Materials Science & Engineering R-Reports, **25,** 123-154 (1999)

37. www.azom.com,

38. J.E. Butler, Y.A. Mankelevich, A. Cheesman, J. Ma, and M.N.R. Ashfold, *Understanding the chemical vapor deposition of diamond: recent progress.* Journal of Physics-Condensed Matter, **21,** (2009)

39. K. Kobashi, K. Nishimura, Y. Kawate, and T. Horiuchi, *Synthesis of diamonds by use of microwave plasma chemical-vapor deposition - morphology and growth of diamond films.* Physical Review B, **38,** 4067-4084 (1988)

40. Z. Sitar, W. Liu, P.C. Yang, C.A. Wolden, R. Schlesser, and J.T. Prater, *Heteroepitaxial nucleation of diamond on nickel.* Diamond and Related Materials, **7,** 276-282 (1998)

41. M. Daenen, O.A. Williams, J. D'Haen, K. Haenen, and M. Nesladek, *Seeding, growth and characterization of nanocrystalline diamond films on various substrates.* Physica Status Solidi a-Applications and Materials Science, **203,** 3005-3010 (2006)

42. J.C. Arnault, L. Demuynck, C. Speisser, and F. Le Normand, *Mechanisms of CVD diamond nucleation and growth on mechanically scratched Si(100) surfaces.* European Physical Journal B, **11,** 327-343 (1999)

43. X. Jiang, C.P. Klages, R. Zachai, M. Hartweg, and H.J. Fusser, *Epitaxial diamond thin-films on (001) silicon substrates.* Applied Physics Letters, **62,** 3438-3440 (1993)

44. Y.C. Chen, X.Y. Zhong, A.R. Konicek, D.S. Grierson, N.H. Tai, I.N. Lin, B. Kabius, J.M. Hiller, A.V. Sumant, R.W. Carpick, and O. Auciello, *Synthesis and characterization of smooth ultrananocrystalline diamond films via low pressure bias-enhanced nucleation and growth.* Applied Physics Letters, **92,** 3 (2008)

45. Y. Chakk, R. Brener, and A. Hoffman, *Enhancement of diamond nucleation by ultrasonic substrate abrasion with a mixture of metal and diamond particles.* Applied Physics Letters, **66,** 2819-2821 (1995)

46. L.X. Shao, E.Q. Xie, D.Y. He, G.H. Chen, and K. Xu, *Nucleation and growth of CVD diamond films on smooth Si substrate pretreated by nanodiamond powders.* Journal of Inorganic Materials, **13,** 927-931 (1998)

47. J. Buhler and Y. Prior, *Study of morphological behavior of single diamond crystals.* Journal of Crystal Growth, **209,** 779-788 (2000)

48. T. Yano, D.A. Tryk, K. Hashimoto, and A. Fujishima, *Electrochemical behavior of highly conductive boron-doped diamond electrodes for oxygen reduction in alkaline solution.* Journal of the Electrochemical Society, **145,** 1870-1876 (1998)

49. J. Achard, F. Silva, O. Brinza, A. Tallaire, and A. Gicquel, *Coupled effect of nitrogen addition and surface temperature on the morphology and the kinetics of thick CVD diamond single crystals.* Diamond and Related Materials, **16,** 685-689 (2007)

50. C.J. Tang, A.J. Neves, S. Pereira, A.J.S. Fernandes, J. Gracio, and M.C. Carmo, *Effect of nitrogen and oxygen addition on morphology and texture of diamond films (from polycrystalline to nanocrystalline).* Diamond and Related Materials, **17,** 72-78 (2008)

51. F. Silva, J. Achard, X. Bonnin, O. Brinza, A. Michau, A. Secroun, K. De Corte, S. Felton, M. Newton, and A. Gicquel, *Single crystal CVD diamond growth strategy by the use of a 3D geometrical model: Growth on (113) oriented substrates.* Diamond and Related Materials, **17,** 1067-1075 (2008)

52. F. Silva, X. Bonnin, J. Achard, O. Brinza, A. Michau, and A. Gicquel, *Geometric modeling of homoepitaxial CVD diamond growth: I. The {100}{111}{110}{113} system.* Journal of Crystal Growth, **310,** 187-203 (2008)

53. H. Yamada, A. Chayahara, Y. Mokuno, H. Umezawa, S.-i. Shikata, and S.-i. Fujimori, *Fabrication of 1 Inch Mosaic Crystal Diamond Wafers.* Applied Physics Express, **3,** 051301 (2010)

54. Q. Liang, C.S. Yan, Y.F. Meng, J. Lai, S. Krasnicki, H.K. Mao, and R.J. Hemley, *Recent advances in high-growth rate single-crystal CVD diamond.* Diamond and Related Materials, **18,** 698-703 (2009)

55. A.M. Zaitsev, *optical properties of a diamond*. 1998.

56. A. Mainwood, F.P. Larkins, and A.M. Stoneham, *Structure and motion of the self-interstitial in diamond.* Solid-State Electronics, **21,** 1431-1433 (1978)

57. M.E. Newton, B.A. Campbell, D.J. Twitchen, J.M. Baker, and T.R. Anthony, *Recombination-enhanced diffusion of self-interstitial atoms and vacancy-interstitial recombination in diamond.* Diamond and Related Materials, **11,** 618-622 (2002)

58. H.E. Smith, G. Davies, M.E. Newton, and H. Kanda, *Structure of the self-interstitial in diamond.* Physical Review B, **69,** (2004)

59. D.J. Twitchen, D.C. Hunt, M.E. Newton, J.M. Baker, T.R. Anthony, and W.F. Banholzer, *Electron paramagnetic resonance (EPR) and optical absorption studies of defects created in diamond by electron irradiation damage at 100 and 350 K.* Physica B, **274,** 628-631 (1999)

60. D.C. Hunt, D.J. Twitchen, M.E. Newton, J.M. Baker, T.R. Anthony, W.F. Banholzer, and S.S. Vagarali, *Identification of the neutral carbon [100]-split interstitial in diamond.* Physical Review B, **61,** 3863-3876 (2000)

61. J.P. Goss, B.J. Coomer, R. Jones, T.D. Shaw, P.R. Briddon, M. Rayson, and S. Oberg, *Self-interstitial aggregation in diamond.* Physical Review B, **63,** (2001)

62. G. Davies, *Charge states of vacancy in diamond.* Nature, **269,** 498-500 (1977)

63. G. Davies, S.C. Lawson, A.T. Collins, A. Mainwood, and S.J. Sharp, *Vacancy-related centers in diamond.* Physical Review B, **46,** 13157-13170 (1992)

64. G. Davies and C.M. Penchina, *Effect of uniaxial stress on GR1 doublet in diamond.* Proceedings of the Royal Society of London Series a-Mathematical Physical and Engineering Sciences, **338,** 359-374 (1974)

65. J. Isoya, H. Kanda, Y. Uchida, S.C. Lawson, S. Yamasaki, H. Itoh, and Y. Morita, *EPR identification of the negatively charged vacancy in diamond.* Physical Review B, **45,** 1436-1439 (1992)

66. D.J. Twitchen, M.E. Newton, J.M. Baker, O.D. Tucker, T.R. Anthony, and W.F. Banholzer, *Electron-paramagnetic-resonance measurements on the di-<001>-split interstitial center (R1) in diamond.* Physical Review B, **54,** 6988-6998 (1996)

67. J.A. Vanwyk, O.D. Tucker, M.E. Newton, J.M. Baker, G.S. Woods, and P. Spear, *MAGNETIC-RESONANCE MEASUREMENTS ON THE (5)A(2) EXCITED-STATE OF THE NEUTRAL VACANCY IN DIAMOND.* Physical Review B, **52,** 12657-12667 (1995)

68. F.C. Warldermann, P. Olivero, J. Nunn, K. Surmacz, Z.Y. Wang, D. Jaksch, R.A. Taylor, I.A. Walmsley, M. Draganski, P. Reichart, A.D. Greentree, D.N. Jamieson, and S. Prawer, *Creating diamond color centers for quantum optical applications.* Diamond and Related Materials, **16,** 1887-1895 (2007)

69. M.A. Leawilson, J.N. Lomer, and J.A. Vanwyk, *ELECTRON-SPIN-RESONANCE OF THE R4/W6 DEFECT IN IRRADIATED DIAMOND.* Philosophical Magazine B-Physics of Condensed Matter Statistical Mechanics Electronic Optical and Magnetic Properties, **72,** 81-89 (1995)

70. D.J. Twitchen, M.E. Newton, J.M. Baker, T.R. Anthony, and W.F. Banholzer, *Electron-paramagnetic-resonance measurements on the divacancy defect center R4/W6 in diamond.* Physical Review B, **59,** 12900-12910 (1999)

71. W.V. Smith, P.P. Sorokin, I.L. Gelles, and G.J. Lasher, *Electron-spin resonance of nitrogen donors in diamond.* Physical Review, **115,** 1546-1552 (1959)

72. A. Mainwood, *Nitrogen and nitrogen-vacancy complexes and their formation in diamond.* Physical Review B, **49,** 7934-7940 (1994)

73. G. Davies, *A-nitrogen aggregate in diamond-its symmetry and possible structure.* Journal of Physics C-Solid State Physics, **9,** L537-L542 (1976)

74. G. Davies and M.F. Hamer, *Optical studies of 1.945 eV vibronic band in diamond.* Proceedings of the Royal Society of London Series a-Mathematical Physical and Engineering Sciences, **348,** 285-298 (1976)

75. X.F. He, N.B. Manson, and P.T.H. Fisk, *Paramagnetic-resonance of photoexcited N-V defects in diamond. 1. level anticrossing in the (3)A ground-state.* Physical Review B, **47,** 8809-8815 (1993)

76. X.F. He, N.B. Manson, and P.T.H. Fisk, *Paramagnetic-resonance of photoexcited N-V defects in diamond. 2. hyperfine interaction with the N-14 nucleus.* Physical Review B, **47,** 8816-8822 (1993)

77. M.H. Nazaré and A.J. Neves, *Properties, growth and applications of diamond* 2001: London : Institution of Electrical Engineers.

78. K. Iakoubovskii, G.J. Adriaenssens, and M. Nesladek, *Photochromism of vacancy-related centres in diamond.* Journal of Physics-Condensed Matter, **12,** 189-199 (2000)

79. Y. Mita, *Change of absorption spectra in type-Ib diamond with heavy neutron irradiation.* Physical Review B, **53,** 11360-11364 (1996)

80. T. Gaebel, M. Domhan, C. Wittmann, I. Popa, F. Jelezko, J. Rabeau, A. Greentree, S. Prawer, E. Trajkov, P.R. Hemmer, and J. Wrachtrup, *Photochromism in single nitrogen-vacancy defect in diamond.* Applied Physics B-Lasers and Optics, **82,** 243-246 (2006)

81. V.A. Nadolinny, A.P. Yelisseyev, J.M. Baker, M.E. Newton, D.J. Twitchen, S.C. Lawson, O.P. Yuryeva, and B.N. Feigelson, *A study of C-13 hyperfine structure in the EPR of nickel-nitrogen-containing centres in diamond and correlation with their optical properties.* Journal of Physics-Condensed Matter, **11,** 7357-7376 (1999)

82. A. Yelisseyev and H. Kanda, *Optical Centers related to 3d transition metals in diamond.* New Diamond and Frontier Carbon Technology, **17,** 127-178 (2007)

83. I. Kiflawi, H. Kanda, and S.C. Lawson, *The effect of the growth rate on the concentration of nitrogen and transition metal impurities in HPHT synthetic diamonds.* Diamond and Related Materials, **11,** 204-211 (2002)

84. M.H. Nazare, A.J. Neves, and G. Davies, *Optical studies of the 1.40-eV Ni center in diamond.* Physical Review B (Condensed Matter)|Physical Review B (Condensed Matter), **43,** 14196-205 (1991)

85. K. Iakoubovskii and G. Davies, *Vibronic effects in the 1.4-eV optical center in diamond.* Physical Review B, **70,** (2004)

86. V.A. Nadolinny, A.P. Yelisseyev, J.M. Baker, D.J. Twitchen, M.E. Newton, B.N. Feigelson, and O.P. Yuryeva, *Mechanisms of nitrogen aggregation in nickel- and cobalt-containing synthetic diamonds.* Diamond and Related Materials, **9,** 883-886 (2000)

87. A.T. Collins, H. Kanda, J. Isoya, C.A.J. Ammerlaan, and J.A. van Wyk, *Correlation between optical absorption and EPR in high-pressure diamond grown from a nickel solvent catalyst.* Diamond and Related Materials, **7,** 333-338 (1998)

88. A. Yelisseyev, S. Lawson, I. Sildos, A. Osvet, V. Nadolinny, B. Feigelson, J.M. Baker, M. Newton, and O. Yuryeva, *Effect of HPHT annealing on the*

photoluminescence of synthetic diamonds grown in the Fe-Ni-C system. Diamond and Related Materials, **12,** 2147-2168 (2003)

89. I.N. Kupriyanov, V.A. Gusev, Y.M. Borzdov, A.A. Kalinin, and Y.N. Pal'yanov, *Photoluminescence study of annealed nickel- and nitrogen-containing synthetic diamond.* Diamond and Related Materials, **8,** 1301-1309 (1999)

90. K. Iakoubovskii, *Ni-vacancy defect in diamond detected by electron spin resonance.* Physical Review B, **70,** (2004)

91. K. Iakoubovskii, A. Stesmans, B. Nouwen, and G.J. Adriaenssens, *ESR and optical evidence for a Ni vacancy center in CVD diamond.* Physical Review B, **62,** 16587-16594 (2000)

92. G. Balasubramanian, P. Neumann, D. Twitchen, M. Markham, R. Kolesov, N. Mizuochi, J. Isoya, J. Achard, J. Beck, J. Tissler, V. Jacques, P.R. Hemmer, F. Jelezko, and J. Wratchtrup, *Ultralong spin coherence time in isotopically engineered diamond.* Nature Materials, **8,** 383-387 (2009)

93. A.M. Edmonds, M.E. Newton, P.M. Martineau, D.J. Twitchen, and S.D. Williams, *Electron paramagnetic resonance studies of silicon-related defects in diamond.* Physical Review B, **77,** (2008)

94. A.M. Zaitsev, *Vibronic spectra of impurity-related optical centers in diamond.* Physical Review B, **61,** 12909-12922 (2000)

95. I.N. Kupriyanov, V.A. Gusev, Y.N. Pal'yanov, Y.M. Borzdov, and A.G. Sokol, *Photoluminescence excitation study of cobalt-related optical centers in high-pressure high-temperature diamond.* Diamond and Related Materials, **10,** 59-62 (2001)

96. R. Larico, L.V.C. Assali, W.V.M. Machado, and J.F. Justo, *Cobalt-related impurity centers in diamond: electronic properties and hyperfine parameters.* Journal of Physics-Condensed Matter, **20,** (2008)

97. S.C. Lawson, H. Kanda, K. Watanabe, I. Kiflawi, Y. Sato, and A.T. Collins, *Spectroscopic study of cobalt-related optical centers in synthetic diamond.* Journal of Applied Physics, **79,** 4348-4357 (1996)

98. A.A. Gippius and A.T. Collins, *Defect-induced structure of the 991.8 nm titanium luminescence line in diamond.* Solid State Communications, **88,** 637-638 (1993)

99. C.D. Clark, H. Kanda, I. Kiflawi, and G. Sittas, *silicon defects in diamond.* Physical Review B, **51,** 16681-16688 (1995)

100. G. Sittas, H. Kanda, I. Kiflawi, and P.M. Spear, *Growth and characterization of Si-doped diamond single crystals grown by the HTHP method.* Diamond and Related Materials, **5,** 866-869 (1996)

101. V.S. Vavilov, A.A. Gippius, A.M. Zaitsev, B.V. Deryagin, B.V. Spitsyn, and A.E. Aleksenko, *Investigation of the cathodoluminescence of epitaxial diamond films.* Soviet Physics Semiconductors-Ussr, **14,** 1078-1079 (1980)

102. J.P. Goss, R. Jones, S.J. Breuer, P.R. Briddon, and S. Oberg, *The twelve-line 1.682eV luminescence center in diamond and the vacancy-silicon complex.* Physical Review Letters, **77,** 3041-3044 (1996)

103. S. Prawer and R. Kalish, *Ion-beam induced transformation of diamond.* Physical Review B, **51,** 15711-15722 (1995)

104. R. Kalish. *Doping of diamond*. 1999.

105. R. Kalish, C. UzanSaguy, B. Philosoph, V. Richter, J.P. Lagrange, E. Gheeraert, A. Deneuville, and A.T. Collins. *Nitrogen doping of diamond by ion implantation*. 1997.

106. www.SRIM.org,

107. P.A. Stolk, H.J. Gossmann, D.J. Eaglesham, D.C. Jacobson, C.S. Rafferty, G.H. Gilmer, M. Jaraiz, J.M. Poate, H.S. Luftman, and T.E. Haynes, *Physical mechanisms of transient enhanced dopant diffusion in ion-implanted silicon.* Journal of Applied Physics, **81,** 6031-6050 (1997)

108. J.F. Prins, *Ion-implanted N-type diamond - electrical evidence.* Diamond and Related Materials, **4,** 580-585 (1995)

109. J.F. Prins, *Ion implantation of diamond for electronic applications.* Semiconductor Science and Technology, **18,** S27-S33 (2003)

110. J. Martin, R. Wannemacher, J. Teichert, L. Bischoff, and B. Kohler, *Generation and detection of fluorescent color centers in diamond with submicron resolution.* Applied Physics Letters, **75,** 3096-3098 (1999)

111. J.F. Prins. *Ion-implanted N-type diamond - electrical evidence*. 1995.

112. S. Prawer, C. Uzansaguy, G. Braunstein, and R. Kalish, *Can N-type doping of diamond be achieved by Li or Na ion-implantation.* Applied Physics Letters, **63,** 2502-2504 (1993)

113. K. Okano, S. Koizumi, S.R.P. Silva, and G.A.J. Amaratunga, *Low-threshold cold cathodes made of nitrogen-doped chemical-vapour-deposited diamond.* Nature, **381,** 140-141 (1996)

114. J. Meijer, B. Burchard, M. Domhan, C. Wittmann, T. Gaebel, I. Popa, F. Jelezko, and J. Wrachtrup, *Generation of single color centers by focused nitrogen implantation.* Applied Physics Letters, **87,** (2005)

115. J.R. Rabeau, P. Reichart, G. Tamanyan, D.N. Jamieson, S. Prawer, F. Jelezko, T. Gaebel, I. Popa, M. Domhan, and J. Wrachtrup, *Implantation of labelled single nitrogen vacancy centers in diamond using N-15.* Applied Physics Letters, **88,** 023113 (2006)

116. J. Meijer, S. Pezzagna, T. Vogel, B. Burchard, H.H. Bukow, I.W. Rangelow, Y. Sarov, H. Wiggers, I. Plumel, F. Jelezko, J. Wrachtrup, F. Schmidt-Kaler, W. Schnitzler, and K. Singer, *Towards the implanting of ions and positioning of nanoparticles with nm spatial resolution.* Applied Physics a-Materials Science & Processing, **91,** 567-571 (2008)

117. V.A. Martinovich, A.V. Turukhin, A.M. Zaitsev, and A.A. Gorokhovsky, *Photoluminescence spectra of xenon implanted natural diamonds.* Journal of Luminescence, **102,** 785-790 (2003)

118. A.A. Bergman, A.M. Zaitsev, and A.A. Gorokhovsky, *Polarization of luminescence and site symmetry of the Xe center in diamond.* Journal of Luminescence, **125,** 92-96 (2007)

119. A.M. Zaitsev, A.A. Bergman, A.A. Gorokhovsky, and M.B. Huang, *Diamond light emitting diode activated with Xe optical centers.* Physica Status Solidi a-Applications and Materials Science, **203,** 638-642 (2006)

120. A.A. Bergman, A.M. Zaitsev, M.B. Huang, and A.A. Gorokhovsky, *Photoluminescence and Raman studies of Xe ion-implanted diamonds: Dependence on implantation dose.* Journal of Luminescence, **129,** 1524-1526 (2009)

121. A.P. Yelisseyev, J.W. Steeds, Y.V. Babich, and B.N. Feigelson, *A new approach to investigation of nickel defect transformation in the HPHT synthetic diamonds using local optical spectroscopy.* Diamond and Related Materials, **15,** 1886-1890 (2006)

122. A.A. Gippius, V.S. Vavilov, A.M. Zaitsev, and B.S. Zhakupbekov, *Defects production and interaction in ion-implanted diamond.* Physica B & C, **116,** 187-194 (1983)

123. S. Prawer, *ION-IMPLANTATION OF DIAMOND AND DIAMOND FILMS.* Diamond and Related Materials, **4,** 862-872 (1995)

124. J.F. Prins, *ION-IMPLANTED STRUCTURES AND DOPED LAYERS IN DIAMOND.* Materials Science Reports, **7,** 271-364 (1992)

125. F. Fontaine, C. UzanSaguy, B. Philosoph, and R. Kalish, *Boron implantation in situ annealing procedure for optimal p-type properties of diamond.* Applied Physics Letters, **68,** 2264-2266 (1996)

126. C. Uzan-Saguy, R. Kalish, R. Walker, D.N. Jamieson, and S. Prawer, *Formation of delta-doped, buried conducting layers in diamond, by high-energy, B-ion implantation.* Diamond and Related Materials, **7,** 1429-1432 (1998)

127. C.A. Breeding and W.Y. Wang, *Occurrence of the Si-V defect center in natural colorless gem diamonds.* Diamond and Related Materials, **17,** 1335-1344 (2008)

128. H. Sternschulte, K. Thonke, R. Sauer, P.C. Munzinger, and P. Michler, *1.681-Ev Luminescence center in chemical-vapor-deposited homoepitaxial diamond films.* Physical Review B, **50,** 14554-14560 (1994)

129. T. Feng and B.D. Schwartz, *Characteristics and origin of the 1.681 eV luminescence center in chemical-vapor-deposited diamond films.* Journal of Applied Physics, **73,** 1415-1425 (1993)

130. http://www.mikroskopie.org/2008/01/26/types-of-confocal-microscopy/,

131. E. Rittweger, K.Y. Han, S.E. Irvine, C. Eggeling, and S.W. Hell, *STED microscopy reveals crystal colour centres with nanometric resolution.* Nature Photonics, **3,** 144-147 (2009)

132. R.H. Brown and R.Q. Twiss, *Correlation between photons in 2 coherent beams of light.* Nature, **177,** 27-29 (1956)

133. R. Alleaume, F. Treussart, J.M. Courty, and J.F. Roch, *Photon statistics characterization of a single-photon source.* New Journal of Physics, **6,** (2004)

134. M. Keller, B. Lange, K. Hayasaka, W. Lange, and H. Walther, *Continuous generation of single photons with controlled waveform in an ion-trap cavity system.* Nature, **431,** 1075-1078 (2004)

135. T. Aoki, B. Dayan, E. Wilcut, W.P. Bowen, A.S. Parkins, T.J. Kippenberg, K.J. Vahala, and H.J. Kimble, *Observation of strong coupling between one atom and a monolithic microresonator.* Nature, **443,** 671-674 (2006)

136. J. Beugnon, M.P.A. Jones, J. Dingjan, B. Darquie, G. Messin, A. Browaeys, and P. Grangier, *Quantum interference between two single photons emitted by independently trapped atoms.* Nature, **440,** 779-782 (2006)

137. D.L. Moehring, P. Maunz, S. Olmschenk, K.C. Younge, D.N. Matsukevich, L.M. Duan, and C. Monroe, *Entanglement of single-atom quantum bits at a distance.* Nature, **449,** 68-U48 (2007)

138. P. Michler, Imamo, and A. gbreve, *Quantum correlation among photons from a single quantum dot at room temperature.* Nature, **406,** 968-970 (2000)

139. X.Y. Wang, X.F. Ren, K. Kahen, M.A. Hahn, M. Rajeswaran, S. Maccagnano-Zacher, J. Silcox, G.E. Cragg, A.L. Efros, and T.D. Krauss, *Non-blinking semiconductor nanocrystals.* Nature, **459,** 686-689 (2009)

140. A.J. Bennett, R.B. Patel, A.J. Shields, K. Cooper, P. Atkinson, C.A. Nicoll, and D.A. Ritchie, *Indistinguishable photons from a diode.* Applied Physics Letters, **92,** (2008)

141. A. Hogele, C. Galland, M. Winger, and A. Imamoglu, *Photon antibunching in the photoluminescence spectra of a single carbon nanotube.* Physical Review Letters, **100,** (2008)

142. A. Tribu, G. Sallen, T. Aichele, R. Andre, J.P. Poizat, C. Bougerol, S. Tatarenko, and K. Kheng, *A High-Temperature Single-Photon Source from Nanowire Quantum Dots.* Nano Letters, **8,** 4326-4329 (2008)

143. T. Basche, W.E. Moerner, M. Orrit, and H. Talon, *Photon antibunching in the fluorescence of a single dye molecule trapped in a solid.* Physical Review Letters, **69,** 1516-1519 (1992)

144. C. Brunel, B. Lounis, P. Tamarat, and M. Orrit, *Triggered source of single photons based on controlled single molecule fluorescence.* Physical Review Letters, **83,** 2722-2725 (1999)

145. B. Lounis and W.E. Moerner, *Single photons on demand from a single molecule at room temperature.* Nature, **407,** 491-493 (2000)

146. C. Toninelli, K. Early, J. Bremi, A. Renn, S. Gotzinger, and V. Sandoghdar, *Near-infrared single-photons from aligned molecules in ultrathin crystalline films at room temperature.* Optics Express, **18,** 6577-6582 (2010)

147. A. Beveratos, R. Brouri, T. Gacoin, J.P. Poizat, and P. Grangier, *Nonclassical radiation from diamond nanocrystals.* Physical Review A, **64,** (2001)

148. A. Beveratos, S. Kuhn, R. Brouri, T. Gacoin, J.P. Poizat, and P. Grangier, *Room temperature stable single-photon source.* European Physical Journal D, **18,** 191-196 (2002)

149. J. Walker, *OPTICAL STUDY OF TR12 AND H-3 DEFECTS IN IRRADIATED DIAMOND.* Journal of Physics C-Solid State Physics, **10,** 3031-3037 (1977)

150. G. Davies, C. Foy, and K. Odonnell, *THE TR12 VIBRONIC BAND IN DIAMOND.* Journal of Physics C-Solid State Physics, **14,** 4153-4165 (1981)

151. B. Naydenov, R. Kolesov, A. Batalov, J. Meijer, S. Pezzagna, D. Rogalla, F. Jelezko, and J. Wrachtrup, *Engineering single photon emitters by ion implantation in diamond.* Applied Physics Letters, **95,** 3 (2009)

152. E. Ampem-Lassen, D.A. Simpson, B.C. Gibson, S. Trpkovski, F.M. Hossain, S.T. Huntington, K. Ganesan, L.C.L. Hollenberg, and S. Prawer, *Nano-manipulation of diamond-based single photon sources.* Optics Express, **17,** 11287-11293 (2009)

153. T. van der Sar, E.C. Heeres, G.M. Dmochowski, G. de Lange, L. Robledo, T.H. Oosterkamp, and R. Hanson, *Nanopositioning of a diamond nanocrystal containing a single nitrogen-vacancy defect center.* Applied Physics Letters, **94,** (2009)

154. M. Gregor, R. Henze, T. Schroder, and O. Benson, *On-demand positioning of a preselected quantum emitter on a fiber-coupled toroidal microresonator.* Applied Physics Letters, **95,** 153110 (2009)

155. S. Schietinger, M. Barth, T. Alchele, and O. Benson, *Plasmon-Enhanced Single Photon Emission from a Nanoassembled Metal-Diamond Hybrid Structure at Room Temperature.* Nano Letters, **9,** 1694-1698 (2009)

156. S. Schietinger, T. Schroder, and O. Benson, *One-by-One Coupling of Single Defect Centers in Nanodiamonds to High-Q Modes of an Optical Microresonator.* Nano Letters, **8,** 3911-3915 (2008)

157. V. Jacques, E. Wu, F. Grosshans, F. Treussart, P. Grangier, A. Aspect, and J.F. Roch, *Experimental realization of Wheeler's delayed-choice gedanken experiment.* Science, **315,** 966-968 (2007)

158. K.Y. Han, K.I. Willig, E. Rittweger, F. Jelezko, C. Eggeling, and S.W. Hell, *Three-Dimensional Stimulated Emission Depletion Microscopy of Nitrogen-Vacancy Centers in Diamond Using Continuous-Wave Light.* Nano Letters, **9,** 3323-3329 (2009)

159. V. Giovannetti, S. Lloyd, and L. Maccone, *Quantum metrology.* Physical Review Letters, **96,** (2006)

160. A.N. Boto, P. Kok, D.S. Abrams, S.L. Braunstein, C.P. Williams, and J.P. Dowling, *Quantum interferometric optical lithography: Exploiting entanglement to beat the diffraction limit.* Physical Review Letters, **85,** 2733-2736 (2000)

161. P. Kok, W.J. Munro, K. Nemoto, T.C. Ralph, J.P. Dowling, and G.J. Milburn, *Linear optical quantum computing with photonic qubits.* Reviews of Modern Physics, **79,** 135-174 (2007)

162. C.H. Bennett and G. Brassard. in *Proceedings of the IEEE International Conference on Computers, Systems and Signal Processing*. 1984. Bangalore: (IEEE, New York.

163. A.A. Bettiol, C.G. Ryan, D.N. Jamieson, and S. Prawer, *Imaging Ni segregation in synthetic diamond using ionoluminescence (IL) and particle induced X-ray*

emission (PIXE). Nuclear Instruments & Methods in Physics Research Section B-Beam Interactions with Materials and Atoms, **181,** 225-230 (2001)

164. L. Bischoff, *Alloy liquid metal ion sources and their application in mass separated focused ion beams.* Ultramicroscopy, **103,** 59-66 (2005)

165. A.S. Barnard, *Diamond standard in diagnostics: nanodiamond biolabels make their mark.* Analyst, **134,** 1751-1764 (2009)

166. A. Krueger, *Diamond nanoparticles: Jewels for chemistry and physics.* Advanced Materials, **20,** 2445-+ (2008)

167. A.M. Schrand, S.A.C. Hens, and O.A. Shenderova, *Nanodiamond Particles: Properties and Perspectives for Bioapplications.* Critical Reviews in Solid State and Materials Sciences, **34,** 18-74 (2009)

168. A. Tallaire, J. Achard, F. Silva, R.S. Sussmann, and A. Gicquel, *Homoepitaxial deposition of high-quality thick diamond films: effect of growth parameters.* Diamond and Related Materials, **14,** 249-254 (2005)

169. F. Silva, J. Achard, O. Brinza, X. Bonnin, K. Hassouni, A. Anthonis, K. De Corte, and J. Barjon, *High quality, large surface area, homoepitaxial MPACVD diamond growth.* Diamond and Related Materials, **18,** 683-697 (2009)

170. P.M. Martineau, M.P. Gaukroger, K.B. Guy, S.C. Lawson, D.J. Twitchen, I. Friel, J.O. Hansen, G.C. Summerton, T.P.G. Addison, and R. Burns, *High crystalline quality single crystal chemical vapour deposition diamond.* Journal of Physics-Condensed Matter, **21,** 8 (2009)

171. J. Achard, A. Tallaire, R. Sussmann, F. Silva, and A. Gicquel, *The control of growth parameters in the synthesis of high-quality single crystalline diamond by CVD.* Journal of Crystal Growth, **284,** 396-405 (2005)

172. O.A. Williams, O. Douheret, M. Daenen, K. Haenen, E. Osawa, and M. Takahashi, *Enhanced diamond nucleation on monodispersed nanocrystalline diamond.* Chemical Physics Letters, **445,** 255-258 (2007)

173. O.A. Williams, M. Daenen, J. D'Haen, K. Haenen, J. Maes, V.V. Moshchalkov, M. Nesladek, and D.M. Gruen, *Comparison of the growth and properties of ultrananocrystalline diamond and nanocrystalline diamond.* Diamond and Related Materials, **15,** 654-658 (2006)

174. J. Philip, P. Hess, T. Feygelson, J.E. Butler, S. Chattopadhyay, K.H. Chen, and L.C. Chen, *Elastic, mechanical, and thermal properties of nanocrystalline diamond films.* Journal of Applied Physics, **93,** 2164-2171 (2003)

175. T. Sharda, T. Soga, T. Jimbo, and M. Umeno, *Biased enhanced growth of nanocrystalline diamond films by microwave plasma chemical vapor deposition.* Diamond and Related Materials, **9,** 1331-1335 (2000)

176. W. Kulisch, C. Popov, H. Rauscher, L. Sirghi, T. Sasaki, S. Bliznakov, and F. Rossi, *Investigation of the nucleation and growth mechanisms of nanocrystalline diamond/amorphous carbon nanocomposite films.* Diamond and Related Materials, **17,** 1116-1121 (2008)

177. C.A. Rego, P.W. May, E.C. Williamson, M.N.R. Ashfold, Q.S. Chia, K.N. Rosser, and N.M. Everitt, *CVD diamond growth on germanium for IR window applications.* Diamond and Related Materials, **3,** 939-941 (1994)

178. P.W. May, H.Y. Tsai, W.N. Wang, and J.A. Smith, *Deposition of CVD diamond onto GaN.* Diamond and Related Materials, **15,** 526-530 (2006)

179. P.W. May, C.A. Rego, C.G. Trevor, E.C. Williamson, M.N.R. Ashfold, K.N. Rosser, and N.M. Everitt, *Deposition of diamond films on sapphire - studies of interfacial properties of and patterning techniques.* Diamond and Related Materials, **3,** 1375-1380 (1994)

180. J.R. Rabeau, A. Stacey, A. Rabeau, S. Prawer, F. Jelezko, I. Mirza, and J. Wrachtrup, *Single nitrogen vacancy centers in chemical vapor deposited diamond nanocrystals.* Nano Letters, **7,** 3433-3437 (2007)

181. J.R. Rabeau, S.T. Huntington, A.D. Greentree, and S. Prawer, *Diamond chemical-vapor deposition on optical fibers for fluorescence waveguiding.* Applied Physics Letters, **86,** (2005)

182. J. Achard, F. Silva, A. Tallaire, X. Bonnin, G. Lombardi, K. Hassouni, and A. Gicquel, *High quality MPACVD diamond single crystal growth: high microwave power density regime.* Journal of Physics D-Applied Physics, **40,** 6175-6188 (2007)

183. R. Samlenski, C. Haug, R. Brenn, C. Wild, R. Locher, and P. Koidl, *INCORPORATION OF NITROGEN IN CHEMICAL-VAPOR-DEPOSITION DIAMOND.* Applied Physics Letters, **67,** 2798-2800 (1995)

184. A. Secroun, O. Brinza, A. Tardieu, J. Achard, F. Silva, X. Bonnin, K. De Corte, A. Anthonis, M.E. Newton, J. Ristein, P. Geithner, and A. Gicquel, *Dislocation imaging for electronics application crystal selection.* Physica Status Solidi a-Applications and Materials Science, **204,** 4298-4304 (2007)

185. A. Tallaire, J. Achard, F. Silva, R.S. Sussmann, A. Gicquel, and E. Rzepka. *Oxygen plasma pre-treatments for high quality homoepitaxial CVD diamond deposition*. 2004: Wiley-V C H Verlag Gmbh.

186. C.J. Tang, S.M.S. Pereira, A.J.S. Fernandes, A.J. Neves, J. Gracio, I.K. Bdikin, M.R. Soares, L.S. Fu, L.P. Gu, A.L. Kholkin, and M.C. Carmo, *Synthesis and structural characterization of highly < 1 0 0 >-oriented {100}-faceted nanocrystalline diamond films by microwave plasma chemical vapor deposition.* Journal of Crystal Growth, **311,** 2258-2264 (2009)

187. S. Prawer and R.J. Nemanich, *Raman spectroscopy of diamond and doped diamond.* Philosophical Transactions of the Royal Society of London Series a-Mathematical Physical and Engineering Sciences, **362,** 2537-2565 (2004)

188. K.W. Sun, J.Y. Wang, and T.Y. Ko, *Raman spectroscopy of single nanodiamond: Phonon-confinement effects.* Applied Physics Letters, **92,** (2008)

189. S. Prawer, K.W. Nugent, D.N. Jamieson, J.O. Orwa, L.A. Bursill, and J.L. Peng, *The Raman spectrum of nanocrystalline diamond.* Chemical Physics Letters, **332,** 93-97 (2000)

190. J.E. Butler and I. Oleynik, *A mechanism for crystal twinning in the growth of diamond by chemical vapour deposition.* Philosophical Transactions of the Royal Society a-Mathematical Physical and Engineering Sciences, **366,** 295-310 (2008)

191. D. Shechtman, *Twin quintuplet surfaces in CVD diamond.* Journal of Materials Science, **41,** 7720-7724 (2006)

192. A. Kruger, F. Kataoka, M. Ozawa, T. Fujino, Y. Suzuki, A.E. Aleksenskii, A.Y. Vul, and E. Osawa, *Unusually tight aggregation in detonation nanodiamond: Identification and disintegration.* Carbon, **43,** 1722-1730 (2005)

193. E.D. Eidelman, V.I. Siklitsky, L.V. Sharonova, M.A. Yagovkina, A.Y. Vul, M. Takahashi, M. Inakuma, M. Ozawa, and E. Osawa, *A stable suspension of single ultrananocrystalline diamond particles.* Diamond and Related Materials, **14,** 1765-1769 (2005)

194. X.Y. Xu, Z.M. Yu, Y.W. Zhu, and B.C. Wang, *Influence of surface modification adopting thermal treatments on dispersion of detonation nanodiamond.* Journal of Solid State Chemistry, **178,** 688-693 (2005)

195. G.Z. Cao, J.J. Schermer, W.J.P. vanEnckevort, W. Elst, and L.J. Giling, *Growth of {100} textured diamond films by the addition of nitrogen.* Journal of Applied Physics, **79,** 1357-1364 (1996)

196. E. Wu, V. Jacques, H.P. Zeng, P. Grangier, F. Treussart, and J.F. Roch, *Narrow-band single-photon emission in the near infrared for quantum key distribution.* Optics Express, **14,** 1296-1303 (2006)

197. R. Kolesov, B. Grotz, G. Balasubramanian, R.J. Stohr, A.A.L. Nicolet, P.R. Hemmer, F. Jelezko, and J. Wrachtrup, *Wave-particle duality of single surface plasmon polaritons.* Nature Physics, **5,** 470-474 (2009)

198. J.P. Boudou, P.A. Curmi, F. Jelezko, J. Wrachtrup, P. Aubert, M. Sennour, G. Balasubramanian, R. Reuter, A. Thorel, and E. Gaffet, *High yield fabrication of fluorescent nanodiamonds.* Nanotechnology, **20,** (2009)

199. Y.R. Chang, H.Y. Lee, K. Chen, C.C. Chang, D.S. Tsai, C.C. Fu, T.S. Lim, Y.K. Tzeng, C.Y. Fang, C.C. Han, H.C. Chang, and W. Fann, *Mass production and dynamic imaging of fluorescent nanodiamonds.* Nature Nanotechnology, **3,** 284-288 (2008)

200. D.N. Jamieson, C. Yang, T. Hopf, S.M. Hearne, C.I. Pakes, S. Prawer, M. Mitic, E. Gauja, S.E. Andresen, F.E. Hudson, A.S. Dzurak, and R.G. Clark, *Controlled shallow single-ion implantation in silicon using an active substrate for sub-20-keV ions.* Applied Physics Letters, **86,** (2005)

201. C.C. Fu, H.Y. Lee, K. Chen, T.S. Lim, H.Y. Wu, P.K. Lin, P.K. Wei, P.H. Tsao, H.C. Chang, and W. Fann, *Characterization and application of single fluorescent nanodiamonds as cellular biomarkers.* Proceedings of the National Academy of Sciences of the United States of America, **104,** 727-732 (2007)

202. J. Tisler, G. Balasubramanian, B. Naydenov, R. Kolesov, B. Grotz, R. Reuter, J.P. Boudou, P.A. Curmi, M. Sennour, A. Thorel, M. Borsch, K. Aulenbacher, R. Erdmann, P.R. Hemmer, F. Jelezko, and J. Wrachtrup, *Fluorescence and Spin Properties of Defects in Single Digit Nanodiamonds.* Acs Nano, **3,** 1959-1965 (2009)

203. M. Wolfer, A. Kriele, O.A. Williams, H. Obloh, C.C. Leancu, and C.E. Nebel, *Nickel doping of nitrogen enriched CVD-diamond for the production of single photon emitters.* Physica Status Solidi a-Applications and Materials Science, **206,** 2012-2015 (2009)

204. K.J. Gordon, V. Fernandez, G.S. Buller, I. Rech, S.D. Cova, and P.D. Townsend, *Quantum key distribution system clocked at 2 GHz.* Optics Express, **13,** 3015-3020 (2005)

205. M.P. Hiscocks, K. Ganesan, B.C. Gibson, S.T. Huntington, F. Ladouceur, and S. Prawer, *Diamond waveguides fabricated by reactive ion etching.* Optics Express, **16,** 19512-19519 (2008)

206. A.A. Gorokhovsky, A.V. Turukhin, R.R. Alfano, and W. Phillips, *Photoluminescence vibration structure of Si center in chemical-vapor-deposited diamond.* Applied Physics Letters, **66,** 43-45 (1995)

207. D. Steinmetz, E. Neu, J. Meijer, W. Bolse, and C. Becher, *Single photon emitters based on Ni/Si related defects in single crystalline diamond.* arXiv:1007.0202v3 (2010)

208. S. Koizumi and M. Suzuki, *n-type doping of diamond.* Physica Status Solidi a-Applications and Materials Science, **203,** 3358-3366 (2006)

209. L. Bi, Y. He, J.Y. Feng, and Z.J. Zhang, *Nickel induced phase separation and nanocrystal growth in Si-rich silica films.* Nanotechnology, **17,** 2289-2293 (2006)

210. D.Y. Choi, J.H. Lee, D.S. Kim, and S.T. Jung, *Formation of plasma induced surface damage in silica glass etching for optical waveguides.* Journal of Applied Physics, **95,** 8400-8407 (2004)

211. M.W. McCutcheon and M. Loncar, *Design of a silicon nitride photonic crystal nanocavity with a Quality factor of one million for coupling to a diamond nanocrystal.* Optics Express, **16,** 19136-19145 (2008)

212. T.M. Babinec, B.J.M. Hausmann, M. Khan, Y.A. Zhang, J.R. Maze, P.R. Hemmer, and M. Loncar, *A diamond nanowire single-photon source.* Nature Nanotechnology, **5,** 195-199 (2010)

213. J.P. Hadden, J.P. Harrison, A.C. Stanley-Clarke, L. Marseglia, Y.-L.D. Ho, B.R. Patton, J.L. O'Brien, and J.G. Rarity, *Strongly enhanced photon collection from diamond defect centres under micro-fabricated integrated solid immersion lenses* arXiv:1006.2093 (2010)

214. D.A. Simpson, E. Ampem-Lassen, B.C. Gibson, S. Trpkovski, F.M. Hossain, S.T. Huntington, A.D. Greentree, L.C.L. Hollenberg, and S. Prawer, *A highly efficient two level diamond based single photon source.* Applied Physics Letters, **94,** 203107 (2009)

215. T.M. Hensen, M.J.A. de Dood, and A. Polman, *Luminescence quantum efficiency and local optical density of states in thin film ruby made by ion implantation.* Journal of Applied Physics, **88,** 5142-5147 (2000)

216. T.H. Maiman, *Stimulated optical radiation in ruby.* Nature, **187,** 493-494 (1960)

217. S. Strauf, N.G. Stoltz, M.T. Rakher, L.A. Coldren, P.M. Petroff, and D. Bouwmeester, *High-frequency single-photon source with polarization control.* Nature Photonics, **1,** 704-708 (2007)

218. B.R. Smith, D.W. Inglis, B. Sandnes, J.R. Rabeau, A.V. Zvyagin, D. Gruber, C.J. Noble, R. Vogel, E. Osawa, and T. Plakhotnik, *Five-Nanometer Diamond with Luminescent Nitrogen-Vacancy Defect Centers.* Small, **5,** 1649-1653 (2009)

219. J.Y. Cheung, C.J. Chunnilall, E.R. Woolliams, N.P. Fox, J.R. Mountford, J. Wang, and P.J. Thomas, *The quantum candela: a re-definition of the standard units for optical radiation.* Journal of Modern Optics, **54,** 373-396 (2007)

220. D.F. Nelson and M.D. Sturge, *RELATION BETWEEN ABSORPTION AND EMISSION IN REGION OF R LINES OF RUBY.* Physical Review, **137,** 1117-& (1965)

221. C. Santori, D. Fattal, S.M. Spillane, M. Fiorentino, R.G. Beausoleil, A.D. Greentree, P. Olivero, M. Draganski, J.R. Rabeau, P. Reichart, B.C. Gibson, S. Rubanov, D.N. Jamieson, and S. Prawer, *Coherent population trapping in diamond N-V centers at zero magnetic field.* Optics Express, **14,** 7986-U1 (2006)

222. H. Conzelmann, K. Graff, and E.R. Weber, *Chromium and chromium-boron pairs in silicon.* Applied Physics a-Materials Science & Processing, **30,** 169-175 (1983)

223. J. Schmidt, R. Krain, K. Bothe, G. Pensl, and S. Beljakowa, *Recombination activity of interstitial chromium and chromium-boron pairs in silicon.* Journal of Applied Physics, **102,** (2007)

224. F. Jelezko and J. Wrachtrup, *Single defect centres in diamond: A review.* Physica Status Solidi a-Applications and Materials Science, **203,** 3207-3225 (2006)

225. M. Pierre and M.I. Sargent, *Elements of quantum optics* 1999: New York : Springer, c1999.

226. www.qcvictoria.com,

227. R.J. Epstein, F.M. Mendoza, Y.K. Kato, and D.D. Awschalom, *Anisotropic interactions of a single spin and dark-spin spectroscopy in diamond.* Nature Physics, **1,** 94-98 (2005)

228. T.P.M. Alegre, C. Santori, G. Medeiros-Ribeiro, and R.G. Beausoleil, *Polarization-selective excitation of nitrogen vacancy centers in diamond.* Physical Review B, **76,** (2007)

229. S.A. Empedocles, R. Neuhauser, and M.G. Bawendi, *Three-dimensional orientation measurements of symmetric single chromophores using polarization microscopy.* Nature, **399,** 126-130 (1999)

230. F. Kaiser, V. Jacques, A. Batalov, P. Siyushev, F. Jelezko, and J. Wrachtrup, *Polarization properties of single photons emitted by nitrogen-vacancy defect in diamond at low temperature.* arXiv:0906.3426, (2009)

231. K.M.C. Fu, C. Santori, P.E. Barclay, L.J. Rogers, N.B. Manson, and R.G. Beausoleil, *Observation of the Dynamic Jahn-Teller Effect in the Excited States of Nitrogen-Vacancy Centers in Diamond.* Physical Review Letters, **103,** (2009)

232. P. Tamarat, T. Gaebel, J.R. Rabeau, M. Khan, A.D. Greentree, H. Wilson, L.C.L. Hollenberg, S. Prawer, P. Hemmer, F. Jelezko, and J. Wrachtrup, *Stark shift control of single optical centers in diamond.* Physical Review Letters, **97,** (2006)

233. A. Batalov, C. Zierl, T. Gaebel, P. Neumann, I.Y. Chan, G. Balasubramanian, P.R. Hemmer, F. Jelezko, and J. Wrachtrup, *Temporal coherence of photons emitted by single nitrogen-vacancy defect centers in diamond using optical Rabi-oscillations.* Physical Review Letters, **100,** (2008)

234. C. Santori, P. Tamarat, P. Neumann, J. Wrachtrup, D. Fattal, R.G. Beausoleil, J. Rabeau, P. Olivero, A.D. Greentree, S. Prawer, F. Jelezko, and P. Hemmer, *Coherent population trapping of single spins in diamond under optical excitation.* Physical Review Letters, **97,** (2006)

235. K.M.C. Fu, C. Santori, P.E. Barclay, I. Aharonovich, S. Prawer, N. Meyer, A.M. Holm, and R.G. Beausoleil, *Coupling of nitrogen-vacancy centers in diamond to a GaP waveguide.* Applied Physics Letters, **93,** 203107 (2008)

236. P.E. Barclay, K.M. Fu, C. Santori, and R.G. Beausoleil, *Hybrid photonic crystal cavity and waveguide for coupling to diamond NV-centers.* Optics Express, **17,** 9588-9601 (2009)

237. J. Isoya, H. Kanda, J.R. Norris, J. Tang, and M.K. Bowman, *FOURIER-TRANSFORM AND CONTINUOUS-WAVE EPR STUDIES OF NICKEL IN SYNTHETIC DIAMOND - SITE AND SPIN MULTIPLICITY.* Physical Review B, **41,** 3905-3913 (1990)

238. J. Michel, J.L. Benton, R.F. Ferrante, D.C. Jacobson, D.J. Eaglesham, E.A. Fitzgerald, Y.H. Xie, J.M. Poate, and L.C. Kimerling, *Impurity enhancement of the 1.54-MU-M Er3+ luminescence in silicon.* Journal of Applied Physics, **70,** 2672-2678 (1991)

239. P.N. Favennec, H. Lharidon, D. Moutonnet, M. Salvi, and M. Gauneau, *Optical activation of Er3+ implanted in silicon by oxygen impurities.* Japanese Journal of Applied Physics Part 2-Letters, **29,** L524-L526 (1990)

240. X. Brokmann, L. Coolen, M. Dahan, and J.P. Hermier, *Measurement of the radiative and nonradiative decay rates of single CdSe nanocrystals through a controlled modification of their spontaneous emission.* Physical Review Letters, **93,** (2004)

241. P.E. Barclay, K.M.C. Fu, C. Santori, and R.G. Beausoleil, *Chip-based microcavities coupled to nitrogen-vacancy centers in single crystal diamond.* Applied Physics Letters, **95,** 191115 (2009)

242. A. Kinkhabwala, Z.F. Yu, S.H. Fan, Y. Avlasevich, K. Mullen, and W.E. Moerner, *Large single-molecule fluorescence enhancements produced by a bowtie nanoantenna.* Nature Photonics, **3,** 654-657 (2009)

243. O.L. Muskens, V. Giannini, J.A. Sanchez-Gil, and J.G. Rivas, *Strong enhancement of the radiative decay rate of emitters by single plasmonic nanoantennas.* Nano Letters, **7,** 2871-2875 (2007)

244. T.H. Taminiau, F.D. Stefani, and N.F. van Hulst, *Single emitters coupled to plasmonic nano-antennas: angular emission and collection efficiency.* New Journal of Physics, **10,** (2008)

245. C. Vion, P. Spinicelli, L. Coolen, C. Schwob, J.M. Frigerio, J.P. Hermier, and A.E. Maitre, *Controlled modification of single colloidal CdSe/ZnS nanocrystal fluorescence through interactions with a gold surface.* Optics Express, **18,** 7440-7455 (2010)

246. M. Bohmer and J. Enderlein, *Orientation imaging of single molecules by wide-field epifluorescence microscopy.* Journal of the Optical Society of America B-Optical Physics, **20,** 554-559 (2003)

247. D. Patra, I. Gregor, J. Enderlein, and M. Sauer, *Defocused imaging of quantum-dot angular distribution of radiation.* Applied Physics Letters, **87,** (2005)

248. M.A. Lieb, J.M. Zavislan, and L. Novotny, *Single-molecule orientations determined by direct emission pattern imaging.* Journal of the Optical Society of America B-Optical Physics, **21,** 1210-1215 (2004)

249. J.J. Macklin, J.K. Trautman, T.D. Harris, and L.E. Brus, *Imaging and time-resolved spectroscopy of single molecules at an interface.* Science, **272,** 255-258 (1996)

250. B.C. Buchler, T. Kalkbrenner, C. Hettich, and V. Sandoghdar, *Measuring the quantum efficiency of the optical emission of single radiating dipoles using a scanning mirror.* Physical Review Letters, **95,** (2005)

251. A. Gruber, A. Drabenstedt, C. Tietz, L. Fleury, J. Wrachtrup, and C. vonBorczyskowski, *Scanning confocal optical microscopy and magnetic resonance on single defect centers.* Science, **276,** 2012-2014 (1997)

252. A.T. Collins, M.F. Thomaz, and M.I.B. Jorge, *Luminescence decay time of the 1.945 eV center in type IB diamond.* Journal of Physics C-Solid State Physics, **16,** 2177-2181 (1983)

253. R.M. Dickson, D.J. Norris, and W.E. Moerner, *Simultaneous imaging of individual molecules aligned both parallel and perpendicular to the optic axis.* Physical Review Letters, **81,** 5322-5325 (1998)

254. W. Lukosz and R.E. Kunz, *Fluorescence lifetime of magnetic and electric dipoles near a dielectric interface.* Optics Communications, **20,** 195-199 (1977)

255. X. Brokmann, L. Coolen, J.P. Hermier, and M. Dahan, *Emission properties of single CdSe/ZnS quantum dots close to a dielectric interface.* Chemical Physics, **318,** 91-98 (2005)

256. K. Sanaka, A. Pawlis, T.D. Ladd, K. Lischka, and Y. Yamamoto, *Indistinguishable Photons from Independent Semiconductor Nanostructures.* Physical Review Letters, **103,** (2009)

257. A. Kiraz, M. Ehrl, T. Hellerer, O.E. Mustecaplioglu, C. Brauchle, and A. Zumbusch, *Indistinguishable photons from a single molecule.* Physical Review Letters, **94,** (2005)

258. R. Lettow, V. Ahtee, R. Pfab, A. Renn, E. Ikonen, S. Gotzinger, and V. Sandoghdar, *Realization of two Fourier-limited solid-state single-photon sources.* Optics Express, **15,** 15842-15847 (2007)

259. V. Ahtee, R. Lettow, R. Pfab, A. Renn, E. Ikonen, S. Gotzinger, and V. Sandoghdar, *Molecules as sources for indistinguishable single photons.* Journal of Modern Optics, **56,** 161-166 (2009)

260. C.K. Hong, Z.Y. Ou, and L. Mandel, *Measurement of subpicosecond time intervals between 2 photons by interference.* Physical Review Letters, **59,** 2044-2046 (1987)

261. A.J. Bennett, R.B. Patel, C.A. Nicoll, D.A. Ritchie, and A.J. Shields, *Interference of dissimilar photon sources.* Nature Physics, **5,** 715-717 (2009)

262. Y. Shen, T.M. Sweeney, and H. Wang, *Zero-phonon linewidth of single nitrogen vacancy centers in diamond nanocrystals.* Physical Review B, **77,** (2008)

263. J.R. Weber, W.F. Koehl, J.B. Varley, A. Janotti, B.B. Buckley, C.G. Van de Walle, and D.D. Awschalom, *Quantum computing with defects.* Proceedings of the National Academy of Sciences of the United States of America, **107,** 8513-8518 (2010)

Appendix A. Normalization of the $g^{(2)}(\tau)$ function and the instrument response function.

The normalization of the $g^{(2)}(\tau)$ function is inferred from the recorded coincidence count rate, $c(\tau)$, and given by the following equation:

$$g^{(2)}(\tau) = \frac{c(\tau)}{R_1 R_2 T w} \quad \text{(A. 1)}$$

where T is the total integration time, R_1 and R_2 are the count rates recorded on each APD and w is width of the time bin. This normalization does not take into account any residual background light, associated with the emission.

To correct for the background, the count rate from the center only, S, and the count rate from the background only, B are defined (so that the total count rate is $S+B$). Then, the $g^{(2)}(\tau)$ can be written as:

$$g^{(2)}_{corr}(\tau) = [g^{(2)}(\tau) - (1-\rho^2)]/\rho^2 \quad \text{(A. 2)}$$

where $\rho = S/(S+B)$ and is measured independently for each run.

In single crystal diamond, the estimation of the background is typically performed by moving the laser few microns away from the center. In case of CVD nanodiamonds however, this method is not so accurate, since the grown crystals contain multiple centers and defects which are excited together with the center of interest. An alternative method is to measure the background by rotating the excitation polarization until minimum luminescence is achieved, and monitor the vanishing of the dip in the $g^{(2)}(\tau)$ function to confirm that the residual light has Poissonian statistics. This technique provides a more precise estimation of the background level.

Although theoretically, for a perfect single photon emitter the $g^{(2)}(0)$ should vanish completely, in an experiment, the normalized $g^{(2)}(0)$ never reaches zero, even if the signal to background is extremely high. The deviation from zero is attributed to the instrument response function (IRF), also known as temporal jitter, of the detectors and the electronics.

To achieve good fit of the experimental data, the fitting function should be the convolution of the theoretical $g^{(2)}(\tau)$ function (for a two/three level system) with the IRF. The IRF is given by:

$$J(\tau-\tau') = \frac{1}{\sqrt{2\pi}\sigma} e^{-\frac{(\tau-\tau')^2}{2\sigma^2}} \qquad \text{(A. 3)}$$

Where σ is the FWHM of the IRF function measured for our experimental setup (σ = 50 ps). Consequently, the measured second order correlation function is given by:

$$g^{(2)}_{meas}(\tau) = \int_{-\infty}^{\infty} J(\tau-\tau') g^{(2)}_{corr}(\tau') d\tau' \qquad \text{(A. 4)}$$

This function was used to fit the $g^{(2)}(\tau)$ functions in this thesis, unless otherwise stated.

Appendix B. List of Publications

Refereed journal publications

A. Stacey, **I. Aharonovich**, S. Prawer, and J.E. Butler, *"Controlled synthesis of high quality micro/nano-diamonds by microwave plasma chemical vapor deposition"*, Diamond and Related Materials 18, 51, (2009)

I. Aharonovich, C.Y. Zhou, A. Stacey, F. Treussart, J.F. Roch, and S. Prawer, *"Formation of color centers in nanodiamonds by plasma assisted diffusion of impurities from the growth substrate"*, Applied Physics Letters, 93, 243112, (2008).

I. Aharonovich, C.Y. Zhou, A. Stacey, J. Orwa, S. Castelletto, D. Simpson, A.D. Greentree, F. Treussart, J.F. Roch, and S. Prawer, *"Enhanced single-photon emission in the near infrared from a diamond color center"*, Physical Review B 79, 235316, (2009).

K.M.C. Fu, C. Santori, P.E. Barclay, **I. Aharonovich**, S. Prawer, N. Meyer, A.M. Holm, and R.G. Beausoleil, *"Coupling of nitrogen-vacancy centers in diamond to a GaP waveguide"*, Applied Physics Letters 93, 203107, (2008).

I. Aharonovich, S. Castelletto, D.A. Simpson, A. Stacey, J. McCallum, A.D. Greentree, and S. Prawer, *"Two-Level Ultrabright Single Photon Emission from Diamond Nanocrystals"*, Nano Letters, 9, 3191, (2009).

P. Siyushev, V. Jacques, **I. Aharonovich**, F. Kaiser, T. Muller, L. Lombez, M. Atature, S. Castelletto, S. Prawer, F. Jelezko, and J. Wrachtrup, *"Low-temperature optical characterization of a near-infrared single-photon emitter in nanodiamonds"*, New Journal of Physics, 11, 113029, (2009)

I. Aharonovich, C. Santori, B. A. Fairchild, J. Orwa, K. Ganesan, K.M.C. Fu, R.G. Beausoleil, A. D. Greentree, and S. Prawer, *"Producing optimized ensembles of nitrogen-*

vacancy color centers for quantum information applications", Journal of Applied Physics 106, 124904 (2009)

J. O. Orwa, **I. Aharonovich**, F. Jelezko, G. Balasubramanian, P. Balog, M. Markham, D. J. Twitchen, A. D. Greentree, and S. Prawer, *"Nickel related optical centers in diamond created by ion implantation"*, Journal of Applied Physics 107, 093512 (2010)

I. Aharonovich, S. Castelletto, D.A. Simpson, B. C. Johnston, J. McCallum, A. D. Greentree, and S. Prawer, *"Chromium single-photon emitters in diamond fabricated by ion implantation"*, Physical Review B, 81, 121201 (R) (2010).

I. Aharonovich, S. Castelletto, D. A. Simpson, A. D. Greentree, and S. Prawer, *"Photophysics of novel diamond based single photon emitters"*, Physical Review A, 81, 043813, (2010)

S. Castelletto, **I. Aharonovich**, B. Gibson, B. Johnson and S. Prawer, *"Imaging and quantum efficiency measurement of chromium emitters in diamond"*, Physical Review Letters, in press (2010)

Conference presentations (Oral)

I. Aharonovich et al., "*Fabrication of Nickel single photon centres in diamond for quantum optical applications*", International Conference of Nanoscience and Nanotechnology (ICONN), 2008, Melbourne, Australia

I. Aharonovich et al., "*Fabrication of Nickel single photon centres in diamond for quantum optical applications*", New Diamond and Nano Carbon (NDNC), 2008, Taipei, Taiwan

I. Aharonovich et al., "*Fabrication of Nickel single photon centres in diamond for quantum optical applications*", International conference on electronic materials (ICEM), 2008, Sydney, Australia

I. Aharonovich et al., "*Towards Diamond based ultra bright single photon source*", Hole Burning and Single Molecules (HBSM), 2009, Palm Cove, Australia

I. Aharonovich et al., "*Ultra bright single photon emission from diamond nanocrystals*" European Conference on Diamond and Related materials, 2009, Athens, Greece
I. Aharonovich et al., "*Ultra bright single photon emission from diamond nanocrystals*" Materials Research Society-Falls Meeting, 2009, Boston, USA

I. Aharonovich et al., "*Ultra bright single photon emission from diamond nanocrystals*" International Conference of Nanoscience and Nanotechnology (ICONN), 2010, Sydney, Australia

I. Aharonovich et al., "*Novel single photon emitters based on color centers in diamond*" International Conference of Physics of Semiconductors (ICPS), 2010, Seoul, Korea

I. Aharonovich et al., ***Invited talk*** "*Impurities in diamond: new sources for quantum communications*" SPIE, 2010, San Diego, USA

Refereed conference proceedings

J.O. Orwa, A.D. Greentree, **I. Aharonovich**, A.D.C. Alves, J. Van Donkelaar, A. Stacey and S. Prawer, "*Fabrication of single optical centers in diamond - a review*", Journal of Luminescence, (2010) Proceedings of HBSM 2009

I. Aharonovich and S. Prawer, "*Fabrication strategies for diamond based ultra bright single photon sources*", Diamond and Related Materials, (2010) Proceedings of European Conference on Diamond and Related materials, 2009

Patents

I. Aharonovich and S. Prawer, "*A Method for fabricating a material*", PCT/AU2009/000877